Laser Direct Deposition of Metal Matrix Diamond Composite

by

Mehrdad Iravani-Tabrizipour

A thesis
presented to the University of Waterloo
in fulfillment of the
thesis requirement for the degree of
Doctor of Philosophy
in
Mechanical and Mechatronics Engineering

Waterloo, Ontario, Canada, 2015

Author's Declaration

I hereby declare that I am the sole author of this thesis. This is a true copy of the thesis, including any required final revisions, as accepted by my examiners.

I understand that my thesis may be made electronically available to the public.

Abstract

Diamond, the hardest natural material known to humankind, is an ideal candidate for cutting and wear application, however implementing diamond in tooling is not without its challenges. Consequentially, these challenges cause diamond tools to be very expensive. Additionally, current diamond tools do not capitalize on the full potential of diamond material properties. The most significant challenge associated with using diamond in tooling is trying to avoid diamond graphitization at high temperatures during the tool manufacturing process. Finding an alternative way to fabricate improved performance and better priced diamond tools will revolutionize tooling industry. Laser direct deposition of diamond particles has the potential for production of higher performance and lower priced diamond tools. This is largely due to the low interaction time and high cooling rates involved with the deposition process. The process zone is exposed to high temperatures for a very short time and is followed by very high cooling rates.

This research investigates the deposition of a metal matrix diamond composite on mild steel, addressing the associated issues and challenges with the deposition process. These issues include the decomposition of diamond, diamond particle wetting, chemical bonding of the diamond particles and the matrix, diamond retention capacity of the matrix, clad-substrate bonding, porosity and micro cracks, and diamond particles distribution in the deposited clad.

A transient three dimensional temperature dependent finite element model for pre-placed laser cladding is developed in order to develop insight into the process window. The model is developed by ANSYS © finite element software. The governing equations, boundary conditions and assumptions used in the model are discussed. Additionally the effects of the direct laser deposition process parameters on the melt pool temperature,

cooling rate, and exposure time to high temperatures are investigated. The influence of process parameters on the increase of the melt pool temperature during deposition of a clad is also studied.

An experimental study on deposition of ((Cu80Sn20)90Ti10)75+25 diamond weight percent via pre-placed laser cladding on a mild steel substrate is presented. The effects of using both a continuous wave and pulsed laser deposition are explored. The effects of process parameters on diamond decomposition, clad-substrate bonding, porosity and micro-cracks, wetting and chemical bonding of diamond particles, diamond particles distribution in the deposited clad, and the effect of dilution are investigated. The experimental results are in agreement with the trends predicted by the modeling.

Both the modeling and pre-placed laser deposition experiments provide an estimation of the process window for blown powder laser deposition. Extensive sets of experiments are conducted for the deposition by blown powder laser cladding. Cross sectional analysis is performed on both transverse and longitudinal cut-planes of the deposited clads. This is performed using Scanning Electron Microscope, Energy-Dispersive X-ray spectroscopy, and nano-indentation. Deposited diamond particles are characterized by Raman spectroscopy and a trend demonstrating reduced diamond graphitization is detected.

A study of deposited diamond particles reveals that an interfacial titanium carbide layer is formed between diamond particles and the matrix. This layer is only formed when iron is not present at the vicinity of the diamond particles. In the presence of iron, it forms the interfacial layer which is surrounded by a titanium rich layer. This observation indicates that iron has higher affinity to react with diamond as opposed to titanium. It is also observed that the iron reaction with diamond results in diamond degradation and graphitization.

A thermal analysis study of reaction of each elements of the matrix Reaction of each elements of the matrix (titanium, copper, and tin) and iron with diamond up to the temperature of 1300°C is conducted using Differential Scanning Calorimetry. This study reveals that mechanism of reaction between titanium and diamond is completely different from that of iron and diamond. It is found that reaction of titanium with diamond initiates when titanium transforms from α to β at 880-900°C. The formation of a titanium carbide layer starts at this temperature by diffusing titanium into the surface of diamond particles which results in nucleation of titanium carbide on the diamond surface. As this layer grows, the diffusion of titanium into the surface of the diamond becomes more difficult, thus the growth of the titanium carbide layer slows down until stops completely at a certain thickness. Graphitization of diamond does not occur. When the thickness of the titanium carbide layer reaches its maximum, it becomes brittle in a way that can be separated from the diamond particle. The reaction of iron-diamond initiates before transformation of ferrite to austenite begins (below 900°C). It starts via diffusion of detached carbon atoms from the diamond into the iron particles and continues until the melting of the solution at around 1150°C. The melting causes higher levels of diamond decomposition and higher solution of carbon in iron. This results in extreme degradation of diamond particles. Although the solubility of carbon in iron is limited, detaching of carbon atoms from diamond continues past the solubility limit, resulting in super saturation of iron matrix and presence of large graphite inclusions in the iron matrix. On the other hand, iron diffuses into the decomposed diamond particles accelerating the decomposition. This results in a significant carbon atoms detachment from the diamond particles. As a result, high fraction of the remaining carbon atoms decompose to graphite or react with the iron. In fact, not only does the iron react with the diamond, but it also acts as a catalyzer for diamond graphitization. The DSC study reveals that copper and tin neither react nor wet

the diamond particles.

It is found that diamond-laser interaction before reaching the melt-pool plays an important role in diamond graphitization. Therefore, the effect of process parameters on the diamond-laser interaction are studied and optimized to obtain the minimum laser-diamond interaction as well as minimum temperature rise in diamond particles before joining the molten pool. Experimental analysis indicates that the temperature rise of diamond particles passing the laser beam is only partially responsible for diamond graphitization. Diamond reaction with oxygen at the elevated temperatures due to laser interaction is determined to be the major element of diamond graphitization. A specialized nozzle is designed to provide better protection of the powder stream against the penetration of oxygen. The nozzle design accomplishes this by providing an annular inert gas stream which surrounds the powder stream. Employing this specialized nozzle in conjunction with optimized deposition process parameters significantly reduces diamond graphitization.

Optimum process parameters which can minimize the dilution are determined by experimental analysis. Using these parameters, diamond degradation in the deposition is drastically reduced. In an attempt to further eliminate the dilution of deposition by iron, as well as decrease the effective input energy into the process zone an intermediate layer with the composition of Cu-20Sn weight percent is added. The intermediate layer has a thickness of approximately 0.5 mm and is deposited directly on the mild steel substrate. Deposition of the metal matrix-diamond particles on the intermediate layer results in elimination of dilution and almost no graphitization. An interfacial titanium carbide layer with a thickness in the range of 150-350 nm is observed.

The substrates with and without the intermediate layer are pre-heated to 700°C prior to performing the deposition. The pre-heating decreases the required effective input energy by approximately 16.7 to 17.5 percent for the substrate without intermediate layer and

around 15 percent for the substrate with intermediate layer. The preheating has no effect on presence of iron in the deposition on the substrates with the intermediate layer, since without pre-heating, the presence of iron in the deposit is already negligible; however it reduces the dilution in the deposition on the substrates when no intermediate layer is present.

Effects of process parameters on dilution, clad substrate bonding, and aspect ratio are studied. Using experimental analysis, an equation is developed to calculate the aspect ratio from the process parameters. Furthermore, for minimizing dilution, obtaining strong clad-substrate bonding, and obtaining acceptable aspect ratio a set of inequalities (constraints) to be satisfied by process parameters is determined. From these constraints the process window is obtained.

In summary, through theoretical and experimental studies, this research develops a practical and reliable metal matrix diamond composite fabrication technology using laser deposition technique. The new fabrication technology can be used in developing high performance tools and highly wear resistance surfaces.

Acknowledgements

I am forever indebted to my supervisor, professor Amir Khajepour, who with great energy and devotion led me during my PhD. Special thanks to my co-supervisor, professor Shahrzad Esmaeili, whom this would have not been accomplished without her support. Many thanks to the committee members of my Ph.D., professor Ehsan Toyserkani, professor Mary Wells, and professor Walter Duley, who were a source of help and constructive suggestions. Many thanks to the external examiner, professor Daolun Chen for taking the time to review my thesis and provide valuable constructive recommendations.

Many people either directly or indirectly supported me during this PhD. I would like to thank them all specially those who I forgot to mention their names here. My gratitude to my colleagues and friends at University of Waterloo who I had the privilege to work or spend time with: Masoud Alimardani, Christ Paul, Meysar Zeinali, Jeff McIssac, Ali Emamian, Vahid Fallah, Arshad Harooni, Mohammad Farshidianfar, Soroush Hassanpour, Kamran Shavezipur, Farnaz Maleki, Mohsen Azimi, Saman Mohammadi, Ali Najafi, Ali Hosseini, Babak Ebrahimi, Sara Aghakazem, Niki Makki, Dariush Ghaffari, Masoud Ansari, Hamidreza Alemohammad, Mihaela Vlasea, Ehsan Hashemi, Pegah Pezeshkpour, Mark Whitby, Amir Azhari, Saeed Khosravani, Mojgan Ghareh, Keivan Ahmadi, Roozbeh Borjian, Sherry Toufighian, Nasim Paryab, Philip Meszaros, Yaser Shanjani, Andrew Pinkerton, Negar Rasti, Ahmad Basalah, Hanieh Aghighi, Laleh Durali, Hamed Jamshidifar, Mansour Ataei, Yadollah Rasekhipour, Mohammad Pirani, Reza Zarringhalam, Milad Jalali, Milad Khazraee, Yahya Mahmood khani, Pedram Mehraram, Reza Mirmiri, Ali Roostaei, Andre Bodo, Hasan Toplar, Peyman Karimi, Khanh Nguyen, Ankur Agrawal, Abtin Athari, Mohammad Basiri, Omid Aminfar, Ramesh Periasmary, Homeyra Pourmohammadali, Orang VahidAraghi, Sina Valadkhan, Brian Fan, Ayyoub Rezaeeian, Neda Darvandi, Alireza Kasaiezadeh, Mohamad Pournazari, Amir Fazeli, Matthew Asselin,

Amin Kamalzadeh, Shahin Karimi, Saleh Tabandeh, Mohammad Biglarbeigian, Hamid Bolandhemat, Panthea Sepehrband and Philippe Meszaros.

I would also like to acknowledge the financial support from the National Resources and Engineering Research Council Canada Graduate Scholarship (NSERC), the Government of Ontario for the Ontario Graduate Scholarship (OGS), University of Waterloo for President's Graduate Scholarship and Mechanical and Mechatronics Engineering Graduate Scholarship.

Last but not least, I want to thank my parents, Ahmad and Fatemeh, and my brothers, Amir and Milad. They have been there for me whenever I have needed them. There are no words to express how much that means to me.

Dedication

To my beloved parents

Table of Contents

[1]This nozzle was designed by the author. It was built, developed, and characterized by Arshad Harooni.

List of Tables

List of Figures

Nomenclature

(I_D/I_G) intergrated intensity ratio of D band over G band , see equation (4.4), page 76

α percentage of voidage in powder bed, see equation (3.32), page 53

α concentration of graphitized diamond, see equation (2.11), page 20

β absorptivity, see equation (3.19), page 44

β absorptivity, see equation (3.28), page 52

β absorptivity, see equation (3.4), page 40

β_p absorptivity of laser beam by powder particles, see equation (3.13), page 43

β_w substrate absorptivity, see equation (3.14), page 43

ΔT_p temperature increase of a powder particle before reaching the melt pool, see equation (6.1), page 149

$\Delta\omega$ Raman shift, see equation (4.3), page 74

$\dot{m}_p$ powder feed rate, see equation (3.12), page 42

ϵ_t emissivity, see equation (3.4), page 40

η_p powder catchment efficiency, see equation (3.13), page 43

Γ irradiated surface area by laser beam, see equation (3.4), page 40

Γ laser irradiated surface area, see equation (3.28), page 52

γ surface tension, see equation (3.6), page 41

λ wavelength in a vaccum, see equation (6.5), page 155

λ_l wavelength of laser, see equation (4.3), page 74

λ_s wavelength of scattered light, see equation (4.3), page 74

$\mathbf{n}$ normal vector of the surface, see equation (3.4), page 40

$\mathbf{U}$ scanning velocity of laser beam, see equation (3.1), page 39

μ viscosity, see equation (3.2), page 39

ν growth rate, see equation (2.9), page 15

ν_p powder particles velocity, see equation (3.12), page 42

Ω powder bed surface, see equation (3.28), page 52

Ω workpiece surfaces, see equation (3.4), page 40

$\partial T/\partial t$ cooling rate, see equation (3.34), page 59

ρ density of particle, see equation (6.8), page 171

ρ density of powder, see equation (3.12), page 42

ρ density of the powder particles, see equation (3.22), page 49

ρ density, see equation (3.1), page 39

ρ_{tot} density of diamond
, see equation (6.9), page 173

ρ_{tot} density of mixture of diamond particles and the matrix
, see equation (6.9), page 173

ρ_f density of the liquid, see equation (6.7), page 171

ρ_p density of a powder particle, see equation (6.1), page 150

σ Stefan-Boltzman constant, see equation (3.4), page 40

τ interaction time, see equation (4.7), page 89

θ_{jet} angle of powder jet with respect to horizontal line, see equation (3.12), page 42

$\triangle H_{Fe}$ energy of transformation of pure iron for currie temperature, see equation (5.1), page 128

$\triangle H_{mix}$ energy of transformation of the mixture for Currie temperature, see equation (5.1), page 128

A spread area, see equation (3.22), page 49

A_0 pre-exponential factor, see equation (2.11), page 20

a_α absorpivity, see equation (6.1), page 150

a_α absorptivity coefficient, see equation (6.15), page 175

a_α absorptivity coefficient, see equation (6.19), page 177

A_p cross section area of a particle, see equation (6.1), page 149

B buoyancy force, see equation (6.7), page 171

b a constant, see equation (6.18), page 177

c correction factor, see equation (3.33), page 54

c_p specific heat capacity, see equation (3.1), page 39

c_p specific heat, see equation (6.1), page 149

D laser beam diameter on the substrate, see equation (6.15), page 175

d laser beam diameter, see equation (4.7), page 89

D_0 bond dissociation energy, see equation (2.12), page 20

d_b laser beam diameter, see equation (6.3), page 150

E energy per pulse, see equation (4.1), page 69

$E_{\min}$ minimum energy required to deposit a continuous clad on a substrate, see equation (6.16), page 176

E_{ac} activation energy, see equation (2.11), page 20

E_{eff} power density as energy input into the unit area of process zone per unit time, see equation (6.19), page 177

E_l excitation laser energy used in Raman spectroscopy, see equation (4.4), page 75

f fraction transformation, see equation (2.9), page 15

f pulse frequency, see equation (4.1), page 69

$f(x, y, z, t)$ function presenting the melt pool-substrate interface, see equation (3.9), page 41

f_{Fe} mass fraction of iron in the mixture, see equation (5.1), page 128

$f_{m_{\text{dia}}}$ mass fraction of diamond, see equation (6.9), page 173

f_{net} net buoyancy force acting on the particle, see equation (6.8), page 171

$f_{V_{\text{dia}}}$ volume fraction of diamond particle in the mixture
, see equation (6.9), page 173

G Gibbs free energy, see equation (2.1), page 11

g standard gravity, see equation (3.2), page 39

g standard gravity, see equation (6.7), page 171

H enthalpy, see equation (2.1), page 11

h height of clad, see equation (6.14), page 175

$H(T)$ enthalpy, see equation (3.23), page 50

H_c height of the clad, see equation (3.21), page 44

h_c convection coefficient, see equation (3.28), page 52

h_c heat convection coefficient, see equation (3.4), page 40

I laser beam intensity, see equation (6.1), page 149

I light intensity, see equation (6.5), page 155

$I(x, y, z, t)$ laser energy distribution on the surface, see equation (3.4), page 40

I_0 intensity scale factor, see equation (3.27), page 51

I_0 original intensity, see equation (6.5), page 155

K thermal conductivity, see equation (3.19), page 44

K thermal conductivity, see equation (3.34), page 59

K thermal contact conductance of the powder bed-substrate interface, see equation (3.25), page 50

k Boltzmann's constant, see equation (2.6), page 13

k aspect ratio, see equation (6.14), page 175

k extinction coefficient, see equation (6.5), page 155

k thermal conductivity, see equation (3.1), page 39

$K(T)$ temperature dependent conductivity of metal in liquid state, see equation (3.33), page 54

K_{air} thermal conductivity of air filled spaces between powder particles, see equation (3.32), page 53

K_e effective conductivity of powder bed below melting point, see equation (3.32), page 53

$K_e(T)$ effective conductivity in the presence of thermocapilary flow, see equation (3.33), page 54

K_p thermal conductivity of powder material in bulk form, see equation (3.32), page 53

L_a in-plane crystallite size, see equation (4.4), page 75

L_m latent heat of fusion, see equation (3.24), page 50

m mass of the spread powder, see equation (3.22), page 49

m_{dia} mass of diamond particles
, see equation (6.9), page 173

m_{tot} total mass of diamond particles and the matrix
, see equation (6.9), page 173

m_p mass of a particle, see equation (6.1), page 149

N nucleation rate, see equation (2.9), page 15

n numerical exponent, see equation (2.9), page 15

P equivalent power, see equation (4.1), page 69

P laser output power, see equation (6.15), page 175

P laser power, see equation (3.27), page 51

P laser power, see equation (6.2), page 150

P pressure, see equation (2.4), page 12

p pressure, see equation (3.2), page 39

P_{at} attenuated power, see equation (3.12), page 42

P_{eff} absorbed power, see equation (3.34), page 59

P_l laser power, see equation (3.19), page 44

P_l average laser power, see equation (3.12), page 42

Q specific power, see equation (3.1), page 39

Q transferred heat to a particle by passing through the laser beam, see equation (6.1), page 149

q heat flux, see equation (3.25), page 50

R clad surface curvature, see equation (3.6), page 41

R universal constant, see equation (2.8), page 14

R universal gas constant, see equation (2.11), page 20

r distance from center of the laser beam, see equation (3.27), page 51

r_0 beam radius, see equation (3.27), page 51

r_0 laser beam radius, see equation (3.19), page 44

r_{jet} powder jet radius, see equation (3.12), page 42

r_b beam radius, see equation (6.2), page 150

r_l beam radius, see equation (3.12), page 42

r_p radius of a particle, see equation (6.1), page 150

r_p radius of powder particles, see equation (3.12), page 42

S entropy, see equation (2.1), page 11

s attenuation coefficient, see equation (6.15), page 175

s attenuation coefficient, see equation (6.19), page 177

S_c area of the melt pool, see equation (3.21), page 44

T melting point of surface, see equation (3.34), page 59

T temperature, see equation (2.11), page 20

T temperature, see equation (2.1), page 11

T temperature, see equation (3.1), page 39

t thickness of powder bed, see equation (3.32), page 53

t time that a particle is exposed by laser beam, see equation (6.1), page 149

t time, see equation (3.1), page 39

$T(W)$ fluctuatoinal temperature, see equation (2.12), page 20

T_0 ambient temperature, see equation (3.34), page 59

T_0 ambient temperature, see equation (3.4), page 40

t_{eff} effective thickness of the powder bed, see equation (3.22), page 49

T_b temperature of the bottom layer of the powder bed, see equation (3.25), page 50

t_{eff} effective thickness of the powder bed, see equation (3.32), page 53

T_l liquidus temperature, see equation (3.24), page 50

T_{mp} temperature of the melt pool boundary, see equation (3.20), page 44

T_s solidus temperature, see equation (3.24), page 50

T_s temperature of the top layer of the substrate, see equation (3.25), page 50

U internal energy, see equation (2.4), page 12

u_x, u_y, and, u_z fluid velocity components inside melt pool, see equation (3.9), page 41

V scanning velocity, see equation (6.15), page 175

V volume of the object, see equation (6.7), page 171

V volume, see equation (2.4), page 12

v laser scanning speed, see equation (4.7), page 89

v scanning speed, see equation (3.34), page 59

V_{2D} volume of 2D graphites, see equation (4.5), page 77

V_{3D} volume of 3D graphites, see equation (4.5), page 77

V_{dia} volume of diamond particles
, see equation (6.9), page 173

V_{tot} the total volume of diamond particles and the matrix
, see equation (6.9), page 173

V_p volume of a particle, see equation (6.1), page 150

v_p velocity of particle, see equation (6.3), page 150

w width of clad, see equation (6.14), page 175

x distance that a particle travels through laser beam, see equation (6.3), page 150

Chapter 1

Introduction

Diamond is a material with superior properties which has attracted human's attention since its discovery. Diamond properties make it the best candidate for cutting and wear resistant applications. Diamond is twice as hard as its closest competitor, cubic boron nitride, and it has the highest thermal conductivity. However, implementation of diamond in tools is expensive and challenging. The most important challenge is diamond transformation to graphite at high temperatures resulting in many restrictions on fabrication of diamond tools . Hence, finding an alternative solution to fabricate higher performance, better priced diamond tools will revolutionize tooling industry.

Laser cladding has the potential to be employed for production of higher performance, lower priced diamond tools mainly due to the facts that in laser cladding the process zone is exposed to high temperatures for a very short period of time due to having a very high cooling rate with limited heat affected zone. To utilize the laser direct deposition in diamond particles deposition, various issues and challenges such as diamond decomposition, wetting and chemical bonding of diamond particles, diamond retention capacity of the ma-

trix, clad-substrate bonding, porosity and micro cracks, and diamond particles distribution in the deposited clad, should be addressed.

In this study, deposition of metal matrix diamond composite on mild steel is investigated, and associated issues and challenges such as diamond decomposition, wetting and chemical bonding of diamond particles, clad-substrate bonding, porosity and micro-cracks, diamond particles distribution in the deposited clad, and effects of dilution are scrutinized. Modeling and experimental analysis are conducted in order to find optimum process parameters to resolve the issues and improve the properties of deposited materials.

1.1 Thesis Layout

This thesis is arranged in 7 chapters, including the current chapter, Introduction. In the following a brief review of the upcoming chapters are presented.

Background and Literature Review: In this chapter, carbon properties, graphite and diamond properties, and carbon phase diagram are reviewed. Thermodynamics of diamond graphitization and its mechanisms are explained. Kinetics of diamond graphitization is presented. Applications of diamond and the growing trend of diamond applications are stated. Different kinds of diamond tools and their manufacturing methods are also reviewed. Laser cladding process and advantages of using laser cladding for the fabrication of diamond tools are discussed. At the end the contributions of the research are presented.

Laser-MMC Thermal Modeling: A transient three dimensional temperature dependent finite element model for pre-placed laser cladding is developed. The model is developed in ANSYS©14 finite element software. Governing equations, boundary

conditions and assumptions are discussed. The effect of process parameters on melt pool temperature, cooling rate, and exposure time to high temperatures is investigated using the developed model. The influence of process parameters on the increase of melt pool temperature during deposition of a clad is studied.

Experiments and Results: Different sets of conducted experiments on deposition of ((Cu80Sn20)90Ti10)75+25 wt% diamond by pre-placed laser cladding on mild steel substrate are described. A continuous wave and a pulsed laser are employed as the source of energy. The effect of process parameters on diamond decomposition, clad-substrate bonding, porosity and micro-cracks, wetting and chemical bonding of diamond particles, diamond particles distribution in the deposited clad, and the effect of dilution are investigated. The experimental results are compared with the modeling results.

Thermal Analysis of Diamond-Matrix Reactions: Diamond reaction with each constituent of the matrix and iron from substrate is studied by Differential Scanning Calorimetry (DSC). Wetting, bonding, and reaction of diamond particles with each of these metals will be studied.

Discussions: comprehensive study of the process and discussion on how the issues are addressed in this study will be discussed in detail.

Summary, Conclusionts, Contributions, and Recommendations: Conclusions of this study, its contributions and recommendations for future work will be presented in this chapter.

Chapter 2

Background and Literature Review

In this chapter, general characteristics of carbon in graphite and diamond forms, and carbon phase diagram are reviewed. Thermodynamics of diamond graphitization and its mechanisms are explained. Kinetics of diamond graphitization is presented. Applications of diamond and the growing trend of diamond applications are stated. Different kinds of diamond tools and their manufacturing methods are reviewed. Laser cladding process and advantages of using laser cladding for the fabrication of diamond tools are discussed at the end.

2.1 Carbon and Its Allotropes

Carbon with atomic number of 6 is located in 14^{th} group of periodic table along with silicon, germanium, and tin. Carbon is one of the most abundant elements in nature. Graphite, diamond, amorphous carbon (such as soot and charcoal), and fullerenes are allotropes of carbon. Fullerenes was discovered in 1985. It exists in different shapes such as spherical

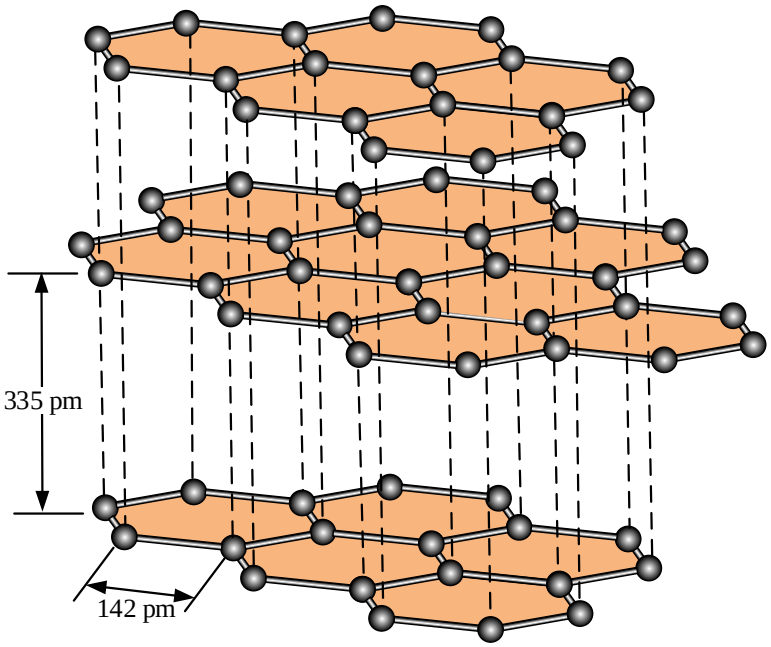

Figure 2.1: Atomic structure of graphite [6]

and cylindrical (carbon nano-tubes). This allotrope of carbon has been under extensive research due to its applications. Graphite has layered structure. In every layer, each carbon atom is connected to three other atoms by covalent bonds. Carbon atoms of each layer are connected to carbon atoms of adjacent layers by weak Van Der Waals bonds. Figure 2.1 depicts the structure of Graphite [6]. As it can be seen in the figure, carbon-carbon distance in a layer is 142 pm, whereas the distance between two adjacent layers is 335 pm [6]. The layered structure of graphite makes it one of the softest materials. Graphite is both a good heat conductor and a good electrical conductor.

Diamond has a network structure of carbon atoms in which each carbon atom is connected to 4 adjacent carbon atoms by strong covalent bonds as shown in Figure 2.2 [6]. As one can notice form the figure, the carbon- carbon distance is 154 pm [6]. Diamond has unique properties which has drawn great interest in science and technology. Some of these

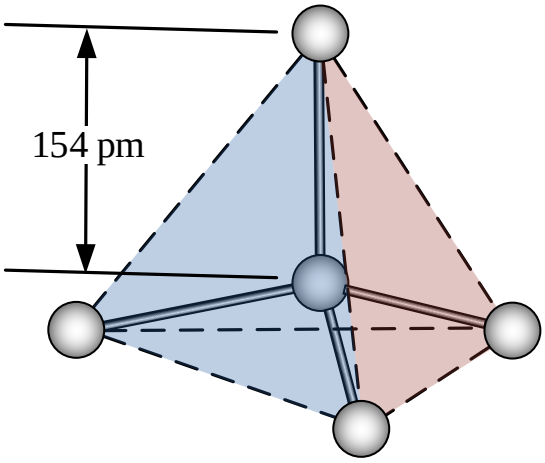

Figure 2.2: Atomic structure of diamond [6]

properties are as follows [12]:

1. Hardest material in nature
2. Highest thermal conductivity at ambient temperature
3. Electrical insulator
4. Unaffected by moderate heat, acid, and radiation
5. One of the most chemically resistant materials
6. Very low thermal expansion
7. Low friction coefficient
8. Small dielectric constant
9. Large hole mobility

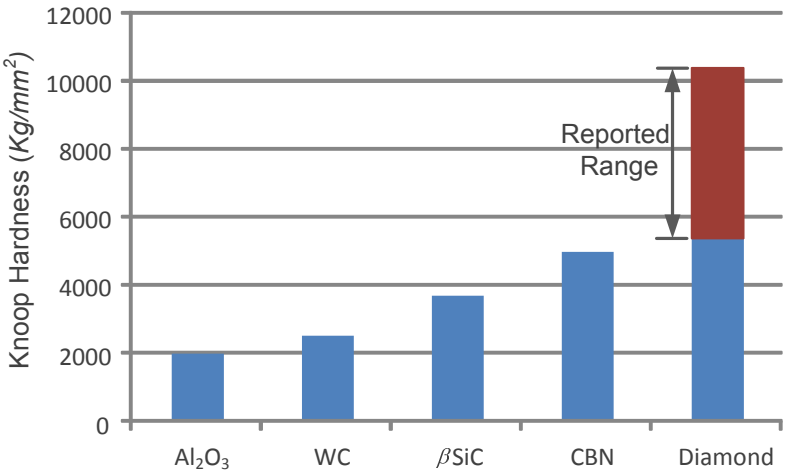

Figure 2.3: A comparison between hardness of diamond and some other hard materials [6]

Due to these unique properties it can be applied in a variety of applications such as, coatings for cutting tools, abrasive coatings, coating for bearings , heat sinks for electronic devices, and as a semi-conductor [12]. Diamond has found application in oil industry, mining, processing of stone and rocks, machining of hard materials, glass, ceramics, metals, etc [8, 13].

Diamond is the hardest material, therefore, measuring its hardness is a challenging task. Depending on crystal orientation, hardness of diamond varies in the range of 5700 kg/mm^2 to more than 10400 kg/mm^2 [6]. Figure 2.3 shows a comparison between hardness of diamond and some other hard materials. At ambient condition, thermal conductivity of diamond is around 5 times higher than that of copper, and 15 times greater than that of silicon [12]. Diamond is a perfect candidate for abrasive and wear resistant applications due to having the desired properties for these applications including, being the hardest material, having highest thermal conductivity, having low thermal expansion, and having low friction coefficient. These properties also make it ideal for coating of cutting tools. Diamond can be applied for coating of bearings because of its high thermal conductivity,

low thermal expansion, and low friction coefficient. It can also be used in heat sinks of electronic devices owing to its high thermal conductivity and low thermal expansion. Diamond has superior semi-conduction properties compared to silicon [12].

2.2 Growing Applications of Diamond

Application of diamond in industry, specifically as abrasive coating, has been drastically increased during last couple of decades. This is partly due to advances in manufacturing of synthetic diamond which resulted in reducing the cost of production of synthetic diamond. This in turn has made the manufacturing of diamond tooling feasible [14]. On the other hand, manufacturing of diamond coated tools has been improved by introducing of enhanced manufacturing techniques such as powder metallurgy and several sintering techniques [15].

Until 1950's the only available diamond was natural diamond [8]. In 1955 General Electric managed to synthesize diamond by High Pressure, High Temperature process (HPHT) [8]. Since then, application of diamond in industry has been drastically expanded . In 1960's wire diamond saw was developed for cutting of stone [8]. In 1970's diamond saw was produced and polycrystalline diamond (PCD) was commercialized [8]. In 1990's synthesizing of polycrystalline diamond in low pressure by various Chemical Vapour Deposition (CVD) methods revolutionized the diamond industry [8]. The demand for industrial diamond has been soaring, the consumption of diamond has been increased from 100 million carats in 1980 to 380 million in 1990 and 1 billion carats in 2000 [8].

New development in production of synthetic diamond in 2000's expedited growth of diamond demand dramatically. In 2008, production of only synthetic diamond surpassed 4.55 billion carats [16]. China expanded its production from 17 million carats in 2003 to

more than 4 billion carats in 2008 to become the world leading synthetic diamond producer [16]. Currently, synthetic diamond accounts for 98 percent of the diamond used in industry [17]. This is due to the fact that the quality of synthetic diamond during production can be controlled. Moreover, synthetic diamond has the capability to be customized for specific applications [17].

According to U.S. Geological Survey (USGS) report in Jan 2015 [17], computer chip production, machinery construction, machinery manufacturing, mining services (drilling for mineral, oil, and gas exploration), stone cutting and polishing, and transportation systems (infrastructure and vehicles) are among major consumers of industrial diamond. Diamond has superior electronic properties compared to silicon [12], which makes it an ideal candidate for electronic industry. Recent developments along with current extensive research are lifting the technological barriers for implementing diamond in electronic industry.

In 2009, development in CVD of synthetic diamond by utilizing microwave plasma technology led to growth of practically pure diamond [17]. These developments and introducing enhanced lower cost production of diamond resulted in substantial price reduction in diamond. Average price of imported synthetic diamond powder to US decreased from \$0.27 per carat in 2005 to \$0.15 per carat in 2008 [17], and \$0.11 per carat in 2014 [18]. Diamond price decline is expected to continue due to ongoing developments in diamond production.

Low-priced diamond opens a new window in industry, since diamond properties are substantially superior to its competitors such as cemented carbide in tooling industry. Diamond is the best candidate available for abrasive industry, wear and corrosion resistant coatings, special lenses for laser radiation equipment, heat sinks in electrical circuits, wire drawing, computing, etc [16]. The reason that industry uses cemented carbides in tooling

industry, lies in two facts. Firstly, these materials are much cheaper compared to diamond, and secondly implementation of diamond in tools has technological barriers. These two factors contributed to expensive diamond tooling. Thus, use of diamond is limited to applications that there in no alternative process. With significant improvement in diamond production, diamond becomes more cost-effective, and therefore, overcoming technological barriers that prevent use of diamond in super abrasive industry will lead to significant advancements in the industry.

2.3 Carbon Phase Diagram

Figure 2.4 shows carbon phase diagram [7]. As it can be seen in the figure, at ambient temperature and pressure, the stable phase of carbon is graphite. At ambient temperature, diamond is the stable phase only at pressures above 1.5 GPa [7]. Increasing temperature increases stability of graphite, and therefore the pressure at which diamond turns out to be the stable phase becomes even higher. These facts can be shown using thermodynamic relations. Gibbs free energy is defined as [19]:

$$G = H - TS \tag{2.1}$$

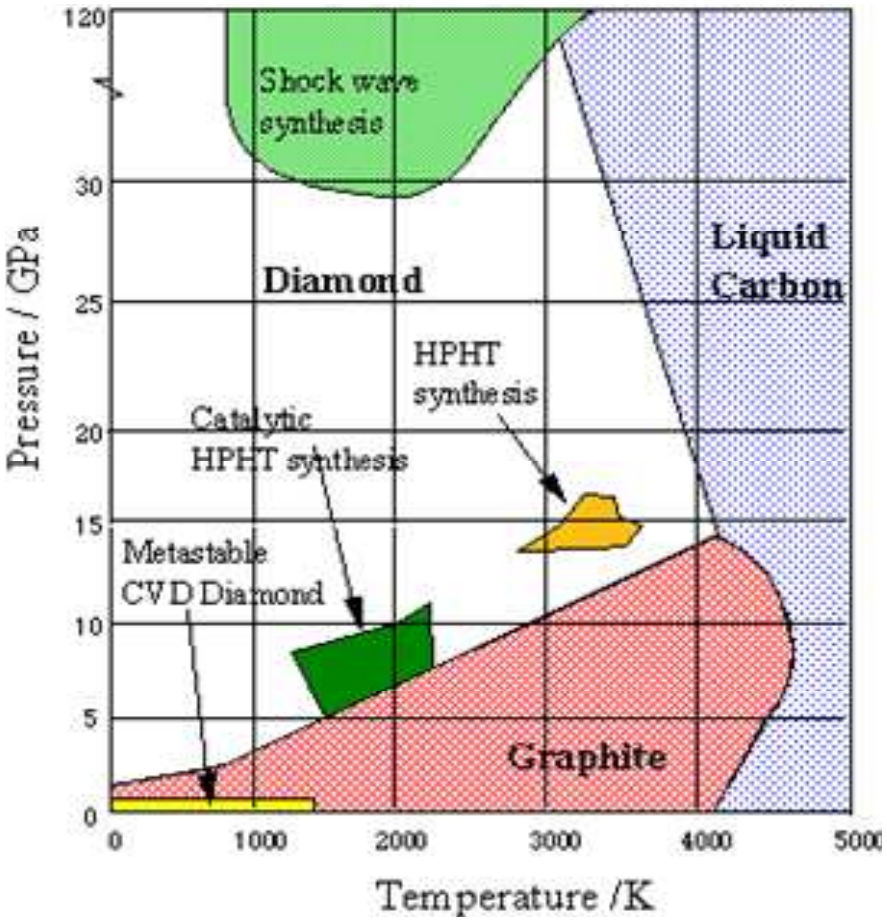

Figure 2.4: Carbon phase diagram [7]

where, G is Gibbs free energy [J], H is enthalpy [J], T is temperature [K], S is entropy [J/K].

A material is at stable equilibrium phase when it is at its lowest Gibbs free energy where we have [19]

$$dG = 0 \tag{2.2}$$

At ambient conditions, the value of G for diamond is 2.9 KJ, whereas it is zero for graphite, as a result, graphite is the stable phase. If pressure is increased while temperature is kept constant at ambient temperature, then

$$\left(\frac{\partial G}{\partial P}\right)_{T_0} = \left(\frac{\partial H}{\partial P}\right)_{T_0} - T\left(\frac{\partial S}{\partial P}\right)_{T_0} \tag{2.3}$$

Since diamond and graphite are in solid state at ambient temperature, therefore $\left(\frac{\partial S}{\partial P}\right)_{T_0} \approx 0$, and Equation (2.3) becomes

$$\left(\frac{\partial G}{\partial P}\right)_{T_0} = \left(\frac{\partial H}{\partial P}\right)_{T_0} \tag{2.4}$$

plugging $H = U + PV$, where, U is internal energy [J], P is pressure [N/m^2], and V is volume [m^3], into Equation (2.4)

$$\left(\frac{\partial G}{\partial P}\right)_{T_0} = \left(\frac{\partial U}{\partial P}\right)_{T_0} + V + P\left(\frac{\partial V}{\partial P}\right)_{T_0} \tag{2.5}$$

Again since both diamond and graphite are solid, $\left(\frac{\partial U}{\partial P}\right)_{T_0} \approx 0$ and $\left(\frac{\partial V}{\partial P}\right)_{T_0} \approx 0$, therefore

$$\left(\frac{\partial G}{\partial P}\right)_{T_0} = V \Longrightarrow G_{T_0,P} \approx G_{T_0,P_0} + V(P - P_0) \tag{2.6}$$

Since the molar volume of graphite is higher than that of diamond, the increase in G of graphite with increasing pressure is greater than that of diamond; therefore diamond becomes more stable than graphite at pressures above 1.5 GPa as it is shown in Figure

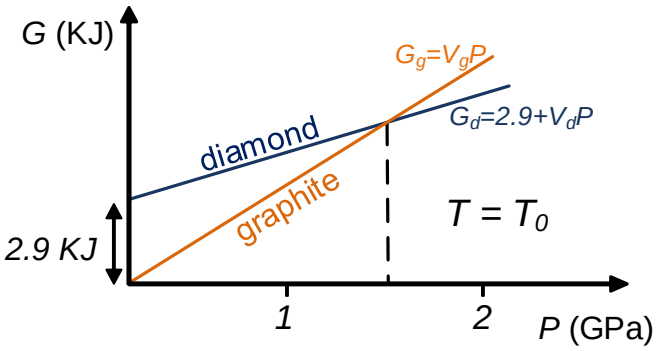

Figure 2.5: Variation of Gibbs free energy of diamond and graphite with respect to pressure

2.5 [6].

However, diamond exists at ambient condition. The reason for that, lies in the fact that diamond is a metastable phase of carbon, meaning that its Gibbs free energy is at a local minimum, as opposed to Gibbs free energy of graphite which is at the lowest minimum possible value as shown graphically in Figure 2.6 [19]. Therefore, although the driving force $\Delta G = G_2 - G_1$ for transformation of diamond to graphite is negative, meaning that the transformation results in a state with a lower free energy and therefore it should happen, activation free energy barrier, ΔG^a, is needed to make it happen as it is shown in Figure 2.6 [19]. Therefore, for transformation of diamond to graphite, carbon atoms should pass through activated state with free energy of ΔG^a higher than free energy of diamond. The shown energies in Figure 2.6 are average energy of many atoms. However, the energy of each atom due to its random thermal motion, fluctuates and at times its energy may reach activated state energy, which is called thermal activation . The probability of free energy of an atom to reach the activated state energy is expressed by $\exp(-\Delta G^a/kT)$ [19], where k is Boltzmann's constant, therefore rate of transformation can be represented by [19]

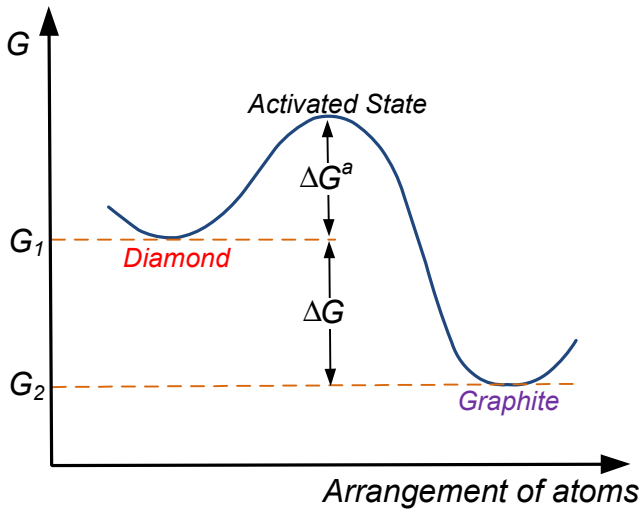

Figure 2.6: Transformation of diamond to graphite, passing through activated state

$$\text{Rate of Transfromantion} \propto \exp\left(-\frac{\Delta G^a}{kT}\right) \tag{2.7}$$

writing in molar form, and use $\Delta G^a = \Delta H^a - T\Delta S^a$ results in *Arrhenius rate equation* [19]

$$\text{Rate of Transfromantion} \propto \exp\left(-\frac{\Delta H^a}{RT}\right) \tag{2.8}$$

where, R is universal constant for gases. Equation (2.8) shows that rate of transformation is highly dependent on temperature and with increase in temperature, the transformation rate increases.

As a result, diamond exists at room temperature and pressure due to the fact that its transformation rate to graphite is infinitesimally small and level of transformation is

not detectable. In other words, diamond is kinetically stable, not thermodynamically. Therefore, kinetics plays a significant role in transformation of diamond to graphite.

2.4 Transformation of Diamond to Graphite: A Kinetic Problem

As mentioned in Section 2.3, the transformation of diamond to graphite at room temperature is not detectable. The transformation rate increases substantially with increase in temperature. Usually, the kinetics of transformation is studied by using TTT diagram where fraction of transformation is plotted as a function of temperature and time, however to the best of author's knowledge; there is no TTT diagram for diamond-graphite transformation at ambient pressure.

Among various developed models for prediction of the kinetics of general $\alpha \longrightarrow \beta$ phase transformation, *Johnson-Mehl-Avrami (JMA)* equation is the most well known. The JMA model is considered a semi-empirical model expressed as follows [19]

$$f = 1 - \exp\left(-kt^n\right) \tag{2.9}$$

where, f is fraction transformation, $k = \pi N \nu^3/3$, N is the nucleation rate, ν is the growth rate, and n is a numerical exponent which varies from $1 - 4$.

If nucleation mechanism does not change with temperature, then n is not temperature dependent; however, k is highly temperature dependent since N and ν are highly temperature dependent.

Since $1 - \exp(-z) \simeq z$ for $z \ll 1$, therefore Equation (2.9), for short times, can be written as [19]

$$f = kt^n \tag{2.10}$$

therefore, the fraction of transformation is proportional to power n of time, and it rapidly increases with temperature increase.

The information about diamond-graphite transformation rate at various temperatures is very limited. The transformation of diamond to graphite is not detectable below a specific temperature, beyond that temperature, the transformation rate rapidly increases with temperature increase. In vacuum environment, the transformation initiates around 1700°C and rapidly increases up to 2100°C at which 0.1 carat diamond is completely transformed to graphite in less than three minutes [20].

The researchers found that since graphite has lower density compared to diamond, the graphitization mostly occurs at the surface of diamond [1]. The internal graphitization of diamond is limited to micro-cracks and inclusions [20].

Two mechanisms are suggested for transformation of diamond to graphite in the literature. In the first mechanism, groups of carbon atoms are detached from surface of diamond, and develop a disordered activated phase . Then, this phase is quickly converted to stable graphite [21, 22, 1]. In the other mechanism, a single carbon atom breaks away from the surface of diamond as opposed to groups of atoms in the first mechanism. Detachment of a carbon atom occurs by breaking of three carbon-carbon bonds in $\{111\}$ surfaces and by breaking of two carbon- carbon bonds in $\{110\}$ surfaces [1].

The graphitization of octahedral surfaces is an auto catalytic process . It begins at

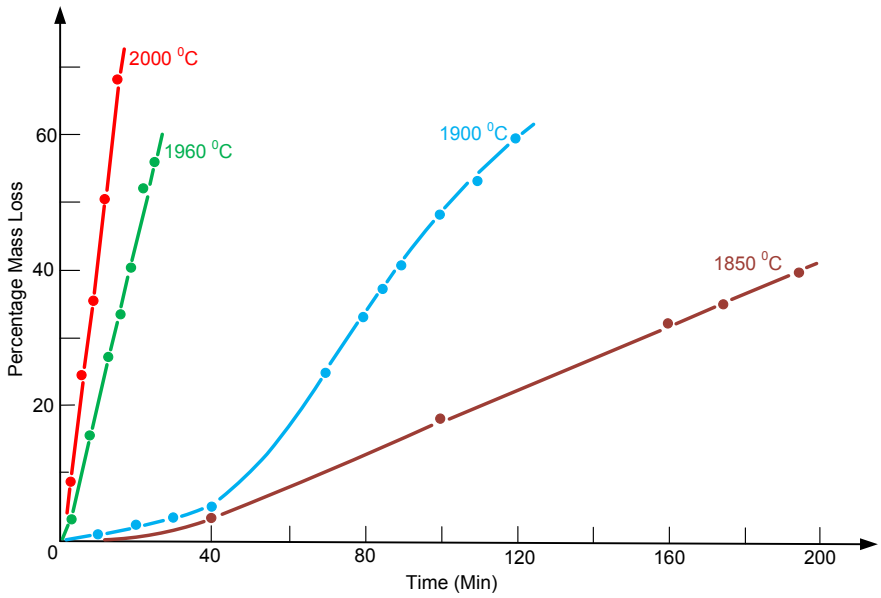

Figure 2.7: Diamond-graphite transformation versus time at vacuum condition at temperatures between 1850°C and 2000°C [1]

discrete nuclei and proceeds with stretching them. The number of active sites grows with time until the entire surface is covered with them. Graphitization continues while the density of active sites remains constant [1].

Howes [20] investigated graphitization of diamond at vacuum condition at temperatures between 1700°C to 2100°C. The size of the studied diamond particles was 0.02 g (0.1 carat). The complete graphitization of diamonds due to surface graphitization reported as a function of temperature and time. At 1700°C it took more than 12 hours for complete graphitization. Graphitization completed in between 10 to 30 minutes at 1900°C. Graphitization becomes significantly faster at 2100°C where the complete graphitization was reached between 10 seconds to 3 minutes.

Davies and Evans [1] studied graphitization rate of diamond at temperatures between 1850°C and 2000°C and at a pressure less than 3 mPa which can nearly be considered as

vacuum condition. They used natural diamond with each diamond particle weighed around 0.02 g. First, diamonds were preheated at 1600°C, then the specimen quickly heated to reach the desired temperature between 1850°C and 2000°C. Specimen were kept at four different temperatures, 1850°C, 1900°C, 1960°C, and 2000°C for different times. After each experiment, the diamond particles which were covered with graphite were rapidly cooled at room temperature. Then, the graphite was dissolved from diamond surface by heating the particles in a boiling acid mixture, and the mass loss was measured. Figure 2.7 shows the result of their experiments where percentage mass loss plotted versus time.

As it can be seen in Figure 2.7, the transformation rate is highly sensitive to temperature, and with increase of temperature from 1850°C to 2000°C, the slope of temperature constant line substantially increases. It can also be noted that at each temperature, the transformation rate is slower at the beginning, then there is a jump and the transformation rate significantly increases . This can be due to the fact that, at the beginning of the transformation the number of active sites is limited, given time, active sites spread out, and as a result, the transformation rate rises. On the other hand, increasing temperature decreases the length of first stage considerably, as the first stage for 1850°C and 1900°C is around 40 minutes, whereas it is less than 5 minutes for 1960°C and 2000°C.

Andreev [2] investigated experimental results of previous researchers in which two different mechanisms of graphitization were observed, graphitization based on diffusive mechanism for T<2000 K and the explosive disintegration and spontaneous graphitization for T>2000 K where diamond was heated in a vacuum or an inert condition. The activation energy for the diffusive mechanism was reported as $E_{\text{ac}} = 336 \pm 21$ kJ/mol while for T>2000 K it was reported as $E_{\text{ac}} = 42 \pm 8$ kJ/mol which is markedly lower than the former one.

Figure 2.8 shows the reproduced plot from Andreev [2]. The plot is based on an

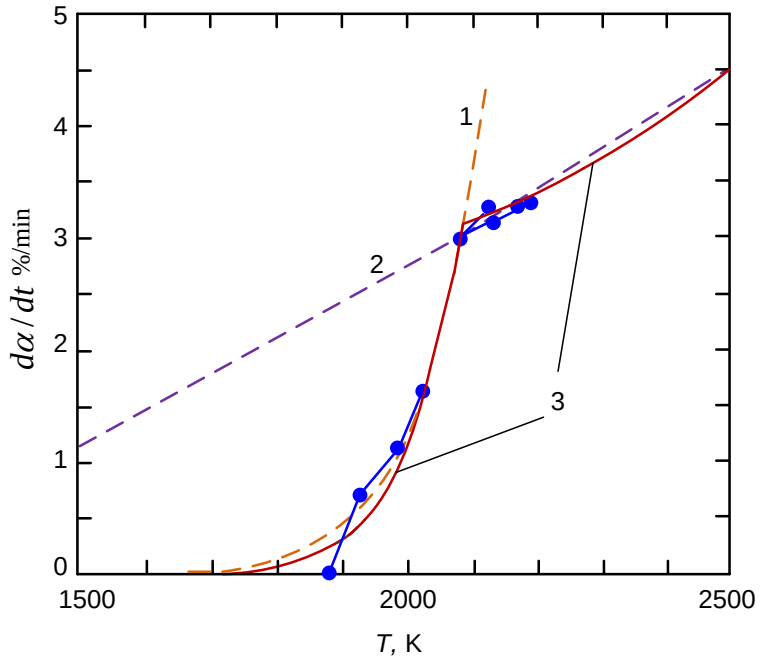

Figure 2.8: Graphs of the graphitization rate of diamond reproduced from reference [2]. Curve 1 and 2 are Arrhenius type equations with activation energy of $E_{\mathrm{ac}} = 336$ kJ/mol and $E_{\mathrm{ac}} = 42$ kJ/mol, respectively. Curve 3 is from Equation (2.12). Experimental data were taken from literature [2].

Arrhenius type equation, as follows

$$\frac{d\alpha}{dt} = A_0 \exp\left(-\frac{E_{\text{ac}}}{RT}\right) \tag{2.11}$$

where, α is concentration of graphitized diamond, A_0 is pre-exponential factor, E_{ac} is activation energy [kJ/mol], R is universal gas constant which is equal to 8.314×10^{-3} kJ/molK, and T is temperature [K]. This equation was used to fit two curves into the experimental data taken from literatures. In curve 1, E_{ac}=336 kJ/mol and in curve 2, E_{ac} =42 kJ/mol were considered. The fitted values of pre-exponential factor were calculated as $A_0 = 8 \times 10^8$ %/min and $A_0 = 34$ %/min for curve 1 and curve 2, respectively.

In order to theoretically describe the aforementioned phenomenon and its kinetics, Andreev [2] developed a model by approximation of a model based on interatomic interaction potential. Theoretical description of the model in detail which is based on atomic mechanism of spontaneous graphitization is beyond the scope of this research. Graphitization by disintegration has two barriers, first the energy barrier as a result of bond dissociation energy D_0 and second the force barrier owing to the "ultimate strength" of the bond F_{max} which requires a specific threshold energy $\triangle Q_{bar}$ and a specific temperature T_{bar}. In the model, the Arrhenius equation is modified to [2]

$$\frac{d\alpha}{dt} = A_0 \exp\left(-\frac{D_0}{RT\,(W)}\right) \tag{2.12}$$

where, D_0 is the bond dissociation energy which is equal to the first activation energy E_{ac1}, and $T\,(W)$ is the fluctuatoinal temperature which is a function of the parametric value of the lattice temperature T and the Boltzmann probability factor W for the overcoming the

barrier $\triangle Q_{bar}$, and is defined as [2]

$$T(W) = T \exp\left[\frac{3}{8RT}\left(\triangle H^0(T) - \left\|\triangle Q_{bar} - \triangle H^0(T)\right\|\right)\right] \tag{2.13}$$

where

$$\triangle H^0(T) = \int_0^T c_p dT \tag{2.14}$$

Curve 3 in Figure 2.8 is the result of fitting Equation (2.12) to the experimental results where $D_0 = 339.4$ kJ/mol, $\triangle Q_{\text{bar}} = 38.45$ kJ/mol, and $A_0 = 1.55 \times 10^4$ %/min [2].

By looking at Figure 2.7, one can notice that diamond transformation versus time is a straight line for each temperature for most parts of the four plots except for T=1850°C where the transformation is not a straight line at the beginning and at the end. Therefore, with a good accuracy, it can be assumed that the diamond transformation versus time while temperature is constant is linear meaning that the transformation rate which is first derivative of the transformation with respect to time (the slope of each line in Figure 2.7) is constant. This is in agreement with Arrhenius equation since by considering temperature constant, the transformation rate would be constant.

In order to compare the result of the Arrhenius equation used by Andreev [2] by the experimental data from Figure 2.7 [1], transformation rate was calculated by Equation 2.11 where, $A_0 = 34$ %/min and E_{ac}=42 kJ/mol for the four temperatures in Figure 2.7 (1850°C, 1900°C, 1960°C and 2000°C). The calculated values are presented in Table 2.1. The slope of each line in Figure 2.7 which corresponds to the transformation rate also presented in the Table 2.1. It can be seen that there is a significant difference between the experimental results and the calculated results by the Arrhenius equation at temperatures of 1850°C and 1900°C, while there is a good agreement at 1960°C. The two values at 2000°C are different

Table 2.1: Comparison between transformation rate from experimental results [1] and calculated by the Arrhenius equation used in [2]

Temperature (K)	2123	2173	2233	2273
Transformation rate from experimental results (Figure 2.7 [1]) (%/min)	0.235	0.66	3.6	4.47
Transformation rate calculated by the Arrhenius equation (Equation 2.11 [2]) (%/min)	3.15	3.33	3.54	3.68

by around 18%. This indicates that there is not a reliable model in the literature which can predict transformation rate of diamond graphitization for temperatures above 1850°C.

2.5 Transformation of Diamond to Graphite: Effect of Environment

In addition to temperature, graphitization of diamond is highly influenced by the environment. At a vacuum condition, the transformation of diamond to graphite is not significant up to 1700°C. In the presence of an inert gas the temperature at which the graphitization starts is lower than at a vacuum condition. When diamond in fine powder form is in contact with pure oxygen, its oxidation commences at 250°C and accelerates at 600°C [6]. It has also been reported that when diamond is exposed to an oxygen jet, it burns at 720°C according to the following reaction [6]

$$\mathrm{C\,(diamond)} + \mathrm{O_2(g)} \longrightarrow \mathrm{CO_2(g)}$$

Since the product of the reaction is in gas form, no surface passivation occurs [6].

Therefore, the diamond surface is continuously exposed to oxygen and reaction carries on endlessly. Oxidation is slower in air and it starts at around 500°C [6]. At the ambient temperature, oxygen is chemisorbed into the diamond surface in the air, if given enough time [6]. This contributes to reducing the diamond friction coefficient [6]. Diamond graphitization is not detectable up to 2000°C in presence of hydrogen [6].

Presence of metals, especially carbide formers or carbon soluble metals such as cobalt, iron, nickel, aluminum, and thallium can reduce the temperature of transformation significantly. The transformation occurs as low as 500°C in the presence of cobalt [6]. Reaction of diamond with iron, nickel, aluminum, and thallium begins at around 1000°C [6].

2.6 Manufacturing Methods of Diamond Cutting Tools

There are various kinds of diamond tools produced by different manufacturing routes. Figure 2.9 shows the diamond tools categorized based on their manufacturing method. As it can be seen in the figure, diamond tools can be divided into the following groups [8]:

Loose diamond abrasives: micron size diamond powders in paste or liquid suspension. They are mostly used for polishing and fine grinding of metallographic, ceramic, and mineralogical specimens, finishing of diamond tools, profiling and calibration of diamond wire- drawing dies, polishing gemstones, sizing and finishing hardened steel and tungsten carbide tool components, etc [8].

Single-crystals diamonds: They can be natural or synthetic; however utilization of synthetic diamond is on the rise due to its better quality, uniformity of shape and crystallographic orientation, and better performance. They are used as cutting and dressing tools, and wire-drawing dies [8].

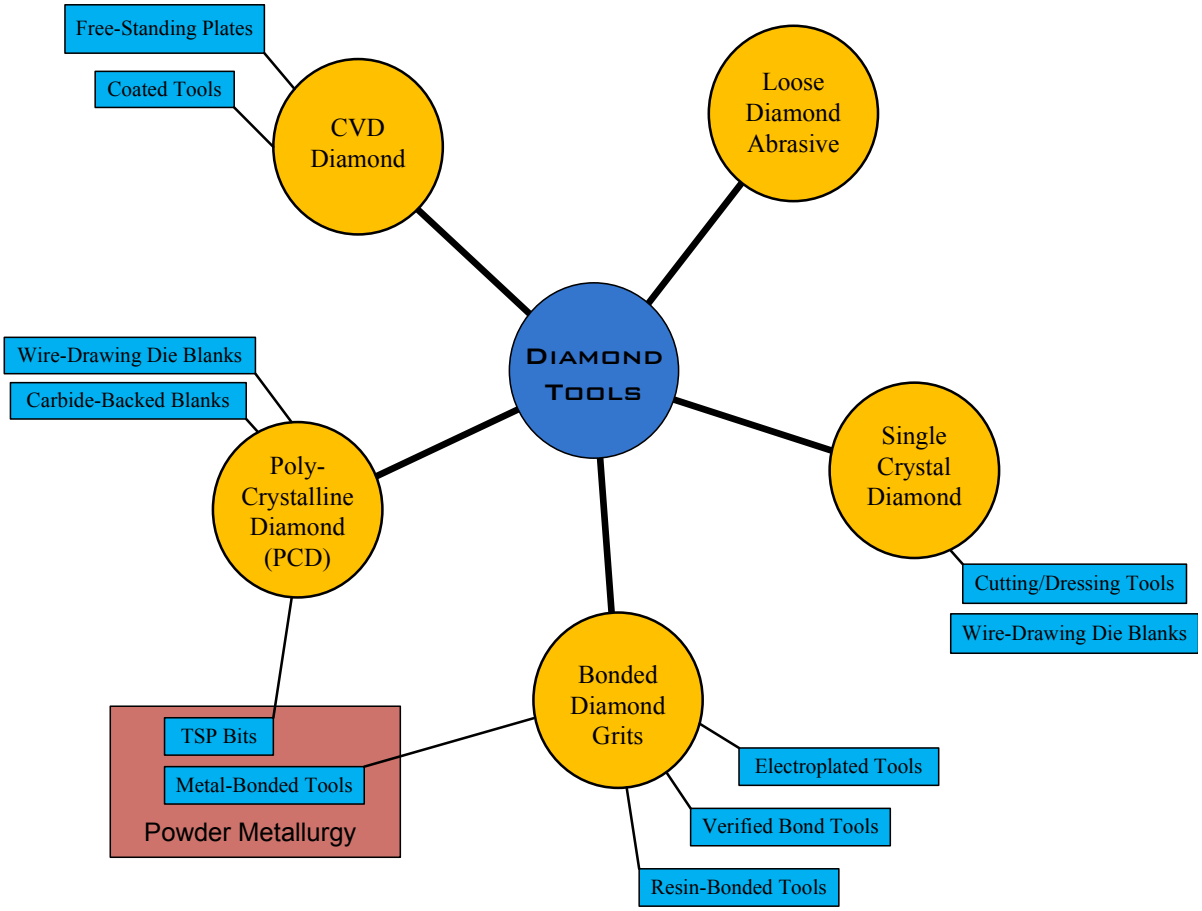

Figure 2.9: Categorization of diamond tools based on their manufacturing methods [8]

Polycrystalline Diamond (PCD): consists of many small diamond particles joined together with the help of metallic or non-metallic binding phase. The mixture is heated to the temperature between 1200°C to 1600°C with the pressure of around 6 GPa. It is used in many industrial applications, in high temperature drawing of wire, and carbide-backed blanks, to name a few [8].

CVD diamond: is synthetic diamond produced by the use of Chemical Vapour Deposition . A carbon carrier gas such as methane along with hydrogen is deposited into CVD reactor in which gases are decomposed. Different sources of energy in CVD reactor for decomposition of gases can be used like electric arc, hot filament, microwave, and combustion flame. The gaseous carbon can nucleate on a substrate and form a diamond film on it while hydrogen removes non-diamond deposition which makes the deposited diamond almost pure. Moreover, since no metal catalyst is used in this method, deposited diamond has no metallic inclusion. Deposition of diamond plate up to 1.2 mm was realized with this method. The fabricated plate can be cut by laser or EDM for different applications. Coating of tools by CVD can be an alternative way for production of diamond tools, however still some improvement should be taken place in order to make this method cost effective [8].

Bonded diamond grits and powders: most of diamond tools are placed in this category. Diamond powders and grits, either synthetic or natural, are bonded to the substrate by metallic or non-metallic bonds using different manufacturing methods. Almost all of these manufacturing methods utilize powder metallurgy to some extent. Based on the manufacturing methods and the matrices, bonded diamond grits and powders can be divided into different groups which they are discussed in the following sections [8].

Resin Bonded Tools

In Resin bonded tools, diamond particles are bonded to the substrate by resin bonds based on either phenolic resins or, more thermally stable, phenol- aralkyl resins [8, 23]. Diamond particles are mixed with the resin bond and are poured into a hot press mould. The prepared diamond rim is adhered to the body of the tool by proper adhesive materials. Alternatively, the mixture can be hot pressed to the body of the tool where adhesive materials were applied. Resin bonded tools are cost effective and have applications in grinding of cemented carbides, oxide and non-oxide ceramics, and fine grinding and polishing of stones [8].

Vitrified Bond Tools

The bond in these tools is mainly composed of the constituent of glass, SiO_2, Na_2O, and CaO. The mixture of bond and diamond powders is cold pressed, and subsequently is burnt in a furnace at 900°C-950°C at inert atmosphere. Alternatively, the mixture can be hot pressed at 730°C. These tools have porous structure which leads to higher circulation of the coolant in the process zone. Moreover, the debris is removed from process zone in a more effective way. Vitrified bond tools have limited applications as opposed to other diamond tools. They can be utilized in grinding single crystal and PCD diamond tools, cemented carbides and ceramics, and some composite materials [8].

Metal Bonded Tools

In these tools, diamond is implemented in a metallic matrix. These tools can be divided into electroplated tools and tools that are produced by powder metallurgy [8].

Electroplated Tools

These tools are fabricated by electro-deposition of the working layer to the tool body. First diamond is attached to the working layer; then the tool is submerged into an electrolyte in which a coating of metallic matrix is electro-deposited on the tool. The matrix is mostly pure nickel but nickel alloys can also be used. Both diamond grits and powders are used. These tools has found applications in sawing, grinding, brushing, and surface finishing of glass, porcelain, cemented carbides, refractory materials, and plastics. They are also used in dentistry [8].

Metal Bonded Tools Produced by Powder Metallurgy

These tools comprise two third of all kinds of bonded diamond grits and powders tools. A number of powder metallurgy technologies are included in fabrication process of nearly all of them. The fabrication of these tools consists of two stages (although in special cases, these two steps are performed at the same time)

1. Production of diamond impregnated working layer
2. Attaching the working layer to the tool body

The common fabrication steps for production of diamond impregnated working layer are described in the following section [8].

Fabrication Steps for Production of Diamond Impregnated Working Layer

Konstanty [8] divided the steps for production of diamond impregnated working layer into the following:

Matrix Powder Preparation In this step, different components of the chosen matrix are combined with binding agents and lubricants such as paraffin oil, monoethylene glycol. Subsequently, a granulation treatment is performed in order to achieve the desired flow and packing characteristics. Then diamond particles are added to the matrix. Appropriate procedures are carried out so as to obtain uniform distribution of components [8].

Cold Pressing/Sintering, or Hot Pressing The mixture is cold pressed at low to medium pressures in order to get rid of porosity and to make the mixture dense. Following that, the mixture is sintered. The alternative route to cold pressing/sintering is hot pressing in which heat and pressure are applied to the mixture at the same time. In hot pressing, the mixture is kept at high temperature and pressure for 2-3 minutes which is significantly shorter than that of sintering. On the other hand, the elevated temperature in hot pressing is considerably lower than that of sintering; however, the mixture is under high pressure simultaneously in order to obtain a dense mixture [8].

Hot Isostatic Pressing (HIP) The sintering or hot pressing can be followed by Hot Isostatic Pressuring (HIP) in which isostatic pressure generated by a hot inert gas is applied to the mixture to further remove porosity. Pressure can go as high as 200 MPa in HIP section. Because of this high pressure, the porosities that need a temperature of higher than 1100°C to be eliminated can be removed at a considerably lower temperature. This decreases the possibility of diamond degradation and as a result, HIP is gradually integrated into the fabrication process of metal bonded diamond tools [8].

Deburring A number of produced diamond impregnated segments need some cleaning and finishing which are usually performed by use of coarse alumina or silicon carbide grit

[8].

Attaching the Working Layer to the Tool Body

Laser welding or brazing are usually used to attach the end product to the tool body. The tool body is mostly made of steel in order to be strong enough to carry the applied load during operation. Bending strength of the joint in laser welding can reach 1800 MPa, whereas that in brazing is around 350-600 MPa. Therefore, the joint in laser welding is much stronger and the probability of breakdown of the joint is much less. In order to avoid generation of excessive thermal stresses during brazing which leads to deformation and reducing strength of the tool body, the temperature in the most of cases should not go higher than 700°C, and the brazing should be carried out as fast as possible. High cooling rate in laser welding can lead to generation of brittle martensite structure in HAZ. To address this issue low carbon steel is mostly used for the body. For the same reason, there should be a diamond-free layer made from proper material in the working segment of the joint to generate an appropriate joint. Brazing is mostly used for production of tools for wet processing of natural stone as opposed to laser welding which is mostly employed in fabrication of small diameter, dry cutting circular blades. Attachment of the end product to the tool body is followed by dressing in which some materials around diamond particles are taken off in order to provide adequate protrusion of diamond particles to optimize cutting performance of the tool [8].

2.7 Alternative Fabrication Processes of Diamond Tools

Recently, new manufacturing methods were developed for production of metal bond diamond tools. These methods are briefly explained in the following.

2.7.1 Brazing

A thin layer of matrix-diamond slurry is placed on the surface of the tool body. Subsequently, the part is heated in a vacuum furnace leading to formation of a thin layer of diamond-matrix bonded to the steel substrate. Differently, the steel substrate can be covered with a thin layer of glue followed by uniformly distributing diamond particles on the covered surface. Then, suspension of matrix powder is sprayed on the covered surface. After that, the part is placed in the furnace. Active brazes and nickel-base alloys are employed as the matrix. Active brazes are silver-base alloys with titanium as the active element which facilitates diamond-matrix wetting and enhances the chemical bonding. Nickel-base alloys are combination of nickel, chromium, and silicon. Nickel-base alloys are mechanically stronger compared to active brazes which are relatively soft. Brazing temperature is around 900°C-950°C for active brazes and around 1000°C-1050°C for the nickel-base alloys. Brazing benefits from having control over distribution of diamond particles, lower use of diamond, and perfect protrusion which lead to high cutting rate and long tool life [24, 8].

2.7.2 Laser Cladding

Lang and Bergmann [25] reported the use of laser cladding for deposition of diamond embedded metal matrix materials. Bronze-based metal powder as the matrix was mixed with diamond and the mixture was fed into the process zone while low carbon steel was chosen as the substrate. 1 kW Nd-YAG laser was used as the source of energy. Sidewards arranged mould for better shaping of the deposited materials and also side cooling was employed. It was reported that side cooling changed grain size of the metal matrix. It was claimed that good bondings existed both between the matrix-diamond particles and

between the clad- substrate. Moreover, it was claimed that the honing tool produced by this method not only had a better performance compared to conventionally made honing tools but also it had a longer tool life.

Dia Lux Company [26] reported direct deposition of diamond and bronze-based metal powder by laser cladding for production of diamond-impregnated blades. The blade was clamped between two chilled moulds during deposition. The produced blade was compared with conventional blades. The produced blade showed a slightly longer tool life for cutting asphalt, and around three times longer tool life for cutting concrete. The report lacks revealing scientific data about the degree of degradation of diamond particles, diamond particles distribution, the bonding of matrix to the diamond particles, and the bonding of the matrix to the substrate.

2.8 Laser Cladding, a Fabrication Route for Diamond Tools

Laser cladding is operated by different methods, among which dynamic blown powder and pre-placed method are more common. In dynamic blown powder laser cladding, or dynamic powder blowing, the added materials mostly in powder form are mixed with an inert gas and fed by a powder feeder system into the process zone where the powder and a thin layer of the substrate are melted by the use of laser energy to form a molten pool [27]. Figure 2.10 shows a schematic view of blown powder laser cladding process. In pre-placed laser cladding, the additive materials are spread on the substrate. Laser irradiates the surface of powder bed which leads to melting of the powder bed and a thin layer of the substrate [27]. Generation of relative motion between laser beam and substrate yields to a

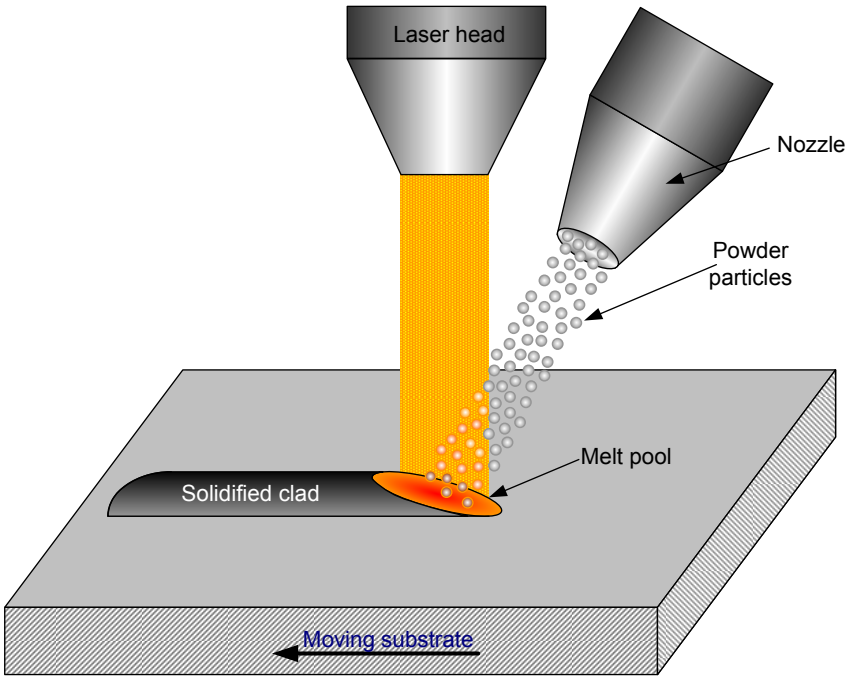

Figure 2.10: A schematic view of dynamic blown powder laser cladding process

moving molten pool on the substrate. Successive solidified materials generate a track of the deposited material on the substrate. In this way, a proper coating or an entire component can be made in a layer by layer fashion [27]. Pre-placed laser cladding is usually used for detection of the process window, whereas the blown powder method is used for coating and fabrication of components.

Laser cladding process benefits from having unique features such as very high cooling rate, low heat affected zone (HAZ), and low dilution [28, 27]. These features result in enhanced mechanical properties, fine microstructure, and homogeneous structure [27]. Laser cladding is a versatile technology which can be employed in coating, part repair, and rapid prototyping [27].

Introducing laser cladding as an alternative way of production of diamond impregnated tools has many advantages. It eliminates all time-consuming and expensive steps of conventional production methods such as matrix powder preparation, cold pressing/sintering, or hot pressing, hot isostatic pressing (HIP), welding and brazing. Instead the mixture of diamond and metal powders are deposited directly on the substrate in one step. This reduces the production time and cost significantly.

In conventional methods, the mixture of diamond and matrix is not heated enough to develop strong chemical bonding between diamond particles and the matrix. Therefore, the product suffers from the lack of enough wetting of diamond particles. The reason behind that lies in the fact that if the mixture is exposed to required temperature for developing chemical bond between diamond and the matrix, the diamond itself will be decomposed. Therefore, in conventional methods, there is always a compromise between chemical bonding and diamond decomposition.

Chemical bond between diamond and the matrix is of highest importance in diamond

impregnated tool. Without strong chemical bonding, the matrix should only rely on mechanical bonding which is not enough under high loading condition to firmly hold the diamond particles at their places; as a result, diamond particles are detached from the matrix. This results in degradation of tool performance and reducing tool life [8].

However, the case is different in laser cladding, since the mixture is adequately heated to melt the matrix and to develop a strong chemical bonding. On the other hand, diamond particles are not decomposed due to the fact that laser cladding has a very high cooling rate; therefore, diamond particles are exposed to a high temperature for a very short amount of time. In other words, although the temperature in laser cladding goes as high as it is necessary for melting the matrix and initiating good bonding between matrix and diamond particles and between clad and the substrate, however for diamond graphitization high temperature and time are needed which laser cladding does not provide the latter.

Scott et. al. [29], and Dewar et. al [30] compared liquid and solid phase bonding between copper-base alloys and diamond. The maximum thickness of the reacted layer (carbide layer) after several hours of contact in solid-phase bonded samples was 100 Angstrom, whereas for the liquid-phase bonded samples the thickness of a completed interfacial layer started from about 1000 Angstrom. This indicates that the thickness of the generated carbide layer in the case of solid-phase bonding is not sufficient to generate a strong bonding between diamond and the matrix. In fact the problem of solid phase bonding is that it cannot generate a carbide layer with sufficient thickness whereas that of liquid bonding is control of thickness of carbide layer since in liquid-phase bonding the carbide layer grows very fast to become excessively thick which degrades the bonding strength. The authors reported the maximum bonding strength of liquid-phase bonded and solid-phase bonded samples as 42 $kgmm^{-2}$, and 24.2 $kgmm^{-2}$, respectively. Therefore, laser direct deposition in which liquid-phase bonding occurs has a great advantage over conventional manufacturing

methods which rely on solid-phase bonding.

In addition, the heat affected zone (HAZ) in laser cladding is limited and local; as a result, process does not have an effect on the properties of other parts of the diamond tool. Therefore the process can be employed for applications where only a small part of a tool has to be processed.

Therefore, laser cladding has the potential to be employed for production of higher performance, lower price diamond tools; however, various major issues and challenges should be addressed. In other words, utilizing laser cladding in diamond tool industry, will revolutionize the tooling industry, provided that the associated issues and challenges are addressed and optimum process parameters for obtaining desired properties are identified.

Although, laser cladding was introduced for fabrication of diamond tools by Lang and Bergmann [25], and Dia Lux Company [26]; however, to the best of author's knowledge, most of issues and challenges such as diamond decomposition, wetting and chemical bonding of diamond particles, matrix diamond retention capacity, mechanical properties of deposited clad, clad-substrate bonding, diamond particle distribution in the deposited clad, wearness properties of matrix, porosity and micro-cracks, dilution, excessive thermal stresses, and delamination of clad have not been investigated and optimum process parameters have not been identified.

Therefore, it is needed that this process is studied in detail to address the associated issues and challenges. In this research by use of modeling and experimental analysis, deposition of metal matrix diamond composite on mild steel is scrutinized, and above mentioned issues and challenges are addressed. Modeling and experimental analysis are utilized in order to identify optimum process parameters and conditions to resolve the issues and to obtain the desired properties.

2.9 Matrix Selection

One of the most important issues of diamond coated tools is the wear resistance of the coat. Diamond particles are pulled out of the matrix during the wear. As a result, the retention capacity of the matrix is one of the most important issues of any matrix. Strength of the matrix and the retention capacity of the matrix are important factors in wear resistance of the coat. Therefore, the matrix should :

1. Hold diamond particles firmly,
2. Be strong enough,
3. Wear at the same rate of diamond loss.

Fast wear of matrix results in diamond pullout. Alternatively, if the matrix wears slower than diamond break down, the tool surface will be polished which is known as "glazing effect" [8]. Therefore, if the matrix is too soft, it results in fast wearing of the matrix and premature pullouts of diamond particles. In contrast, if the matrix is too wear resistant, it results in glazing effect [8].

On the other hand, the wear resistance of the matrix should be consistent with respect to the abrasiveness of the work-piece. When the work-piece is hard, the removal rate of the work-piece is low and the removed materials are fine, consequently, the wearing of the matrix is slow. Conversely, when the work-piece is soft, the removal rate is high and the removed materials are coarse which accelerates the wearing of the matrix [8].

Empirical study has revealed that copper-tin alloy has similar performance to cobalt based alloys for the use in diamond impregnated tools [26]. Copper-tin alloy has shown better performance in using for tooling of less abrasive materials as opposed to cobalt

based alloys [26]. However, a copper-tin alloy has weak wetting characteristic to diamond. Addition of titanium to the matrix drastically enhances the wetting properties of the matrix [26, 31]. Considering the above-mentioned rationales, copper-tin-titanium was selected as the matrix in this study.

Chapter 3

Laser-MMC Thermal Modeling

As mentioned in Chapter 2, in explaining the kinetics of diamond graphitization, the maximum temperature and the exposure time to high temperatures should be kept as low as possible. In other words, the maximum temperature should not exceed the required temperature for melting the matrix and a thin layer of the substrate. Moreover, the exposure time to this maximum temperature should be as short as possible. In addition, the cooling rate needs to be as high as possible. On the other hand, melt pool temperature increases during deposition of a clad as a result of accumulated heat. In fact, melt pool temperature can be quite different at the beginning of the clad and at the end depending upon factors such as substrate volume, deposition volume, deposition rate, scanning speed, and laser power. Therefore, change of process parameters is necessary in order to keep the melt pool temperature constant. As a result, not only the process window is quite narrow but also it is varying. Therefore, finding optimized parameters and altering them during the process according to the aforementioned necessary conditions by trial and error and empirical methods would be almost impossible. Therefore, analytical and numerical modeling

of the process which can reveal the relationship between the process parameters and the process outcomes are inevitable. In this Chapter thermal modeling of the deposition will be studied.

3.1 Melt-Pool Modeling

3.1.1 Governing Equations

When laser with the specified intensity distribution irradiates on a substrate, the transient temperature distribution $T(x, y, z)$ is determined by three dimensional heat conduction equation as [27, 32]

$$\frac{\partial(\rho c_p T)}{\partial t} + \mathbf{U}.\nabla(\rho c_p T) + \nabla.(-k\nabla T) = Q \tag{3.1}$$

where, Q is specific power or generated power per unit volume of the substrate [W/m^3], ρ is density [kg/m^3], c_p is specific heat capacity [J/kgK], T is temperature [K], t is time [s], $\mathbf{U}$ is the scanning velocity of laser beam [m/s], k is the thermal conductivity [W/mK].

Another governing equation is the conservation of momentum which is Newton's second law applied in fluid flow [27, 32, 33]

$$\frac{\partial(\rho\mathbf{U})}{\partial t} + (\rho\mathbf{U}.\nabla)\mathbf{U} = \rho g - \nabla p + \mu\nabla.(\nabla\mathbf{U}) \tag{3.2}$$

where, g is standard gravity [m/s^2], μ is viscosity [kg/sm], p is pressure [N/m^2].

The continuity equation is the other governing equation [27, 32]

$$\nabla \mathbf{U} = 0 \tag{3.3}$$

These three equations can be solved analytically in specific cases; however, solving these equations analytically is not possible most of the time.

3.1.2 Boundary Conditions

Among many complicated boundary conditions that should be satisfied during the process, some are more important such as:

- The boundary condition equation that models laser beam and powder flux (in case of blown powder laser cladding) as a surface heat source and heat flux [27]

$$-K(\nabla T.\mathbf{n}) \mid_{\Omega} = \begin{cases} \beta I(x,y,z,t) - h_c(T-T_0) - \epsilon_t \sigma (T^4 - T_0^4) & \text{if} \quad \Omega \in \Gamma \\ \\ -h_c(T-T_0) - \epsilon_t \sigma (T^4 - T_0^4) & \text{if} \quad \Omega \notin \Gamma \end{cases} \tag{3.4}$$

where,$\mathbf{n}$ is the normal vector of the surface, x, y, and z are space coordinates [m], $I(x,y,z,t)$ is the laser energy distribution on the surface [W/m^2], β is absorptivity (absorption factor), h_c is the heat convection coefficient [W/m^{2}K], ϵ_t is emissivity, σ is the Stefan-Boltzman constant, 5.67×10^{-8}[W/m$^2 K^4$], Ω is the workpiece surfaces [m^2], Γ is the irradiated surface area by laser beam [m^2], T_0 is the ambient temperature [K].

- Assuming $\mathbf{n}$ on the surface of melt pool is vertical, (parallel to g, standard gravity),

the surface tension is determined by [27]

$$\nabla p + \rho g z = (2\mu \frac{\partial \mathbf{U}}{\partial n}.\mathbf{n}) + \frac{\gamma}{R} \tag{3.5}$$

and

$$\mathbf{U}.\mathbf{n} = 0 \tag{3.6}$$

where, γ is surface tension [N/m], R is clad surface curvature [m].

- At the solid-liquid interface

$$f(x, y, z, t) = \text{Const.} \tag{3.7}$$

$$u_x = u_y = u_z = 0 \tag{3.8}$$

$$T = T_m \tag{3.9}$$

where, $f(x, y, z, t)$ is a function presenting the melt pool-substrate interface, u_x, u_y, and,u_z are fluid velocity components inside melt pool [m/s].
It should be noted that these boundary conditions are only valid when the cladding material is a pure element, and in case of alloys freezing range is considered.

- The boundary conditions for initial and infinite time are

$$T(x, y, z, t) \mid_{t=0} = T_0 \tag{3.10}$$

$$T(x, y, z, t) \mid_{t=\infty} = T_0 \tag{3.11}$$

3.1.3 Developed Models in the Literature

Picasso *et al.* [34] and Kaplan and Groboth [35] modeled blown powder laser cladding by splitting the process into two steps, interaction of powder particles with laser beam , and generation of melt pool and clad. In the first step, powder particles are irradiated and pre-heated by laser beam on their routes to the molten pool. At the same time, powder particles obstruct some parts of the laser beam from reaching the substrate which was called shadowing effect. In this approach, the shadowing effect of powder particles on each other was ignored. Considering the geometry of the process such as, laser beam diameter, powder jet diameter, powder particle sizes, and the slope of powder jet, and using energy balance, Picaso *et al.* [34] calculated the powder attenuation by

$$\frac{P_{at}}{P_l} = \begin{cases} \dfrac{\dot{m}_p}{2\rho r_l r_p \nu_p \cos\theta_{\text{jet}}} & if \quad r_{jet} < r_l \\ \\ \dfrac{\dot{m}_p}{2\rho r_{jet} r_p \nu_p \cos\theta_{\text{jet}}} & if \quad r_{jet} \geq r_l \end{cases} \tag{3.12}$$

where,P_{at} is the attenuated power, P_l is the average laser power, $\dot{m}_p$ is the powder feed rate, ρ is the density of powder, r_l is beam radius, r_p is radius of powder particles, r_{jet} is powder jet radius, ν_p is powder particles velocity, θ_{jet} is the angle of powder jet with respect to horizontal line.

The portion of attenuated power which returns to the melt pool as powder particles with elevated temperature, P_{P_1}, was calculated as [34]

$$P_{P_1} = \eta_p \beta_p P_l \frac{P_{at}}{P_l} \tag{3.13}$$

where, η_p is powder catchment efficiency, β_p is absorptivity of laser beam by powder particles. Some of laser irradiation is reflected by the substrate and hit back the powder particles that are joining the melt pool. The power that this phenomenon adds to the process zone, P_{P_2},was computed as [34]

$$P_{P_2} = \eta_p \beta_p (1 - \beta_w) P_l (1 - \frac{P_{at}}{P_l}) \frac{P_{at}}{P_l} \tag{3.14}$$

where, β_w is substrate absorptivity. Therefore, the power that is added to the melt pool by joining powder particles, P_P, was calculated as [34]

$$P_P = P_{P_1} + P_{P_2} \tag{3.15}$$

The power that is added to the melt pool by direct laser irradiation, P_d, was calculated as

$$P_d = \beta_w P_l (1 - \frac{P_{at}}{P_l}) \tag{3.16}$$

As a result, the absorbed laser energy by the process zone can be calculated as [34, 27]

$$P_w = P_d + P_P \tag{3.17}$$

The second step, generation of the melt pool and the clad, is more challenging due to complexity of the geometry of the melt pool and the clad. Picasso *et al.* [34] assumed that the geometry of the melt pool in laser lading is similar to that of the melt pool in laser surface melting. This assumption facilitates calculation of temperature distribution in the substrate by considering the source of energy as a moving Gaussian heat source on

a semi-infinite substrate. Kaplan and Groboth determined the temperature distribution as [35]:

$$T(x,y,z) = T_0 + \frac{\beta P_l}{K r_0} \int_0^\infty \frac{\exp(-H)}{(2\pi^3)^{1/2}(1+\mu^2)} d\mu \tag{3.18}$$

where, H is defined as

$$H(\mu) = \frac{(x + \mu^{2\mathrm{R}/2})^2 + y^2}{2(1+\mu^2)} + \frac{z^2}{2\mu^2} \tag{3.19}$$

β is absorptivity, P_l is laser power, K is thermal conductivity, r_0 is laser beam radius.

The boundary of melt pool can be determined by the boundary condition,

$$T(x,y,z,t) = T_{mp} \tag{3.20}$$

where, T_{mp} is the temperature of the melt pool boundary. Height of the clad is calculated by mass balance equation,

$$\eta_p \dot{m}_p = \rho \nu_l H_c S_c \tag{3.21}$$

where, H_c is the height of the clad, S_c is area of the melt pool.

This analytical model provides good insight about the process and its results are valuable for prediction of process behavior where moderate accuracy is sufficient. However, due to the aforementioned assumptions, and other simplified assumptions such as considering material properties temperature-independent, the results are associated with some degrees of error.

Toyserkani *et al.* [36, 37] improved the modelling of the process by introducing a numerical modelling which takes into account variations of the melt pool shape during the process. It was assumed that the relations between the powder stream and the melt pool are decoupled. Melt pool boundary is determined assuming there is no powder stream. Then, assuming no laser radiation, the additive materials join the intersection of melt pool boundary and powder stream which leads to deposition of an additional layer on the intersection. Thermal analysis of the additional layer and the substrate yields a new melt pool boundary. Appropriate number of iteration is carried out until the geometry of the clad is determined. The experimental verifications showed a strong agreement with the model predictions.

3.1.4 Model Description

As mentioned in the previous chapter, diamond decomposition rate is highly sensitive to temperature, and exposure time to high temperature, therefore it is desired to keep maximum temperature (melt pool temperature) at the minimum required temperature for obtaining a good clad-substrate bonding. In this study the matrix is composed of copper, tin, and titanium with the melting temperature of 1084.62°C, 231.93°C, and 1668°C, respectively [9]. The substrate is mild steel with the melting point of 1530°C [9]. However, there is no need to melt titanium completely which will be discussed in next chapter. Therefore the desired temperature of the melt pool is between 1600°C and 1700°C. On the other hand, the melt pool temperature at the end of clad could be much higher than that at the beginning of the clad because of accumulated heat. As a result, not only the process window is quite narrow but also it is varying. Therefore, the process parameters should be changed during the process in order to maintain the melt pool temperature constant and

to keep the cooling rate at its maximum. Achieving this by trial and error approach and empirical methods is almost impossible. Therefore, developing a model which can reveal the relationship between the process parameters and the process outcomes is inevitable. The developed model can be employed to identify the optimum process parameters for initiation of the process and to change them during the process accordingly.

To achieve these goals, a finite element model using ANSYS© Parameter Developing Language (APDL) in ANSYS© 14 was developed. As mentioned earlier, pre-placed laser cladding is mostly used for process window identification and for analyzing the process, therefore, for the initial step, it was opted to develop a FEM model for pre-placed laser cladding which its modelling is less complicated and can provide enough insight for detection of process window.

The developed model is a three dimensional temperature dependent transient model which can simulate clad generation during the process. The influence of process parameters such as scanning speed V, laser power P, clad thickness L, and laser beam diameter D, on process outcomes such as temperature distribution, and cooling rate can be scrutinized.

Powder bed was considered as a bulk material while the spaces between powder particles were taken into account by considering lower heat conductivity before melting of powder particles as well as by considering the effective thickness of powder bed as opposed to its real thickness [38]. Source of energy was considered as a continuous wave (CW) laser.

When laser scans through surface of the powder bed, the temperature of the powder bed increases until it reaches the particles melting point. Before melting point, the heat is transferred by conduction between solid particles (solid to solid contact) inside the powder bed. Between the powder bed and the substrate, heat is conducted by passing through thermal contact resistance. Beyond melting point, the mechanism is changing to

liquid to solid contact inside powder bed. After melting the powder bed, the high thermal contact resistance between powder bed and substrate vanishes resulting in an intensified heat conduction between liquid powder bed and the substrate. Next, a thin layer of the substrate melts if the absorbed energy by the liquid powder bed is high enough to pass adequate heat to the substrate for melting. As a result, a melt pool containing mixture of added materials and the substrate is formed on the substrate. After laser spot moves forward, the temperature falls rapidly, the melt pool solidifies and an interface between the clad and the substrate is formed.

The following assumptions were made in the development of the model:

- The effect of fluid flow inside the melt pool was considered as a correction factor to thermal conductivity. This assumption has been used by many researchers.
- The surface of the melt pool was considered flat similar to other studies in the literature.
- The effect of mixing additive material with the substrate in the melt pool on the thermal analysis was ignored. This could not be a major source of error since the thermal properties of the added material and the substrate at high temperature are close.
- Since major part of the chosen matrix is pure copper, the added material was considered as pure copper instead of ((Cu80Sn20)90Ti10)75+ 25 wt% diamond. This cannot contribute to a high amount of error since 54% of the matrix is copper and 25% is diamond with much higher thermal conductivity. Therefore, considering the entire deposit as copper would provide good approximation.

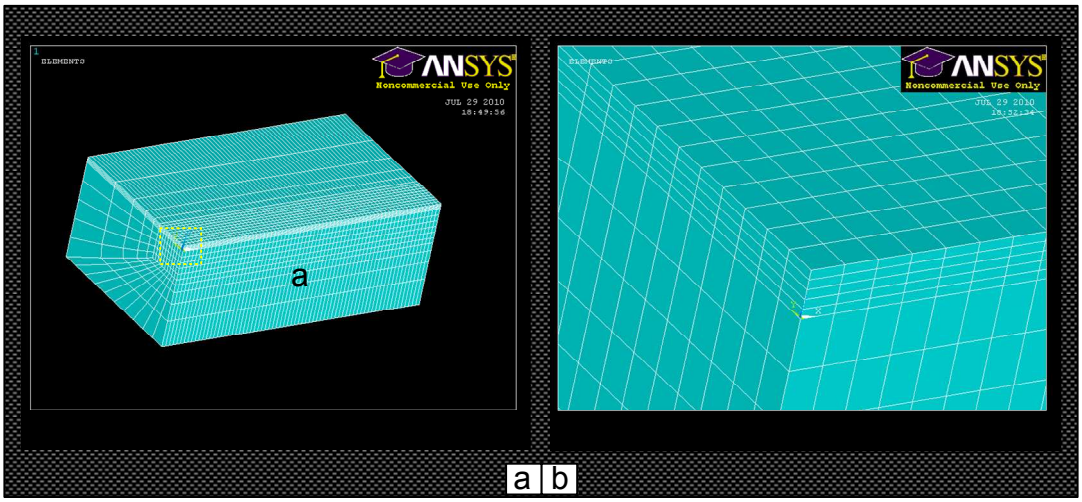

Figure 3.1: FEM model of the substrate and the powder bed along with their meshings and elements. a) the entire view b) a magnified view of a corner

The substrate was chosen as AISI 1030 mild steel (0.25-0.28 wt% carbon). Dimensions of the substrate was chosen as 14 mm×8 mm×5 mm (length × width × thickness) while the powder bed thickness was 0.5 mm. The substrate in the model was chosen very small compared to the substrate used in the experiments with dimensions of 120 mm×38 mm×5 mm (length × width × thickness) which makes its volume 40 times larger than that of the model. The reason behind this lies in the fact that the developed model is computationally intensive, therefore the substrate in the model was chosen 40 times smaller than the substrate in the experiments. This decreased the required elements significantly, and in turn it reduced the computation time. However, assigning a smaller substrate to the model decreases the cooling rate drastically, which is a very important parameter in this study. In future, a better computational facility would be utilized in order to run the models. Figure 3.1 illustrates the FEM model of the substrate and powder bed along with their meshing and elements.

The powder bed was considered as a continuum medium; however, there are some

empty spaces between powder particles filled with air. As a result, in order to account for spaces between powder particles, the effective thickness of powder bed was calculated as [38]:

$$t_{\text{eff}} = \frac{m}{\rho A} \tag{3.22}$$

where, t_{eff} is effective thickness of the powder bed [m], m is mass of the spread powder [kg], ρ is density of the powder particles [kg/m^3], A is the spread area [m^2].

This will be the effective thickness of the powder bed as well as the clad height. Below melting point temperature, the conductivity of powder bed is low, whereas, beyond melting point temperature, powder bed melts and conductivity soars sharply. Element Solid 70, which has the capability to consider 3-D thermal conduction both in steady state or transient thermal analysis, was assigned to the main body of the powder bed and the substrate [38]. Contact analysis of ANSYS© by using Contact 174-Target 170 pair elements which are surface to surface contact elements was employed in order to model the thermal contact resistance between the powder bed and the substrate [38]. The elements in the bottom layer of the powder bed were chosen as Contact 174 whereas the elements of the top layer of the substrate were chosen as Target 170 [38]. In order to consider convection and radiation, element Surf 152 was assigned to top layer of powder bed and the sides of the substrate. This element considers heat transfer by radiation and convection to the surroundings [38].

If thermal conductivity is considered isotropic, then Equation (3.1) can be modified to [39]

$$\frac{\partial H(T)}{\partial t} = K(T)\left(\frac{\partial^2 T}{\partial x^2} + \frac{\partial^2 T}{\partial y^2} + \frac{\partial^2 T}{\partial z^2}\right) + Q \tag{3.23}$$

where, $H(T)$ is enthalpy. Writing the energy equation using enthalpy has the advantage of considering phase change by heat of fusion [27]

$$H(T) = \begin{cases} \rho \int_{273}^{T} c_p dT & \text{if} \quad T \leq T_s \\ \\ \rho \int_{273}^{T} c_p dT + \rho L_m & \text{if} \quad T \geq T_l \end{cases} \tag{3.24}$$

where, L_m is latent heat of fusion, T_s is solidus temperature, and T_l is liquidus temperature. Although the additive material was considered as pure copper, however a mushy zone with the range of 30 degrees was considered. For this range, $H(T)$ was calculated by interpolation between solidus and liquidus temperatures.

The powder bed and substrate were coupled by the Contact174-Target170 contact pair; as a result, the heat flux is calculated by [38]

$$q = K(T_b - T_s) \tag{3.25}$$

where, q is heat flux, K is thermal contact conductance of the powder bed-substrate interface which is the reciprocal of thermal resistance of interface [W/m^{2}K], T_b is the temperature of the bottom layer of the powder bed [K], T_s is the temperature of the top layer of the substrate [K].

When T_b is below the liquidus temperature of the additive material K is considered as

$K = 0$ W/m^{2}K, above liquidus temperature K is considered as $K = 10^9$ W/m^{2}K [38]. In fact, thermal resistance is very high before the power bed melts, whereas, after the powder bed melts and molten layer contacts the substrate, the thermal contact becomes virtually perfect.

Laser source was considered as continuous wave (CW) with Gaussian beam distribution and TEM$_{00}$ mode. The wave length of the laser was considered between $1064 - 1070$ nm which corresponds to the wave length of the Nd-YAG laser (1064 nm) and Fiber laser (1070 nm) in the ALFα lab at the University of Waterloo. $I(r)$, power intensity distribution for Gaussian beam with TEM$_{00}$ is calculated by [27]

$$I(r) = I_0 \exp\left[-2\left(\frac{r}{r_0}\right)^2\right] \tag{3.26}$$

where,

$$r = \sqrt{x^2 + y^2} \qquad I_0 = \frac{2P}{\pi r_0^2} \tag{3.27}$$

r is distance from center of the laser beam [m], I_0 is intensity scale factor [W/m^2], r_0 is beam radius [m], P is laser power [W].

Laser irradiation was modeled as a heat flux on the surface of the powder bed by using Equation (3.4) as

$$q = \begin{cases} \beta \dfrac{2P}{\pi r_0^2} \exp\left[-2\left(\dfrac{r}{r_0}\right)^2\right] - h_c\left(T - T_0\right) - \epsilon_t \sigma\left(T^4 - T_0^4\right) & \text{if} \quad \Omega \in \Gamma \\ \\ -h_c\left(T - T_0\right) - \epsilon_t \sigma\left(T^4 - T_0^4\right) & \text{if} \quad \Omega \notin \Gamma \end{cases} \tag{3.28}$$

where, Ω is the powder bed surface [m^2], Γ is the laser irradiated surface area [m^2] h_c is convection coefficient, β is absorptivity.

Convection coefficient was considered as 12.8 W/m^2K [40]. Absorptivity of a perfectly flat and clean surface of copper for 1.06 μm wave length laser is only 0.01 [39]. This number increases with the temperature rise, and goes up to 0.25 for around 1000 K [39]. However, these numbers are for a completely flat and clean surface, and absorptivity is much higher for coarse surfaces. As a result, the average absorptivity was considered as 0.25 for the entire process.

Heat loss through three sides of the substrate is determined by

$$q = -h_c\left(T - T_0\right) - \epsilon_t \sigma\left(T^4 - T_0^4\right) \tag{3.29}$$

effective emissivity ϵ_t was considered as 0.8 for the entire model.

The forth side (plane "a" in Figure 3.1) is a symmetrical plane and its boundary condition is

$$q = \frac{\partial T}{\partial y} = 0 \tag{3.30}$$

the bottom plane of substrate was considered insulated and therefore

$$q = \frac{\partial T}{\partial z} = 0 \tag{3.31}$$

Conductivity of powder bed due to existence of air filled spaces between powder particles is significantly lower than conductivity of the material in bulk form. Effective conductivity of powder bed was calculated by [40, 38]

$$\log \frac{K_e}{K_{air}} = \left(0.280 - 0.757 \log \alpha - 0.057 \log \frac{K_p}{K_{air}}\right) \log \frac{K_p}{K_{air}} \tag{3.32}$$

where, α is percentage of voidage in powder bed which is determined by [38]

$$\alpha = \frac{t - t_{eff}}{t}$$

t is the thickness of powder bed which is 0.5 mm in this study, t_{eff} is the effective thickness of the powder bed which was calculated by Equation (3.22) as 0.28 mm, as a result α was calculated as 0.44 [38], K_e is the effective conductivity of powder bed below melting point [W/mK], K_{air} is the thermal conductivity of air filled spaces between powder particles which is reported by Rohsennow *et al.* as 26.2×10^{-3} W/mK [40, 38], K_p is the thermal conductivity of powder material in bulk form which is 398 W/mK, as a result, the effective conductivity of powder bed was calculated as 25.14 W/mK [38].

Conductivity of powder bed was considered constant up to the melting point. After melting, temperature dependent conductivity of copper in liquid state was extracted from

literature [41]. Researchers [27] have considered the effect of thermocapilary flow and Marangoni effect inside melt pool on conductivity by introducing a correction factor

$$K_e(T) = cK(T) \tag{3.33}$$

where, $K_e(T)$ is the effective conductivity in the presence of thermocapilary flow [W/mK], c is a correction factor, $K(T)$ is the temperature dependent conductivity of metal in liquid state [W/mK], value of c should be greater than 2 and in this study was considered as 2.5.

Figure 3.2a shows the conductivity of powder bed and melt pool as a function of temperature. Temperature dependent conductivity of solidified clad was extracted from literature [41] as shown in Figure 3.2b. Conductivity of substrate, below melting point, was considered as conductivity of iron in solid state as a function of temperature [41]. Above melting point, the extracted values for liquid state was multiplied by a factor of 2.5 as shown in Figure 3.2c.

Enthalpy was calculated by Equation (3.24) where specific heat and density were considered temperature dependent. Enthalpy of the powder bed and the solidified clad as a function of temperature is shown in Figure 3.3a, whereas Figure 3.3b depicts enthalpy of the substrate as a function of temperature.

3.1.5 Numerical Solution Algorithm

The motion of laser beam was simulated by a multiple load step approach where transient thermal field of process was acquired as follows [38]:

1. Using element die and birth feature of ANSYS, Contact 174/Target 170 pair contact

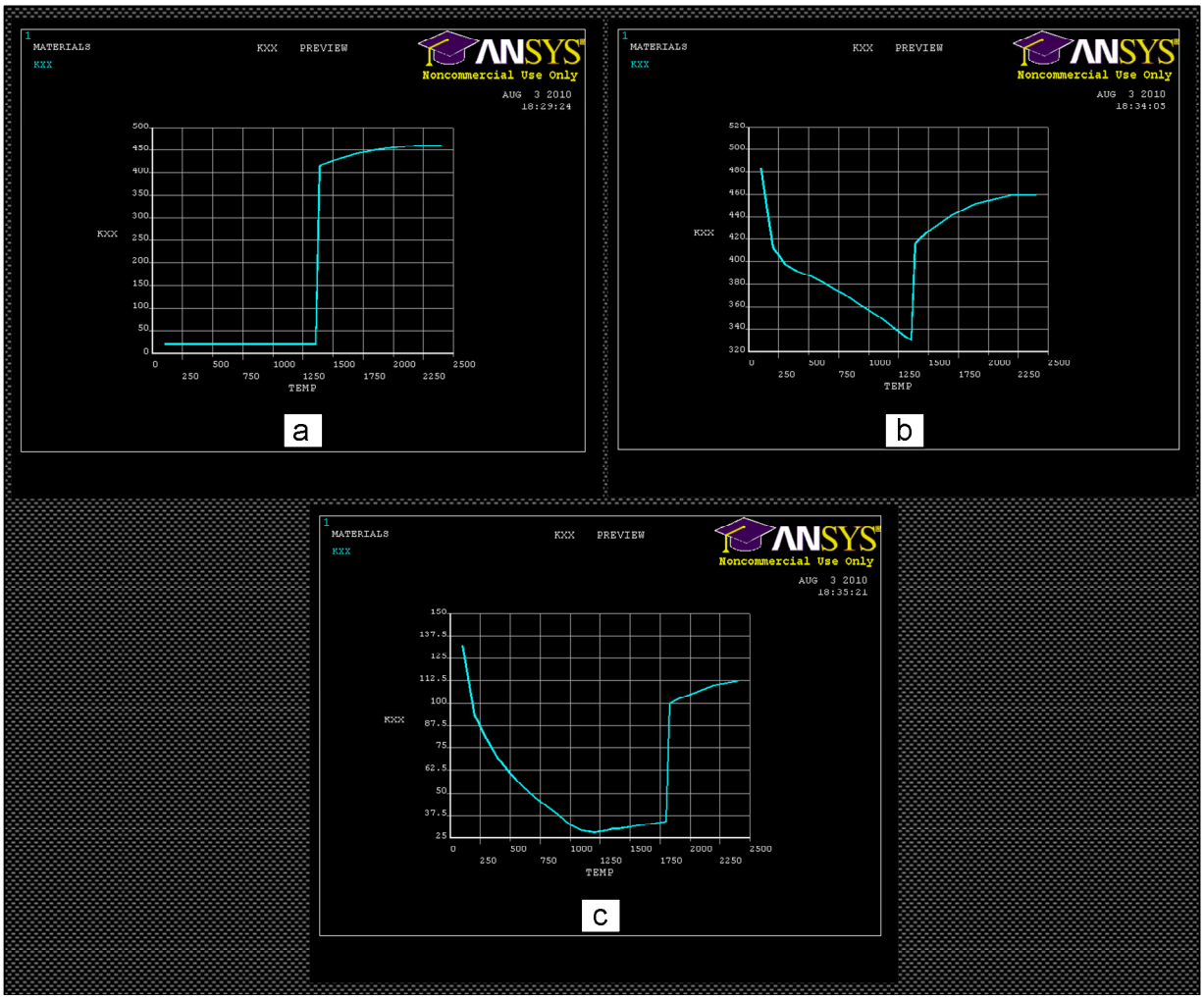

Figure 3.2: Temperature dependent thermal conductivity of the materials used in the experiments, a) Thermal conductivity of the powder bed, b) Thermal conductivity of the solidified clad, c) Thermal conductivity of the substrate.

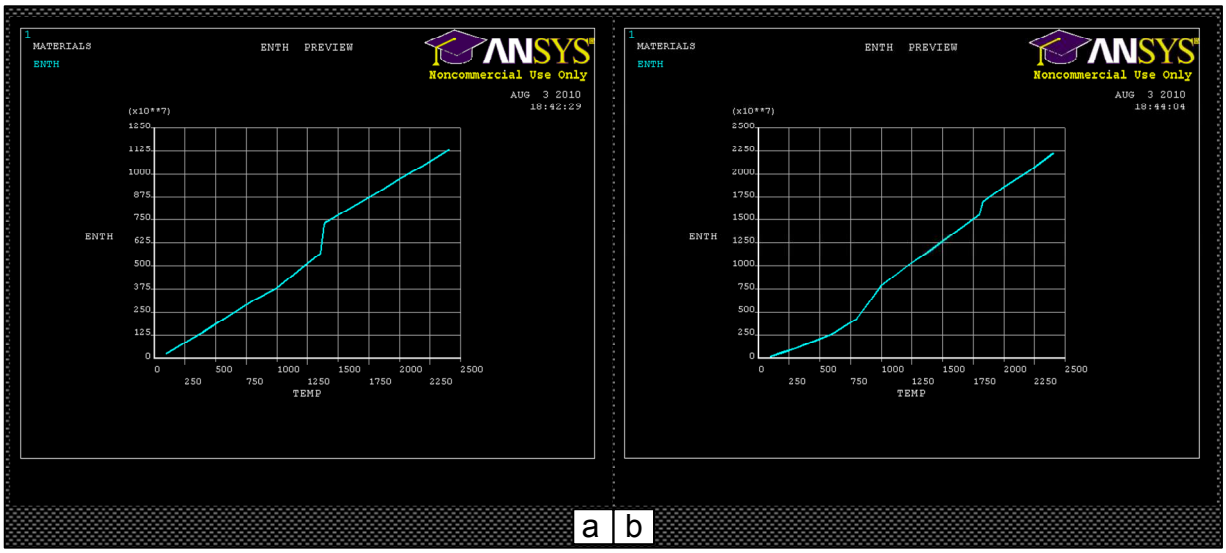

Figure 3.3: Enthalpy of the materials during the process. a) Enthalpy of the powder bed and the solidified clad, b) Enthalpy of the substrate.

elements are deactivated (killing element) at the beginning to consider high thermal resistance between powder bed and substrate.

2. Laser beam irradiation is modeled by heat flux. Therefore, powder bed is heated and the temperature field of powder bed increases.

3. At the end of each load step, the temperature field of powder bed is checked with its liquidus temperature; when the temperature is greater than liquidus temperature, Contact 174/Target 170 pair contact elements are activated (giving birth to the element). As a result, high thermal resistance between powder bed and substrate vanishes.

4. The laser moves to the next location by moving heat flux and steps 2-4 are repeated until the end of track.

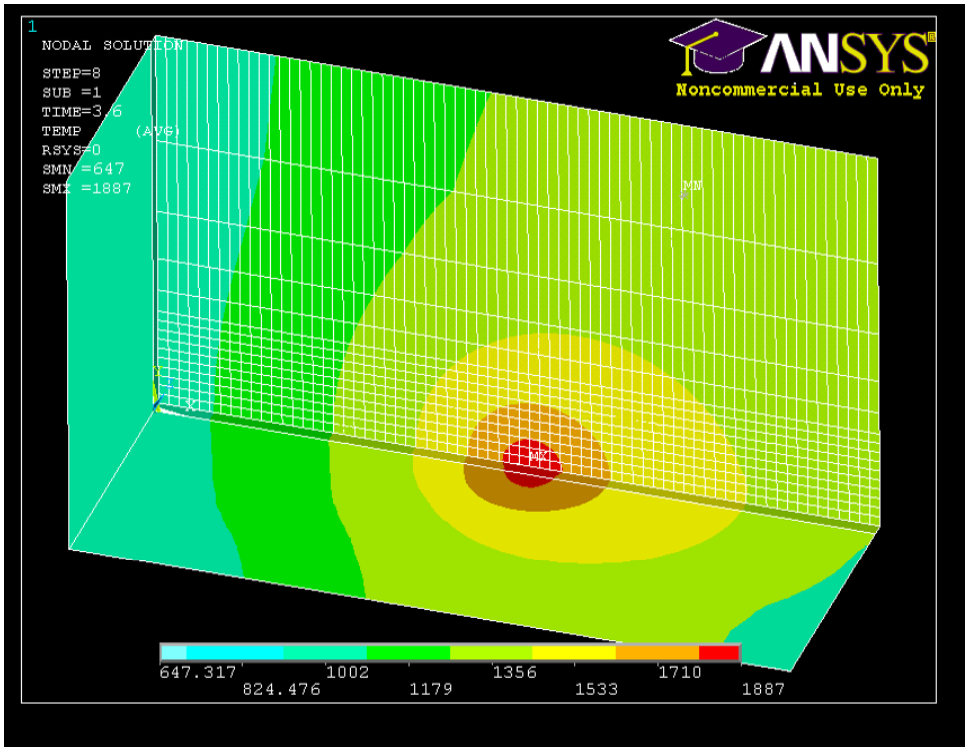

Figure 3.4: Temperature profile of the melt pool and the substrate

3.2 Analysis and Discussions

Figure 3.4 illustrates the temperature profile of the melt pool and the substrate at $t = 3.6\,\text{s}$, where laser power is 400 W , scan speed is 2 mm/s , and laser beam diameter is 2 mm. Radiation and convection heat loss during the process with the above mentioned parameters was calculated as 0.26 W and 0.47 W respectively, which shows that dominant heat transfer mechanism is conduction and effect of convection and radiation are insignificant. The melt pool temperature is 1614°C which is close enough to the process window.

Therefore, the described model can be used for detection of process window and to study the effect of process parameters such as, laser power P, scanning speed velocity V,

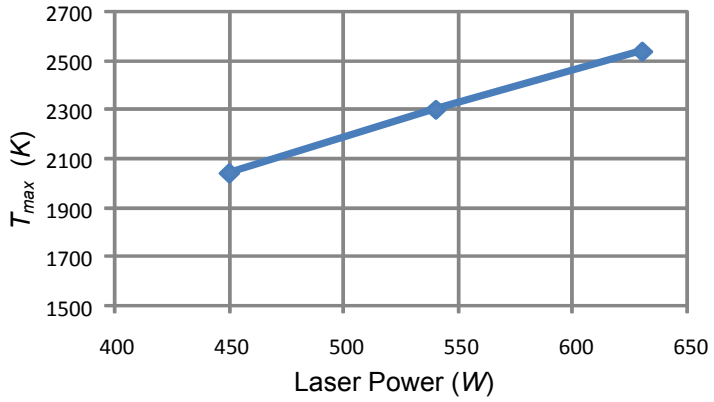

Figure 3.5: Variation of $T_{\max}$ with respect to laser power

laser beam diameter D, substrate dimensions, clad thickness L on temperature profile, and cooling rate during the process. Among these process parameters laser power P, and scanning speed velocity V have the main effect on the process outputs, therefore their effect are discussed in the following sections.

3.2.1 Effect of Laser Power

In order to study the effect of laser power on maximum temperature at a certain point of the clad, a node with the highest temperature almost at the middle of the clad length (half the length of scanning line) was considered. The model was run with three different powers while scanning speed was kept constant at 2 mm/s . In the first run power was 450 W and for each subsequent run, the power increased by 90 W which is 20% of initial value (450, 540, 630 W). In Figure 3.5 the maximum temperature of the node was plotted against power. As one can notice from Figure 3.5 the maximum temperature is highly influenced by change in power as 90 W increase in power (20%) was resulted in around 250 degrees temperature rise in the melt pool.

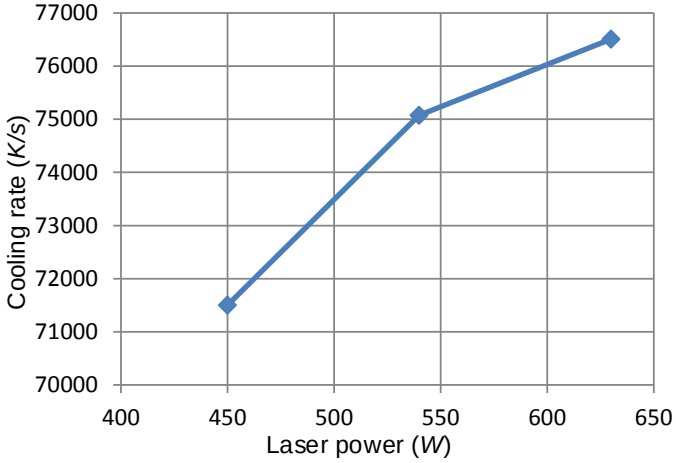

Figure 3.6: Variation of cooling rate with respect to laser power

Maximum cooling rate of the above mentioned node was plotted against power in Figure 3.6. As it can be seen, the cooling rate increases with power increase, however the increase in cooling rate is not significant as the increase of the power from 450 W to 630 W only increases the cooling rate by around 7% . Therefore, increasing power significantly increases the maximum temperature, but the increase in cooling rate is not considerable. As a result, excessive input power should be avoided in order to prevent diamond graphitization.

The calculated cooling rate by the model is in agreement with Rosenthal equation [39] for estimation of cooling rate when a point heat source moves through surface of a semi-infinite work piece which is written as

$$\frac{\partial T}{\partial t} = -2\pi K \left(\frac{v}{P_{eff}}\right)(T - T_0)^2 \tag{3.34}$$

where, $\partial T/\partial t$ is cooling rate, K is thermal conductivity, v is scanning speed, P_{eff} is absorbed power, T is the melting point of surface, and T_0 is ambient temperature. Using

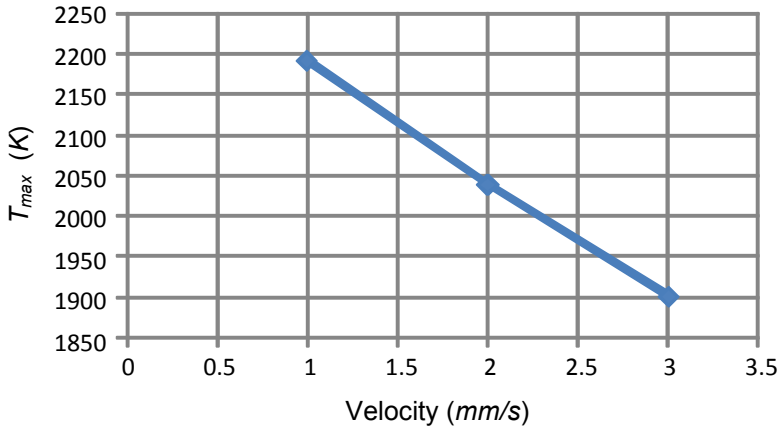

Figure 3.7: Variation of $T_{\max}$ with respect to scanning speed

this formula, and plugging in $K = 350\,\mathrm{W/mK}$, $P = 450 \times 0.25 = 112.5\,\mathrm{W}$, $v = 2\,\mathrm{mm/s}$, $T = 1530°\mathrm{C}$, and $T_0 = 25°\mathrm{C}$ into the formula yields $\partial T/\partial t = 98000\,\mathrm{K/s}$ which is in agreement with the calculated value by the model, $71500\,\mathrm{K/s}$. The difference between the two values can be due to low thermal conductivity of power bed owing to presence of air filled voids. On the other hand, Rosenthal equation considers heat source as a point source on semi infinite work piece assuming no melting and constant thermal properties, therefore it only provides an estimation of cooling rate.

3.2.2 Effect of Scanning Velocity

The same node was considered to study the effect of scanning velocity, however this time power was kept constant at 450 W while scanning speed was varied from 1 to 3 mm/s with increments of 1 mm/s. The maximum temperature of the node was plotted against scanning speed as shown in Figure 3.7. As it can be seen in the figure, the maximum temperature decreased with the increase in velocity; however, the maximum temperature is not as sensitive to velocity change as it is to power change, since with increasing velocity

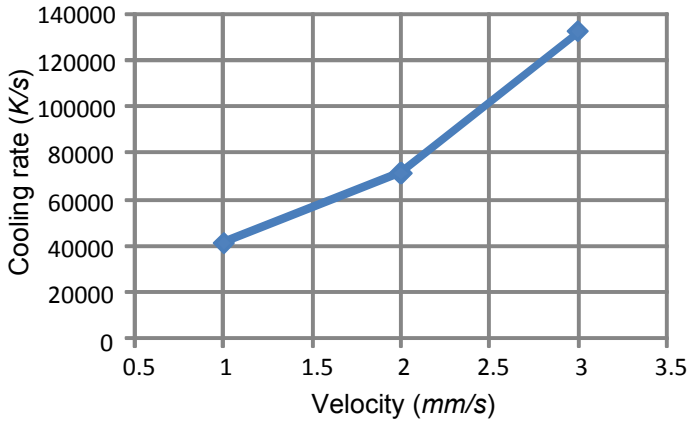

Figure 3.8: Variation of cooling rate with respect to scanning speed

from 1 mm/s to 2 mm/s (100 percent increase) the temperature only decreased 150°C which is only around 7 percent decrease. The maximum cooling rate was also plotted against velocity as shown in Figure 3.8. As it can be seen in the figure cooling rate considerably increased with the increase of speed.

In summary, it can be concluded that power has dominant effect on maximum temperature and lesser effect on cooling rate, whereas, scanning speed has major effect on cooling rate and minor effect on maximum temperature.

3.2.3 Variation of Maximum Temperature During the Process

Maximum temperature (melt pool temperature) was calculated at different locations along the length of the clad for 3 different powers of 450, 540, and 630 W, while velocity was kept constant at 2 mm/s. Figure 3.9 shows variation of maximum temperature along the length of clad for three mentioned powers. As one can notice from the figure, the melt pool temperature was not constant along the laser trajectory, indeed, it was increased substantially; 304, 403, and 494 degrees increase for 450, 540, and 630 W laser power, respectively.

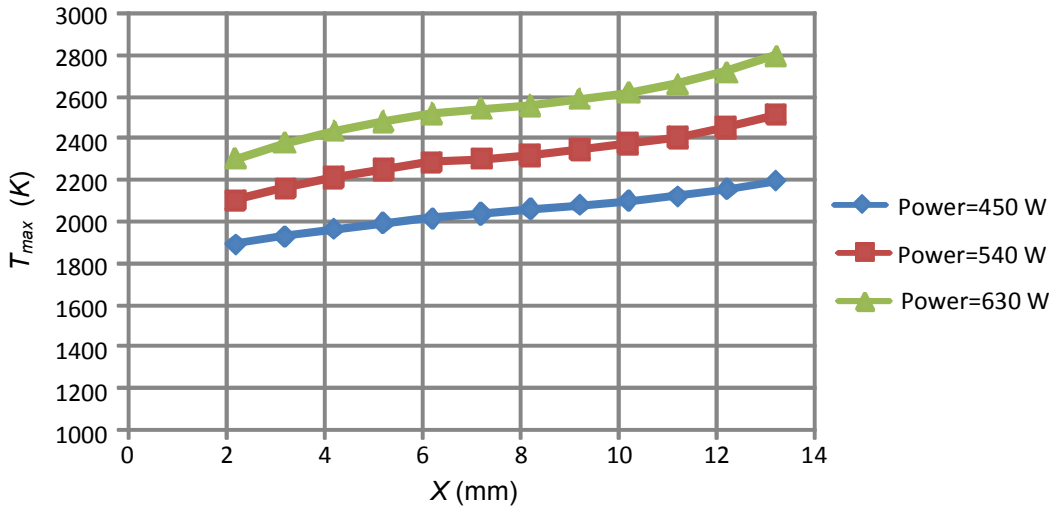

Figure 3.9: Variation of maximum temperature along the length of the clad (different powers)

Therefore, increasing power not only drastically increases the melt pool temperature at one location, but also it increases its variation along the laser scanning trajectory.

The same procedure was repeated for three different velocities 1, 2, and 3 mm/s while the power was kept constant at 450 W. Variation of the melt pool temperature along the length of clad for the three mentioned velocities was shown in Figure 3.10. The melt pool temperature was increased by 353, 304, 192 K along the laser scanning trajectory for 1, 2, and 3 mm/s scanning speed, respectively; therefore increasing speed not only decreases melt pool temperature at one location but also it decreases its variation along the length of the clad.

It should be noted that, these large variations in the melt pool temperature along the length of clad, is partly due to the small dimensions of the substrate in the simulation. The substrate is only 14 mm long while the laser beam diameter is 2 mm, which increases the amount of accumulated heat drastically which in turn results in larger increase in the

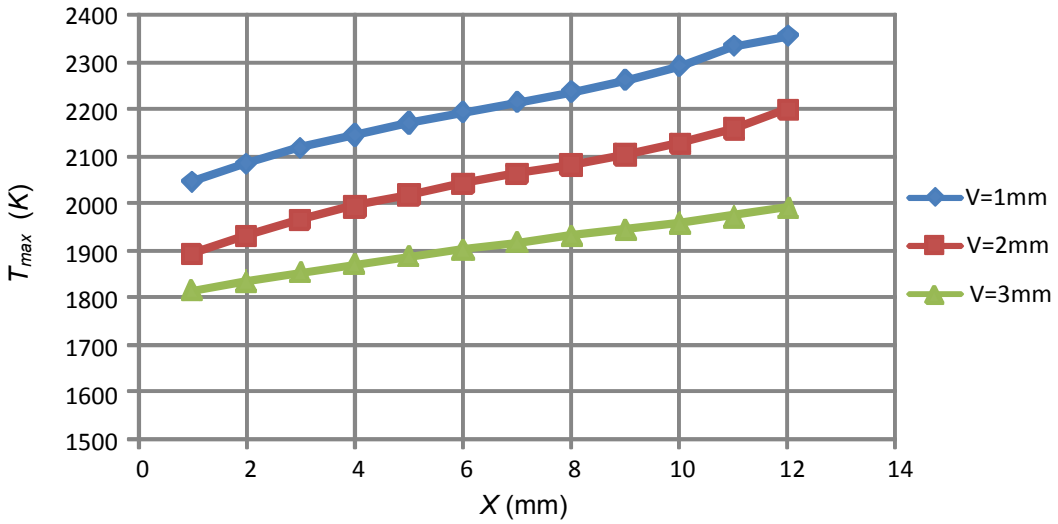

Figure 3.10: Variation of maximum temperature along the length of the clad (different velocities)

melt pool temperature along the laser pathway.

Increase in melt pool temperature along the process makes the deposition of diamond more complicated. The process parameters are acquired for obtaining minimum necessary melt pool temperature at the beginning of process, however after the beginning of process, the melt pool temperature increases during deposition process which in turn accelerates diamond graphitization. Therefore design and integration of a feed back control system which can change the process parameters in real time in order to keep the temperature constant during the process is inevitable.

Chapter 4

Experimental Methodology, Results, and Analysis

In this chapter, the experiments conducted on deposition of the precursor powder mixture of diamond, copper, tin, and titanium by laser cladding on the mild steel substrate are described. Also, results and the associated analysis will be presented.

4.1 Powder Mixture Preparation

In order to make the precursor mixture of diamond, copper, tin, and titanium, powders with the specification shown in Table 4.1 were prepared. Powders of copper, tin, titanium, and diamond with the weight ratio of 54%, 13.5%, 7.5%, and 25%, respectively, were mixed.

In order to mix the constituent powders and obtain a uniform distribution of elements with the desired composition, the ball milling method was used. Ball milling is an effective method to obtain uniform distribution of elements [42]. Powders were placed inside a

Table 4.1: Material powders used in the experiments and their specifications

Material	Particle size	Specifications
Diamond	50 to 63 micron	Synthetic diamond
Copper	44 to 149 micron	99.9% purity, spherical shape
Tin	less than 149 micron	99.5% purity
Titanium	less than 44 micron	99.5% purity

cylindrical glass container. Hard ceramic balls with the diameters of 5 mm were added to the mixture. The container was placed horizontally on the ball mill machine and was rotated for 24 hours around its horizontal axis. The mixture was placed in a furnace and was heated at 115°C for 5 hours in order to eliminate any possible moisture.

4.2 Experimental Set-up

The laser cladding process was performed using the Automated Laser Fabrication (ALFα) facility at the University of Waterloo. A seven axis CNC machine which was customized for conducting laser metal direct deposition was used for providing motion of the substrate, controlling the laser beam focal point, and moving the lateral nozzle. The laser head is integrated in the CNC machine. The substrate was placed in the CNC machine under the laser head. Two lasers were employed as the source of energy for the experiments, a LASAG FLS 1042N Nd:YAG pulsed laser with a maximum power of 1000 W and wavelength of 1064 nm, and an IPG fiber continuous wave laser with the a maximum power of 1100 W and wavelength of 1070 nm. Both lasers have almost purely Gaussian beam energy distribution with TEM_{00} mode. A Sulzer Metco TWIN 10-C powder feeder with a side hopper was employed to convey the mixture of powders and argon to a lateral nozzle for feeding into the process zone (powder feeder system was only used for blown powder laser

depositions). The National Instrument real time operating system (Lab View) was used to control the entire system. A schematic view of the entire system is illustrated in Figure 4.1.

4.3 The Experiments: Pre-placed Laser Cladding

The pre-placed laser cladding was conducted before performing blown powder laser cladding for the following reasons:

- To study the feasibility of the deposition
- It has less complications compared to blown powder laser cladding
- To obtain insights into the process parameters and the results
- To verify the developed numerical model in Chapter 3 by comparing the trends

The substrate was chosen as AISI 1030 mild steel ($0.25 - 0.28$ wt% carbon) with the dimensions of 120 mm $\times$ 38 mm $\times$ 5 mm (length $\times$ width $\times$ thickness). A rectangular groove with the depth of 300 micron and width of 14 mm was machined along the length of each substrate. The substrates were sand blasted and then cleaned with acetone. The powder mixture was spread on the groove as a thin layer with the thickness of 300 micron. Both the CW laser and the pulsed laser were used for the experiments. The beam diameter of both lasers was 1.2 mm on the surface of the powder bed. The length of each clad was equal to the width of the groove (14 mm). The width of each clad was around 1.2 mm which was the laser beam diameter.

A variety of experiments were conducted using different process parameters. Scanning velocity and energy per pulse were varied while pulse frequency and pulse duration were

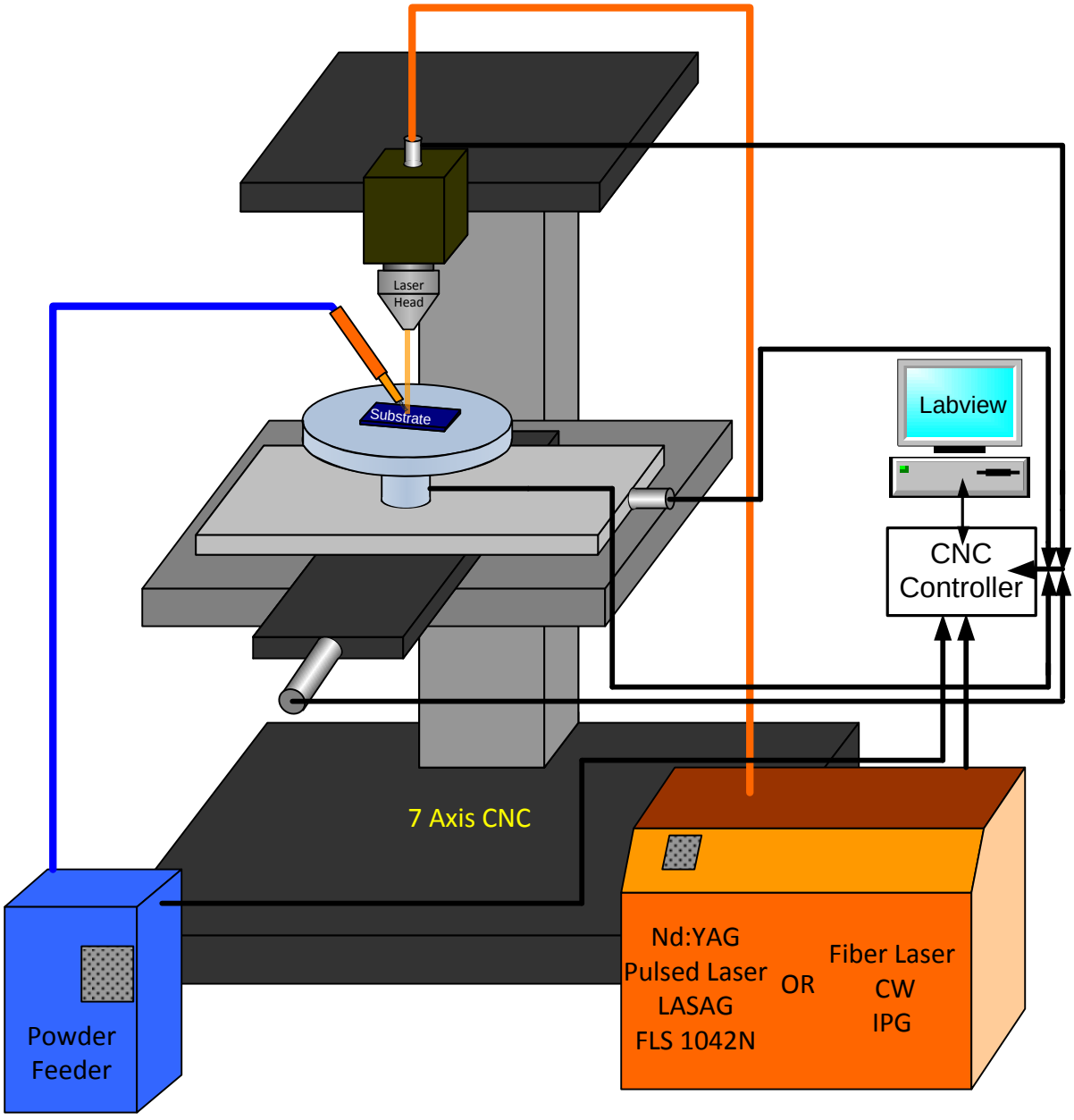

Figure 4.1: A schematic view of the system used for conducting laser direct metal deposition

kept constant during the course of experiments with the pulsed laser. Laser power and scanning velocity were varied for the experiments with the CW laser.

The modeling results were used to narrow down the trial and error window of process parameters during the experiments. Among several experiments, one set of experiments with each laser which essentially demonstrate the effect of process parameters on the process output are presented here. Table 4.2 demonstrates the process parameters of one set of experiments with the CW laser. For the CW laser, power and scanning speed were varied from 280 W to 120 W and from 2 mm/s to 17 mm/s, respectively.

Table 4.2: Process parameters for a selected set of experiments with the CW laser

Power (W)	Scan speed (mm/s)	Visible Quality of clad-substrate bonding
280	2	good bonding
280	3	good bonding
280	4	good bonding
280	5	good bonding
280	9	good bonding
280	12	weak bonding
280	15	weak bonding
280	17	no bonding
200	2	good bonding
200	3	good bonding
200	4	good bonding
200	5	weak bonding
200	6	no bonding
120	2	good bonding
120	3	no bonding
120	4	no bonding

Table 4.3: Process parameters for a selected set of experiments with the pulsed laser

Power (W)	Pulse energy (J)	Frequency (Hz)	Pulse width (ms)	Scan speed (mm/s)	Visible quality of clad-substrate bonding
280	7	40	3	2	good bonding
280	7	40	3	3	good bonding
280	7	40	3	4	good bonding
280	7	40	3	5	weak bonding
280	7	40	3	6	no bonding
200	5	40	3	2	good bonding
200	5	40	3	3	weak bonding
200	5	40	3	4	no bonding
120	3	40	3	2	good bonding
120	3	40	3	3	no bonding
120	3	40	3	4	no bonding

Table 4.3 presents the process parameters of one set of experiments with the pulsed laser. For the pulsed laser, pulse frequency and pulse width were kept constant while pulse energy and scanning speed were varied from 7 J to 3 J and from 2 mm/s to 6 mm/s, respectively. For the pulsed laser, the power can be calculated by

$$P = Ef \tag{4.1}$$

where, P is the equivalent power [W], E is energy per pulse [J], and f is pulse frequency [Hz].

4.4 Characterization Methodology

4.4.1 Deposition and Substrate Characterization

Material characterization was conducted on the polished cross-section and longitudinal-section cuts of the deposited samples. An Olympus BH2-UMA model microscope was utilized for optical microscopy. A Jeol: JSM-6460 scanning electron microscope (SEM), integrated with Oxford Instruments' INCA X-ray chemical analysis instrument (EDS), and a LEO 1530, high-resolution field emission scanning electron microscope (FESEM) equipped with an Energy-dispersive X-ray spectroscopy (EDS) instrument were employed to study the microstructure and chemical compositions of the samples. A SA-HF3 X-Ray generator machine and Cu-Kα radiation with 2 kW power was employed for X-ray diffraction (XRD) test to identify material phases and atomic structures of the deposits.

A Hysitron TI 900 Triboindenter machine was used for nanoindentation tests. The probe was a Berkovich tip which is the standard three-sided pyramidal probe with a total included angle (plane to edge) of 142.3° and a half angle of 65.35° as well as with an average radius of curvature of about 50 nm. This tip is primarily used for bulk materials and thin films greater than 100 nm which makes it suitable for nanoindentation of the samples in this study. Loading and unloading times were 10 second each. The unloading was performed immediately after loading. Load-displacement-time data were obtained during indentation. Elsastic modulus and poisson's ratio of the specimen is calculated by

$$\frac{1}{E_r} = \left(\frac{1-\nu^2}{E}\right)_{\text{Specimen}} + \left(\frac{1-\nu^2}{E}\right)_{\text{Indentor}} \tag{4.2}$$

where, ν is poisson's ratio, E is elastic modulus, and E_r is the reduced elastic modulus. The software of the machine also provided the hardness of the tested point.

4.4.2 Diamond Characterization

Characterization of diamond is of great importance since it is necessary to determine if the diamond particles inside the deposit have kept their original structure, otherwise what degree of graphitization has happened. In this study the deposited diamond particles were characterized by the following methods to detect if any graphitization occurred in the deposited diamond particles and detect the degree of possible graphitization.

1. SEM: Crystalline structure of diamond is visually differentiable from graphite using scanning electron microscopy. However, detecting the degree of diamond graphitization or identification of disordered sp^2 carbons is not possible with this method unless a high degree of graphitization occurred. Figure 4.2 illustrates SEM micrograph of diamond particles used in this study. Figure 4.3 shows two deposited diamond particles which were highly decomposed. As it can be seen, intact diamond particles and decomposed ones can be identified by their different morphologies in the figures, diamond particles have a defined blocky shape and smooth faces, while decomposed diamonds do not show these features. The diamond particles in Figure 4.3 are highly decomposed, however morphology of diamond particles that experienced some degrees of decomposition do not have a noticeable difference from intact diamonds. Therefore, SEM can only be used for identification of high degrees of diamond graphitization.

2. X-Ray Diffraction (XRD) can be used for accurate identification of diamond and graphite. In this study, the diamond particles are around 50 microns. On the other hand, as mentioned in Chapter 2, graphitization begins from diamond surface; therefore in order to detect graphitization with the size of a few microns, an XRD instrument with micro focus capability is needed.

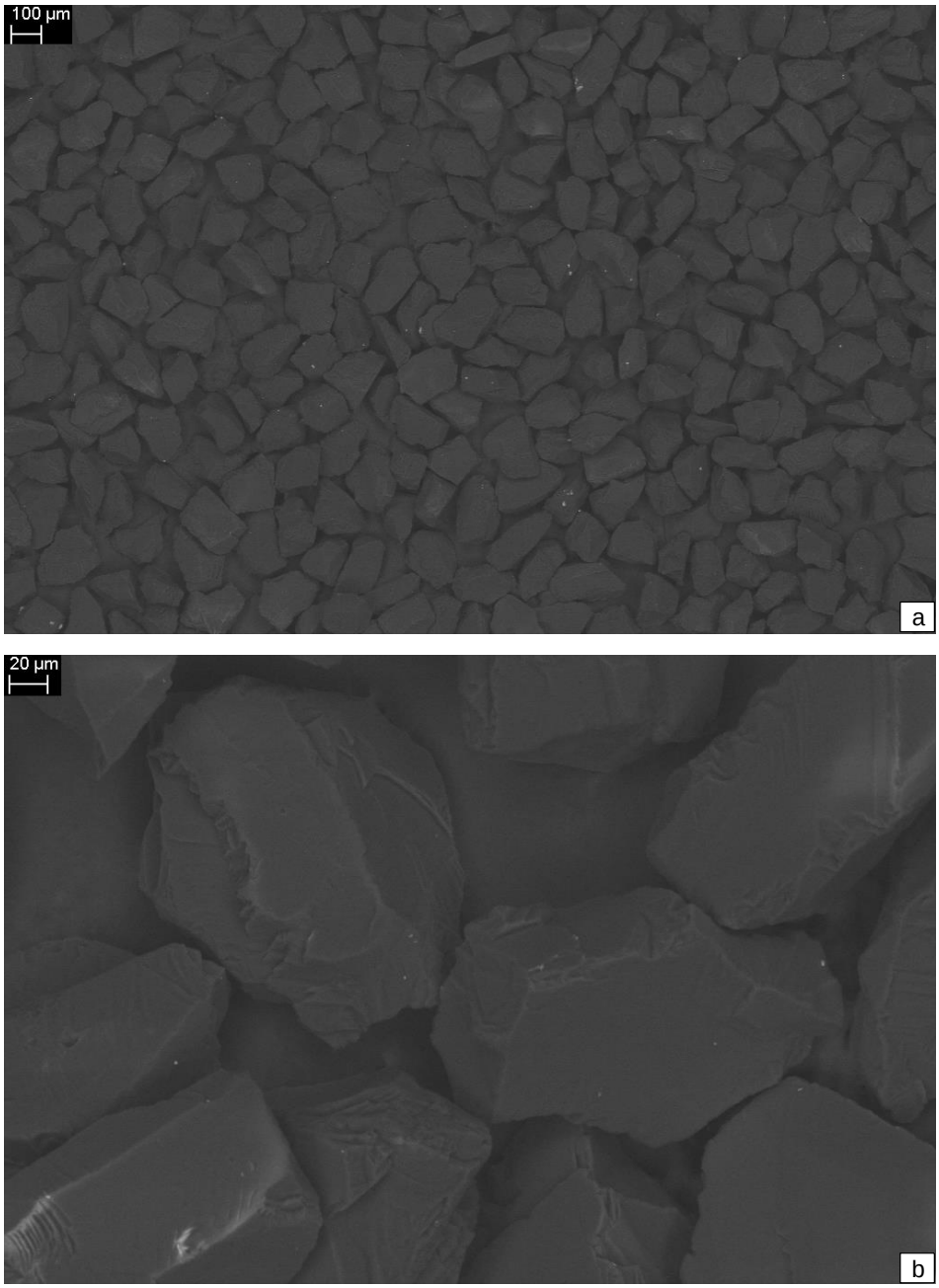

Figure 4.2: SEM microghraph of the diamond powder used in this study

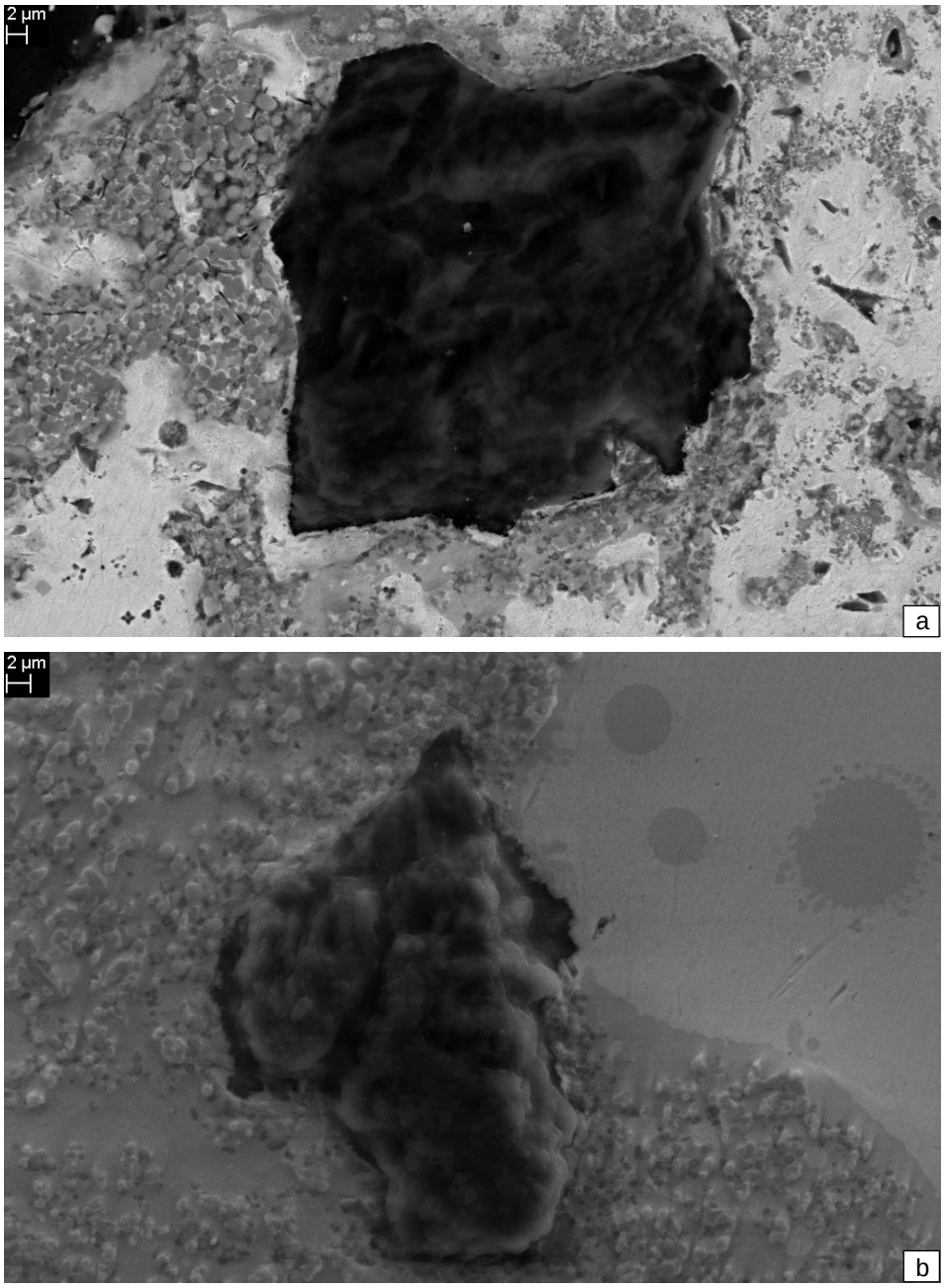

Figure 4.3: Two deposited diamond particles which experienced a high degree of decomposition

3. Raman spectroscopy is the best and most sensitive method for identifying small amount of graphite in a mixture of all other forms of carbon. Raman scattering efficiency for the sp^2-bonded graphite is 500×10^{-7} cm^{-1}, while that of sp^3-bonded diamond is only 9×10^{-7} cm^{-1}. Therefore Raman scattering efficiency of graphite is more than 50 times greater than that of diamond; as a result, any percentage of graphite in a diamond particle can efficiently be identified [12, 43].

Since Raman spectroscopy is the most sensitive way for identification of graphite in a mixture of all forms of carbon which is the case in this study; Raman spectroscopy was used for characterization of diamond in this study.

In Raman spectroscopy, a monochromatic light, usually laser, strikes the molecules of a sample. Laser light interacts with electron cloud and bonds of atoms which causes change in energy of the laser photons. As a result, the wavelength of the reflected light is different from that of the source. This difference provides information about chemical structure and atom bonds of the illuminated molecules [44, 45]. Raman spectrum is expressed in wavenumber which is reciprocal of wavelength. As a result, Raman shift can be expressed by [45]

$$\Delta\omega = \left(\frac{1}{\lambda_l} - \frac{1}{\lambda_s}\right) \times 10^7 \tag{4.3}$$

where, $\Delta\omega$ is Raman shift which is expressed in wavenumber [cm^{-1}], λ_l is the wavelength of laser in nm, and λ_s is the wavelength of scattered light in nm.

It should be noted that the intensity and signal/noise ratio of Raman spectrum are also highly dependent on how well the laser is focused on the plane of the sample. Therefore for the samples with flat planes perpendicular to the laser beam intensity is higher and signal to noise ratio is better whereas for samples that don't have flat planes perpendicular

to laser beam intensity is lower and signal to noise ratio is worse [46].

Diamond is identified by one sharp line at 1332 cm^{-1} [43]. Single crystals graphite has a Raman spectrum with only one peak at around 1575 cm^{-1} this peak is called G band after graphite [43]. Polycrystalline graphite shows in addition to G band another peak at around 1360 cm^{-1} which is called D band after defects [43, 46].

The G band is related to the stretching mode of C-C inside each carbon sheet [47, 48, 43] and exists in spectrum of all graphitic carbons [47]. An increase of less than 15 cm^{-1} in wavenumber might be observed in samples with very small crystal sizes [47]. First order Raman lines are related to structural order of carbon inside each sheet (two dimensional ordering) while the second order bands depend on stacking disorder in the crystallographic c-axis (three-dimensional ordering) [43, 49].

The D band emerges in Raman spectrum of "well-crystallized graphite with small particle size [43]" such as polycrystalline graphite [47, 48, 43]. As the mean crystallite size of graphitic carbon decreases the intensity of D band increases [47], indeed, relative intensity of D band with respect to G band, I_D/I_G, is inversely proprosional to mean crystallite size in the graphite plane, L_a [47, 48, 43, 50, 51]. Cancado *et al.* [50] showed that the ratio of the area of D band over the area of the G band in a Raman spectrum of nanographite is also proportional to the forth power of the excitation laser energy used in the Raman spectroscopy. By experimental analysis, they derived a general formula which determines in-plane crystallite size, L_a, as [50]

$$L_a = \frac{560}{E_l^4} \left(\frac{I_D}{I_G} \right)^{-1} \tag{4.4}$$

where L_a is in-plane crystallite size [nm], E_l is the excitation laser energy used in Raman

spectroscopy [eV], and (I_D/I_G) is the intergrated intensity ratio of D band over G band (the ratio of area of D band with respect to area of G band in the spectrum). Converting E_l to laser wave length, λ_l, results in [50]

$$L_a = \left(2.4 \times 10^{-10}\right) \lambda_l^4 \left(\frac{I_D}{I_G}\right)^{-1} \tag{4.5}$$

where λ_l is in nanometer. Therefore, L_a is proportional to forth power of wavelength of excitation laser and reciprocal of (I_D/I_G).

The width of D and G bands is an indication of how disordered the graphitic carbon is, since coke and charcoal which are greatly disordered carbon have wide D and G band while the D and G band become sharper in glassy carbon and polycrystalline graphite [43]. This is specially true for G band where stretching the band is an indication of disorder within each sheet [43]. Narrow D band also imply that the range of in-plane crystallite sizes is limited [50].

Graphite shows a peak around 2700 which is 2×1350 and is second harmonic of D band [43, 49, 51]. This band is called G′ [51]. Second order bands are related to stacking order of sheets alongside crystallographic c-axis [43, 49]. Researchers realized that G′ band emerges as one peak in turbostratic graphite whereas it appears as a double structure in crystalline graphite [52, 48, 53]. Wilhelm et al. proposed that the double peak of G′ band in crystalline graphite is related to stacking order of sheets along c-axis [54]. This hypothesis was verified when researchers observed that a single peak appears as G band in Raman spectrum of one layer of graphene whereas double peaks emerges as G band in Raman spectrum of multi layers of graphene [51]. Cancado et al. by analysis of Raman spectra of different nanographite samples showed that two-dimentional graphite samples had one peak centered at 2707 cm^{-1} called G'_{2D}, whereas three-dimentional graphite samples had double structure

peaks which can be fitted by two Lorentzian centered at 2687 cm^{-1} and 2727 cm^{-1} called G'_{3DA} and G'_{3DB}, respectively [51]. They observed that samples with concurrent presence of 2D and 3D graphites show peaks which can be fitted by three Lorentzian G'_{3DA}, G'_{2D}, and G'_{3DB}, respectively. When the amount of 3D graphite increases in the samples, the relative integrated intensity (the area of peaks) of G'_{2D} decreases whereas those of G'_{3DA} and G'_{3DB} increases [51]. However, relative integrated intensity of G'_{3DB} with respect to that of G'_{3DA} ($I_{G'_{3DB}}/I_{G'_{3DA}}$) remains constant near 2 [51]. If V is the volume covered by the laser beam, then $V = V_{2D} + V_{3D}$ where V_{2D} and V_{3D} are volumes of 2D and 3D graphites, respectively. Considering $v_{2D} = V_{2D}/V$ and $v_{3D} = V_{3D}/V$, the fractions of 2D and 3D phases in the area covered by the laser beam can be estimated by [51]

$$R = \frac{I_{G'_{3DB}}}{I_{G'_{3DB}} + I_{G'_{2D}}} \tag{4.6}$$

where $v_{3D} = R$ and $v_{2D} = 1 - R$.

Study of Raman Spectra of the Deposited Diamond Particles

Two Raman spectrometers were utilized for characterization of deposited diamond particles. A Senterra dispersive Raman microscope spectrometer equipped with a laser with the wavelength of 532 nm as the source of excitation. The laser beam diameter on the surface of the sample is 2 micron. A Renishaw micro-Raman spectrometer equipped with a laser with the wavelength of 488 nm (blue, Ar ion). The Raman spectrometer has reflected light microscope which allows a mini-analyzed area of 5 micron. The resolution of Raman shift is 0.5 wavenumbers. The microscope has 5, 20, and 50 times objectives. The integration time for all samples was considered as 30 seconds.

Raman spectroscopy was conducted on a few diamond particles of the diamond powder

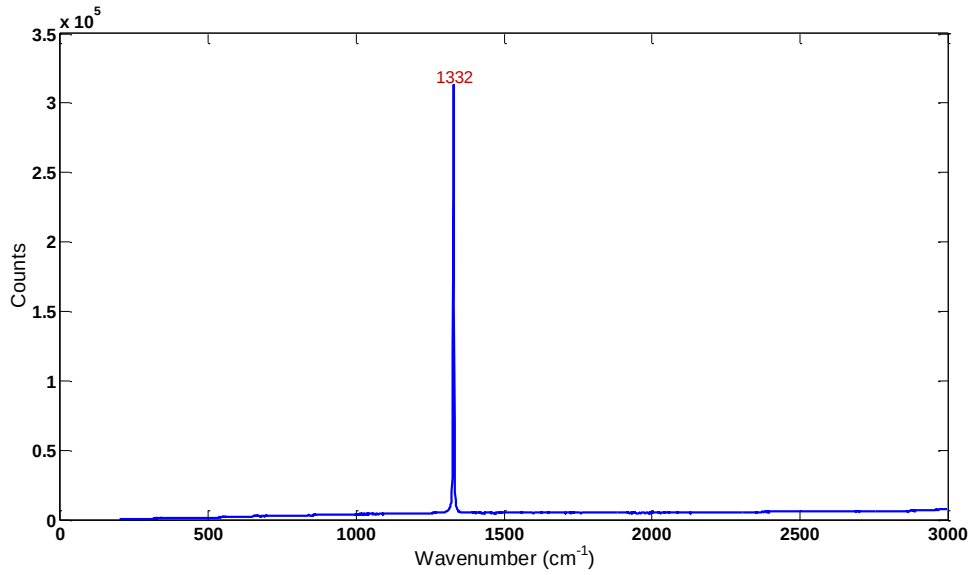

Figure 4.4: Raman spectrum for a selected diamond particle from the diamond powder used in the experiments

used in this study. All acquired spectra were identical with the peak between 1330 cm^{-1} and 1333 cm^{-1}; however mostly at 1332 cm^{-1}.. Figure 4.4 shows the acquired Raman spectrum on one of the diamond particles. As one can see, there is only one sharp line at 1332 cm^{-1} which is the signature of diamond spectrum [43].

Raman spectroscopy was carried out on crystalline graphite powder with the particle size of less than 50 micron and purity of 99%. Figure 4.5 demonstrates the result. The graphite powder had four peaks at 1357 cm^{-1}, 1570 cm^{-1}, 2425 cm^{-1}, and 2720 cm^{-1}. The sharp band at 1580 cm^{-1} (G band) is related to stretching mode of C-C bond at each hexagonal sheet in each layer [43]. The 2724 cm^{-1} (G′) band emerges in the spectrum of polycrystalline graphite [43]. The 1357 cm^{-1} (D) band only emerges in well-crystallized graphite with small particle size [43].

It was desired to identify the diamond graphitization which means to identify three-

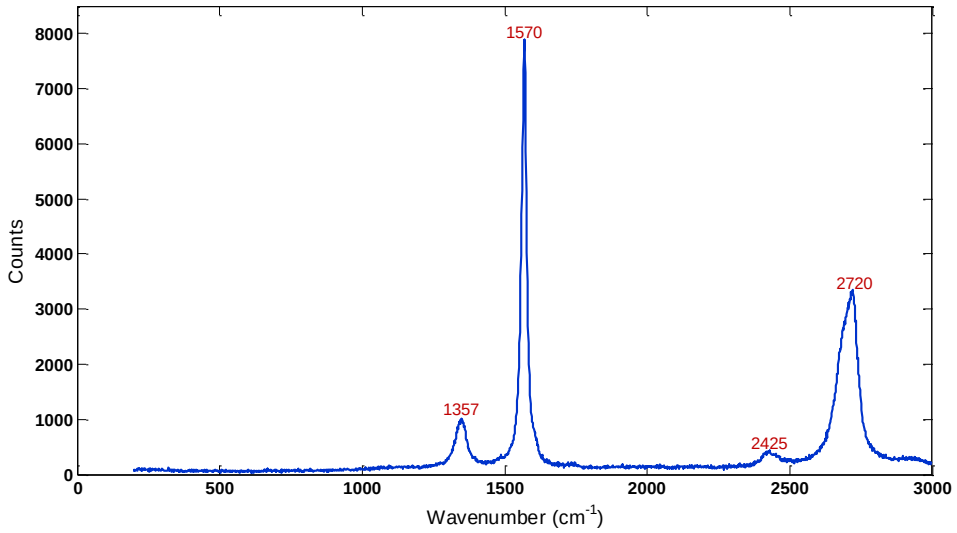

Figure 4.5: Raman spectrum of a graphite particle of crystalline graphite powder with maximum particle size of 45 micron and 99% purity

coordinated carbon atoms with sp^2 hybrid orbital bonds. In fact, these are disordered sp^2 carbons. As mentioned before, Raman spectroscopy is the preferred method for identification of these carbons. Raman spectroscopy was conducted on several diamond particles in each deposit. The acquired Raman spectra can be categorized into five groups. The characteristic Raman spectrum of each group is shown in Figure 4.4 and Figures 4.6 to 4.14.

The first group has practically the same spectrum as diamond powder which was shown in Figure 4.4. This indicates no graphitization was detected in these diamond particles.

A typical Raman spectrum of the second group is presented in Figures 4.6 to 4.8. As it can be seen, there are two peaks in the spectrum, 1332 cm^{-1} band which represents the diamond structure, and 1580 cm^{-1} band (G band) which characterizes the presence of disordered sp^2 carbons. The relative intensity of band 1580 cm^{-1} to 1332 cm^{-1} band varied among collected Raman spectra in this group. This relative intensity shows the degree of

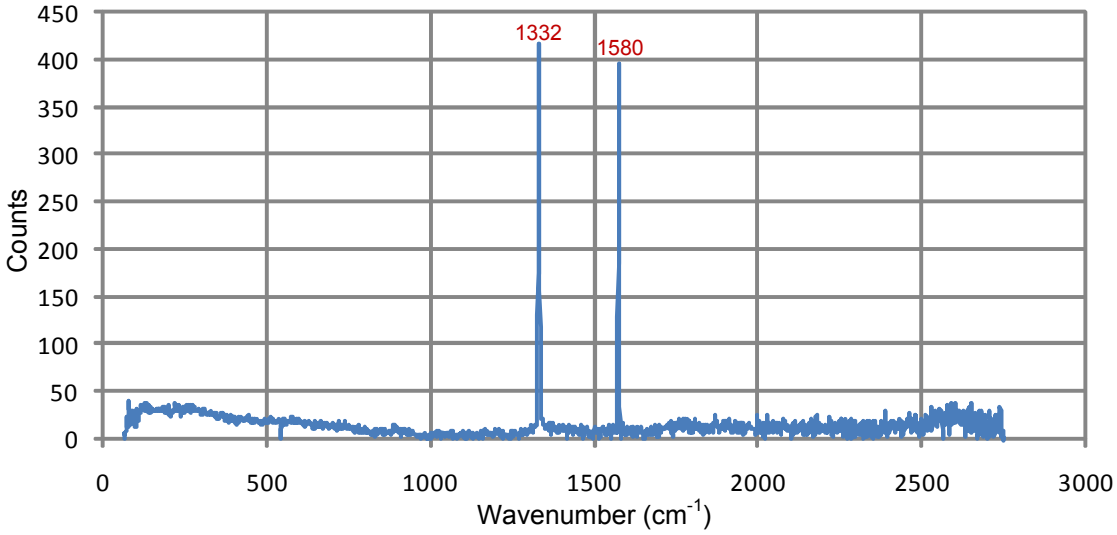

Figure 4.6: A typical Raman spectrum for diamond particles in the second group

presence of disordered sp^2 carbons or degree of graphitization [43], for example the degree of graphitization decreases from Figures 4.6 to 4.8. In addition, band width of 1580 cm^{-1} changed among the collected Raman spectra; this band width is related to the structure of graphitic carbon [43]. The G band was usually centered at 1570 cm^{-1} to 1590 cm^{-1} in the collected Raman spectra. This peak wavenumber is also associated to the structure of graphitic carbon [43]. One can find comprehensive discussions about relation between the aforementioned features of Raman spectrum and the structure of graphitic carbon in the literature which is beyond the scope of this study.

The third group has a typical Raman spectrum as demonstrated in Figure 4.9 and Figure 4.10. As one can see, there are two peaks in the figure, 1332 cm^{-1} and 1357 cm^{-1}(D band) which represent diamond and graphitic carbon, respectively. Like the second group, the relative intensity of 1357 cm^{-1} to 1332 cm^{-1} varied among collected Raman spectra which shows the degree of graphitization, for example the degree of graphitization decreases from 4.9 to Figure 4.10. Likewise, band width of 1357 cm^{-1} which is associated to the structure

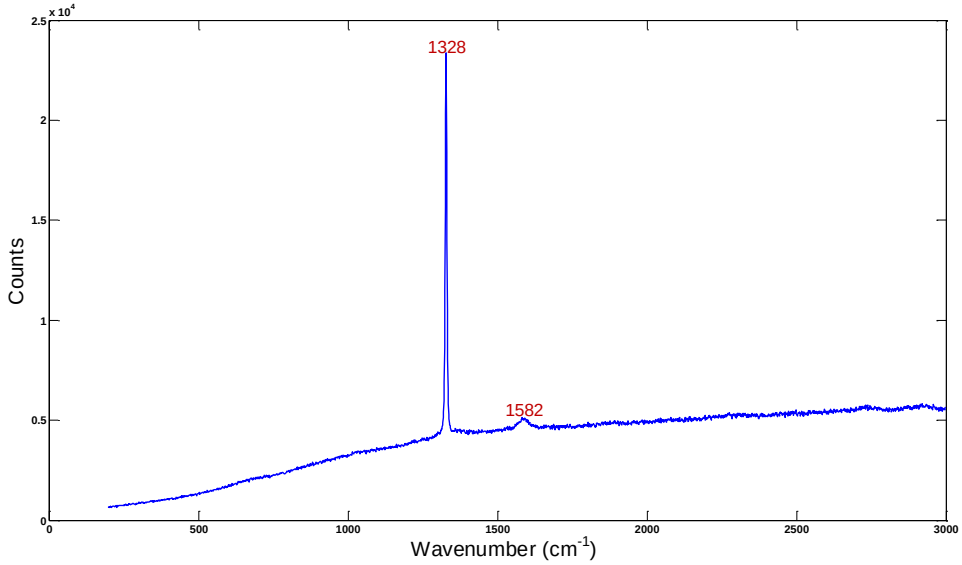

Figure 4.7: A typical Raman spectrum for diamond particles in the second group

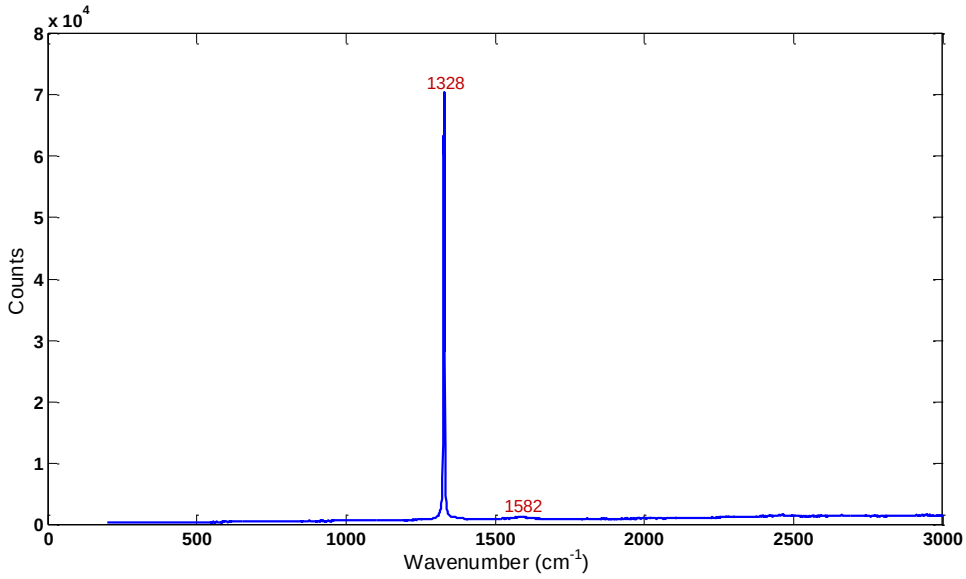

Figure 4.8: A typical Raman spectrum for diamond particles in the second group

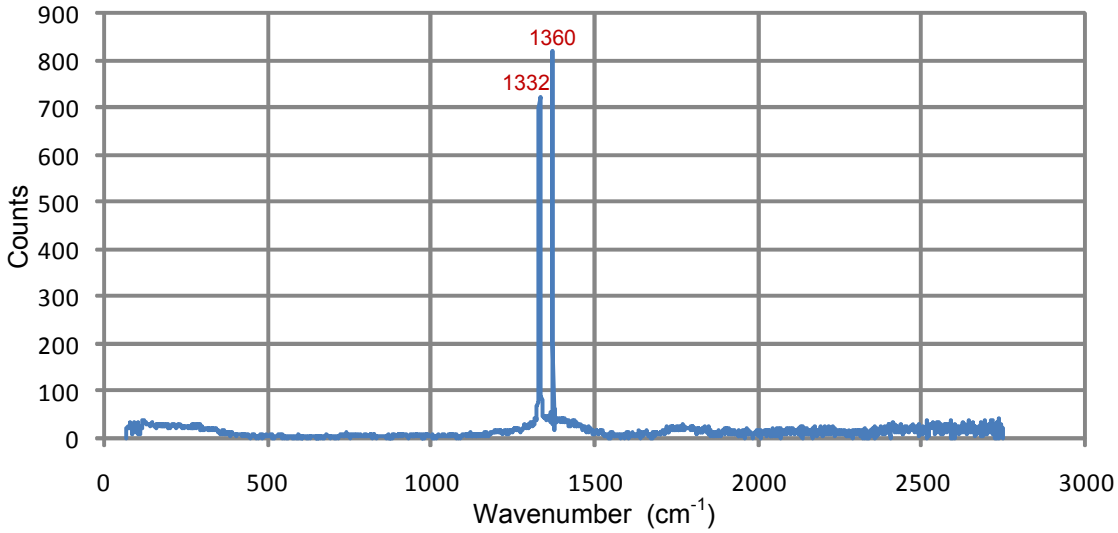

Figure 4.9: A typical Raman spectrum for diamond particles in the third group

of graphitic carbon changed among the collected Raman spectra. The peak wavenumber in D band which is related to the structure of graphitic carbon is usually centered between 1355 cm^{-1} and 1360 cm^{-1} in the collected Raman spectra.

The fourth group (shown in Figure 4.11 and Figure 4.12) has a typical Raman spectrum with four peaks, 1330 cm^{-1}, 1357 cm^{-1}, 1580 cm^{-1}, and 2720 cm^{-1} where the first is the characteristic of diamond and the other three are the characteristics of graphitic carbon. In addition to the changes in relative intensity of 1330 cm^{-1} band to D and G band, peak center of D and G band, and band width of D and G band, D/G relative intensity also changed among the collected Raman spectra. D/G relative intensity is also an important factor associated to structure of graphitic carbon [43]. Relative intensity of G band to 1330 cm^{-1} is a good indication of the degree of graphitization, for example, Figure 4.11 shows a higher degree of graphitization compared to Figure 4.12.

Typical Raman spectra of the fifth group are depicted in Figure 4.13 and Figure 4.14. The Raman spectrum has four peaks, 1358 cm^{-1}, 1580 cm^{-1}, 2720 cm^{-1}, and 2936 cm^{-1}. This

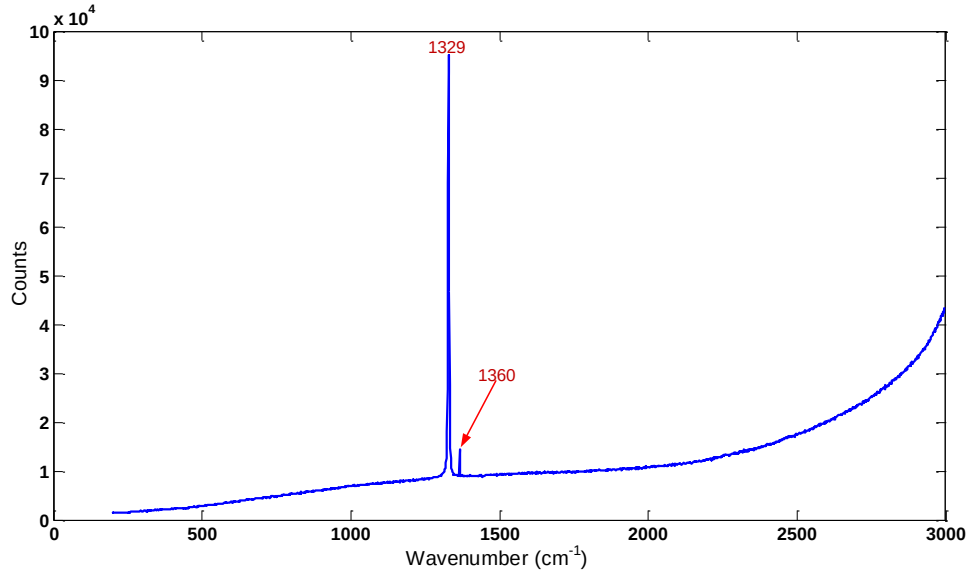

Figure 4.10: A typical Raman spectrum for diamond particles in the third group

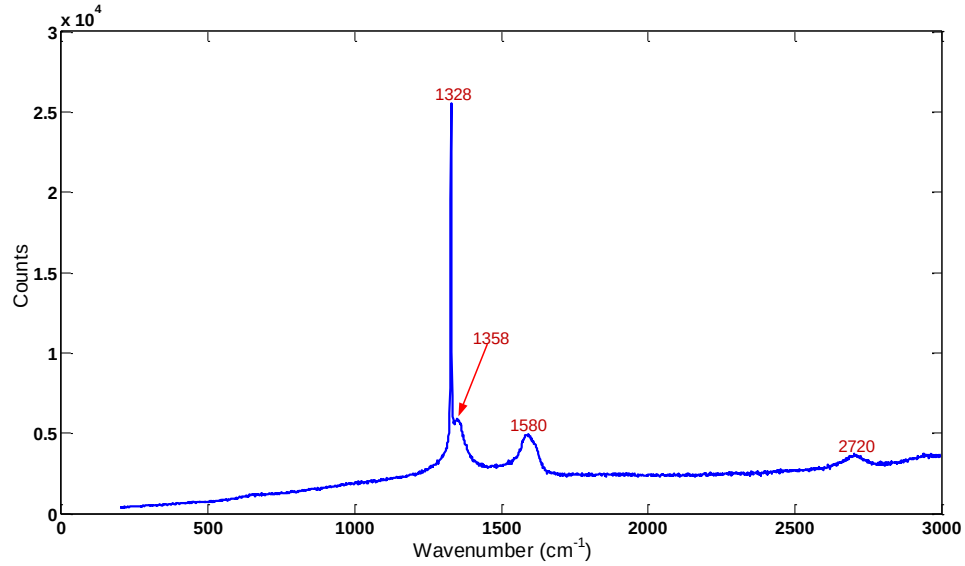

Figure 4.11: A typical Raman spectrum for diamond particles in the forth group

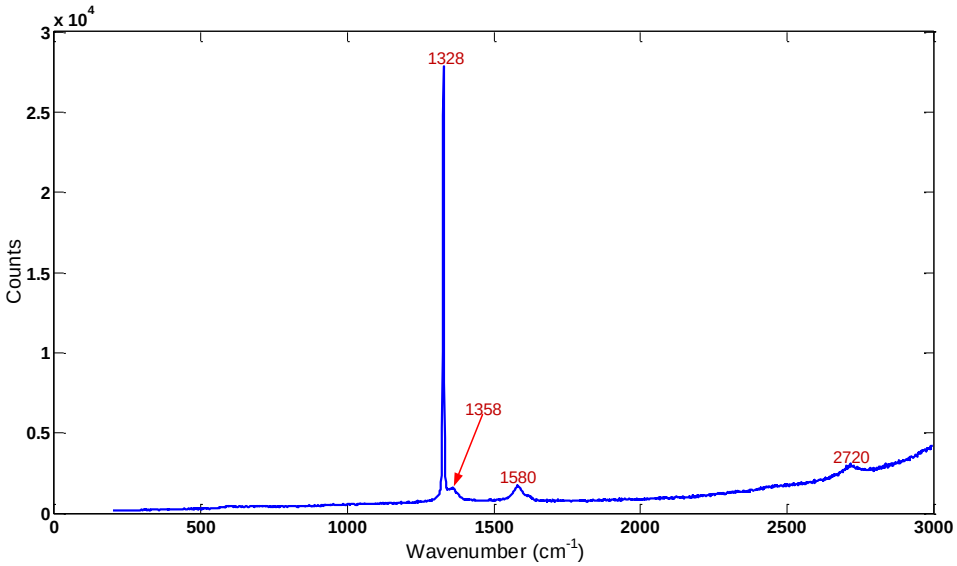

Figure 4.12: A typical Raman spectrum for diamond particles in the forth group

is the only group that does not show 1330 cm^{-1} band which is the signature of diamond. Presence of 2936 cm^{-1} peak along with D, G, and G′ bands match these spectra with the those of noncrystalline graphitic carbons (for the definition of noncrystalline graphitic carbons, one can see [43]) and specifically the glassy carbons.

Among these five groups, group one is an indication of no graphitization, group five shows an extreme level of graphitization. Groups two and three have generally less graphitization compared to group four. In the groups two to four, the level of graphitization can be estimated by the aforementioned relative intensity in each group.

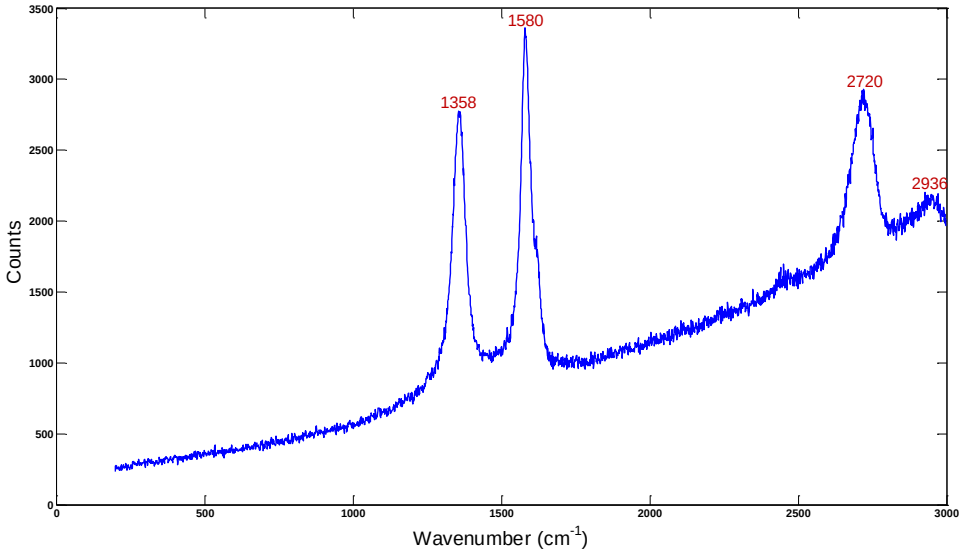

Figure 4.13: A typical Raman spectrum for diamond particles in the fifth group

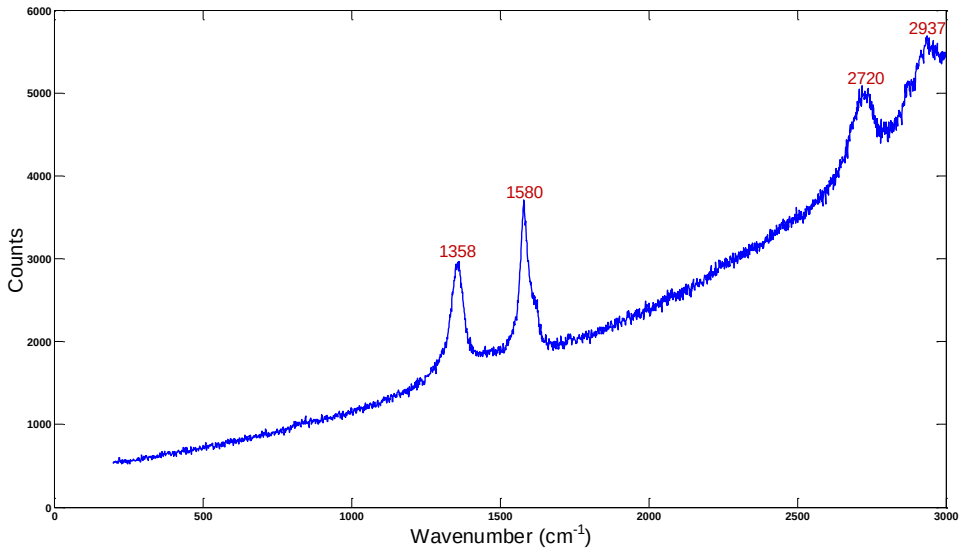

Figure 4.14: A typical Raman spectrum for diamond particles in the fifth group

4.5 Results and Analysis of Pre-placed Deposition

4.5.1 Clad-Substrate Bonding and Matrix Structure

The clad-substrate bonding was categorized in Table 4.2 and 4.3 to "no bonding", "weak bonding", and "good bonding" by examination of microstructure of the polished cross section and longitudinal section cuts of the deposited samples by SEM; where "no bonding" refers to the cases that the clad was detached from the substrate either after deposition, or during cutting the samples, "weak bonding" refers to samples that the SEM image of the clad-substrate interface does not show a uniform and metallurgical bonding or shows presence of porosities, and "good bonding" refers to the samples that the SEM image of the clad-substrate interface shows a solid and metallurgical bonding without presence of any porosity.

As it was predicted, with constant power, excessive increase in scanning speed led to the deterioration of clad-substrate bonding and eventually resulted in no bonding due to the lack of enough energy to melt the substrate. When the velocity exceeds a specific value, the clad itself loses its uniformity and turns into a non cohesive structure as it is shown in Figure 4.15. Figure 4.15 shows a cross section of the deposited clad with the CW laser with the power of 280 W and the scanning speed of 17 mm/s. There is no bonding between the clad and the substrate except at few isolated points, therefore the clad was easily separated from the substrate.

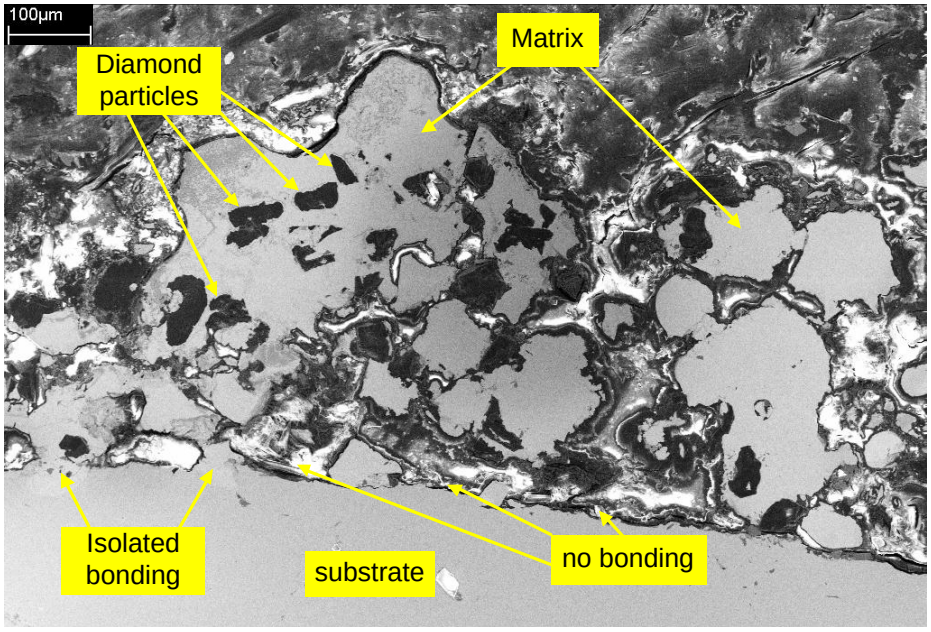

Figure 4.15: A SEM image of a cross section of a deposited clad with little bonding to the substrate and non unified structure

Figure 4.16 depicts a part of longitudinal section of one deposited clad with a good bonding to the substrate. As it can be seen from the figure, the matrix is uniform with no porosity or micro cracks. There is a good bonding between the clad and the substrate, although, there is one micro crack in it. On the other hand, there is a good bonding between diamond particles and the matrix without the presence of any porosity.

Almost all of the samples with good bonding in both tables had the same structure, therefore, regarding the clad-substrate bonding, uniformity of matrix, and porosity and micro-cracks, continuous and pulsed lasers resulted in almost the same clad properties as long as the process parameters were inside the process window. Similarly, no recognizable difference on the above-mentioned characteristics was observed for different powers and speeds presented in the tables.

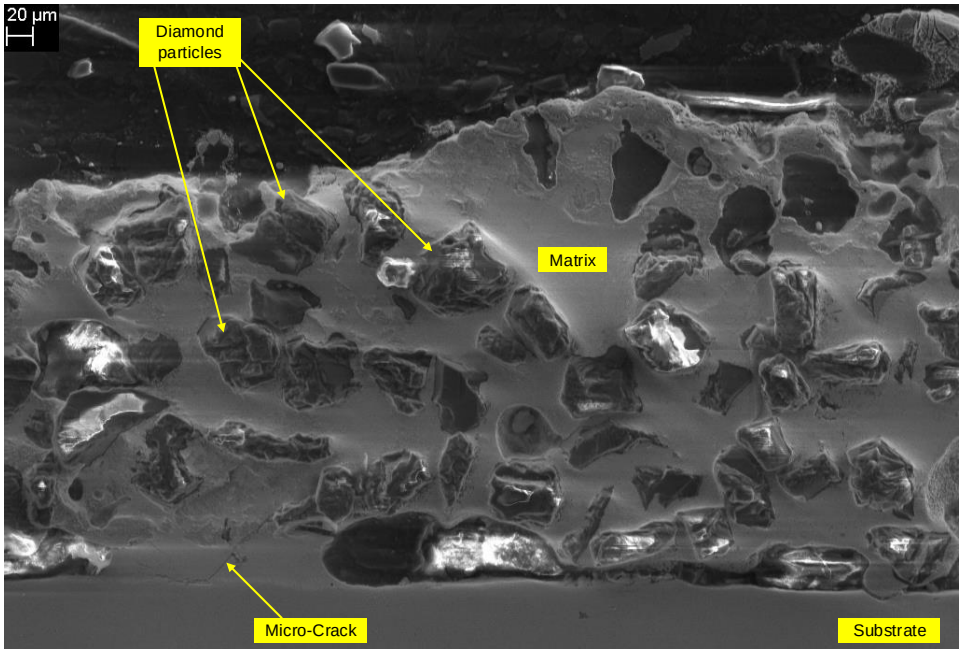

Figure 4.16: A SEM micrograph of a part of a longitudinal section of a deposited clad with a good bonding to the substrate

4.5.2 Diamond Graphitization

Diamond decomposition was measured by the method described in Section 4.4.2. It was found out that increasing the speed while maintaining power constant for the experiments with CW laser resulted in less graphitization. In fact, the clads with no boding have the lowest degrees of graphitization. This trend was similar for three different powers of 280 W, 200 W, and 120 W; however, the result for the deposited clads with higher power along with higher velocity was better than that of the deposited clads with lower power in conjunction with lower speed. As it can be seen in Table 4.2 the maximum scanning speed for making a clad with good bonding was 9 mm/s, 4 mm/s, and 2 mm/s for powers of 280 W, 200 W, and 120 W, respectively. The amount of graphitization for the deposited clad

with a power of 280 W and a speed of 9 mm/s was less than that of the deposited clad with a power of 200 W and a speed of 4 mm/s. Likewise, the degree of graphitization for the case of 200 W and 4 mm/s was less than that of the case of 120 W and 2 mm/s.

Considering that the interaction time for CW laser can be calculated as

$$\tau = \frac{d}{v} \tag{4.7}$$

where, τ is interaction time [s], d is laser beam diameter [mm], and v is scanning speed [mm/s], a higher scanning speed results in a lower interaction time. Therefore, one can assume that among different process parameters which supply relatively equal amount of energy to the process zone, the one with the lowest interaction time would result in the lowest diamond graphitization.

Furthermore, the modeling results showed that the melt pool temperature is highly influenced by power change, whereas, cooling rate is highly influenced by velocity change. Therefore, the case with power of 280 W and velocity of 9 mm/s must have had higher cooling rate as opposed to the case with 120 W power and 2 mm/s speed. At the beginning of the deposited clad where this comparison was conducted, the melt pool temperature of both clad must have been higher than 1530°C which is the melting point of the substrate since both had good clad-substrate bondings. Modeling showed that the case with 280 W power and 9 mm/s must have had a higher melt pool temperature at the beginning of the clad as opposed to the case with 120 W and 2 mm/s. Therefore, it can be concluded that the cooling rate is of primary importance for diamond graphitization. Hence, it is predicted a combination of power and scanning speed in which the scanning speed is as high as possible while the power is high enough to provide the melt pool temperature of

1600°C should develop the best results.

The same trend was observed for the experiments with the pulsed laser. Comparing the results of the pulsed laser to that of the CW laser with the same laser power and scanning speed, diamond particles inside the deposits by the pulsed laser had a slightly lower degree of graphitization than those in the deposits by the CW laser. For instance, the deposited clad with the power of 280 W and the scanning speed of 4mm/s using the pulsed laser had slightly lower graphitization than the clad deposited with the power of 280 W and the scanning speed of 9 mm/s using CW laser.

The reason behind that could lies in the fact that pulsed laser has a lower interaction time compared to CW laser. A lower interaction time in case of a deposition by the pulsed laser is the outcome of the fact that in the pulsed laser the power of the laser within each pulse is significantly higher than the average power of the pulsed laser. In fact the deposit is exposed to a high power within each pulse and then there is the time interval between two pulses which makes the interaction time for the pulsed laser only a fraction of that for the CW laser.

4.5.3 Chemical Bonding of Diamond Particles

The mechanism of diamond retention by the matrix can be mechanical or mechanical in conjunction with chemical [8, 55]. It was reported when the retention mechanism is only mechanical, the most important factor is the yield strength of the matrix; since, in order to pull out the diamond particles from the matrix, the pulling force should be higher than the yield strength of the matrix [8, 55]. The pulling force is associated with the elastic deformation around the diamond particle and the diamond shape. Diamond shape can highly affect stress concentration. As a result, ductility and notch sensitivity of the matrix

are of great importance [8, 56, 57].

In case of mechanical retention, when diamond particles are exposed to the external load, diamond particles slip along their interface with matrix, due to matrix deformation. The static coefficient of friction between diamond and metals is around 0.1 to 0.15 [58]. This low coefficient of friction produces a low friction force which makes the retention capacity low. However, when the chemical retention is added to the case, the slip does not happen at the interface; instead it happens in the matrix just below the interface. As a result, the friction force and in turn retention capacity drastically increases [59, 60, 8].

The presence of carbide former metals in the matrix can wet diamond particles and form carbide on the diamond surface which adds chemical bonding to matrix-diamond interaction [29]. Carbide nucleation can develop on the surface of diamond and form an interfacial layer which supplements mechanical retention. However, it should be noted that if the interfacial layer grows excessively to become too thick, it would deteriorate the matrix by formation of porosity and decreasing the ductility of the matrix. In addition, it can lead to the surface degradation of diamond particles [8].

In addition, the stress between two different crystals is mainly developed as a result of lattice mismatch and the difference between coefficient of thermal expansion [31]. Therefore, growth of an intermediate layer between the diamond particle and the bonding matrix can significantly relieve the interfacial stress and in turn enhance the retention capacity [31]. As a result, existence of the interfacial layer between the diamond and the matrix is critical for enhancing the diamond retention capacity of the matrix, however the thickness of this layer should be less than 1 micron [8].

When titanium and graphite, both in solid form, are in contact in an inert environment the following exothermic reaction can initiate above 950°C and proceeds with increasing

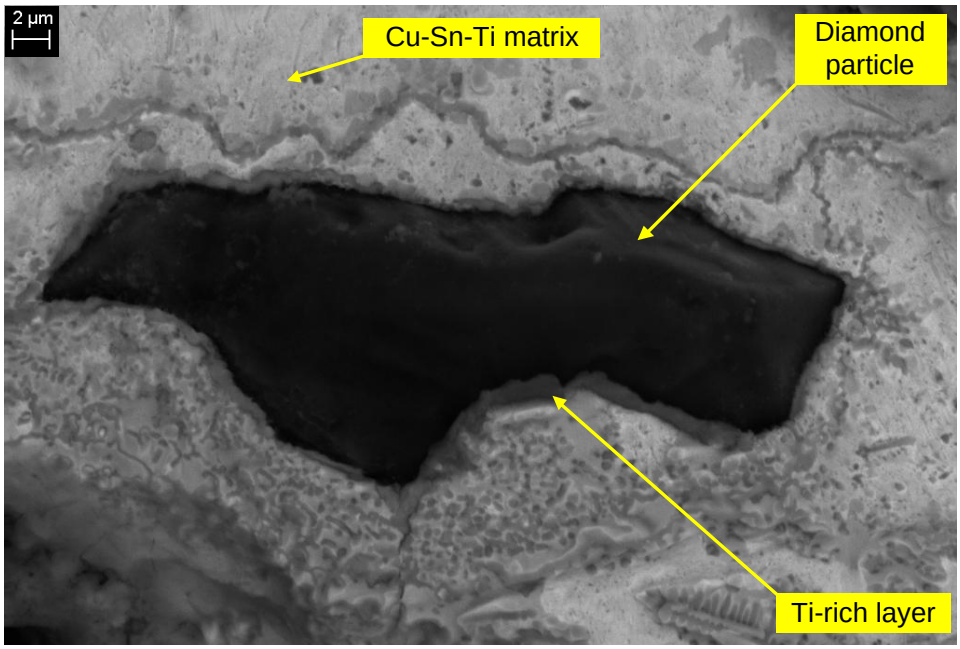

Figure 4.17: A backscattered electron image of a diamond particle which shows that the diamond particle is surrounded by a titanium rich layer

temperature [61]

$$Ti_{(s)}+C_{(s)}=TiC_{(s)}\ , \triangle H_{298}=\text{-}184\ \text{kJ/mole} \tag{4.8}$$

Below the melting point of titanium, the reaction takes place with solid state diffusion of titanium into carbon or TiC interface [61]. The exothermic feature of this reaction can lead to initiation of a self sustained reaction if the heat release by the reaction (184 kJ/mole) is higher than the heat loss to the surrounding. This is the case in combustion synthesis of TiC where the reaction initiates by preheating and proceeds as a self sustained reaction [61].

The case for titanium-diamond reaction is different. Growth of a layer of TiC with a thickness of 500 to 600 nm on a diamond surface was observed when diamond and Cu-10Sn-15Ti alloy powder were kept at 925°C in a vacuum environment for 5 minutes [31]. Study of the interfacial layer using ATEM and HRTEM showed that the TiC layer grows heteroepitaxially on diamond plane with the same crystallographic orientation [31]. It was also reported that the concentration of carbon along the thickness of the layer decreases by moving toward the matrix.

Examination of deposited diamond particles by backscattered electron image of the SEM revealed that they are surrounded by a thin titanium rich layer. Figure 4.17 depicts a backscattered electron image of a deposited diamond particle enclosed by a layer which is darker than the body of the matrix. Since the darker regions in backscattered mode of SEM correspond to lighter materials, this dark layer can be titanium-rich. The thickness of this layer is in the range of 400 nm to 1.25 micron, although the thickness of the layer in most parts is between 600 nm to 800 nm. This diamond particle belongs to a deposited clad by the pulsed laser with the power of 280 W and the scanning speed of 4 mm/s.

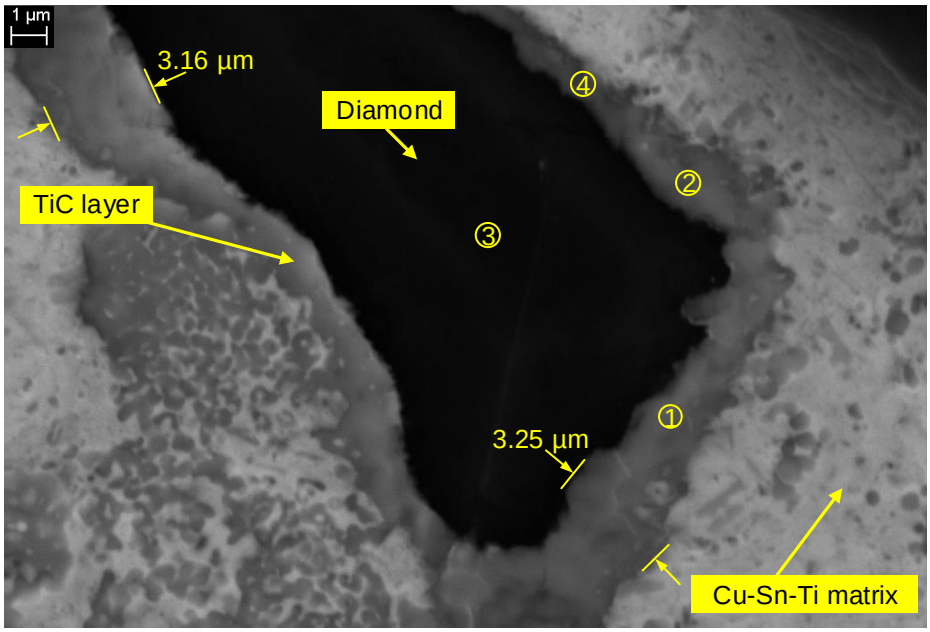

Figure 4.18: A backscattered electron image of a deposited diamond particle enclosed by a TiC layer

Table 4.4: EDS analysis for four points shown in Figure 4.18

Element	C	Ti	Cu	Sn	Fe	Total
Spectrum 1 (At%)	78.52	21.73	1.94	0.24	0.27	100.00
Spectrum 2 (At%)	68.61	28.31	3.29	0.46	0.32	100.00
Spectrum 3 (At%)	100	0	0	0	0	100.00
Spectrum 4 (At%)	57.37	41.34	0.95	0.16	0.18	100.00

Figure 4.18 shows a backscattered electron image with a higher magnification of a different diamond particle from the same clad that the diamond particle in Figure 4.17 belongs to. This diamond particle is also surrounded by a dark layer. As it can be seen in the figure, the thickness of the layer reaches to 3.25 micron at one point. Table 4.4 shows EDS analysis of a few points shown in the Figure 4.18. One can see that the dark layer is composed of titanium and carbon with a small percentage of copper as well as insignificant amounts of iron and tin.

Titanium-carbon phase diagram (See Figure 4.19) shows that maximum atomic percentage of carbon in TiC phase is around 50 percent, however EDS analysis presented in Table 4.4 shows that atomic percentage of carbon at points 1 and 2 is much higher than 50 percent. It can be seen in Figure 4.18 that at points 1 and 2 the thickness of the Ti-rich layer is much thicker than the thickness of Ti-rich layer at point 4 where the atomic percentage of carbon is considerably lower than points 1 and 2. As a result, one can conclude that when the Ti-rich layer is thinner, this layer is mainly composed of TiC phase, however as the layer grows the graphite phase is added to the TiC phase (TiC+C) which reduces the strength of interfacial bonding. On the other hand, EDS line scan on the TiC rich layer indicates that there is a concentration gradient of carbon in the layer as the concetration of carbon decreases along the interfacial layer moving from diamond-intefacial layer to inefacial layer-matrix.

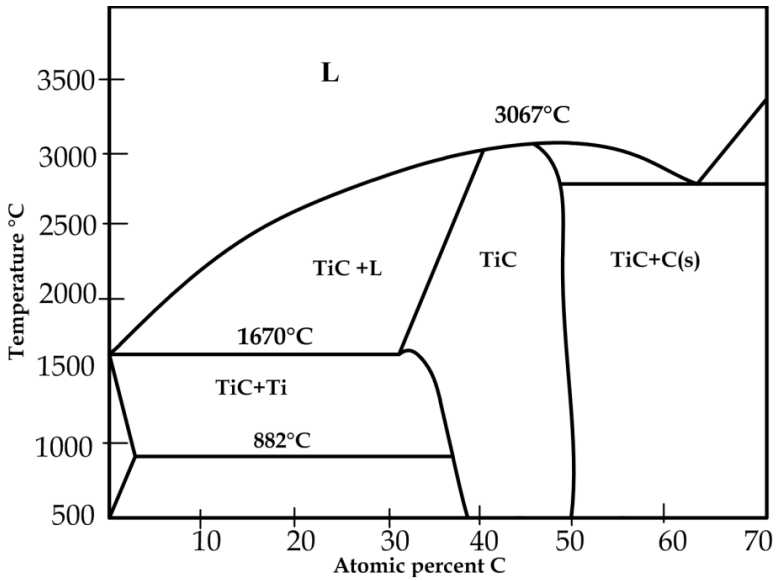

Figure 4.19: Titanium-Carbon phase diagram [9]

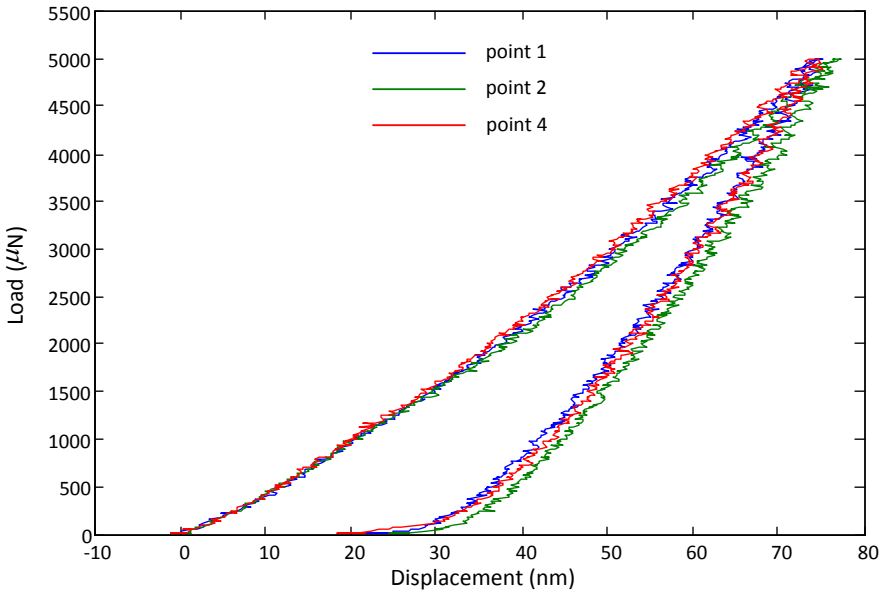

Figure 4.20: Load-displacement diagram acquired by nano-indentation for points 1, 2, and 4 in Figure 4.18

Table 4.5: Calculated hardness and Young's modulus by nano-indentation test for three points shown in Figure 4.18

	Hardness (HV)	Young's modulus (GPa)
Point 1	3088	427.323
Point 2	2894	430.414
Point 4	3043	435.584

Performing nano-indention test on this layer provided mixed results, at some points the result matches the propeties of TiC while at some points does not match. Figure 4.20 depicts load-displacement diagram acquired by the nano-indentation test for 3 points in the 1, 2, and 4 areas shown in Figure 4.18. The calculated hardness and Young's modulus by this test for these three points are shown in Table 4.5 . The calculated results are in match with 2850-3390 HV, 439.43 GPa, the values reported in the literature for Vickers hardness and Young's modulus of titanium carbide, respectively [62]. However, the results of nano-indentation test on different points in the 1 and 2 area of Figure 4.18 does not match with the properties of TiC. Considering the EDS analysis and the results of nano-indentation test, one can conclude that the titanium rich layer around the diamond particles is TiC when the layer is thin and as the layer grows the composition of the layer becomes TiC+C. This results indicates that in order to obtain a strong interfacial bonding between diamond particles and the matrix, the interfacial layer should not become thick.

Comparing the deposited clads by the CW laser with those by the pulsed laser revealed that with the same power and scanning speed, pulsed laser had slightly thinner Ti-rich layer. The thickness of the Ti-rich layer was increased with an increase in laser power or a decrease in scanning speed. Therefore, lower interaction time, higher cooling rate, and lower melt pool temperature are of great importance in growing a TiC layer with the desired thickness. This is in agreement with the conclusion in the study of diamond

graphitization in the deposits. Therefore, having a lower interaction time, a higher cooling rate, and a lower melt pool temperature not only decreases the diamond graphitization, but also it is very important in preventing the TiC layer from growing thick.

4.5.4 Effect of Dilution

Iron attacks diamond at high temperatures and accelerates diamond graphitization. It was mentioned in Chapter 2 that graphitization of diamond in the presence of iron starts at 1000°C [6]. This is partly because of relatively high solubility of carbon in austenite [6]. It can be seen in iron-carbon phase diagram as shown in Figure 4.22 that solution of carbon in iron decreases the melting point of the compound. The melting temperature decreases from 1538°C for pure iron to 1154°C for solution of around 4.3 percent carbon in iron. Therefore, the compound solidifies at a lower temperature, and as a result, diamond particle is exposed to liquid interface for a longer time which intensifies transfer of carbon atoms from diamond into iron which in turn reduces the melting point of the compound further. Indeed, this becomes a loop which results in increasing carbon removal rate from diamond particles. On the other hand, further solution of carbon in austenite results in formation of Fe_3C, cementite, which is a brittle phase and degrade the mechanical properties of the matrix near the diamond particles.

Figure 4.21 depicts a back-scattered electron image of a part of longitudinal-section of the deposited clad by the pulsed laser with the power of 280 W and the scanning speed of 4 mm/s. Table 4.6 presents the EDS analysis of the highlighted regions in the Figure 4.21. The clad-substrate interface shows that only a thin layer of substrate was melted which indicates that the amount of dilution should be acceptable. Although, the amount of dilution is limited, however EDS analysis and the backscattered image shows

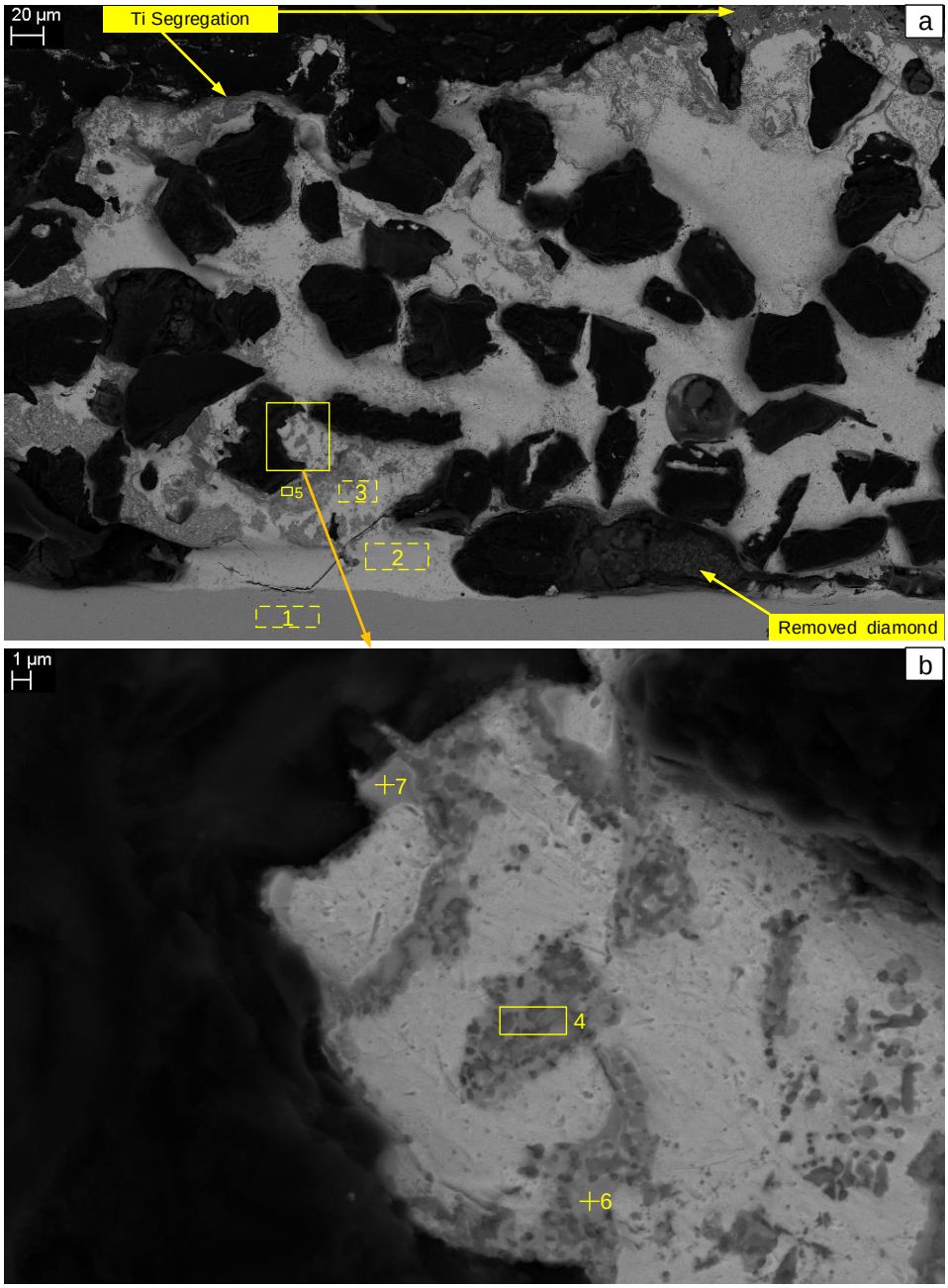

Figure 4.21: a) A backscattered image of a part of a longitudinal section of a deposited clad. b) A backscattered image with a higher magnification of the area shown in part a

Table 4.6: EDS analysis of the highlighted regions in Figure 4.21

Element	C	Fe	Ti	Cu	Sn
Region 1 (At%)	16.66	82.69	0.22	0.28	0.15
Region 2 (At%)	17.47	4.92	0.25	67.61	9.75
Region 3 (At%)	46.87	8.26	5.54	33.40	5.93
Region 4 (At%)	59.21	14.76	19.05	5.94	1.02
Region 5 (At%)	27.29	31.67	32.89	7.27	0.88
Region 6 (At%)	31.86	61.13	2.84	3.84	0.33
Region 7 (At%)	51.70	44.30	1.58	2.13	0.29

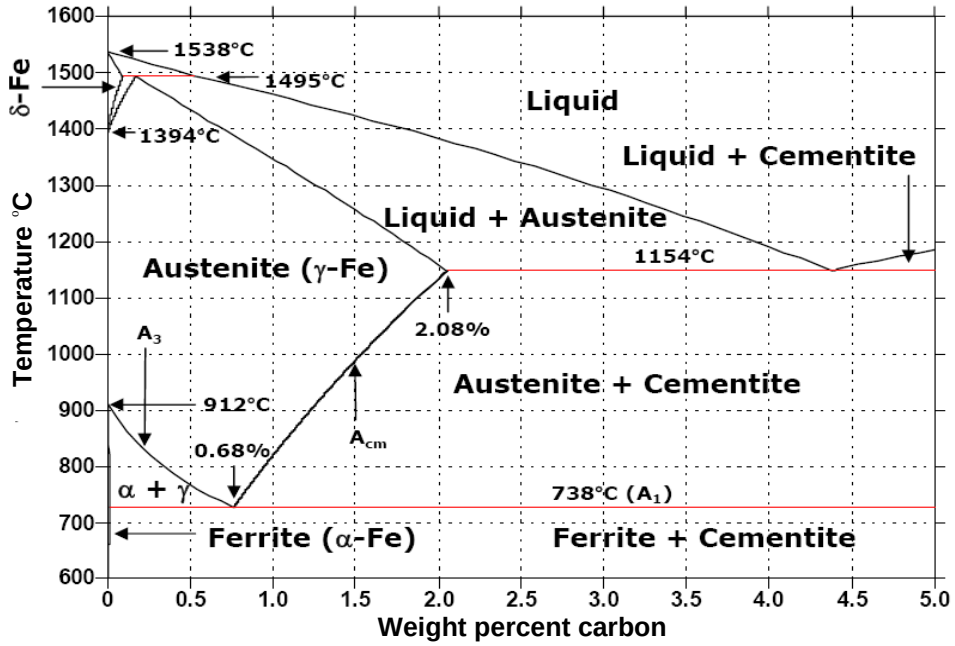

Figure 4.22: Iron carbon phase diagram [10]

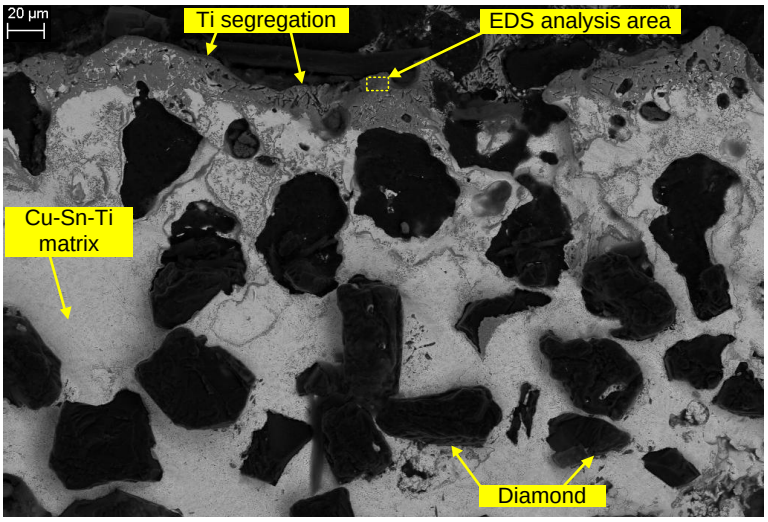

Figure 4.23: A backscattered electron image of a part of a longitudinal section of a deposited clad. Uniform distribution of diamond particles can be observed. Titanium segregation at the surface of the clad is seen.

high concentration of iron at the vicinity of diamond particles. For instance, at point 7 in the Figure 4.21 which is located at interfacial layer between a diamond particle and the matrix, the concentration of iron is 44.30 atomic percent which is extremely high and resulted in formation of an iron-based interfacial layer instead of a titanium-based one. This drastically reduces the strength diamond-matrix bonding. One can also see that a particle near the substrate was removed during the polishing process which is another indication of weak bonding between diamond particles and the deposit. Due to significance of this phenomenon, it will be investigated in greater detail in the following chapters.

4.5.5 Diamond Distribution

Uniform distribution of diamond particles inside the deposited clad is of primary importance, since non-uniform distribution of diamond particles deteriorates wear and abrasive

properties of deposited clad [8]. It can be seen in Figure 4.21a and Figure 4.23 that diamond distribution inside the matrix is almost uniform, although it seems that smaller diamonds are mostly located at lower parts of the clad and larger diamonds are mainly placed at upper parts of the clad. However, this is not the case for all the deposited clads since many of them had non-uniform distribution of diamond particles in cross-section and longitudinal-section specially those deposited with higher laser powers. It seemed that increasing the scanning speed or decreasing the power resulted in a more uniform distribution of diamond particles. Diamond distribution will be studied in more detail in Chapter 6.

Segregation of titanium at the surface of the clads was also observed in many deposited clads. Figure 4.21a and Figure 4.23 show segregation of titanium at the surface of the deposited clads. EDS analysis of the highlighted region in Figure 4.23 revealed the existence of C, Ti, Cu, Sn, and Fe with atomic percentage of 64.66, 33.85, 1.05, 0.24, and 0.19, respectively, which shows this area is mainly composed of titanium and carbon. The segregation of titanium was decreased with increasing the scanning speed or decreasing the power.

4.6 The Experiments: Blown Powder Laser Cladding

By insight acquired from the developed model and by the results of pre-placed deposition demonstrated in previous sections, process window for the deposition by dynamic blown powder was narrowed. However, still many tests were required in order to study the feasibility of conducting an acceptable deposit that has advantages over current conventional methods of depositing metal matrix diamond composite. The experiments were conducted using the same facility used for the pre-placed experiments. The CW laser was

used for the blown powder depositions. The substrate was chosen as AISI 1030 mild steel ($0.25 - 0.28$ wt% carbon) with the dimensions of 100 mm $\times$ 25 mm $\times$ 3.5 mm (length $\times$ width $\times$ thickness). The substrates were sand blasted and then cleaned with acetone.

Table 4.7 presents the process parameters for one set of the conducted experiments. In this set of experiments, laser power and scanning speed were varied whereas powder feed rate, laser beam diameter on the substrate, and carrier gas flow rate were kept constant as 4.9 g/min, 1.5 mm, and 3 dL/min, respectively. Two more sets of experiments are presented in Table A.1. These two sets were conducted with the same combination of laser power and scanning speed of set one, but with different powder feed rates of 2.62 g/min and 7.48 g/min. For these two sets of experiments, laser beam diameter on the substrate, and carrier gas flow rate were kept constant as 1.5 mm, and 3 dL/min, respectively, the same values used in the first set of experiments. The length of all depositions were 20 mm.

Table 4.7: Process parameters for a selected set of blown powder laser cladding experiments

Clad Number	Power (W)	Scan speed (mm/s)	Powder feed rate (g/min)	Beam diameter (mm)	Carrier gas flow rate (dL/min)
1	200	3.33	4.9	1.5	3
2	200	6.66	4.9	1.5	3
3	200	10	4.9	1.5	3
4	200	13.33	4.9	1.5	3
5	200	16.66	4.9	1.5	3
6	200	20	4.9	1.5	3
7	200	23.33	4.9	1.5	3

Table 4.7: Process parameters for a selected set of blown powder laser cladding experiments

Clad Number	Power (W)	Scan speed (mm/s)	Powder feed rate (g/min)	Beam diameter (mm)	Carrier gas flow rate (dL/min)
8	300	3.33	4.9	1.5	3
9	300	6.66	4.9	1.5	3
10	300	10	4.9	1.5	3
11	300	13.33	4.9	1.5	3
12	300	16.66	4.9	1.5	3
13	300	20	4.9	1.5	3
14	300	23.33	4.9	1.5	3
15	400	3.33	4.9	1.5	3
16	400	6.66	4.9	1.5	3
17	400	10	4.9	1.5	3
18	400	13.33	4.9	1.5	3
19	400	16.66	4.9	1.5	3
20	400	20	4.9	1.5	3
21	400	23.33	4.9	1.5	3
22	600	3.33	4.9	1.5	3
23	600	6.66	4.9	1.5	3
24	600	10	4.9	1.5	3
25	600	13.33	4.9	1.5	3
26	600	16.66	4.9	1.5	3

Table 4.7: Process parameters for a selected set of blown powder laser cladding experiments

Clad Number	Power (W)	Scan speed (mm/s)	Powder feed rate (g/min)	Beam diameter (mm)	Carrier gas flow rate (dL/min)
27	600	20	4.9	1.5	3
28	600	23.33	4.9	1.5	3
29	700	3.33	4.9	1.5	3
30	700	6.66	4.9	1.5	3
31	700	10	4.9	1.5	3
32	700	13.33	4.9	1.5	3
33	700	16.66	4.9	1.5	3
34	700	20	4.9	1.5	3
35	700	23.33	4.9	1.5	3
36	800	3.33	4.9	1.5	3
37	800	6.66	4.9	1.5	3
38	800	10	4.9	1.5	3
39	800	13.33	4.9	1.5	3
40	800	16.66	4.9	1.5	3
41	800	20	4.9	1.5	3
42	800	23.33	4.9	1.5	3

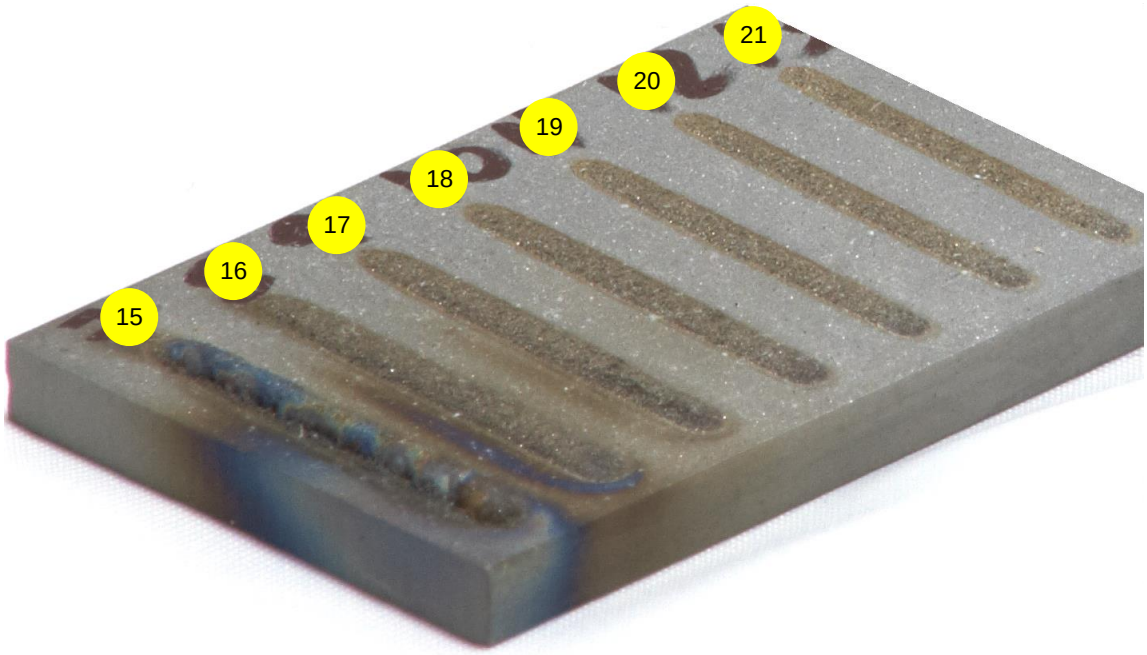

Figure 4.24: A picture of the clad number 15 to 21 of Table 4.7

4.7 Results and Analysis of Blown Powder Deposition

As it was concluded in pre-placed laser cladding in Section 4.3 and the modeling in Chapter 3, the influential conditions for minimizing diamond graphitization and thickness of TiC layer are to keep melt pool temperature and interaction time to a minimum, and to make the cooling rate as high as possible. It was shown that among these defining factors, the latter is more significant. As a result, in the presented sets of experiments, scanning speed started with a relatively high value of 3.33 mm/s (200 mm/min) and went up to 23.33 mm/s (1400 mm/min) by increment of 3.33 mm/s. These scanning speeds were tried for powers of 200, 300, 400, 600, 700, and 800 W.

The deposited clads with the laser power of 200 W (clad number 1 to 7) had low height and width indicating the powder catchment efficiency was very low. The depositions with

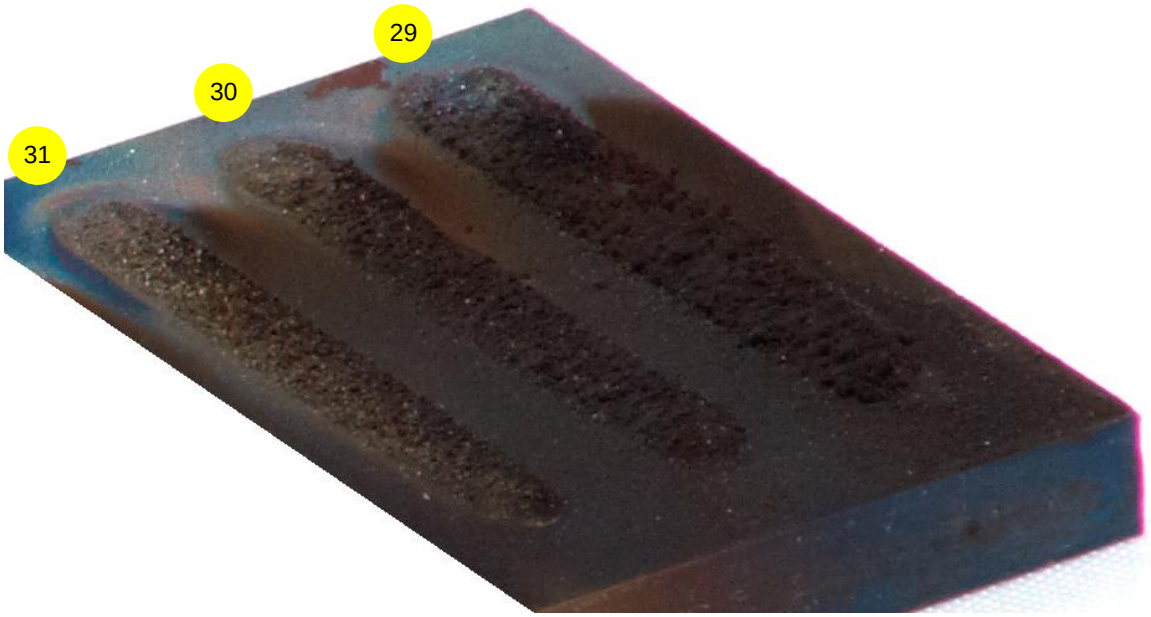

Figure 4.25: A picture of the clad number 29 to 31 of Table 4.7

the laser power of 300 W had higher height and width but they were not in an acceptable range except the one deposited by the scanning speed of 3.33 mm/s (clad number 8) which has much higher height compared to the others in this group, however the clad was not uniform and apparently continuous molten pool was not formed during deposition. Next group of clads were deposited with the power of 400 W. Figure 4.24 shows a picture of these clads. As it can be seen in the figure, these clads have acceptable height and width and have uniform shape. The heat affected zone was very high for the deposit with the scanning speed of 3.33 mm/s but other clads had low HAZ.

The next group of clads in Table 4.7 were deposited with the laser power of 600 W. These clads and the area around them were covered by thin dark film which looked like soot. In addition, the clads looked porous specially those deposited with a lower scanning speed. These features were intensified in the deposited clads with the power of 700 W.

Figure 4.25 shows deposited clads with numbers 29, 30, and 31 in Table 4.7 which were deposited with the power of 700 W and scanning speed of 3.33 mm/s, 6.66 mm/s, and 10 mm/s, respectively. It can be seen in the figure that the clad number 29 is completely covered by soot like film and has a porous structure. Although by increasing scanning speed to 10 mm/s the amount of dark film and porosity of the clad was decreased (see clad number 31 in Figure 4.25), the clad is still covered by a dark film and has a porous structure. The interaction time for deposition of clad number 31 is $\tau = \frac{d}{v} = 150$ ms, which is a low number for laser cladding process [63].

On the other hand, the fact that the area around these clads was covered by a dark film can not be due to a reaction inside the melt pool. Furthermore, burning of diamond particles were even visually clear during the depositions with the laser power of greater than 600 W. Examination by Raman spectroscopy showed that Raman spectrum of this film is similar to Raman spectra of noncrystalline graphitic carbons (see Figures 4.13 and 4.14). Presence of this film can only be the result of burning the diamond particles which indicates exposure of diamond particles to oxygen before reaching the melt pool. This shows that feeding diamond particles with argon does not completely prevent their exposure to oxygen. It was mentioned in Chapter 2 that it was reported that diamond oxidation starts at around 500°C in air [6]. Therefore, the temperature of the diamond particles should have reached 500°C before reaching the melt pool and the diamond particles should have exposed to oxygen before joining the melt pool. This makes laser powder interaction even more important for the case of diamond deposition and as a result the laser powder interaction will be studied in more detail in Chapter 6.

Deposits with the power of 800W produced less dark film on and around the clads. This could be because the dark film (noncrystalline graphitic carbons) is a product of incomplete burning of carbon, therefore having a higher power could have resulted in more

complete burning of carbon according to the reaction

$$\mathrm{C\,(diamond)} + \mathrm{O_2(g)} \longrightarrow \mathrm{CO_2(g)}$$

where the product of the reaction is in gas state and flows away from process zone.

From the aforementioned observations, one can conclude that the laser power plays a significant role in the degree of diamond decomposition for blown powder laser deposition. The laser powers of 300 W and 400 W resulted in good quality clads although results of the laser power of 400 W were better than those of 300 W. The laser power of 200 did not provide enough input energy for formation of a good clad. The laser power of 600 W and higher resulted in burning diamond particles before reaching the melt pool.

Set two and set three of the experiments (presented in Table A.1) which were deposited with the same parameters of set one except different powder feed rates of 7.48 g/min and 2.62 g/min, respectively, showed the same trend. In set two, more diamond burning was observed for the power of 600 W and higher whereas for the power of less that 300 W the amount of deposition became very low. In set three, less diamond burning was observed for the power of 600 and higher while the amount of deposition for the power of less than 300 W was almost the same as set one.

The clad-substrate bonding of the deposited samples was studied using three point bending test and by examination of microstructure of the polished cross section and longitudinal section cuts of the deposited samples by SEM. Almost all deposited samples showed solid and metallurgical bonding without the presence of any porosity, although a few micro cracks was observed in a few samples. Compared to the results of pre-placed deposition, the quality of clad-substrate bonding was better in the samples by blown powder deposition.

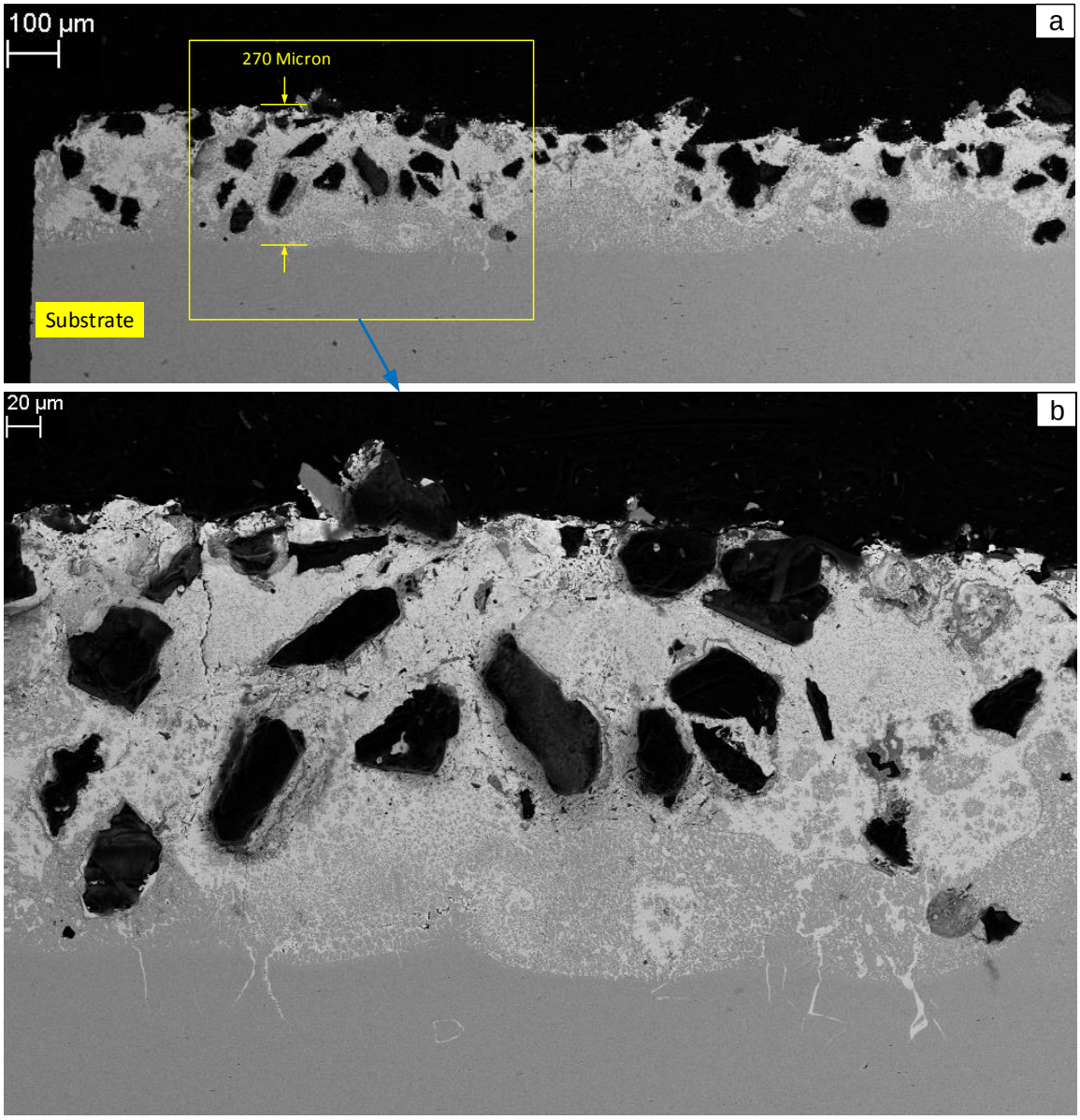

Figure 4.26: a) A back-scattered electron image of a longitudinal section of a part of clad number 17 in Table 4.7. The significant penetration of iron from substrate in the deposit is completely clear in the image. b) a higher magnification of the area shown in part a. It can be observed that iron has even penetrated into the upper parts of the clad.

Figure 4.26a shows a back-scattered electron image of a longitudinal section of a part of clad number 17 in Table 4.7 which has been deposited by the power and the scanning speed of 400 W, and 10 mm/s, respectively. The deposition height is around 0.3 mm. Three points bending shows that the clad-substrate bonding is very strong. Diamond characterization by Raman spectroscopy shows that majority of the diamond particles at upper parts of clad are intact or with a very low degree of graphitization. By moving toward the substrate the level of graphitization increases. As it can be seen in Figure 4.26a and 4.26b the level of dilution is high and high amount of iron penetrated into the deposit. The penetration can be seen even at the upper parts of the deposit although it is much lower than the lower parts of the clad.

Figure 4.27a depicts a back-scattered electron image of an area around a removed diamond particle of the clad number 17 in Table 4.7. One can notice that there are two different layers between the diamond and the matrix, a lighter layer which is in direct contact with the diamond and a darker layer surrounding the lighter layer. The result of EDS line scan of the line shown in Figure 4.27a can be seen in Figure 4.27b. The EDS line scan reveals that the primary layer which is in direct contact with the diamond is iron-rich and the second layer is a titanium-rich layer surrounding the iron-rich layer. This indicates that in presence of iron and titanium, iron has greater affinity to react with diamond, therefore in presence of iron, diamond reacts with iron instead of titanium.

Concentration of carbon in the iron-rich and titanium-rich layers decreases by moving away from the diamond toward the matrix. In addition, the amount of carbon in the iron layer is considerably higher than that of the titanium-rich layer. It was mentioned in Section 4.5.4 that reaction of diamond and iron can result in formation of a brittle phase (Fe_3C) which drastically reduces the strength of diamond-matrix bonding. The diamond particle in the Figure 4.27a was removed during polishing which is an indication of a weak

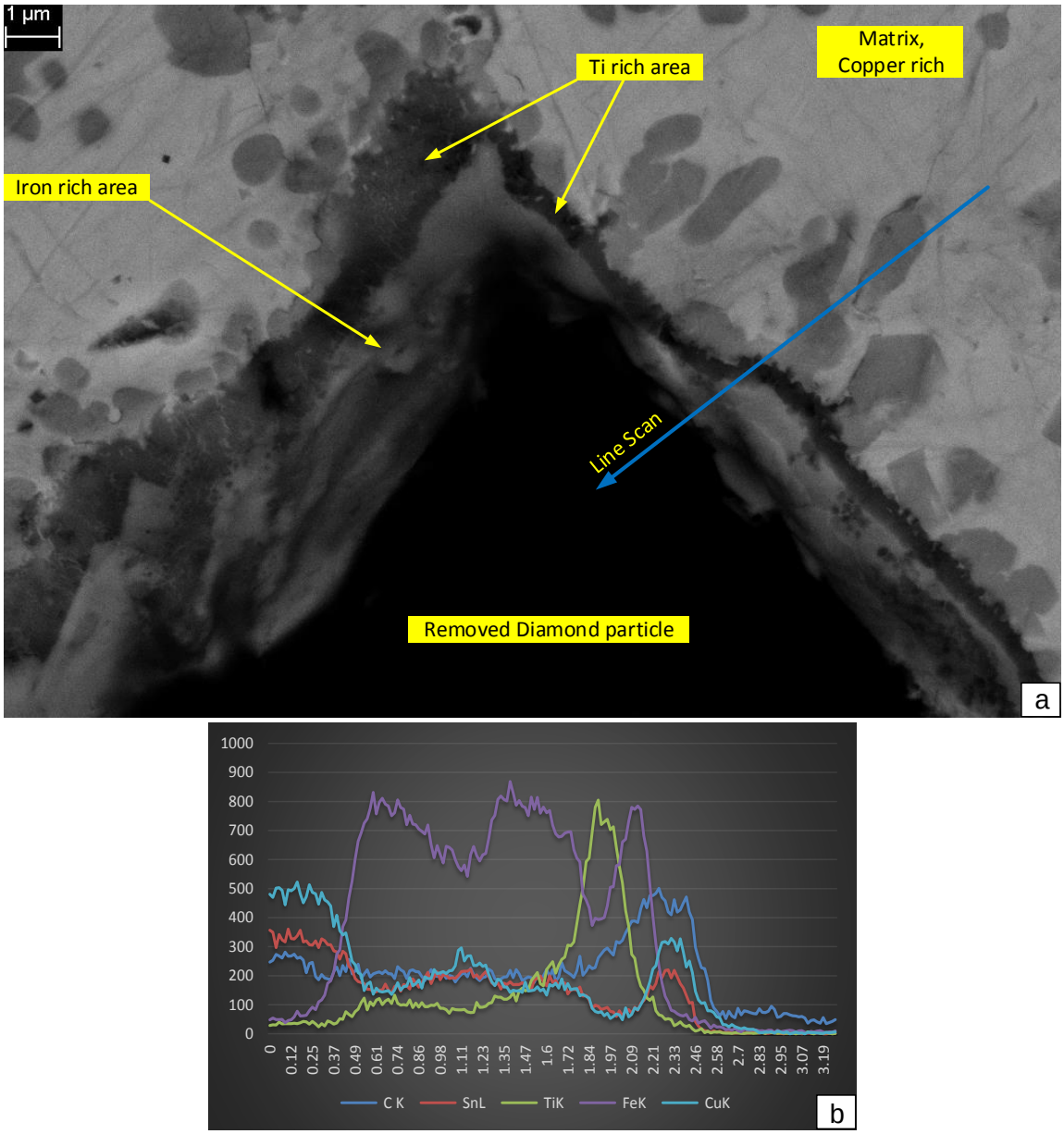

Figure 4.27: a) A back-scattered electron image of an area around a removed diamond particle of the clad number 17 in Table 4.7. An EDS line scan were done on the line shown in the image. b) The result of EDS line scan of the line shown in the part **a** of the figure.

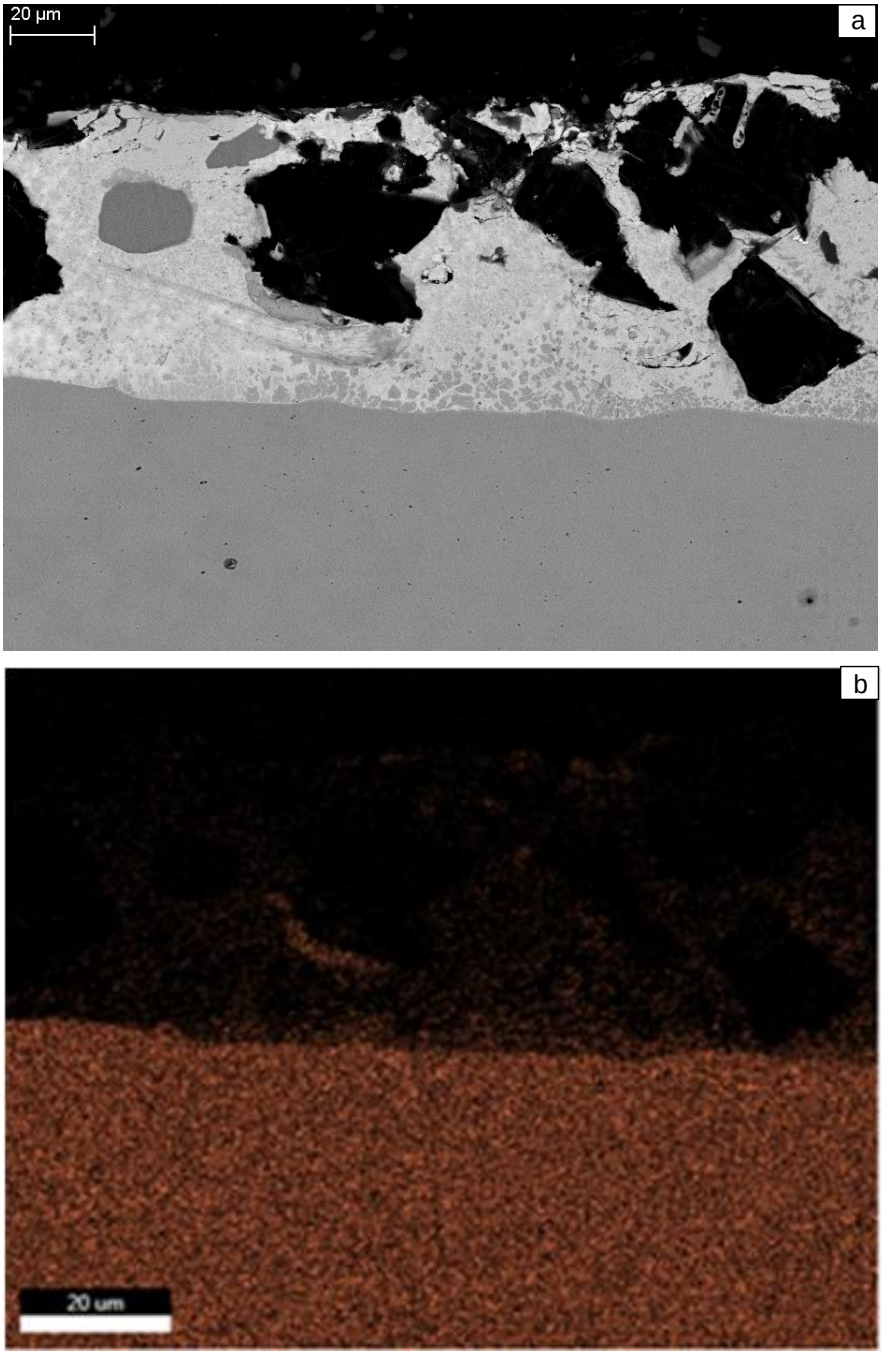

Figure 4.28: a) A back-scattered electron micrograph of a part of a cross section of clad number 17 in Table 4.7 b) EDS elemental mapping of iron of part **a**.

bonding between the diamond and the matrix. In addition, study of diamond particles in the vicinity of iron revealed significantly higher degree of graphitization. Because of the significance of diamond-iron reaction on the quality of the deposit, the mechanism of diamond-reaction will be studied in detail in Chapter 5 by thermal analysis.

Detrimental effects of iron-diamond reaction on the deposit makes the prevention of penetration of iron from substrate into the deposit necessary for a successful deposition. However, even when dilution is limited, iron penetrates into the deposit and disperses in the entire deposit while it mainly concentrates around diamond particles. Figure 4.28a shows a back-scattered electron micrograph of a part of a cross section of clad number 17 in Table 4.7. It can be seen in the figure that the dilution is limited, however EDS elemental mapping of iron presented in part **b** of the figure reveals that iron dispersed in the entire shown area while the concentration is higher around diamond particles although the concentration decreases from bottom to the surface of clad. As a result, the penetration of iron into the deposit is an important issue that should be resolved. This will be discussed in Chapter 6.

Study of the diamond graphitization in the deposited samples showed that the graphitization is higher than the deposited samples by pre-placed laser cladding which is expected due to high level of diamond oxidization before reaching the melt pool. The same trend that was observed in the pre-placed depositions was noticed in the blown powder depositions meaning that a lower interaction time, a higher cooling rate, and a lower melt pool temperature decreased the diamond graphitization. Figure 4.29 shows a back-scattered electron micrograph of a part of a longitudinal section of clad number 29 in Table 4.7. Extreme graphitization can be seen since many diamond particles completely decomposed to graphite and spread in the deposit while it was not dissolved in the matrix. The level of dilution is significant. Graphite inclusions can be seen in the lower parts of deposition

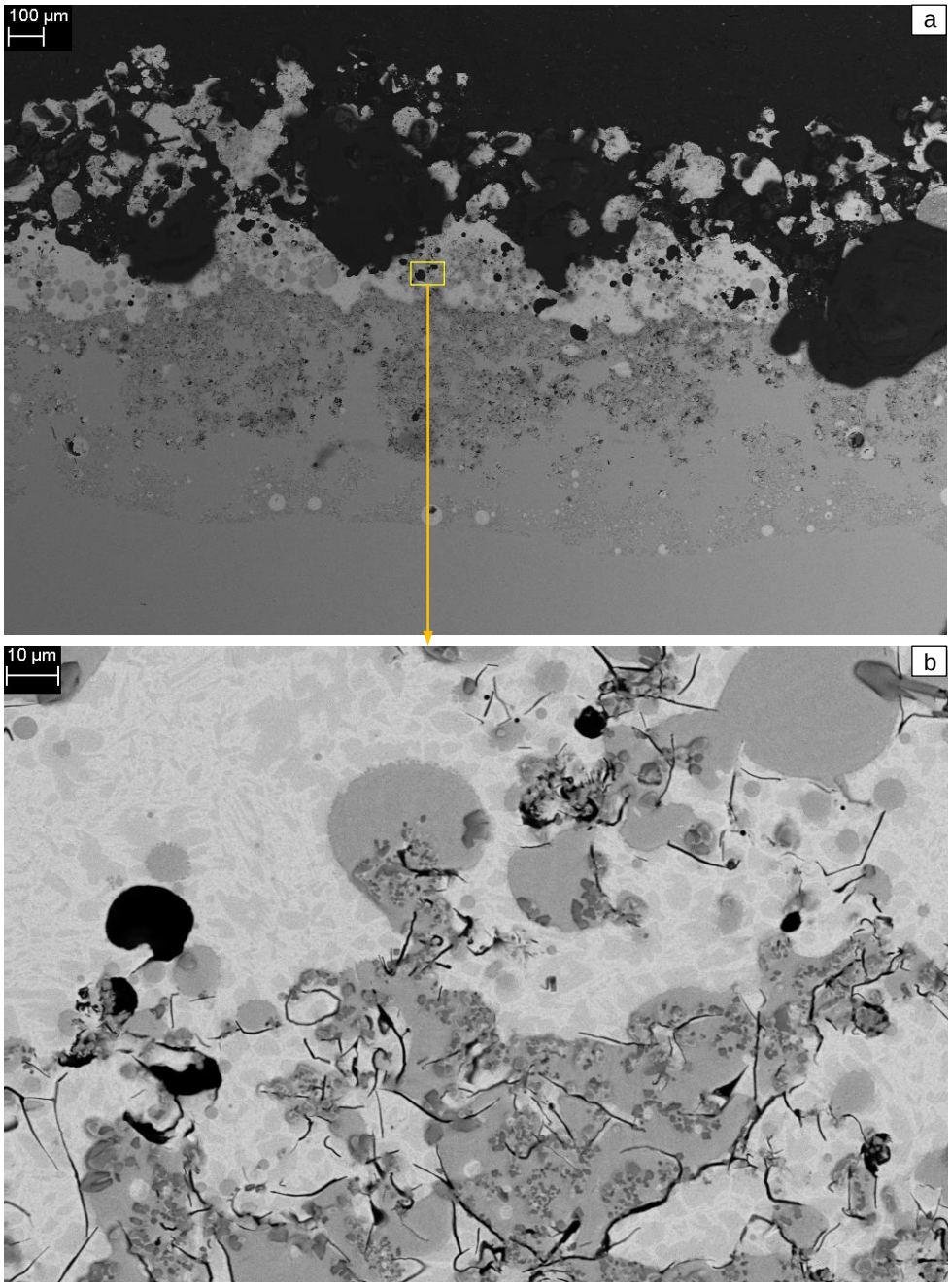

Figure 4.29: a) A back-scattered electron micrograph of a part of a longitudinal section of clad number 29 in Table 4.7. b) Diamond graphitization resulted in existence of carbon inclusions in the matrix.

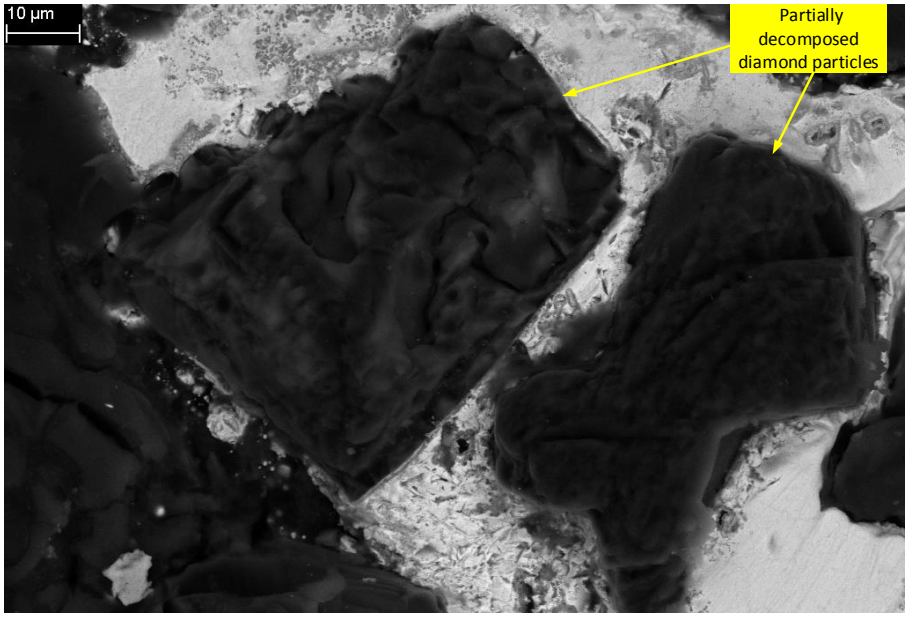

Figure 4.30: A back-scattered electron micrograph of two diamond particles in the clad number 29 in Table 4.7

where no diamond particle is present (see Figure 4.29b). These indicates that considerable amount of carbons detached from diamond particles and solved in the matrix. Figure 4.30 depicts a back-scattered electron micrograph of two diamond particles that experienced partial decomposition . These two diamond particles belong to same sample of Figure 4.29 (clad number 29 in Table 4.7). It can be seen in the figure that a layer of the surface of these two diamonds were decomposed and were nearly detached from the bulk of the diamond particles.

Study of interfacial Ti-rich layer in the deposited sample revealed that in general the deposited samples had a thinner Ti-rich layer as opposed to the deposits by pre-placed laser cladding. The trend was like the trend that was observed in pre-placed deposition meaning that the thickness of the Ti-rich layer was increased with an increase in laser power or a decrease in scanning speed. Therefore, lower interaction time, higher cooling

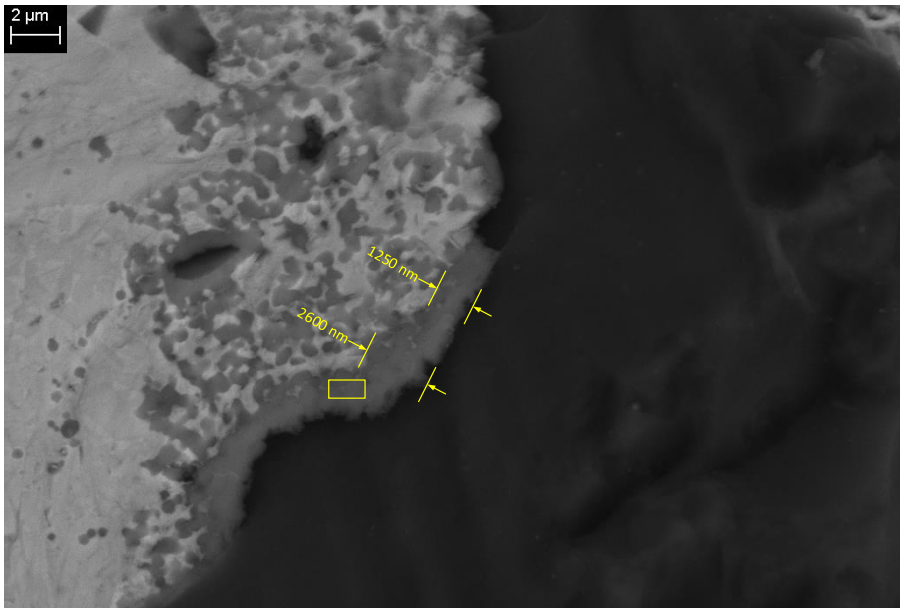

Figure 4.31: A back-scattered electron micrograph of a part of a diamond particle, interfacial layer, and the matrix of the clad number 29 in Table 4.7

rate, and lower melt pool temperature are of great importance in growing a TiC layer with the desired thickness. Figure 4.31 depicts a back-scattered electron micrograph of a part of a diamond particle, interfacial layer, and the matrix of the clad number 15. The Ti-rich layer has a thickness ranging from around 400 nm to 2600 nm. EDS analysis of the area shown by a rectangle in Figure 4.31 shows the existence of C, Ti, O, and Cu atomic percentage of 69.31, 14.32, 14.79, and 1.58, respectively. It is clear that the concentration of carbon is much higher that 50 percent which indicates that the layer is composed of TiC and graphite. Furthermore, the existence of 14.32 percent oxygen indicates the oxidization of the carbide layer which can be the result of diamond oxidization before reaching the melt pool.

In addition, study of interfacial Ti-rich layer in the deposited sample revealed that the growth of Ti-rich layer was limited even in the samples that extreme graphitization

occurred. Figure 4.32 shows a back-scattered electron micrograph of a diamond-matrix interface from the clad number 29 in Table 4.7 which extreme graphitization occurred (see Figures 4.25 and Figure 4.29). It can be seen in part **b** of the figure that the maximum thickness of the interfacial layer is around 1 micron. By examining the diamond-matrix interface in other samples, it was found that the interfacial layer does not become thicker than 3.5 micron.

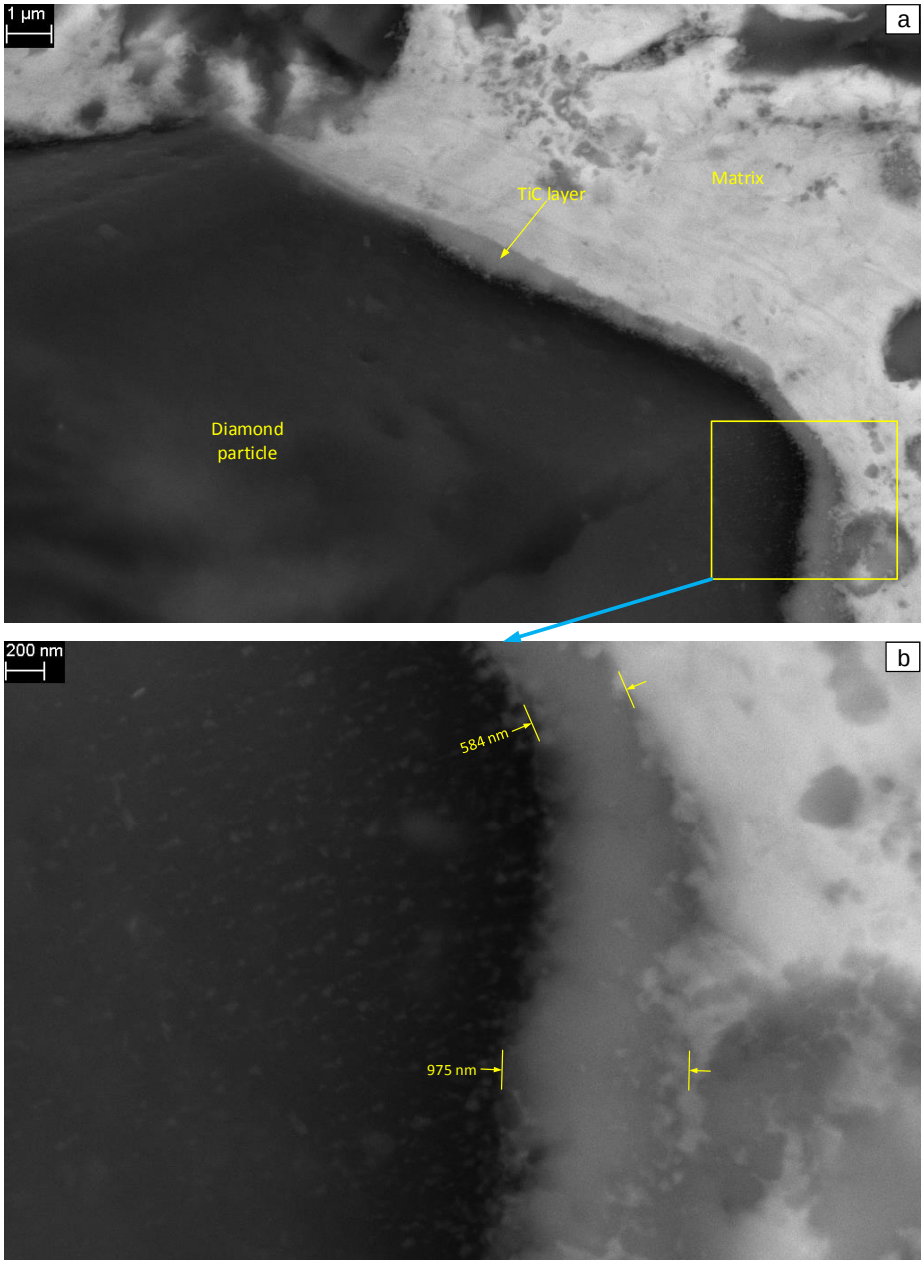

Figure 4.32: a) A back-scattered electron micrograph of a diamond-matrix interface from the clad number 29 in Table 4.7. TiC layer was formed between the diamond particle and the matrix. b) A higher magnification BSE image of the area shown in part **a**. The thickness of the TiC layer does not exceeds 1 micron even when many diamond particles were decomposed in this clad.

Chapter 5

Thermal Analysis of Diamond-Matrix Reactions

As mentioned in Chapter 2, wetting and bonding of diamond by metals play an important role in quality and lifespan of metal bonded diamond tools. In metal bonded diamond tools, diamond particles are embedded in a metal matrix. During operation of diamond tools wetting and bonding of diamond particles to the surrounding matrix determines how well the metal matrix can preserve diamond particles.

In absence of chemical reaction between diamond and metal, only weak Wander Waals forces are present between the two. Therefore the matrix is not capable of holding the diamond particles firmly.

Copper-tin based alloys are extensively used as the metal matrix in diamond tool used in applications where the tool is applied to medium to low abrasive materials. Copper and tin do not wet diamond particles therefore titanium is added to the matrix in order to generate chemical reaction with diamond [8].

However, to the best of author's knowledge, the literature lacks detailed information related to the bonding of diamond and metals. In this chapter thermal analysis of reaction between diamond and Copper, Tin, Titanium, and Iron is presented.

5.1 Differential Scanning Calorimetry

In Differential Scanning Calorimetry (DSC), there are two samples, the sample of interest and the reference sample. The principle of DSC is based upon measuring the alternation of the difference of heat flow rate to the two samples whereas the temperature of the two sample are being controlled [64].

There are two basic kinds of Differential Scanning Calorimetry (DSC), the Power Compensation Differential Scanning Calorimetry (PC-DSC) and the Heat Flux Differential Scanning Calorimetry (HF-DSC). These two are functioning differently however they use the same principle. In both types the measured signal is proportional to the heat flow rate. Temperature difference is measured as a voltage signal. This temperature difference is proportional to the differential heat flow rate [64]. The differential heat flow rate is the measured signal that the DSC instrument provides to the user.

5.2 Materials and Methodology

Powders with the specifications presented in Table 5.1 were prepared. The powders were placed in a furnace and heated at 115°C for 5 hours in order to eliminate any possible moisture.

Mixtures of pure diamond and each one of the pure metal powders were made by placing

Table 5.1: Material powders used in the experiments and their specifications

Material	Particle size (micron)	Specifications
Diamond	50 to 63	Synthetic diamond
Copper	44 to 149	99.9% purity, spherical shape
Tin	less than 149	99.5% purity
Titanium	less than 44	99.5% purity, spherical shape
Iron	less than 44	99.5% purity

diamond powder and each metal powder in equal volume proportion inside glass jars along 1 mm diameter ceramic balls. They were ball milled for 24 hours.

Certain weights of each mixture and pure materials were placed inside alumina crucibles. Heating and cooling cycles were performed by a heat flux Netzsch 404C DSC in inert argon atmosphere. The DSC 404C Pegasus purchased from Netzsch Instruments. This instrument equipped with a high temperature furnace which can operate up to 1500°C. It utilizes a DSC-Cp type measuring head and a type S (Pt10%/Pt-Rh) thermocouple. Netzsch TA software was used for thermal analysis. Material characterization was conducted on heat treated samples by the same instruments described in Chapter 4.

5.3 DSC Experiments

5.3.1 Pure Diamond

Figure 5.1 shows DSC thermal profiles of heating pure diamond powder used in this study up to a peak temperature of 1400°C with heating rate of 40 K/min. The sample was kept at 1400°C for 15 min and then cooled to room temperature with cooling rate of 40 K/min. The purpose of the experiment was to find whether any thermal event occurs during the thermal cycle. As it can be seen in the figure no thermal event occurred during

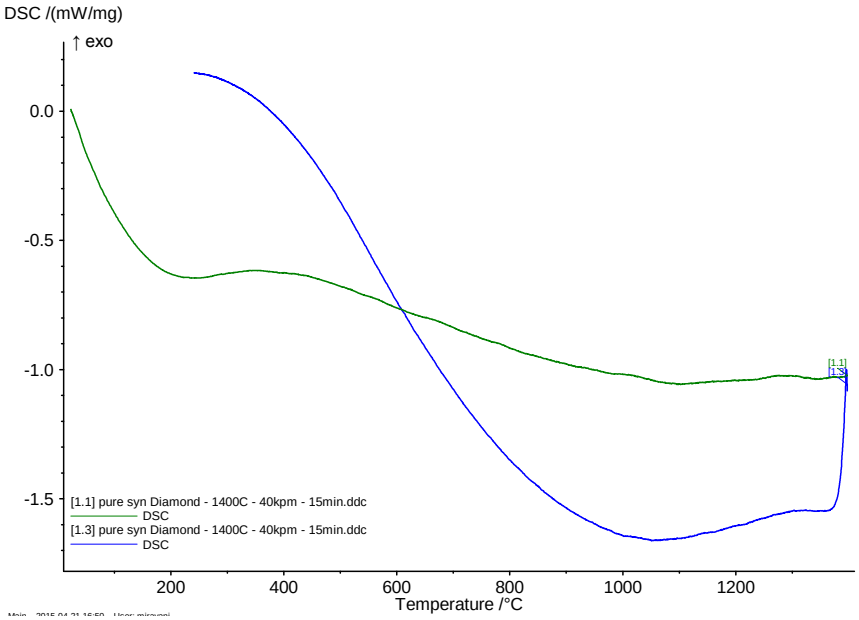

Figure 5.1: DSC heating/cooling curves of the pure diamond powder used in this study.

heating/cooling process which indicates that no thermal transformation occurs in diamond particles up to the temperature of 1400°C in an inert environment. The examination of heat treated diamond particles with Raman spectroscopy showed no trace of graphitization which verifies the DSC result.

5.3.2 Iron-Diamond

Figure 5.2 shows the DSC traces for pure iron. Heating/cooling rate is 20 K/min. The sample was heated to 1300°C, then immediately cooled to room temperature. There is an endothermic peak initiating approximately at 720°C with the peak at 769.4°C and ending at 831°C. This endothermic event corresponds to ferromagnetic transition (Currie temperature) for iron. This is in precise agreement with 770°C reported in the literature [65, 66, 67]. The heat of transformation for this event which can readily be determined by calculating

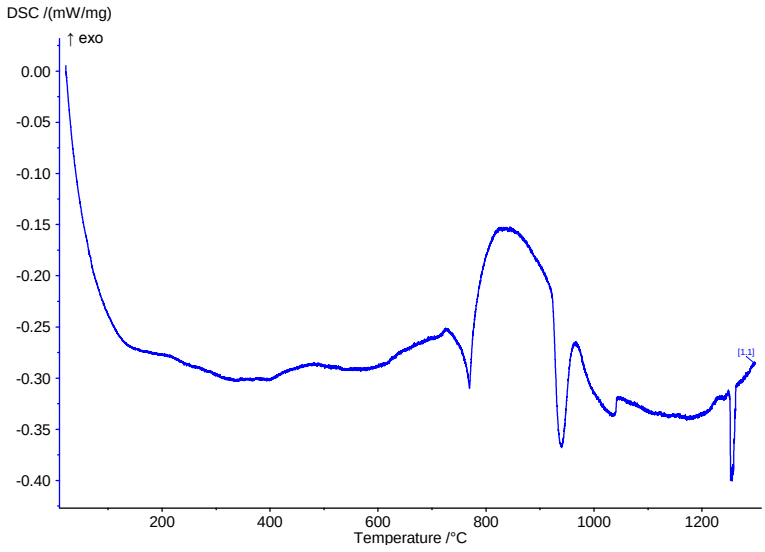

Figure 5.2: DSC heating curve of pure Iron up to the peak temperature of 1300°C

the area under the peak was evaluated as 8.637 J/g. The second and third endothermic are related to ferrite turning to austenite. As it can be seen, the transformation initiates at 923.4°C, however, iron-carbon binary phase diagram (see Figure 4.22) indicates that the transformation should start at 912°C. This shift of temperature is related to heating rate, since phase diagrams corresponds to equilibrium condition where the heating rate is infinitesimal while here is 20 K/min.

Figure 5.3 shows DSC heating curve of iron-diamond mixture. There are two relatively small endothermic peaks with onsets of approximately 740°C and 895°C, respectively. One relatively broad small endothermic peak happens at approximately 1040°C. One large and narrow two staged endothermic peak occurs with onset of approximately 1080°C. Figure 5.4 shows a back scattered electron image of the heat treated mixture. As it can be seen, the heat treated sample composed of two distinctive parts, a part that diamond particles are adhered to each other by solidified iron and a solidified bead. No iron particle has been left and formation of the bead indicates that complete melting occurred during heating.

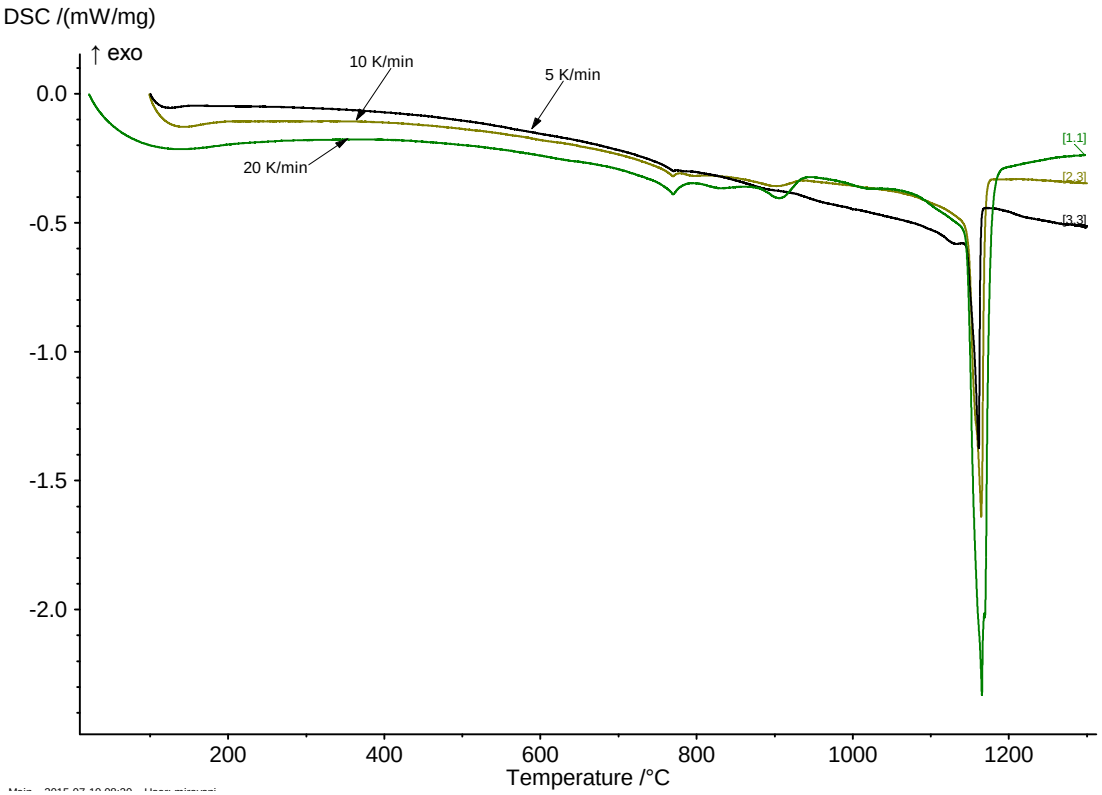

Figure 5.3: DSC heating curves of iron-diamond powder mixture

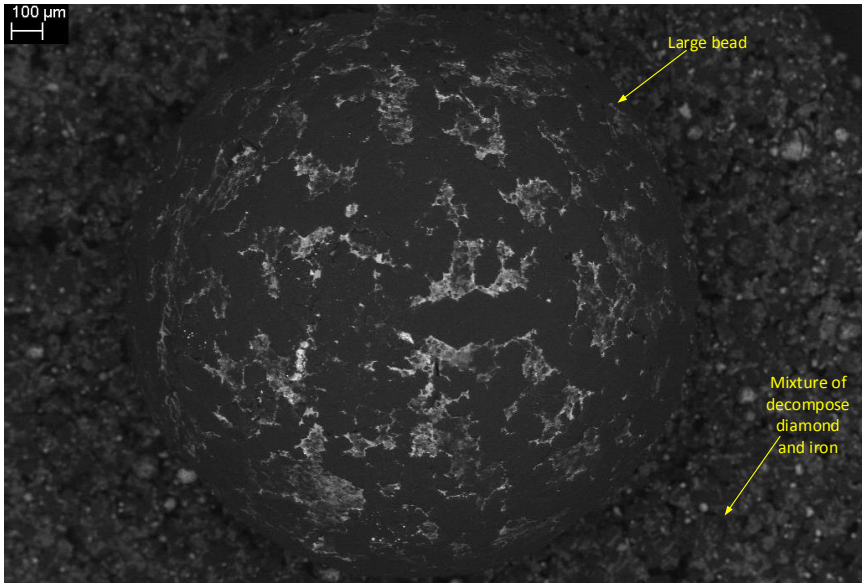

Figure 5.4: A back scattered electron image of the heat treated mixture of iron-diamond. A large bead and decomposed diamond particles adhered to each other by solidified iron

By looking at iron-carbon binary phase diagram (see Figure 4.22), one notices that pure iron melts at 1538°C, as a result, incidence of melting below 1300°C is an indication of diamond iron chemical reaction. In fact, carbon atoms must have solved in iron matrix to bring its melting temperature down. Figure 5.5 depicts a a back scattered electron image of the part of heat treated mixture that diamond particles did not completely dissolve in iron to join the bead. As it can be seen, diamond particles are highly decomposed and partially dissolved in iron. This resulted in melting of iron particles which led to more diamond decomposition into graphite.

The first thermal event is a relatively small endothermic onsetting approximately at 728°C. It reaches to a peak at 769°C and ends at 789°C. Heat of transformation for this thermal event is 3.259 J/g. Considering that this heat only relates to iron mass fraction of

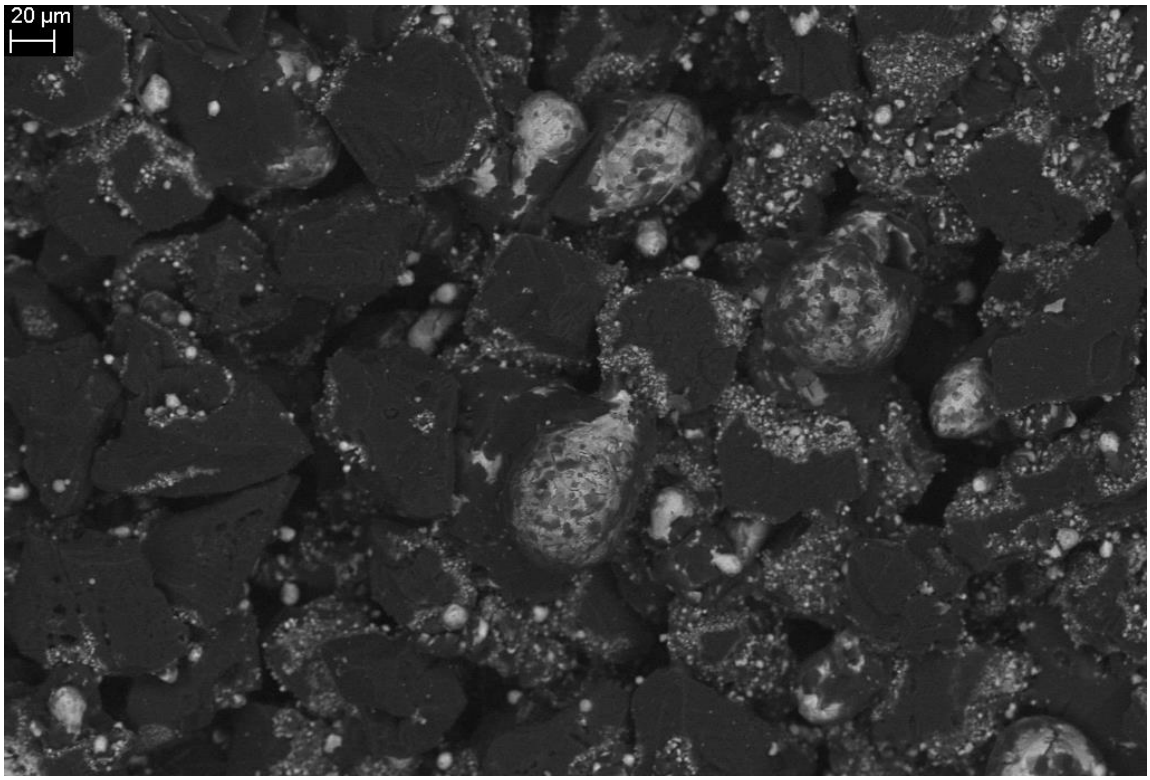

Figure 5.5: A back-scattered electron image of a part of heat treated iron-diamond mixture which shows decomposed diamond particles by diffusion into iron

the mixture, mass fraction of iron can be calculated by [64]

$$f_{Fe} = \frac{\triangle H_{mix}}{\triangle H_{Fe}} \tag{5.1}$$

where f_{Fe} is mass fraction of iron in the mixture, $\triangle H_{Fe}$ is energy of transformation of pure iron for currie temperature, $\triangle H_{mix}$ is energy of transformation of the mixture for Currie temperature. As a result, mass fraction of iron was calculated as 0.683 which is in agreement with the fraction of iron in the precursor mixture as 0.693.

The thermal event corresponding to ferrite to austenite phase transformation (nucleation of austenite) initiated at 923.4°C for pure iron (see Figure 5.2) while that of mixture onsets at 897.2°C. By looking at iron-carbon binary phase diagram (see Figure 4.22), one can notice that this suppression in onset temperature is due to solution of carbon in iron. This corroborates that the reaction between iron and diamond starts before ferrite to austenite transformation begins. The energy of transformation for these peaks calculated by determining the area under each peak as 8.974 J/g and 6.132 J/g for pure iron and the mixture, respectively.

The third thermal event initiates at 981 and reaches to the end at 1065.5°C with the energy of transformation of 3.785 J/g. The eutectic event initiates at 1073°C and reaches to the peak at 1165°C and ends at 1193°C. In eutectic melting, the DSC trace shows two thermal events [64, 68]. First is a peak as a result of melting the eutectic. The second is due to solution of the remaining into the equilibrium melt. The gap between the two peaks is an indication of how close the composition is to the eutectic point. As the composition gets closer to the eutectic point, the gap between the two peaks becomes shorter till at eutectic point where the two peaks merge to one sharp peak [64, 68]. It is clear that the two stage endothermic peak in the range of 1080°C -1100°C is due to

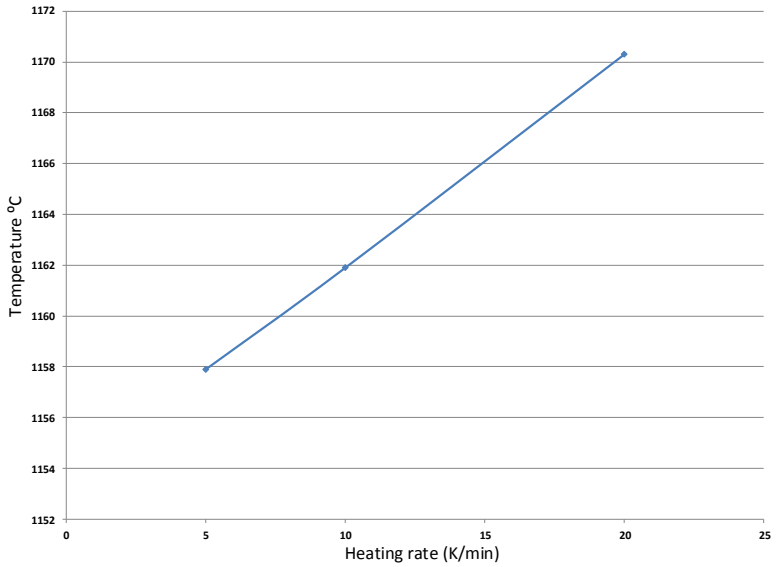

Figure 5.6: Plot of liquidus temperature versus heating rate to find equilibrium liquidus temperature

melting a eutectic system. The two peaks at Figure 5.3 are relatively close which shows the composition is close to eutectic point. The eutectic line was calculated from extrapolated peak onset temperature of first peak. Determination of liquidus line is more complicated. In order to determine the liquidus temperature, DSC heating curves for heating rates of 10 and 5 K/min were also acquired (see Figure 5.3). The extrapolated peak completion temperature [64, 68] of the two stage peak in the range of 1080°C-1100°C of DSC traces for heating rates of 20, 10, and 5 K/min was determined (see Figure 5.3 and Figure 5.6). In Figure 5.6 the determined temperatures are plotted versus the corresponding heating rates. Linear regression of plotted points yields correlation factor of R^2=99.67 which indicates high linearity, as a result, the intersection of regression line and the ordinate (1154°C) represents the corresponding temperature of heating rate of zero K/min at limit which is a good approximation of liquidus temperature. The calculated liquidus temperature of the mixture (1154°C) matches the liquidus temperature of eutectic point in iron-carbon phase

diagram (see Figure 4.22).

Study of microstructure of the DSC heat treated sample revealed that it has eutectic structure with carbon inclusions. Figure 5.7a shows microstructure of the part of the sample that did not join the bead and Figure 5.7b shows microstructure of the bead. It can be seen that the detached carbons from diamonds dissolve in iron up to the limit of around 6 weight percent and the rest would be as unsolved carbon. Therefore, there is no limit for diamond graphitization in presence of iron.

In summary, one can conclude that carbon atoms start detaching their network in diamond and diffuse into iron particles at temperatures below 1000°C . This causes that the iron carbon solution melts at around 1150°C. Melting causes more diamond decomposition and higher solution of carbon in iron. Although the solution of carbon in iron is limited but detaching of carbon atoms from diamond continues which results in super saturation of iron matrix and presence of large graphite inclusions in the iron matrix. On the other hand, iron diffuses into the decomposed diamond and accelerates the decomposition even faster. The result is that a major part of carbon atoms detach from the diamond particles and a high fraction of the remaining carbon atoms decompose to graphite or react with iron. In fact, not only iron reacts with the diamond, but also acts as a catalyzer for diamond graphitization. The result of DSC study is in complete agreement with the experiments which showed that contact with iron has a highly detrimental effect on diamond particles and it should be avoided.

5.3.3 Titanium-Diamond

Figure 5.8 shows the DSC traces for pure titanium and mixture of titanium and diamond. Both samples were heated to 1300°C, then immediately cooled to room temperature by

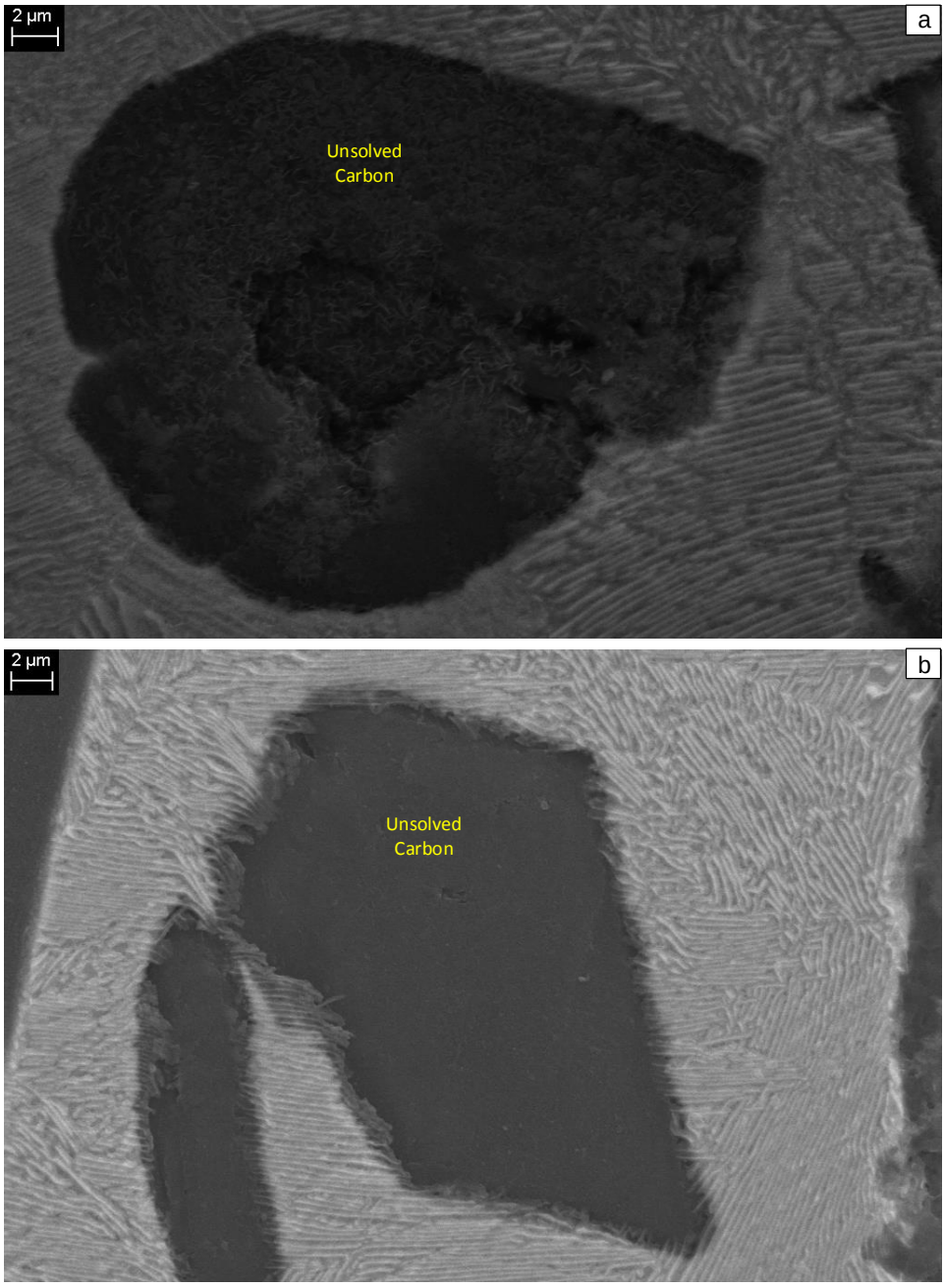

Figure 5.7: a) A back-scattered electron image of a part of heat treated iron-diamond mixture which shows eutectic structure and a decomposed diamond. b)A back-scattered electron image of a part of heat treated iron-diamond mixture which shows eutectic structure and unsolved carbons

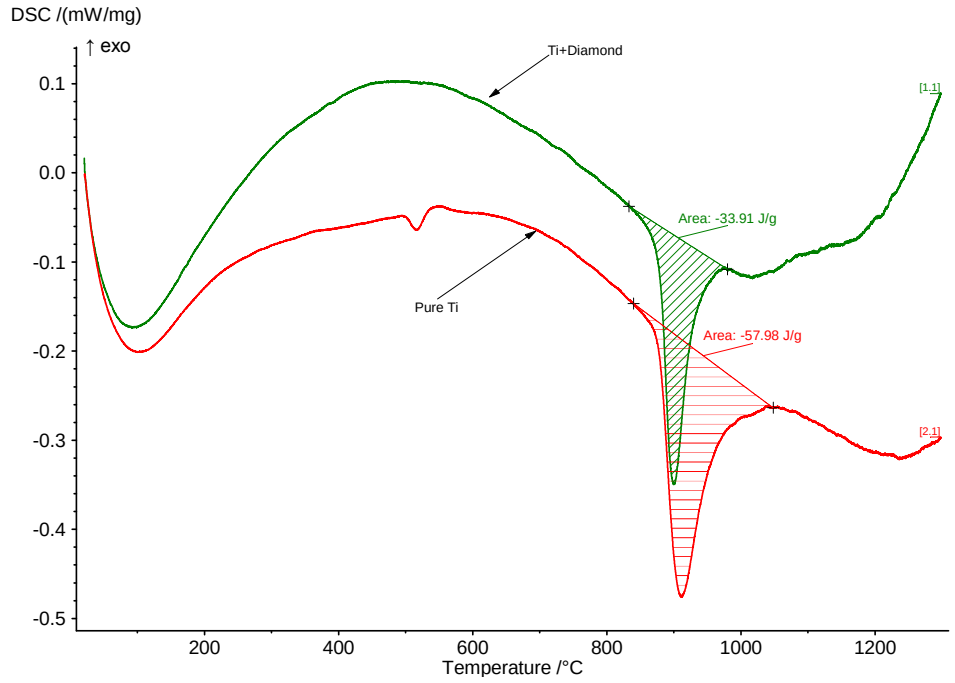

Figure 5.8: DSC heating/cooling profiles of pure titanium and mixture of titanium-diamond

heating and cooling rate of 20 K/min. In heating curve of pure titanium, there is a small endothermic peak around 500°C. The second thermal event is an endothermic event which corresponds to transformation of α-Ti $\rightarrow$ β-Ti of titanium . The onset temperature of this peak is 880°C and the peak is around 900°C. DSC heating profile of mixture of titanium and diamond shows only one endothermic event which corresponds to transformation of α-Ti $\rightarrow$ β-Ti. One can notice that the slope of DSC curve after the endothermic term in the case of pure titanium is negative, while that of the mixture is positive. This could be because of formation of TiC which is exothermic and causes the slope in the DSC curve of the mixture to become positive. It is clear that no melting occurs during the heating of pure titanium or mixture of titanium and diamond. Study of heat treated samples by SEM shows formation of a layer around diamond particles.

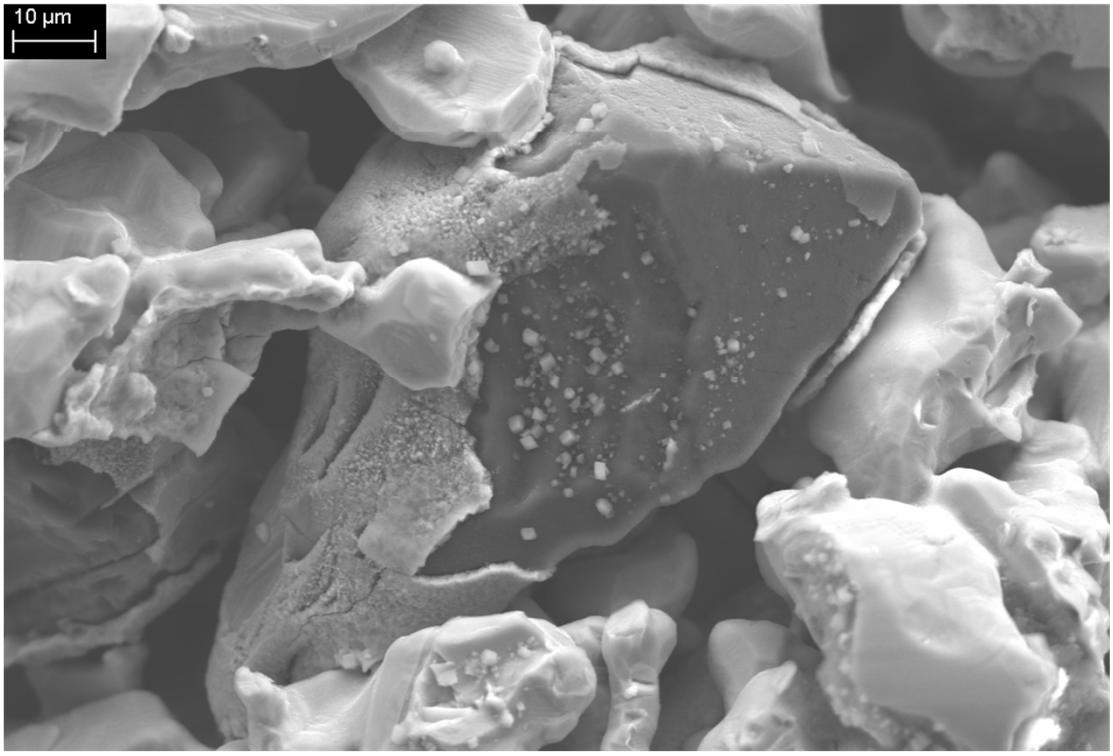

Figure 5.9: A back-scattered electron image of a diamond particle encircled by a titanium-rich layer

Figure 5.9 shows a diamond particle in the heat treated sample by DSC that is surrounded by a titanium-rich layer. The thickness of the Ti-rich layer is around 2 micron or less. Since no melting occurred and spherical titanium particles nearly maintained their shapes, titanium atoms must have left titanium particles and reacted with carbon atoms on the surface of diamond particles. Figure 5.10 shows diffusion of titanium into the surface of a diamond particle and nucleation of TiC on the surface of diamond. Figure 5.11 shows migration of titanium atoms on the surface of a diamond particle and formation of a titanium network. Therefore it could be concluded that a TiC layer is formed by diffusing titanium into the surface of diamond particles which results in nucleation of TiC on the diamond surface. As this layer grows, the diffusion of titanium into the surface of diamond becomes more difficult and the growth of the TiC layer stops at a certain thickness. In other words, the TiC layer provides a passive protection for diamond particles. The diamond particles does not experience any decomposition while they are surrounded by a TiC layer with a thickness of less than 2 micron. On the other hand, it was revealed that no melting of titanium particles occurs whereas some solid sintering of Ti particles happens. It was also revealed that when the TiC layer reaches its maximum thickness, the interfacial bonding between the TiC layer and the diamond particles become very weak in a way that it can be detached from the diamond particle. Figure 5.12 depicts sintering of titanium particles in the heat treated sample by DSC while the TiC layers were separated from diamond particles and are attached to titanium particles. As it can be seen in the figure necking (inter-particle bridging) of spherical Ti particles has happened which is due to reduction in the surface energy of the particles by reduction in the free surface area .

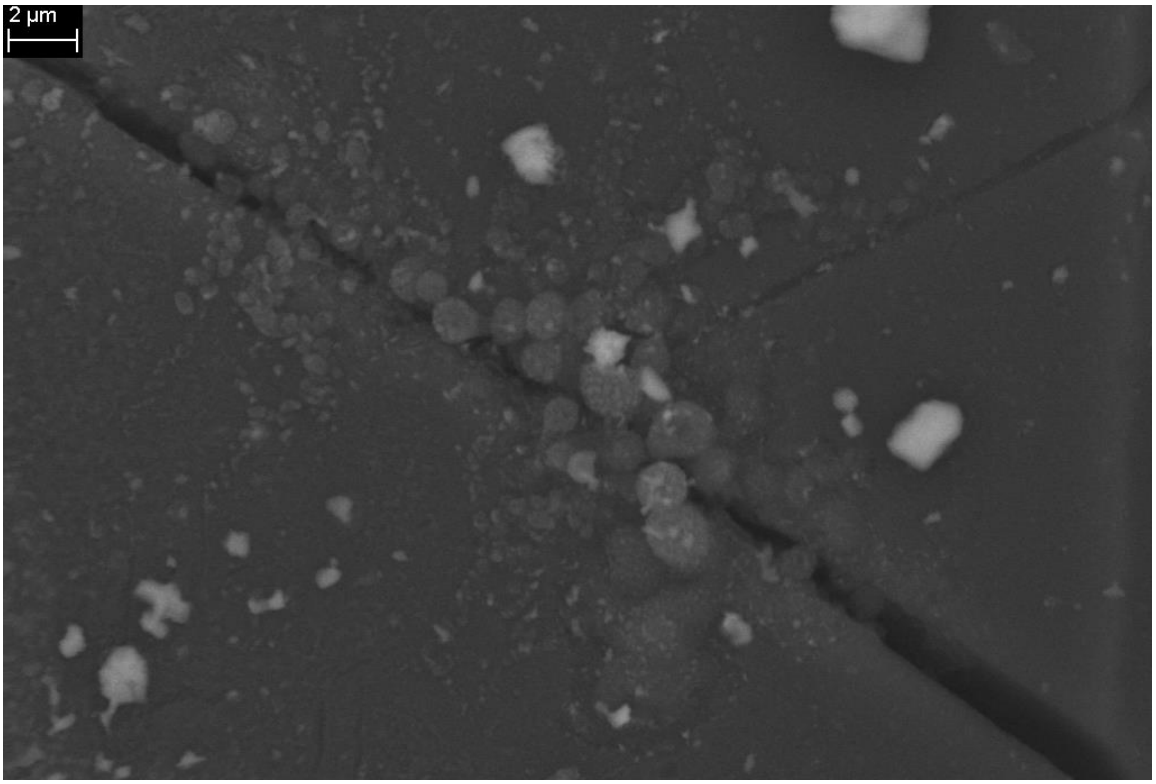

Figure 5.10: A back-scattered electron image of a diamond particle which shows surface diffusion of Ti into the surface of a diamond particle and nucleation of TiC

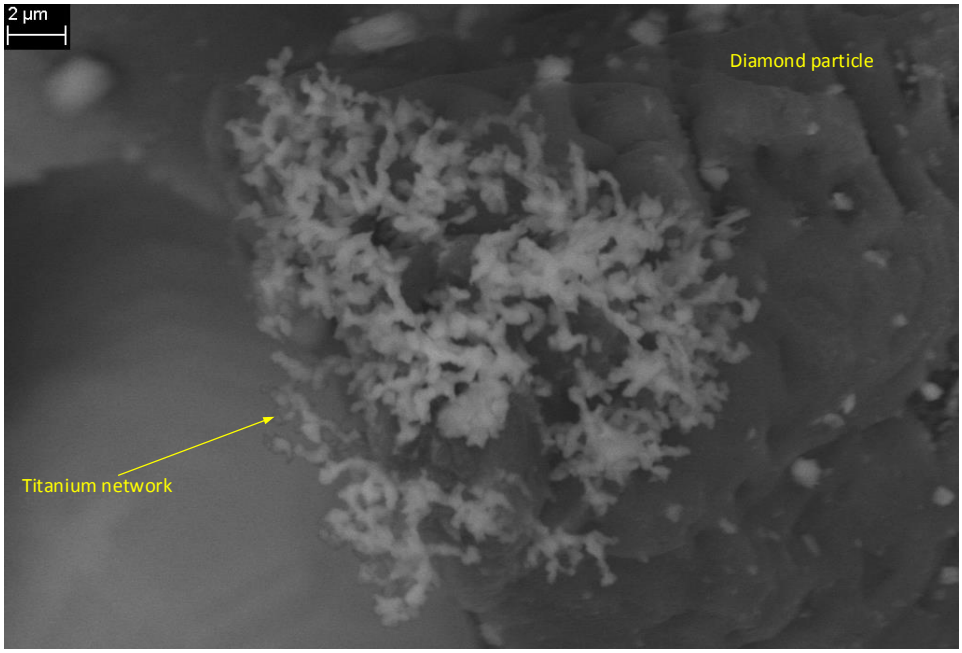

Figure 5.11: A back-scattered electron image of a diamond particle which shows formation of TiC on the surface of a diamond particle

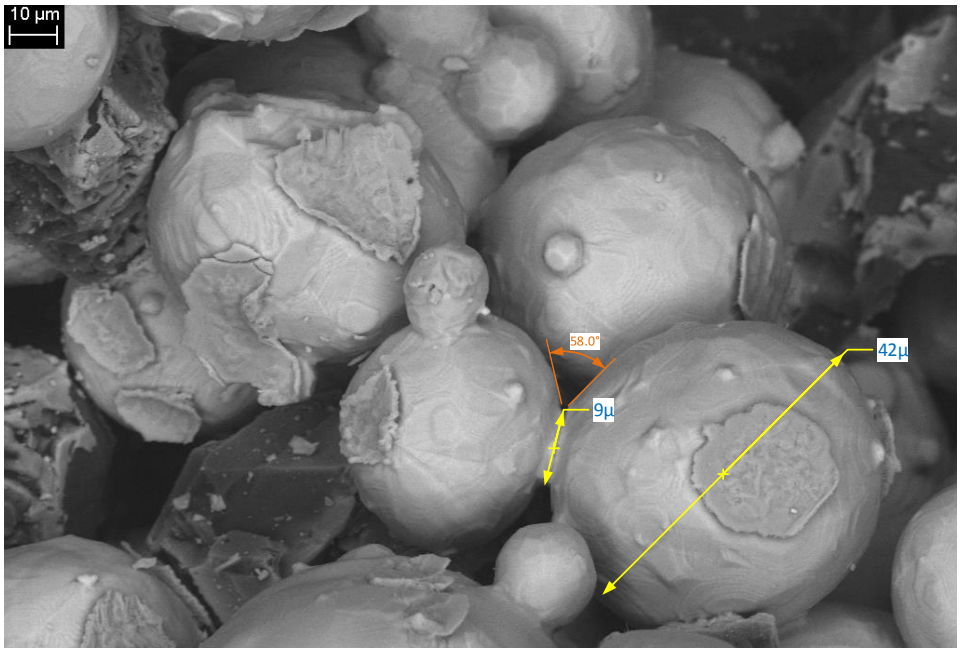

Figure 5.12: A back-scattered electron image which shows sintering of titanium particles and detached TiC layers from diamond particles

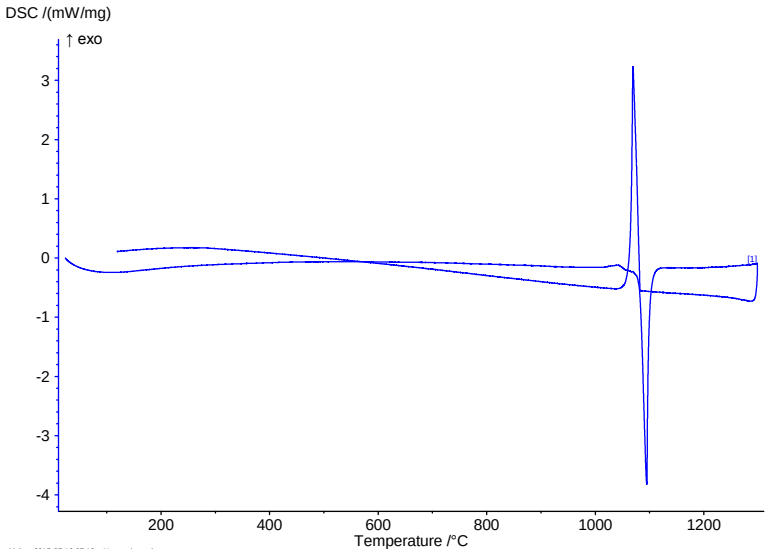

Figure 5.13: DSC profile of heating of Cu-diamond mixture to a peak temperature of 1300°C and cooling down to room temperature

5.3.4 Copper-Diamond

Figure 5.13 represents DSC profile of heating Cu-diamond mixture to a peak temperature of 1300°C and then cooling down to room temperature with heating/cooling rate of 20 K/min. It can be seen that no thermal event occurs other than melting and solidification of copper in the thermal cycle. Study of the heat treated sample by SEM shows that copper neither reacts nor wets diamond (see Figure 5.14).

5.3.5 Tin-Diamond

Figure 5.15 depicts DSC profile of heating Sn-diamond mixture to a peak temperature of 1300°C and then cooling down to room temperature with heating/cooling rate of 20 K/min. One can notice that no thermal event occurs other than melting and solidification of tin in the thermal cycle. Study of the heat treated sample by SEM shows that tin neither reacts

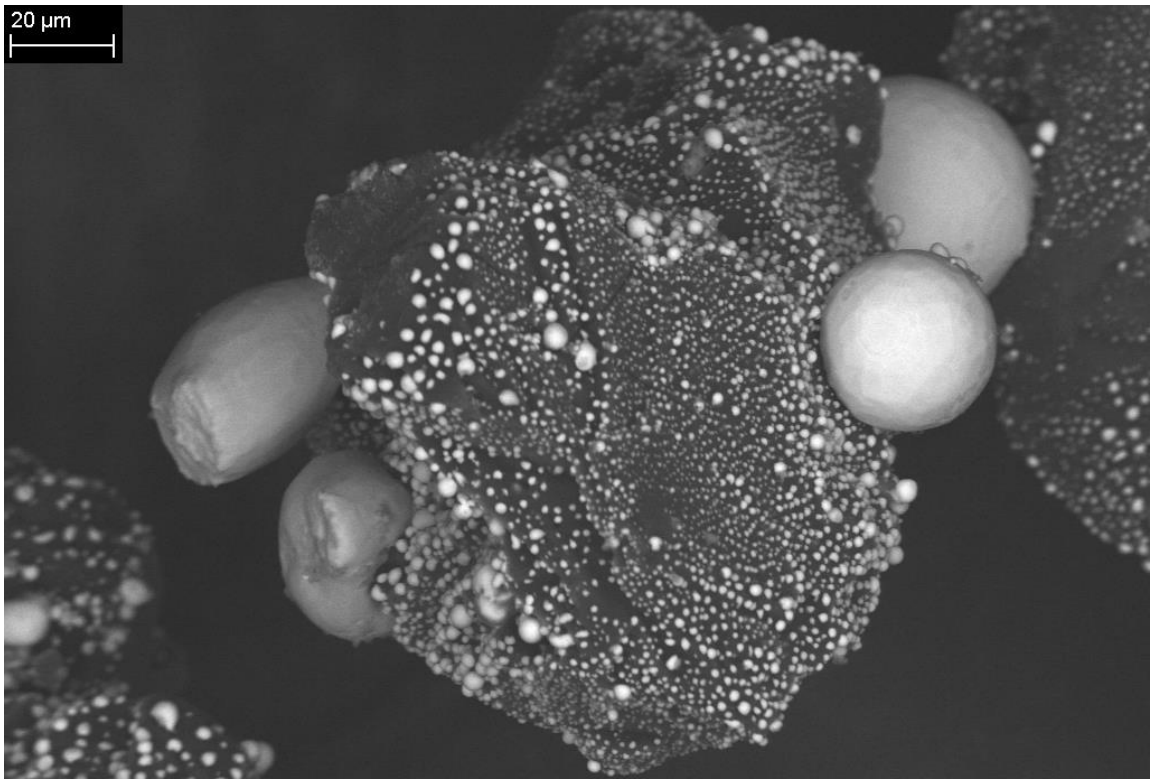

Figure 5.14: A back-scattered electron image of a diamond particle in the DSC heat treated sample of mixture of Cu-diamond

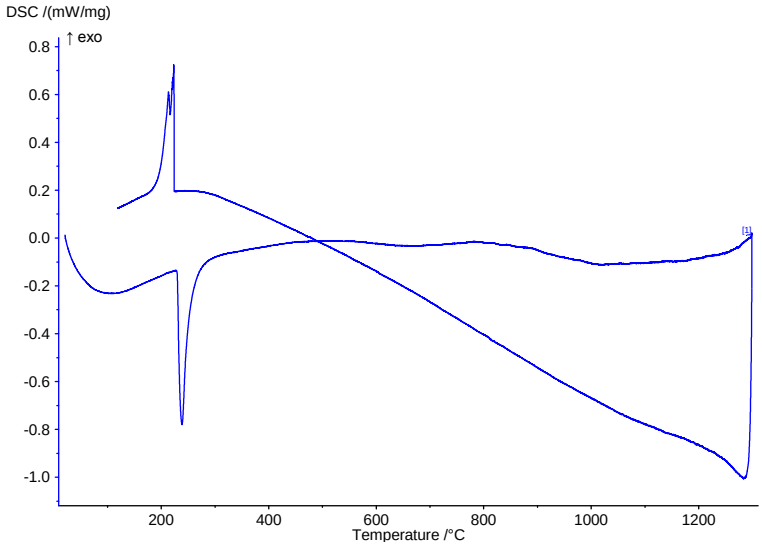

Figure 5.15: DSC profile of heating of Cu-diamond mixture to a peak temperature of 1300°C and cooling down to room temperature

nor wets diamond (see Figure 5.16).

5.3.6 Matrix-Diamond

The precursor matrix-diamond powder mixture used in this study was studied by DSC. Two samples of the powder mixture were separately heated to a peak temperature of 1150°C with a heating rate of 30 K/min, then first sample immediately cooled down to room temperature with cooling rate of 30 K/min, whereas the second one was kept for 30 min at 1150°C and then cooled down to room temperature with cooling rate of 30 K/min. Figure 5.17 depicts the DSC thermal profiles of both cases. As expected the heating profile of the two is similar, however the cooling curves are different in the first solidification peak. The solidification peak for the case with 30 min isothermal hold is narrower compared to the one without isothermal hold. Moreover, the solidification of the one with isothermal hold

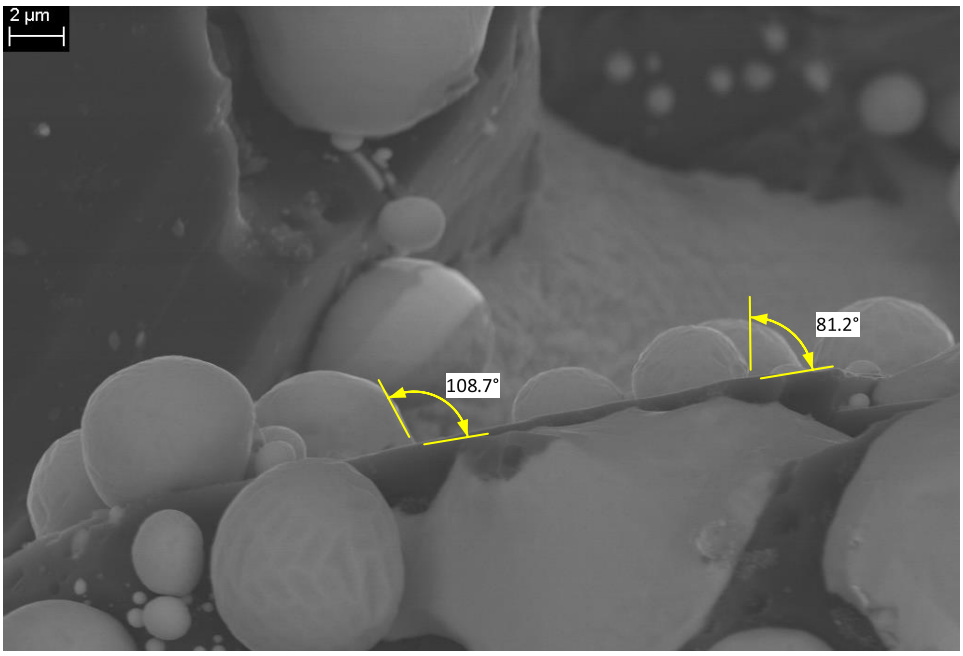

Figure 5.16: A back-scattered electron image of surface of a diamond particle in DSC heat treated sample of mixture of Sn-diamond

is one stage peak while that of the one without isothermal hold is two stage peak. There was no clear evidence of diamond-matrix reaction in the thermal cycles. This is because of the fact that there are three metals in the matrix. These three metals can react with each other, as a result, it is very difficult to differentiate thermal event of diamond-matrix reaction from the thermal events of reactions of metals with each other.

Study of microstructure of the samples by SEM did not reveal any difference in morphology of the matrices. Thickness of diamond-matrix interfacial layer was high and nearly the same for both samples. As it was revealed in Section 5.3.3, the TiC layer growth is limited and after some time the growth stops. Therefore, most likely in the sample without isothermal hold the TiC layer reaches its limit and by giving it more time in the sample with isothermal hold, the thickness of the TiC layer does not change. Figure 5.18 shows a back-scattered electron image of diamond-matrix interfacial layer of a diamond particle inside the sample without the isothermal hold. As it can be seen, the thickness of the layer at one point is around 2 micron which is very high. Study of diamond particles by Raman spectroscopy revealed traces of graphitization on a few diamond particles. This could be due to existence of unsolved graphite in TiC phase. Figure 5.19 depicts Raman spectrum of a particle inside the sample with isothermal hold which shows some traces of graphitization.

5.3.7 Deposit

In order to study the thermal properties of deposited materials, a piece of clad was separated from a deposited clad and it was studied by DSC. The sample was heated to a peak temperature of 1150°C by heating rate of 30 K/min and immediately cooled to room temperature with the same cooling rate. Figure 5.20 depicts the DSC traces of the sample.

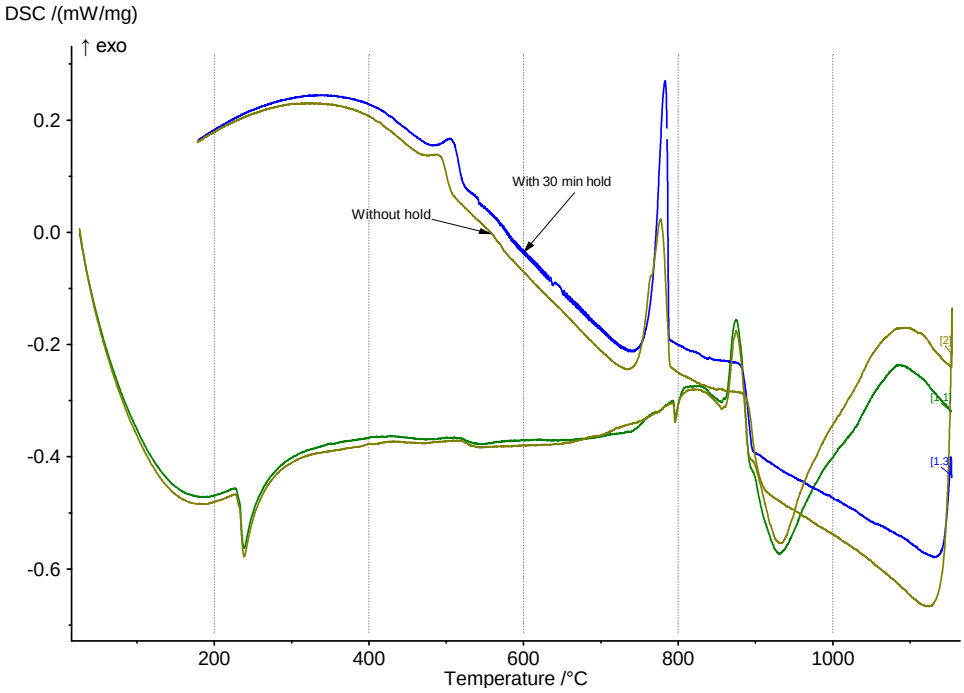

Figure 5.17: DSC heating/cooling curves of matrix-diamond powder with and without isothermal hold

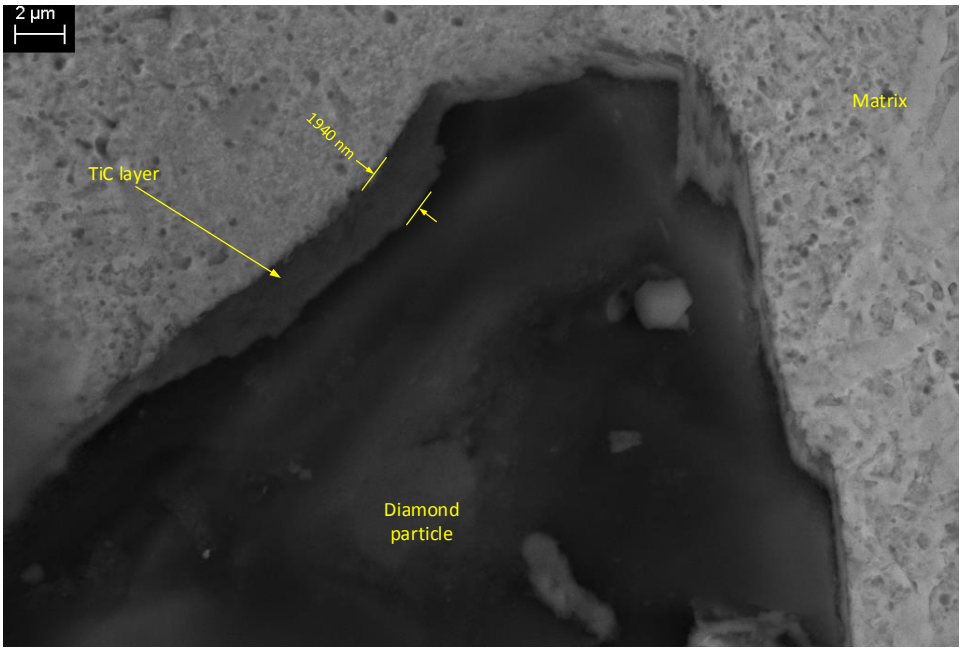

Figure 5.18: A back-scattered electron image of a diamond-matrix interfacial layer inside a heat treated sample by DSC

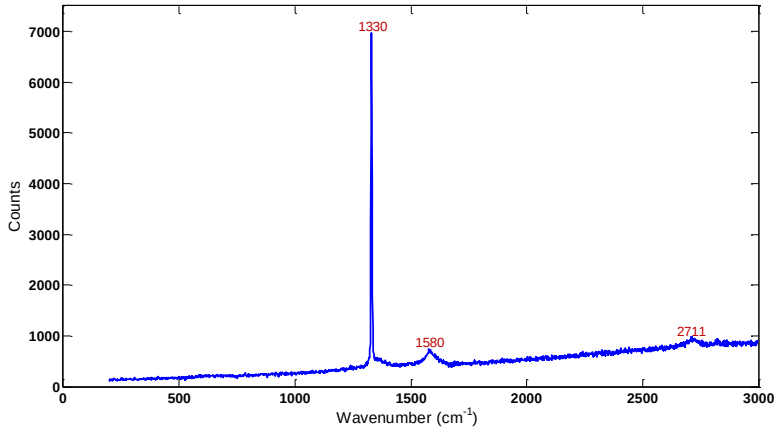

Figure 5.19: Raman spectrum of a diamond particle inside the heat treated sample by DSC up to a peak temperature of 1150°C

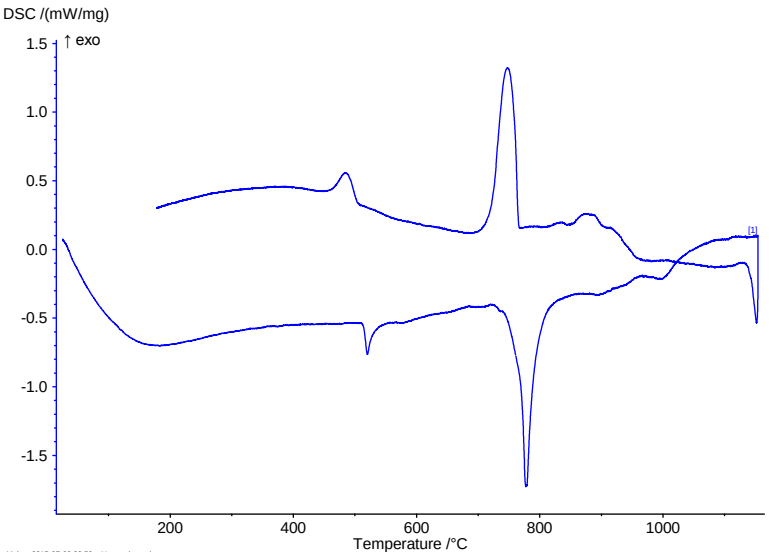

Figure 5.20: DSC heating/cooling curves of a part of a deposited clad

It can be seen that complete melting occurs before 1100°C. This heat treatment increased the thickness of the interfacial layer. The increase at some points was more than twofold. The increase in the thickness of the TiC layer was expected since the interaction time (the time that titanium and diamond are at elevated temperatures) in the deposition of the clad is much shorter than the heat treatment in the DSC study. As it was mentioned in the previous section, the thickness of TiC layer almost reaches its limit in the heating cycles of the DSC study. Therefore, the developed TiC layers in the deposited sample grow during the heating cycles of this DSC study until reaches their limit.

Study of diamond particles in the heat treated sample by Raman spectroscopy showed considerably more graphitization than the sample of heat treated matrix-diamond in the previous section. This could be due to presence of iron in the deposited sample. By going through the heating cycles of the DSC, iron in the sample is given much more time to react with diamond particles and to degrade them.

5.4 Conclusion of the Thermal Analysis

The DSC experiments revealed that mechanism of reaction between titanium and diamond is completely different from that of iron and diamond. Reaction of titanium and diamond starts with transformation of α-Ti $\rightarrow$ β-Ti at 880-900°C. It was also found that a layer of TiC is formed around diamond particles by diffusing titanium into the surface of diamond particles which results in nucleation of TiC on the diamond surface. As this layer grows, the diffusion of titanium into the surface of diamond becomes more difficult, thus the growth of the TiC layer slows down until stops completely at a certain thickness. This TiC layer acts as a passive protection for diamond particles. The diamond particle does not experience any decomposition while surrounded by a TiC layer with a thickness of less than 2 micron. On the other hand, it was revealed that no melting of titanium particles occurs whereas some solid sintering of Ti particles happens. It was also revealed that when the TiC layer reaches its maximum thickness, the interfacial bonding between the TiC layer and the diamond particles becomes very weak and brittle in a way that it can be detached from the diamond particle.

It was found that the reaction between iron and diamond starts before transformation of ferrite to austenite begins (below 900°C). Carbon atoms start detaching from their network in diamond, and diffuse into iron particles. This causes the iron-carbon solution to melt at temperatures around 1150°C. The melting causes higher levels of diamond decomposition and higher solution of carbon in iron. Although the solubility of carbon in iron is limited, detaching of carbon atoms from diamond continues past the solubility limit, resulting in super saturation of iron matrix and presence of large graphite inclusions in the iron matrix. On the other hand, iron diffuses into the decomposed diamond particles accelerating the decomposition. This results in a significant carbon atoms detachment from the diamond

particles. As a result, high fraction of the remaining carbon atoms decompose to graphite or react with the iron. In fact, not only does the iron react with the diamond, but it also acts as a catalyzer for diamond graphitization.

Results of the DSC study are in complete agreement with the experiments showing that contact with iron has a highly detrimental effect on diamond particles and it should be prevented. In the next chapter, possible ways to decrease penetration of iron into the deposit will be investigated.

The DSC experiments using mixtures of copper-diamond and tin-diamond showed that no wetting or chemical reaction occurred between any of these metals and the diamond particles although complete melting of cooper and tin occurred in the two mixtures. The results of this study showed that the existence of titanium in the matrix is necessary.

It was also found that the thickness of the TiC layer reaches its limit in the heat treated samples by DSC which is due to existence of a much higher interaction time as opposed to laser deposition. As a result, the interaction time plays an important role in the growth of the TiC layer. In the next chapter decreasing the interaction time in order to obtain the optimum thickness of the TiC layer will be studied.

Chapter 6

Discussion and Development

Focus of this chapter is to address the issues that were observed during the course of experiments to develop a practical and reliable metal matrix diamond composite fabrication technology using blown powder laser deposition technique. It was shown that the laser-powder interaction plays a significant role in the outcome of deposition, therefore, laser powder interaction is studied in detail. The issue of dilution and penetration of iron from substrate into the deposit are scrutinized and the solutions for addressing these issues are discussed. In addition, minimization of diamond graphitization and thickness of interfacial layer are investigated. Furthermore, optimization of diamond distribution and volume fraction of diamond particles in the deposit is studied.

6.1 Laser-Powder Interaction Mechanism

The mixed powder is carried out by an inert gas which in this study is argon, however the described experiments in Chapter 4 revealed that this does not completely protect powder

particles from exposure to oxygen. In some experiments when the power was high enough, diamond particles were burnt before reaching the melt pool. This makes laser powder interaction even more important for the case of diamond deposition and as a result the laser powder interaction will be studied in more detail in this chapter. In the following, the related models in laser powder interaction in the literature are first reviewed and then a simple model for the laser-powder interaction for the diamond deposition is developed.

Lin [69] measured the laser power attenuation in coaxial blown powder laser cladding. It was shown that the power attenuation depends on many parameters such as shape of the powder flow stream and its configuration with respect to laser beam, powder flow density, the distance powder particles pass through laser beam, and size of particles. It was found that the power attenuation could go up to more than fifty percent. Lin in another paper [11] developed a simple 1D analytical model to predict the temperature of the particles in coaxial laser cladding. In addition, temperature of powder particles was measured by a pin-hole sensor developed using an infrared pyrometer. The temperature of 400 particles were recorded as shown in Figure [11]. As it can be seen, the temperature of the particles are int the range of 500°C to 1300°C while the process parameters were CO_2 laser with the power of 1 kW, powder particles of 304L stainless steel powder with the size in the range of 45 to 105 µm, and powder mass flow rate of 0.05 g/s (3 g/min) with a carrier gas flow rate of 2 l/min.

Picasso *et al* [34] developed a simple analytical model for laser cladding with lateral nozzle. The model considers the laser beam and powder stream as cylinders. Moreover, the shadowing effect of particles over each other in the powder stream was not considered which resulted that the laser power attenuation due to passing the powder cloud to be considered proportional to the projected area of powder particles over the laser beam. Li *et al* [70] quantitatively studied laser powder interaction in laser cladding with side nozzle.

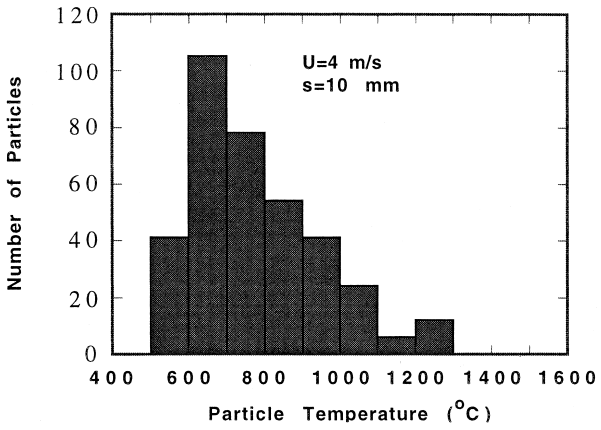

Figure 6.1: Temperature distribution of particles reproduced from [11]

They showed that laser power attenuation decreases as the angle of side nozzle with the substrate (powder jet incident angle) decreases. Fu *et al* [71] developed an analytical model to predict the laser power attenuation and temperature increase of powder particles reaching the substrate. Powder jet incident angles between 45 to 90 degrees were studied. The model predicted that the average temperature of the particles reaching the substrate is decreasing as the jet angle decreases toward 45, however the temperature distribution become more uneven. It was also shown that the laser power density profile changes with altering the jet angle. Liu et al [72] experimentally measured laser power attenuation for 0.13 gs (18 gmin) powder mass flow rate as 9.7 percent for coaxial nozzle. They also developed an analytical model to predict the attenuation of laser power in coaxial nozzle. De Oleveira et al [73] studied the laser powder interaction during coaxial laser direct metal deposition (LDMD). Laser beam attenuation was predicted by using the Beer-Lambert law. The powder distribution across the cross section of the interaction zone was assumed to be uniform which is not the reported case in the literature [74, 75, 76]. Diniz Neto et al [77, 78] developed a physical-computational model for calculating the power attenuation and spatial temperature distribution of powder partilces in lateral and coaxial nozzle. It

was shown that laser beam intensity loses its Gaussian distribution by passing through the powder stream. It was reported that power attenuation almost linearly increasing with increase of powder feed rate. On the other hand, it is exponentially decreasing with increase of particles radius and particles velocity. Pinkerton and Li [75, 79] developed a model for predicting the powder stream and laser power attenuation due to passing through powder stream.

Lin [80] employed FLUENT for numerical simulation of powder stream of a coaxial nozzle. Toyserkani et al [27] developed a numerical model for predicting the powder flow stream in a coaxial nozzle by using FLUENT in conjunction with FEMLAB coupled with MATLAB.

As mentioned in the above literature, some researchers modeled co-axial and some lateral nozzles. In the next section, these two nozzles are compared for the application of diamond deposition.

6.1.1 Coaxial Nozzle versus Lateral Nozzle

The deposit by blown powder laser cladding with side (lateral) nozzle has some advantages and disadvatages over coaxial blown powder laser cladding. The powder catchment efficiency (fraction of powder deposited on susbtrate) by lateral nozzle is higher than that of coaxial nozzle, since the powder stream is more focused in a side nozzle as opposed to that of a coaxial nozzle. This is because of the difficulty to obtain a focused powder stream coming out of an annular outlet which is the case in coaxial nozzle. This in turn makes the surface finish of the deposit by the side nozzle slightly better than that of the coaxial nozzle [63]. On the other hand, the powder stream at the back of the melt pool is partially obstructed from joining the molen pool by solidified parts of the clad [81, 76].

Interaction of powder particles with laser is higher in coaxial nozzle, therefore temperature rise of powder particles and laser power attenuation due to powder cloud are greater [82, 76]. However side nozzle suffers from two important issues. In side nozzle, the powder stream joins the molten pool in one direction which causes directional effect on the deposit [63]. In fact one of the main reasons of using coaxial nozzle is to make the process omni-directional [83, 84, 85]. In addition, in side blown powder laser deposition, the alignment of powder stream and molten pool has significant impact on the deposit [63]. Therefore any alteration of the alignment causes changes in the quality of the deposit which in turn initiates lack of repeatablility issues in the process, whereas in coaxial nozzle the powder flow profile is almost unchanging as long as carrier gas flow rate and powder feed rate are costant. Therefore, in almost all modern laser deposition systems, coaxial laser is prefered [76]. However, as it was mentioned in previous section in the case of deposition of diamond, laser powder interaction plays a more important role and as a result, lateral nozzle was chosen in this study to minimize the diamond laser interaction.

6.1.2 Estimation of Powder Particles Temperature

In order to have an estimate of temperature of powder particles reaching the melt pool, a simple heat balance equation is used

$$\Delta T_p = \frac{Q}{m_p c_p} = \frac{I A_p t a_\alpha}{\rho_p V_p c_p} = \frac{I \pi r_p^2 t a_\alpha}{\rho_p \left(4/3 \pi r_p^3\right) c_p} = \frac{3 I t a_\alpha}{4 \rho_p r_p c_p} \tag{6.1}$$

where, ΔT_p is temperature increase of a powder particle before reaching the melt pool, Q is transferred heat to a particle by passing through the laser beam, m_p is the mass of a particle, c_p is the specific heat of a particle, I is laser beam intensity or irradiance, A_p is cross section area of a particle, t is the time that a particle is exposed by laser beam, a_α

is absorptivity of a powder particle, ρ_p is density of a powder particle, V_p is volume of a particle, r_p is radius of a particle. Assuming that laser power distribution is top hat then

$$I = \frac{P}{\pi r_b^2} \tag{6.2}$$

where, P is laser power, and r_b is the beam radius which is considered constant here. Since it was assumed that the powder particles speed is constant and is equal to the velocity of the carrier gas at the exit of nozzle, the time that a particle is exposed to laser beam can be approximated by

$$t = \frac{x}{v_p} = \frac{d_b/\cos\theta_{\text{jet}}}{v_p} \tag{6.3}$$

where, x is the distance that a particle travels through laser beam, v_p is the velocity of particle, and d_b is laser beam diameter. Plugging in I and t from Equations 6.2, and 6.3 yeilds

$$\Delta T_p = \frac{3Pa_\alpha}{2\pi r_b \rho_p c_p r_p v_p \cos\theta_{\text{jet}}} \tag{6.4}$$

using the values presented in Table 6.1 and Table 6.2 for the parameters in Equations 6.1, 6.2, and 6.3, the temperature increase of a single diamond particle by passing through the laser beam can be approximated as $3897a_\alpha$. As a result, it is clear that the temperature increase of a diamond particle is highly dependent on the absorptivity. However, to the best of knowledge of the author the absorptivity of diamond is unknown [3, 4, 5].

Natural diamond without presence of impurity is transparent to infrared radiation [4], therefore it should not absorb laser radiation with the wavelengnth of 1.06 µm, however impurity in industrial diamond initiates laser absorption. Mei *et al* [4] reported measurement of absorptivity of artificial diamond when exposed to Nd-YAG laser (λ=1.06 µm).They measured the absorptance for the power range of 5 to 30W. At the power of 30W the

Table 6.1: Thermal properties of diamond [3, 4, 5]

Property	Diamond	Titanium	Copper	Tin	Iron
Density, ρ(kg/m^3)	3515	4500	8930	7300	7790
Specific heat, c (J/(kg K))	472	523	471	264	560
Thermal conductivity, (W/m K)	2000	23	375	68	30
Thermal diffusivity, ($\times 10^{-6}$m^2/s)	1207	9.8	112	39	7.5
Melting point,T_m,(°C)	N/A	1677	1083	232	1537
Latent heat of melting, L_m, (kJ/kg)	N/A	392	205	60	272

Table 6.2: The values used in Equation 6.1 to find an approximate value of temperature increase of a diamond particles passing through the laser beam

Parameter	Particle radius (micron)	Beam radius (mm)	Particle velocity (m/s)	θ_{jet} (degree)	Laser power (W)
Value	25	1	2	45	500

absorptivity was around 0.16. Mei et al showed that increase in power of incident laser results in a higher absorptivity. Moreover, they mentioned that the absorptivity was lower for larger diamond particles. In addition, they mentioned that the absorptivity was higher for darker diamond particles. The studied power range (5-30W) is much lower (at least one order of magnitude) than the power range used in this study, therefore the absorptivity should be much higher than the reported values by Mei et al [4]. In addition, the absorptance in a cloud of particles could be different than that of reported by Mei et al [4] due the fact that a cloud of particles can cause multiple reflection of the light inside the cloud. On the other hand, absorptivity depends on the surface roughness of the diamond particles [63, 86], since the surface roughness can cause multiple reflection by the trapped light.

It should be noted that the roughness less than laser beam wavelength has no effect on absorption, therefore any roughness less than laser beam wavelength is considered completely flat surface for the matter of absorption [63]. Examining the diamond particles by

SEM revealed that the roughness of diamond particles on some locations is greater than the laser beam wavelength (λ=1.06 µm) which increases absorptivity. Figure 6.2 shows backscattered electron image of two diamond particles used in this study. As it can be seen in the figure, there are areas that the roughness is higher than laser beam wavelength. Considering the above-mentioned points, the absorptivity of diamond particles should be higher than the reported value in the study by Mei et al [4].

In order to gain an insight into the absorptivity of the diamond particles used in this study the following experiments were conducted. The laser beam was irradiated over a spread of diamond particle on a titanium substrate. Titanium was selected as the substrate since no reaction occurs between diamond particles and titanium at temperatures below 850°C. Table 6.3 presents the process parameters used in these experiments. All samples showed extreme diamond decomposition. Figure 6.3 depicts two back-scattered electron images of a part of sample number 11 in Table 6.3 where the laser power is only 200 W and the scanning speed is 8.33 mm/s. Raman spectra of these extremely decomposed diamond particles is very similar to Raman spectrum of noncrystalline graphitic carbons specifically glassy carbons (see Figures 4.13 and 4.14). These results verify that the absorptivity of the diamond particles used in this study can not be zero.

To further investigate diamond-laser reaction another set of experiments was conducted. The blown powder laser deposition was performed with diamond powder without being mixed with the matrix. The same process parameters of Table 4.7 while a titanium substrate was used as the substrate. This assured that no molten pool initiated and only diamond- laser interaction takes place. The result showed that many diamond burned. On the other hand, in the experiments where power input was high, the deposition was covered by a dark layer of graphite which is another indication of burning diamond particles before reaching the molten pool.

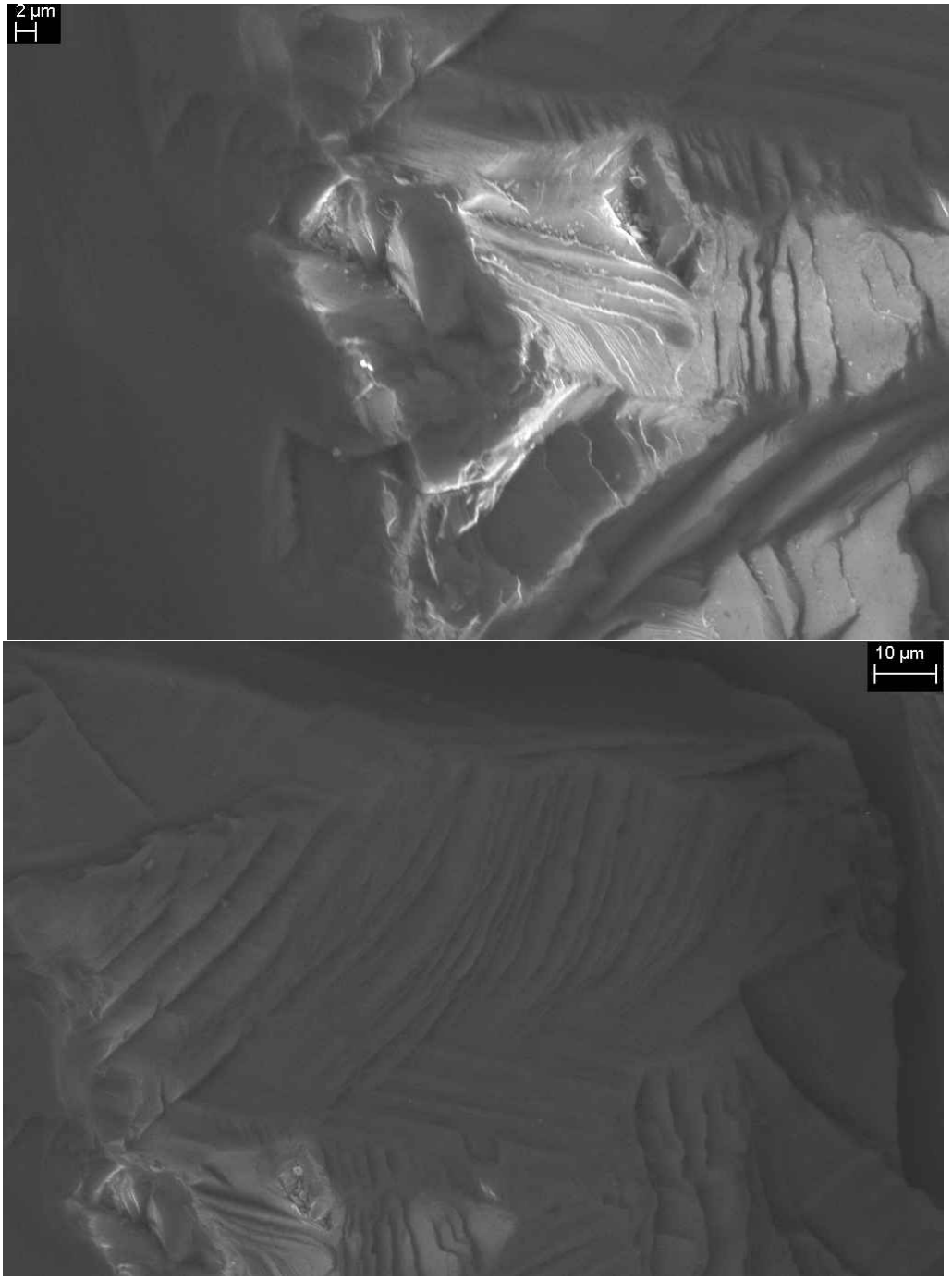

Figure 6.2: Back-scattered electron images of parts of two diamond particles used in this study. The roughness in some parts is clearly greater than the laser wavelength.

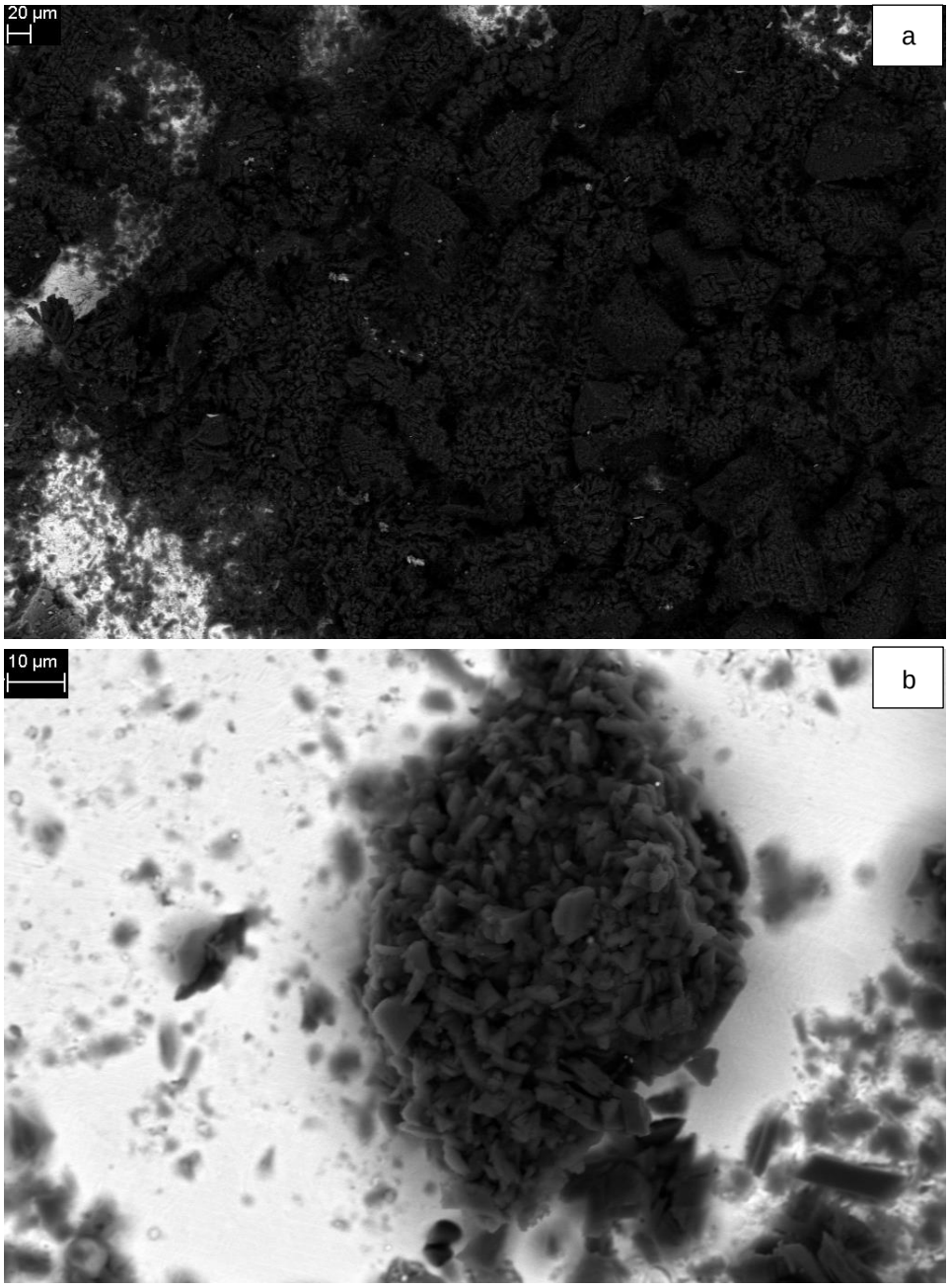

Figure 6.3: a) A back-scattered electron image of a part of sample number 11 in Table6.3. b)A back-scattered electron image of a decomposed diamond particle from sample number 11 in Table 6.3.

Table 6.3: Process parameters for a selected set of experiments

Sample No.	Power (W)	Scan speed (mm/s)	Beam diameter (mm)
1	500	3.33	1.5
2	500	5	1.5
3	500	6.66	1.5
4	500	8.33	1.5
5	400	5	1.5
6	400	16.66	1.5
7	300	5	1.5
8	300	6.66	1.5
9	300	10	1.5
10	200	5	1.5
11	200	8.33	1.5

6.1.3 Coated versus Uncoated Diamond particles

An effective way to increase diamond retention capacity of the MMC is coating of diamond particles by a thin layer (0.1 to 10 µm) of a strong carbide former such as titanium, chromium, silicon, zirconium, tungsten, molybdenum, niobiom and their alloys [8]. The question is whether using coated diamond particles will be beneficial in laser deposition. Absorptance of laser radiation by a specimen happens at a very thin layer of the surface of the material called skin depth, δ'. By Beer-Lambert law [63, 87]

$$I = I_0 \exp\left(-4\pi kz/\lambda\right) \tag{6.5}$$

where, I is light intensity at the depth of z, I_0 is the original intensity, λ is the wavelength in a vaccum, and k is extinction coefficient. Therefore, the distance that beam intensity

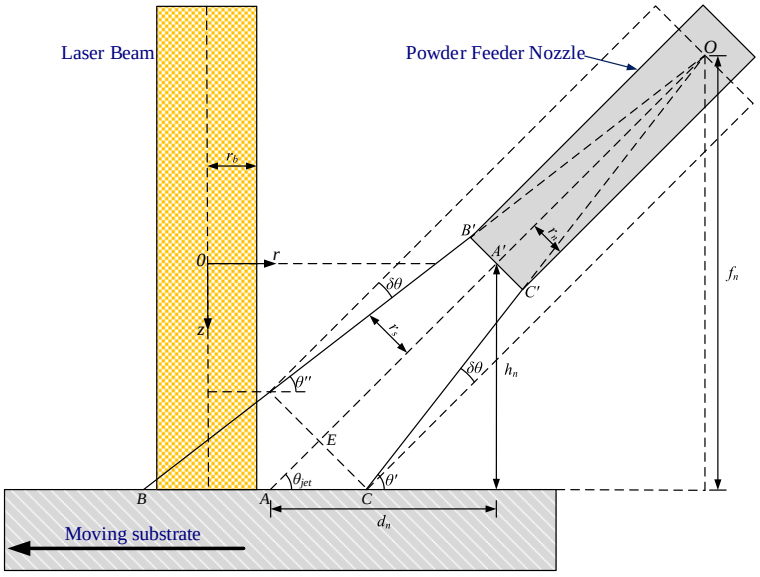

Figure 6.4: Schematic view of a lateral nozzle and laser beam-powder stream configuration. In this figure, center of powder stream is before the center of laser beam on the substrate.

attenuates by a factor of $\frac{1}{e^2}$ (0.13 of the original value) can be calculated as

$$\delta' = \frac{\lambda}{2\pi k} \tag{6.6}$$

For example for titanium, k for the wavelength of λ=1.06 µm is 4 [63], which yields δ'= 0.043 µm. As a result, the absorption of laser beam is conducted by coated metal since the thickness of coating is much higher than the skin depth of metal used for coating. Therefore, the metal absorbs the laser beam not the diamond particle and the heat is transferred to the diamond by conduction.

Since the absorptivity of polished titanium for λ=1.06 µm is 0.37 (It should be noted that this value corresponds to a titanium sample with a polished surface not particles

coated with titanium in a cloud) then $3897a_\alpha$ results to a temperature increase of 1442 °C. This is around the melting point of titanium, and as a result it is possible that titanium melts before reaching the melt pool. Therefore, using metal coated diamond particles results in a much higher temperature elevation of diamond particles. On the other hand, the coated metal or metal carbide can be oxidized which can deteriorate the quality of diamond particles and their bondings to the matrix.

However, the coated metal protects the diamond particle from direct exposure to oxygen. As it was discussed in Section 2.5 diamond decomposition in presence of oxygen occurs at a much lower temperature [6]. The mixed powder is carried out by an inert gas which in this study is argon, however the experiments in this study revealed that this does not completely protect powder particles from exposure to oxygen (see Section 4.7).

Figure 6.5 depicts a schematic view of a lateral nozzle, powder stream, and laser beam that is used to determine the profile of the powder stream. The powder stream expands after exiting the nozzle. Many researchers have shown that assuming the powder stream expands linearly as it is shown in Figure 6.5 is in reasonable agreement with the experiments. It is assumed laser beam diameter is constant in laser powder interaction zone.

6.1.4 Process Parameters and Diamond Particles Interaction

To discuss the impact of the process parameters on the diamond particles temperature, Figures 6.4, 6.5, and 6.6 are used. In Figure 6.4, the laser centerline meets the substrate at a point ahead of the intersection of powder centerlline and substrate. In Figure 6.5, the laser and powder stream centerlines converge at a point on the substrate while in Figure 6.6 the laser is behind the powder centerline.

In case one, (see Figure 6.4) laser beam strikes the substrate by passing through the

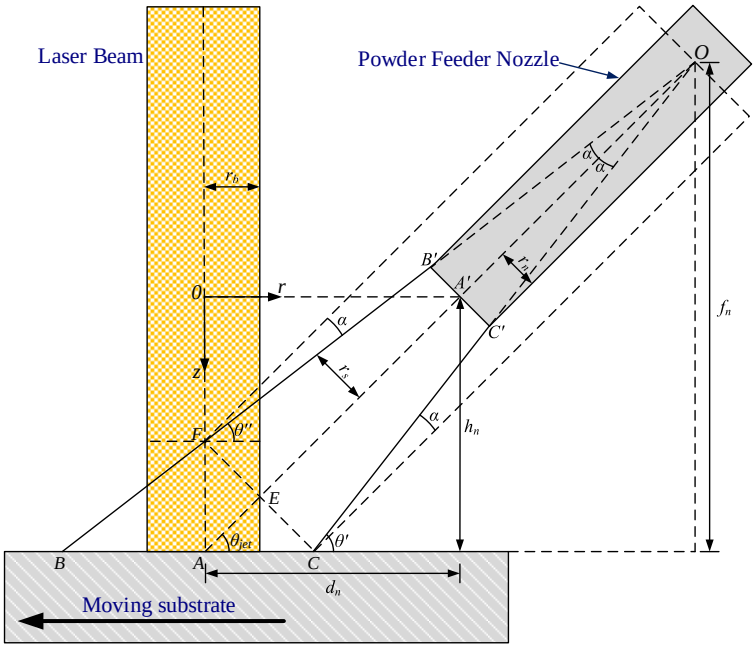

Figure 6.5: Schematic view of a lateral nozzle and laser beam-powder stream configuration. In this figure, center of powder stream and the center of laser beam converge at the same point on the substrate.

minimum portion of the powder stream which makes laser-powder interaction minimum which in turn yields minimum temperature rise in diamond particles. One the other hand, the laser power attenuation due to passing the powder stream is the minimum, therefore higher amount of the laser power is directly absorbed by the melt pool which increases the dilution. Furthermore, a large portion of powder stream hits the substrate in front of the melt pool which results in decreasing the powder catchment efficiency. In addition, this portion of powder stream, after hitting the substrate bounces into the laser-powder interaction zone which on one hand it disturbs the powder stream and on the other hand causes more attenuation in the laser power reaching the melt pool.

In case three (see Figure 6.6), the laser beam reaching the substrate by passing through the maximum portion of powder stream which results in maximum laser-powder interaction and higher temperature of diamond particles reaching the melt-pool. In addition, this causes that more power of laser beam to be attenuated before reaching the melt-pool, which results in less direct absorption of laser energy by the melt-pool. This in turn results in decreasing the amount of dilution. Furthermore, most parts of the powder stream join the melt pool after the laser beam passes the melt-pool which increases the powder catchment efficiency. It should be noted that when this portion of powder reaches the melt-pool, the temperature of the melt pool has been reduced which could result in a partially solidified melt pool, as a result in this case this portion of powder particles does not join the deposited materials.

Case two as it can be seen in Figure 6.5 is between the two previous cases, therefore laser-powder interaction, temperature increase of the diamond particles, dilution, and powder catchment efficiency is between the two previous cases.

Similarly, the nozzle angle, powder divergence angle, and the nozzle position will impact the interaction time of powder particles with laser. The interaction time results in the

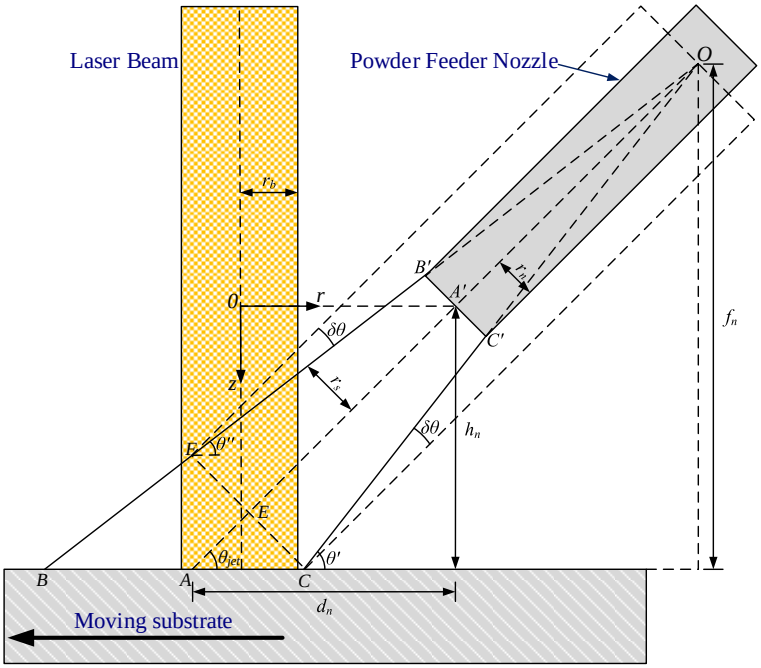

Figure 6.6: Schematic view of a lateral nozzle and laser beam-powder stream configuration. In this figure, center of powder stream is after the center of laser beam on the substrate.

amount of energy the diamond particle will absorb before reaching the substrate. Since diamond particles are prone to fast oxidization, it is important to control this interaction to prevent any oxidization. In addition to the nozzle and laser orientations, the particle speeds will impact the interaction time. The powder speed is controlled through the carrier gas flow rate. It is clear that larger particle sizes will show lower increase in their temperature during their interaction with laser beam.

It should be noted that the laser power has a linear correlation with the amount of energy that the particles could absorb during their interaction with the leaser beam. This however, is not the case in terms of the laser beam diameter at constant power laser. In fact, by decreasing the beam diameter the amount of energy absorbed by the particles will increase.

Using the above discussions, in the experiments, by adjusting the process parameters empirically and numerically, a set of parameters were derived for minimizing laser-diamond particles interactions.

6.2 Design of a New Lateral Nozzle[1]

In order to protect diamond particles from interaction with oxygen, a new lateral nozzle was designed. In the new nozzle as shown in Figure 6.7, the nozzle of the powder-carrier gas stream was placed inside an annular tube. This tube was separately connected to a flow of a shielding gas (argon) which caused that the powder-carrier gas stream to be encircled by the shielding gas. The exterior nozzle provided a laminar flow with a flow rate up to 70 CFH (32.9 L/min), protecting the powder stream and process zone from interaction with oxygen.

[1]This nozzle was designed by the author. It was built, developed, and characterized by Arshad Harooni.

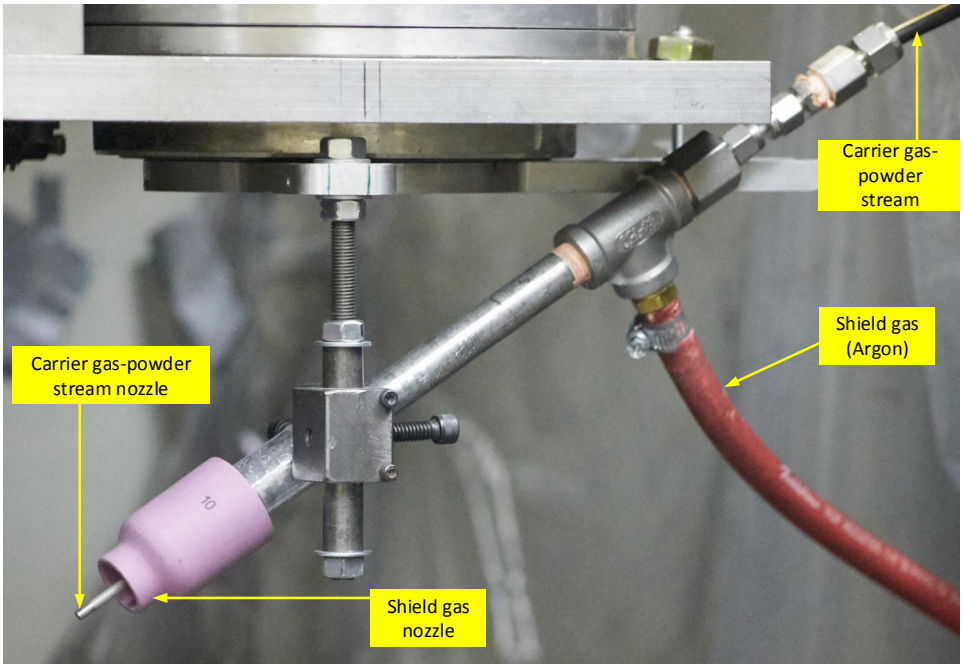

Figure 6.7: A picture of the developed lateral nozzle

The conducted experiments with the developed nozzle showed that burning diamond particles before reaching the molten pool was drastically reduced. Various experiments with different shield gas flow rates were conducted. The results revealed that minimum graphitization produced with the 70 CFH (32.9 L/min) flow rate. In fact, the result of deposition with 70 CFH (32.9 L/min) flow rate barely showed any visible graphitization . EDS analysis on the deposited diamond particles and the diamond-matrix interfacial layer showed considerably lower concentration of oxygen. It should be noted that the shield gas not only protects the diamond particles in the powder stream from interaction with oxygen, but also it protects the melt pool to some extent before solidification which prevents oxidization of the surface of the deposit.

6.3 Deposition of an Intermediate Layer

In Chapter 4 and 5, it was shown that iron has a detrimental effect on diamond. As a result, it is necessary to avoid contacts between iron and diamond particles as much as possible. However, the penetration of iron from the substrate into the deposit is inevitable since in order to have strong bonding between the substrate and the deposit a narrow layer of the substrate should be melted which in turn results in dilution of the deposited matrix by iron. It was shown that even when the melting of the substrate is very limited iron penetrates to the upper part of the deposited clad (See Figure 4.28).

In order to address this problem, a single layer of copper-tin (Cu-20Sn) was first deposited on the substrate. The thickness of the deposited layer was around 0.5 mm. This layer was deposited by the power and the scanning speed of 400 W and 6.66 mm/s, respectively. The overlap between deposited clads was 60 percent. The advantages of deposition of an intermediate layer are twofold, it decreases the amount of dilution of iron drastically,

Table 6.4: Process parameters for a selected set of experiments on substrates with intermediate layer

Clad No.	Power (W)	Scan speed (mm/s)	Powder feed rate (g/min)	Beam diameter (mm)	Carrier gas flow rate (dL/min)
1	400	3.33	4.9	1.5	3
2	400	6.66	4.9	1.5	3
3	400	10	4.9	1.5	3
4	400	13.33	4.9	1.5	3
5	400	16.66	4.9	1.5	3
6	400	20	4.9	1.5	3
7	400	23.33	4.9	1.5	3
8	200	3.33	4.9	1.5	3
9	200	6.66	4.9	1.5	3
10	200	10	4.9	1.5	3
11	200	13.33	4.9	1.5	3
12	200	16.66	4.9	1.5	3
13	200	20	4.9	1.5	3
14	200	23.33	4.9	1.5	3

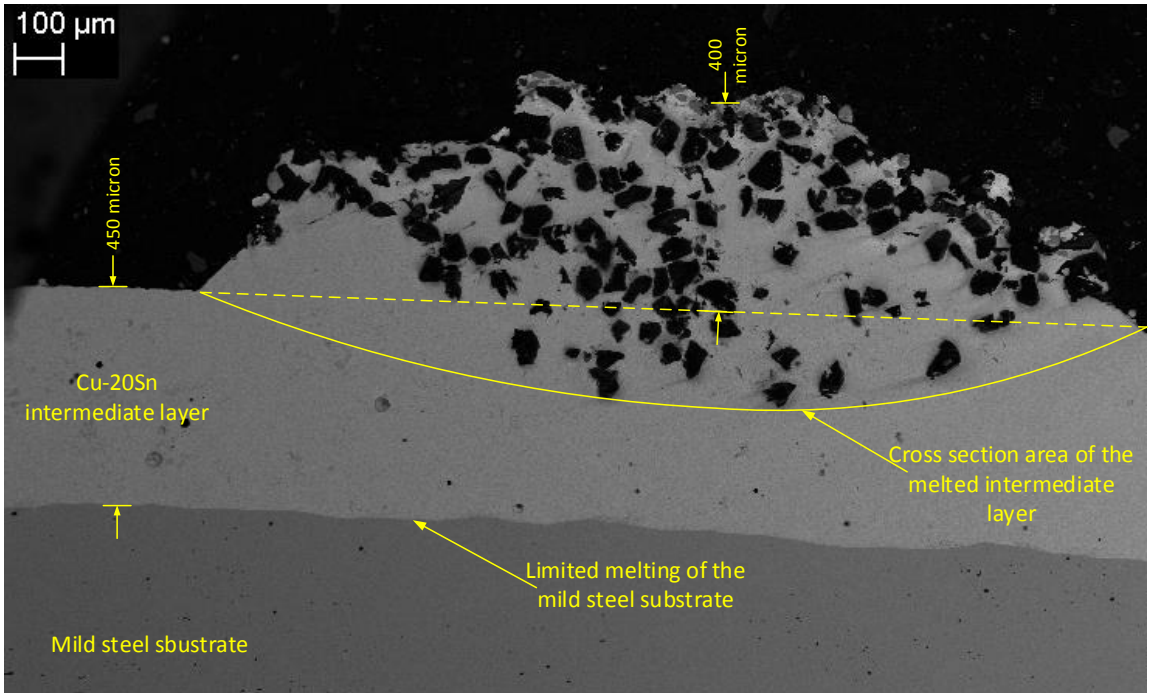

Figure 6.8: A back-scattered electron image of a cross section of clad number 11 in Table 6.4

and it reduces the maximum temperature required for melting the substrate, since by deposition of an intermediate layer of Cu-20Sn, the melting point of substrate decreases from around 1500°C of mild steel to around 900°C of copper-tin (see copper tin phase diagram in Figure B.1).

The surface of the intermediate layer was flattened grinding and then it was sand blasted to increase the absorptivity. Table 6.4 presents the process parameters for one set of the conducted experiments on substrates with intermediate layer. In this set of experiments, laser power and scanning speed were varied whereas powder feed rate, laser beam diameter on the substrate, and carrier gas flow rate were kept constant as 4.9 g/min, 1.5 mm, and 3 dL/min, respectively.

Figure 6.8 displays a back-scattered electron image of a cross section of clad number 11 in Table 6.4 which was deposited by low power of 200W and high scanning speed of 13.33 mm/s. The deposition has a solid metallurgical bonding to the substrate without presence of any porosity of micro-cracks. The examination of deposited diamond particles by Raman spectroscopy showed practically no graphitization. Study of diamond-matrix interfacial layer in the deposit revealed that the Ti-rich layer is markedly thinner as opposed to depositions on substrates without intermediate layer.

Figure 6.9 shows a back-scattered electron image of diamond-matrix interface of the clad number 11 in Table 6.4. The interfacial Ti-rich layer varies from 155 nm to 316 nm which is an optimum range. The clad height is around 400 micron while clad width is around 2 mm, which makes the aspect ratio around 5. As a result of the above-mentioned characteristics, this deposit can be considered as a successful deposit. The only problem that this deposition has is melting of relatively high volume of intermediate layer during the clad deposition which results in high dilution. However since the matrix and the intermediate layer both are composed of copper and tin, this does not have a detrimental effect on the deposit. Decreasing dilution will be discussed in Section 6.7.

6.4 Preheating the Substrate

Steen et al [88] and Gedda et al [89] showed that pre-heating the substrate decreases the effective energy input required for deposition (see Equation 6.19). This indicates that the same deposition can be conducted with the lower power or higher scanning speed which results in a better deposition (lower graphitization, thinner interfacial layer, etc). Therefore, the substrate both with and without intermediate layer were pre-heated to 700°C. Table 6.5 and Table 6.6 present the process parameters for one set of the conducted

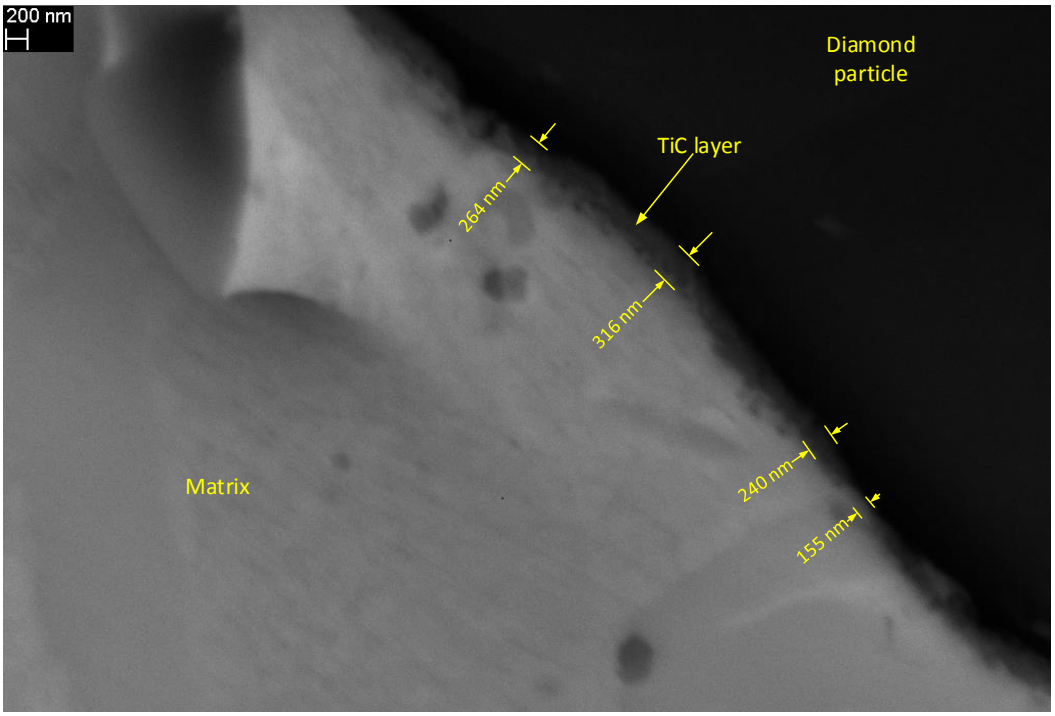

Figure 6.9: A back-scattered electron image of diamond-matrix interface of the clad number 11 in Table 6.4

Table 6.5: Process parameters for a selected set of experiments on pre-heated substrates with intermediate layer

Clad No.	Power (W)	Scan speed (mm/s)	Powder feed rate (g/min)	Beam diameter (mm)	Carrier gas flow rate (dL/min)
1	300	3.33	4.9	1.5	3
2	300	6.66	4.9	1.5	3
3	300	10	4.9	1.5	3
4	300	13.33	4.9	1.5	3
5	300	16.66	4.9	1.5	3
6	300	20	4.9	1.5	3
7	300	23.33	4.9	1.5	3
8	170	3.33	4.9	1.5	3
9	170	6.66	4.9	1.5	3
10	170	10	4.9	1.5	3
11	170	13.33	4.9	1.5	3
12	170	16.66	4.9	1.5	3
13	170	20	4.9	1.5	3
14	170	23.33	4.9	1.5	3

experiments on substrates with intermediate layers and on substrates without intermediate layers, respectively. All of the depositions on substrates with intermediate layers presented in Table 6.5 were successful depositions. Comparing clad number 11 in Table 6.5 with clad number 11 in Table 6.4 showed that these two clads were similar, while the clad with pre-heated substrate had 15 percent less effective energy input. The same trend was observed for the deposition on substrates without intermediate layer, however in this case the preheated samples had 16.7 to 17.5 percent less effective energy input.

Table 6.6: Process parameters for a selected set of experiments on pre-heated substrates without intermediate layer

Clad No.	Power (W)	Scan speed (mm/s)	Powder feed rate (g/min)	Beam diameter (mm)	Carrier gas flow rate (dL/min)
1	330	3.33	4.9	1.5	3
2	330	6.66	4.9	1.5	3
3	330	10	4.9	1.5	3
4	330	13.33	4.9	1.5	3
5	330	16.66	4.9	1.5	3
6	330	20	4.9	1.5	3
7	330	23.33	4.9	1.5	3
8	250	3.33	4.9	1.5	3
9	250	6.66	4.9	1.5	3
10	250	10	4.9	1.5	3
11	250	13.33	4.9	1.5	3
12	250	16.66	4.9	1.5	3
13	250	20	4.9	1.5	3
14	250	23.33	4.9	1.5	3

6.5 Diamond Distribution

Particles inside the melt pool are exposed to three forces, gravitational forces, buoyancy forces, and surface tension gradient forces. Oreper et al. [90] developed a two dimensional model considering different types of forces inside the melt pool . It was concluded that the convection flow forces are the dominant forces inside the melt pool for most of the cases. For laser cladding in which the power intensity is of the order of 10^5 to 10^6 W/cm^2 and interaction time is of the order of 10^{-2} second the dominant forces are convection flow forces driven by surface tension owing to the high temperature gradient inside the melt pool [91]. Chan et al. [32] developed a two dimensional transient model for study of convection flow inside a plane perpendicular to the scanning speed (cross section of a deposited clad). It was assumed that the surface tension is linearly dependent on the high temperature gradient. The model showed that the recirculation velocity near the surface of the melt pool is one to two order of magnitude higher than the scanning velocity. Other research efforts were in agreement with this result and showed that a particle is re-circulated several times inside the melt pool before solidification [91].

On the other hand, these works revealed that the temperature gradient which is proportional to the cooling rate was non-uniform inside the melt pool. Indeed, the cooling rate is maximum at the center of the melt pool and it decreases towards the edges of melt pool where it is minimum. It is also maximum at the surface of the clad while it decreases towards the substrate where it has its minimum value. As a result, the microstructure is the finest at the center and the surface of the clad while it is the coarsest at the bottom and the edges. All the above mentioned studies consider only one material or some alloying elements which are in liquid state inside the melt pool. These materials are properly combined due to re-circulation by convection flow. However, the case for metal matrix

composite is different since there are some solid particles inside the melt pool. On the other hand, the percentage of penetration of substrate materials into the clad is not uniform inside the cross section of clad; in fact at the bottom of the clad is the maximum and it substantially decreases toward the surface of clad. This phenomenon is not in agreement with the aforementioned studies where they predicted that a particle is re-circulated several times inside the melt pool before solidification which should result in uniform penetration of the substrate materials throughout the entire cross section of the clad.

The buoyancy force can be written as

$$B = -\rho_f g V \tag{6.7}$$

where, B is the buoyancy force, ρ_f is density of the liquid, g is standard gravity, and V is the volume of the object.

The difference between particle weight and the buoyancy force can be written as

$$f_{net} = \rho g V - \rho_f g V = (\rho - \rho_f)\, g V \tag{6.8}$$

where f_{net} is the net buoyancy force acting on the particle due to weight and buoyancy force and ρ is density of particle. Therefore, the net force will be an upward force when the particle density is lower than the fluid density.

Diamond density is around 3.5–3.53 g/cm^3 while liquid density at melting point of copper, tin, titanium, and iron is 8.02 g/cm^3, 6.99 g/cm^3, 4.11 g/cm^3, and 6.98 g/cm^3, respectively. As a result, diamond has a lower density compared to density of the liquid melt pool. Therefore, the net buoyancy force drives the diamond particles and titanium to the surface of the clad.

The fact that with increasing scanning speed, distribution of diamond particles is improved and titanium segregation at the surface of clad decreases can be justified as follows. When laser interacts with the melt pool, the dominant forces are the convection flow forces; however when the laser moves forward, the convection flow forces are diminished and at some point the buoyancy forces which are nearly constant during the process become dominant. On the other hand, the viscosity of the melt pool increases due to decreasing temperature. For the diamond particles, the net buoyancy forces are not strong enough to defeat the resistant force due to increasing viscosity. However, some titanium particles in liquid or solid state are small enough to diffuse through the melt pool and segregate at the surface of the melt pool.

Increasing scanning speed enlarges the cooling rate, as a result, the buoyancy forces do not have enough time to drive the diamond particles and titanium to the surface of the clad. Therefore the diamond distribution enhances and titanium segregation at the surface disappears.

As one can notice from Equation (6.8) the net buoyancy force is proportional to the particle volume. Consequently, smaller diamond particles have better distribution. On the other hand for larger diamond particles higher cooling rate is needed in order to obtain uniform distribution.

6.6 Volume Fraction of Deposited Diamond Particles

Needless to mention, adding more diamond particles to the matrix increases the abrasive resistance, however the question is what volume fraction of diamond particles results in a maximum of abrasive resistance. Literature indicates that the abrasive resistance depends on many factors such as shape and size of hard phase particles, ductility of matrix [8].

Assuming other factors are kept constant and considering only the effect of volume fraction of diamond particles, literature denotes that the peak of wear resistance occurs at around 30 percent of the hard face volume fraction [92, 8]. When the volume fraction of hard phase surpasses this amount, a network of the brittle hard phase establishes which accelerate the crack propagation in the structure which reduces the wear resistance [8]. Weight percentage of the diamond particle corresponding to the volume fraction of diamond can be readily calculated by

$$f_{m_{\text{dia}}} = \frac{m_{\text{dia}}}{m_{\text{tot}}} = \frac{\rho_{\text{dia}}}{\rho_{\text{tot}}} \times \frac{V_{\text{dia}}}{V_{\text{tot}}} = \frac{\rho_{\text{dia}}}{\rho_{\text{tot}}} \times f_{V_{\text{dia}}} \tag{6.9}$$

where, $f_{m_{\text{dia}}}$ is mass fraction of diamond, m_{dia} is mass of diamond particles, m_{tot} is total mass of diamond particles and the matrix, ρ_{dia} is density of diamond, ρ_{tot} is density of mixture of diamond particles and the matrix, V_{dia} is volume of diamond particles, V_{tot} is the total volume of diamond particles and the matrix, $f_{V_{\text{dia}}}$ is volume fraction of diamond particle in the mixture. ρ_{tot} can be calculated by

$$\rho_{\text{tot}} = \frac{m_{\text{tot}}}{V_{\text{tot}}} = \frac{m_{\text{matrix}} + m_{\text{dia}}}{V_{\text{tot}}} = \rho_{\text{matrix}} \frac{V_{\text{matrix}}}{V_{\text{tot}}} + \rho_{\text{dia}} \frac{V_{\text{dia}}}{V_{\text{tot}}} \tag{6.10}$$

therefore

$$\rho_{\text{tot}} = \rho_{\text{matrix}} \left(1 - f_{V_{\text{dia}}}\right) + \rho_{\text{dia}} f_{V_{\text{dia}}} = \rho_{\text{matrix}} + \left(\rho_{\text{dia}} - \rho_{\text{matrix}}\right) f_{V_{\text{dia}}} \tag{6.11}$$

plugging Equation 6.11 in Equation 6.9 results in

$$f_{m_{\text{dia}}} = \frac{\rho_{\text{dia}}}{\rho_{\text{matrix}} + \left(\rho_{\text{dia}} - \rho_{\text{matrix}}\right) f_{V_{\text{dia}}}} f_{V_{\text{dia}}} \tag{6.12}$$

as a result, the mass fraction can simply calculated based on the volume fraction. Therefore, by Equation 6.12 using density values in Table 6.7 weight percentage of diamond particles

Table 6.7: Density of MMC, matrix, diamond, and constituents of the matrix

	Copper	Tin	Titanium	Matrix	Diamond	MMC
Density ($g.cm^{-3}$)	8.94	7.365	4.506	7.86	3.5	6.552

corresponding the 30 percent volume fraction was calculated as 16 percent. Therefore, 16 weight percent diamond should be mixed with the matrix as the optimum diamond weight percentage.

On the other hand, the volume percentage of diamond particles inside the deposit can be determined by calculating the area fraction of diamond particles in the cross section of the deposit. The area fraction can be converted to volume fraction by

$$\frac{V_{\text{dia}}}{V_{\text{tot}}} = \left(\frac{A_{\text{dia}}}{A_{\text{tot}}}\right)^{3/2} \tag{6.13}$$

Performing image processing to calculate the fraction area of diamond particles reveals that area fraction of diamond particles in the deposit is around 36 to 41 percent. For example the fraction area of diamond in Figure 6.13 is around 41 percent. The area fraction of 36 to 41 results in volume fraction of 21.6 to 26.3 percent. Using Equation 6.12 the weight percentage of diamond particles in the deposit becomes 10.9 to 13.7 percent. However, this value is around half the 25 weight percent diamond in the precursor powder mixture used for the deposition, which results in arising the question why the diamond weight fraction in the powder and the deposit are considerably different. The reason for this drastic difference could lie in the fact that density of diamond particles is considerably lower than the density of the rest of powder constituents of MMC powder while particle size of diamond is not significantly different from others. This could lead to a decrease in the fraction of diamond particles that join the melt pool as opposed to the fractions of other particles that join

the melt pool. As a result, in this study 25 weight percent of diamond powder were mixed with the matrix powder instead of the calculated value of 16 percent to obtain a volume fraction of around 25 percent in the deposit.

6.7 Effect of Process Parameters on Dilution and Aspect Ratio

Cross section of the deposited clad is an important factor when it comes to depositing clads beside each other to make a layer of deposit. Figure 6.10 shows a schematic view of a clad cross section. In order to deposit clads next to each other without creating porosity in between, angle α should be acute [63]. α relates to the aspect ratio of clad which is defined as

$$\mathrm{k} = \frac{\mathrm{w}}{\mathrm{h}} \tag{6.14}$$

where, k is the aspect ratio, w is the width of clad, and h is the height of clad (see Figure 6.10). Steen et al [88, 63] analyzed the aspect ratio for deposition of Colmonoy® Wallex® PC6 (Stellite® 6) and found that in order to have a deposit without interrun porosity the aspect ratio should be greater than 5. They realized that the aspect ratio of the deposit relates to the term

$$\frac{(P - sP)\, a_\alpha V D}{\dot{m}^2} \tag{6.15}$$

where, P is laser output power, s is attenuation coefficient due to reflection and scattering of laser power by powder cloud, a_α is the absorptivity coefficient, D is laser beam diameter on the substrate, V is scanning velocity, and $\dot{m}$ is powder feed rate.

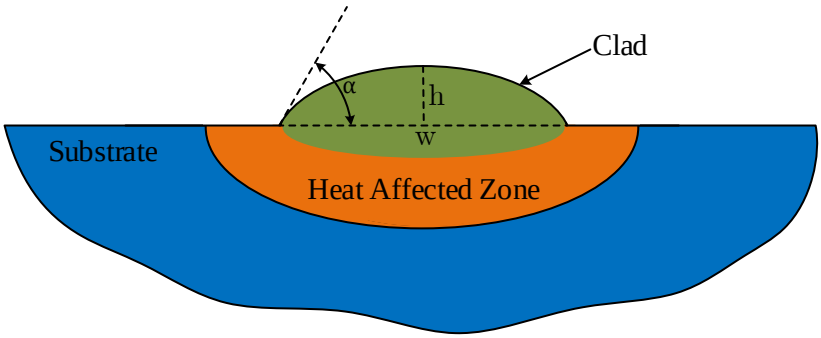

Figure 6.10: A schematic view of cross section of a deposited clad

The temperature at the top of the substrate should reach a high enough value to melt the surface of the substrate or to cause the powder to attach to the substrate and melt on it [88]. This temperature is related to the energy input to unit area of the process zone. Therefore the minimum energy required to deposit a continuous clad was defined by [88, 63]

$$E_{\min} = \frac{(P - sP)\, a_{\alpha}}{DV} \tag{6.16}$$

where, $E_{\min}$ is the minimum energy required to deposit a continuous clad on a substrate, For example this term for deposition of Colmonoy®alloy is 22 J/mm^2 [63], and for deposition of 316 stainless steel on mild steel is 10 J/mm^2 [88] which means there would be no bonding clad regardless of powder feed rate when the value of this term becomes less than the aforementioned values.

When a clad by blown powder deposition is developed, there is usually fusion bonding between substrate and the clad. However, in order to achieve a clad with minimum dilution, without porosity, process window should be determined which means that powder feed rate, laser power, scanning speed should be in a defined range.

Dilution is defined as volume of melted substrate divided by volume of the entire melt

[88]. This can be written as [93]

$$\text{Dilution} = \frac{\text{cross section area of the melted substrate}}{\text{cross section area of the melted substrate+cross section area of the deposit}} \tag{6.17}$$

The leading contribution to dilution originates from melting the substrate near the leading edge of the melt pool [88]. Therefore, existence of extra energy in this region increases the dilution level [88]. Furthermore, at low scanning speeds, remelting of the of the solidified layer at the back of melt pool can cause some dilution, however this does not contribute to a considerable dilution level [88]. Steen et al [88] by using energy balance found that in order to avoid dilution the following equation should be satisfied

$$\frac{(P - sP)\, a_\alpha}{\dot{m} D} \leq b \tag{6.18}$$

where, b is a constant and it should be determined by experiments for each material. For example for Colmonoy® Wallex® PC6, b was determined as 2500 J/gmm [88].

As it was mentioned above, the energy input into the unit area per unit time plays an important role in the characteristics of the deposit and it is called effective energy input [27]. It is defined as [27]

$$E_{\text{eff}} = \frac{P}{DV} \tag{6.19}$$

where, E_{eff} [J/mm^2] is the power density as energy input into the unit area of process zone per unit time. Comparing Equation 6.16 and 6.19, one can notice that s, attenuation coefficient due to reflection and scattering of laser power by powder cloud, and a_α, the absorptivity coefficient, were not considered in Equation 6.19. This is because finding s is a difficult task, and a_α is a property of the materials in the process zone and is nearly constant. The other important term is the mass input into the unit area of process zone

per unit time which is called powder deposition density [27]. It is written as [27]

$$\dot{m}_{\text{den}} = \frac{\dot{m}}{DV} \tag{6.20}$$

As it was mentioned before, the aspect ratio k = w/h should be greater than a certain value to avoid interrun porosity. The aspect ratio versus effective energy for each value of $1/\dot{m}_{\text{den}}$ for the depositions presented in Table 4.7 and Table A.1 was plotted which can be seen in Figure 6.11. By looking at the figure, one can notice that when $1/\dot{m}_{\text{den}}$ is constant, aspect ratio increases almost linearly with increasing E_{eff}. For simpilicity's sake let Ψ denote $1/\dot{m}_{\text{den}}$

$$\Psi = \frac{1}{\dot{m}_{\text{den}}} \tag{6.21}$$

A fitted linear regression for each value of Ψ is shown in Figure 6.11. It can be seen that by increasing Ψ the slope of each line increases. As a result, k can be considered as

$$\text{k} = \frac{\text{w}}{\text{h}} = aE_{\text{eff}} + b \tag{6.22}$$

where a and b are functions of Ψ. Considering a and b as quadratic functions of Ψ, k can be expressed by an equation as

$$\text{k} = \frac{\text{w}}{\text{h}} = \left(a_1\Psi^2 + a_2\Psi + a_3\right) E_{\text{eff}} + b_1\Psi^2 + b_2\Psi + b_3 \tag{6.23}$$

where a_1, a_2, a_3, b_1, b_2, and b_3 are constant. These constants were determined by using Least Square Method (LSM) by Matlab 2013b. The calculated constants are presented in Table 6.8. Equation 6.23 can be rearranged to

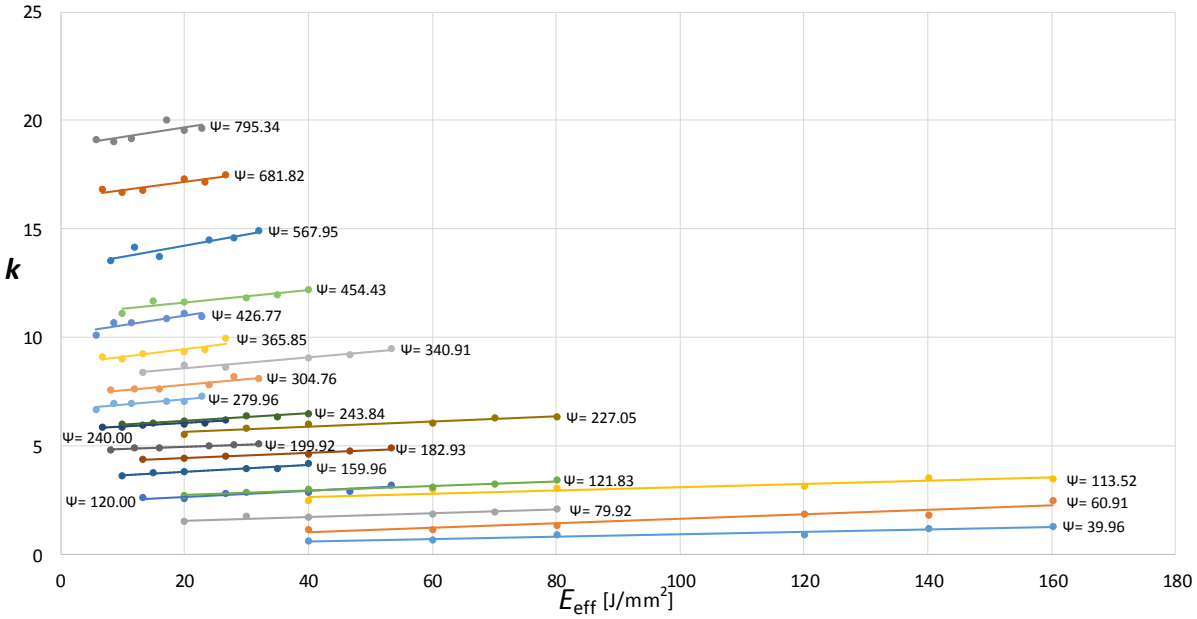

Figure 6.11: Aspect ratio versus E_{eff} for different values of Ψ of deposited clads in Table 4.7 and Table A.1

Table 6.8: Values of the constants in Equation 6.23 and 6.24

	a_1	a_2	a_3	b_1	b_2	b_3
Value	2.757e-08	2.69e-05	0.004926	-5.553e-06	0.02896	-0.867

$$\mathrm{k} = \frac{\mathrm{w}}{\mathrm{h}} = (a_1 E_{\text{eff}} + b_1)\,\Psi^2 + (a_2 E_{\text{eff}} + b_2)\,\Psi + (a_3 E_{\text{eff}} + b_3) \tag{6.24}$$

As a result, an equation for aspect ratio based on the experimental data was determined. It should be noted that this equation is only valid for deposition of the MMC in this study on mild steel, however, this procedure can be used for deposition of any material on any substrate to find an equation for the aspect ratio.

The minimum required effective energy, E_{min} (see Equations 6.16 and 6.19), was determined as $11\,{}^{\text{J}}/_{\text{mm}^2}$ by experimental analysis which means

$$E_{\text{eff}} = \frac{P}{DV} \geq 11\,{}^{\text{J}}/_{\text{mm}^2} \tag{6.25}$$

It was also found that in order to minimize the dilution the following should be satisfied (see Equation 6.18)

$$\frac{P}{\dot{m}D} \leq 2100\,{}^{\text{J}}/_{\text{gmm}} \tag{6.26}$$

As a result, by considering Equations 6.26, 6.25, and 6.24 for the case of the deposition of the MMC on the mild steel substrate in order to have a deposition with minimum dilution, acceptable aspect ratio, and strong clad-substrate bonding the following should be satisfied

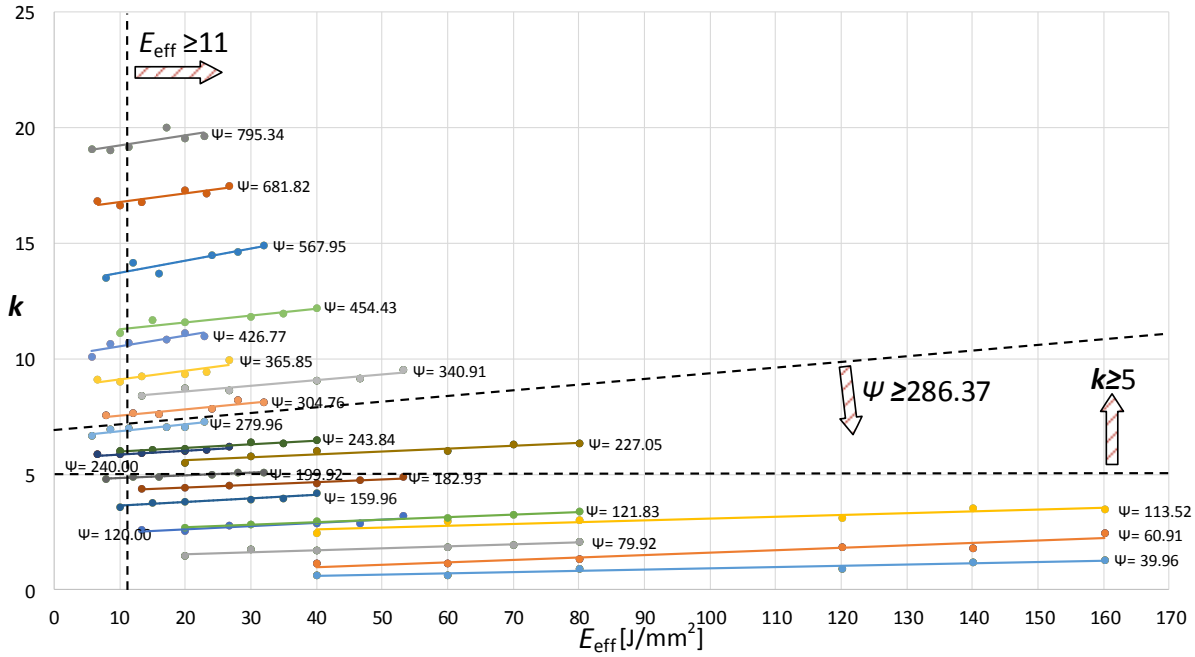

Figure 6.12: Visaul presentation of Equation 6.27

$$\begin{cases} \mathrm{k} = (a_1 E_{\text{eff}} + b_1)\,\Psi^2 + (a_2 E_{\text{eff}} + b_2)\,\Psi + (a_3 E_{\text{eff}} + b_3) \geqslant 5 & \text{Aspect Ratio} \\ E_{\text{eff}} = \dfrac{P}{DV} \geq 11\ {}^{\text{J}}/_{\text{mm}^2} & \text{Clad-Bonding} \\ \dfrac{P}{\dot{m}D} \leq 2100\ {}^{\text{J}}/_{\text{gmm}} & \text{Dilution} \end{cases} \tag{6.27}$$

Visual presentation of these sets of equations was shown in Figure 6.12. The first and sencond terms are clear in the figure. The third term can be written as

$$\frac{P}{\dot{m}D} = \frac{P}{DV} \times \frac{DV}{\dot{m}} \times \frac{1}{D} = E_{\text{eff}} \times \frac{1}{\dot{m}_{\text{den}}} \times \frac{1}{D} \leq 2100\ {}^{\text{J}}/_{\text{gmm}} \tag{6.28}$$

considering D, the beam diameter, as 1.5 mm (beam diameter was constant during the course of experiments), and considering E_{eff} as $11\,^{\text{J}}/_{\text{mm}^2}$, the minium value to get an acceptable clad-substrate bonding results in

$$\Psi = \frac{1}{\dot{m}_{\text{den}}} \leq 286.37$$

which was shown in Figure 6.12. As it can seen, only around 25 depositions meet the criteria by Equation 6.27. Among these depositions those which are closer to intersection of the line $E_{\text{eff}} \geq 11\,^{\text{J}}/_{\text{mm}^2}$ and k $\geqslant 5$ are the optimum depositions.

6.8 Prime Deposition

By applying the discussions in this chapter, successful clads were deposited. As mentioned in Section 6.3, clad number 11 in Table 6.4 has all the features of a successful deposition including, no diamond graphitization, optimum thickness of diamond-matrix interfacial layer, relatively uniform diamond distributions, and aspect ratio of 5. The only problem of that deposition is relatively high amount of dilution which is not have any detrimental effect on the deposit since the intermediate layer and the deposit are both copper based materials. Figure 6.13 shows the deposit which was obtained by using the analysis of Section 6.7 ($\Psi = 199.2$ and $E_{\text{eff}} = 12\,^{\text{J}}/_{\text{mm}^2}$) and using the analysis of Section 6.1.4. A substrate without intermediate layer was selected for the reason that dilution to be differentiated from the deposit. As it can be seen in figure, the dilution is very limited, diamond particles volume fraction in the deposit is 26.3 percent, diamond particles distribution in the deposit is uniform, aspect ratio is 5 (clad height is 0.5 mm and clad width is 2.6 mm), clad-substrate bonding is solid without presence of any porosity or micro-crack.

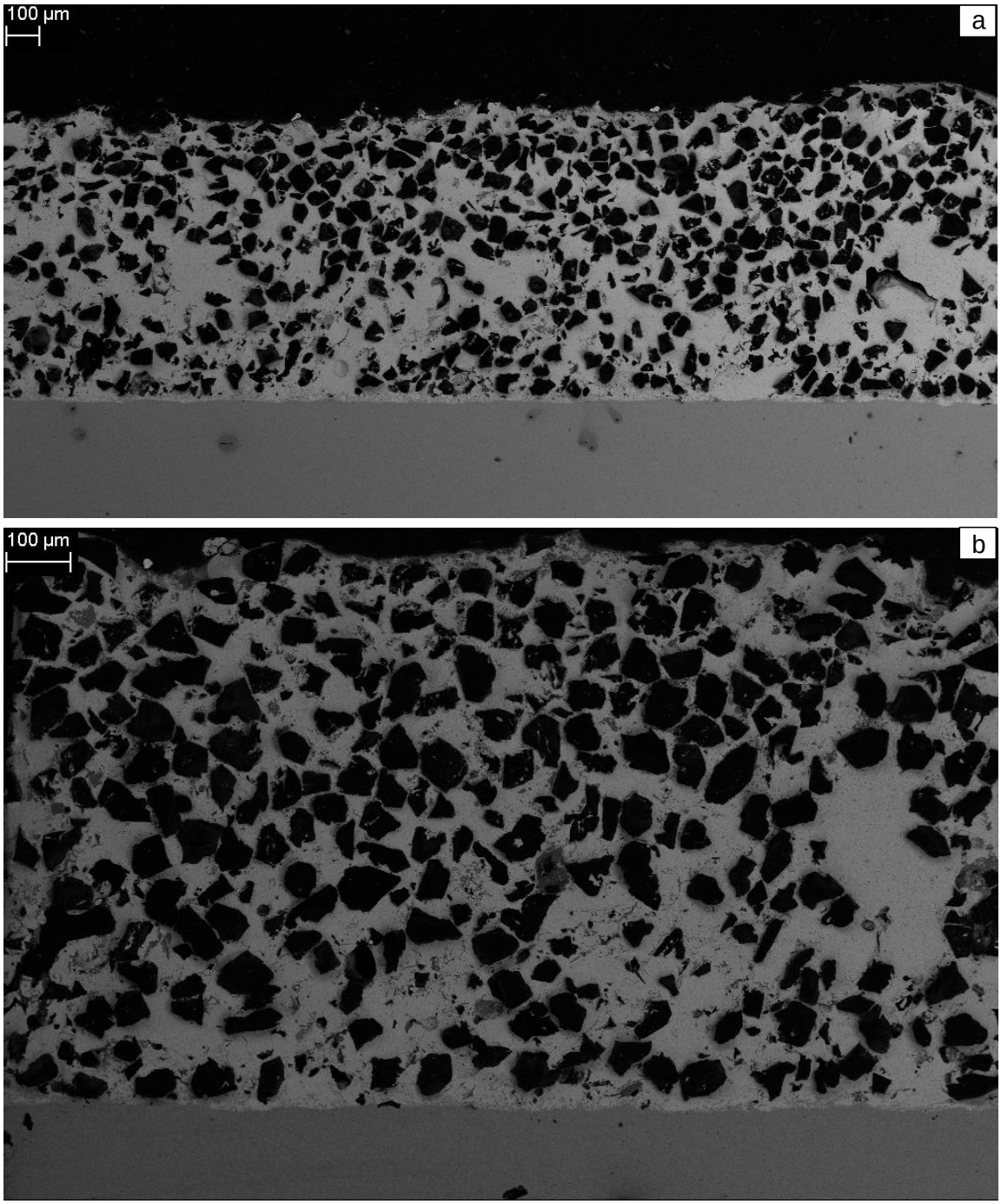

Figure 6.13: A prime deposit by applying the discussion in this study

Chapter 7

Conclusions and Recommendations

In this chapter, summary, conclusions, and contributions of this study are briefly discussed and recommendations for future work are presented.

7.1 Conclusions and Contributions

In this study the process of laser direct deposition of metal matrix diamond composite was investigated and analyzed in detail. The associated challenges and obstacles not only were identified, but also they were addressed. Conclusions and contributions of this study can be summarized as follows:

- It was found that the maximum temperature and exposure time of diamond particles to high temperatures should be kept minimum. A numerical thermal model was developed to find the relationship between the process parameters and outcomes. The developed thermal model facilitated finding the process window for a deposition with minimum necessary temperature along with highest possible cooling rate.

- Graphitization of deposited diamond particles was characterized by Raman spectroscopy and SEM (SEM was only used where the degree of graphitization was very high). The degree of graphitization of deposited diamond particles was characterized by Raman spectroscopy by detecting changes in the Raman spectrum.

- The experiments revealed that the highest cooling rate paired with the required power resulted in a minimum diamond graphitization. As a result, the process window for decreasing the diamond graphitization was detected by experimental analysis.

- Experimental analysis using SEM, EDX, and nano-indentation showed that TiC layer growth is initiated around the deposited diamond particles. Measurement of TiC layer thickness by back scattered SEM showed that a strong correlation exists between, melt pool temperature, high temperature exposure time, and cooling rate and the thickness of the TiC layer, indicating that a higher cooling rate results in a thinner TiC layer whereas a higher temperature or greater exposure time to high temperature causes a thicker TiC layer.

- It was detected that laser-diamond interaction before diamond particles reached the molten pool played a critical role in the process. It was found that the diamond particles could reach high temperatures before joining the melt pool. It was shown that carrying the powder particles by an inert gas (argon) did not fully protected diamond particles from oxygen attack. As it was mentioned the Chapter 2, diamond graphitization could initiate as low as 250°C in presence of pure oxygen and accelerates at 600°C. In fact this is not decomposition of diamond to graphite, it is instead burning of diamond particles. Analytical analysis showed that temperature of diamond particles can go well above 600°C before reaching the melt pool.

- The laser beam-powder stream configuration was studied. Effect of parameters such

as, diamond particle size, mass flow rate, laser beam diameter, angle of lateral nozzle, distance between nozzle and process zone, carrier gas flow rate, velocity of powder particles, and offset distance between center of laser beam and center of powder stream was studied and optimized to obtain minimum temperature increase in diamond particles before reaching the melt pool.

- A new lateral nozzle was designed to protect diamond particles from interaction with oxygen. In the new nozzle the powder-carrier gas stream was surrounded by a flow of a shielding gas (argon) protecting the powder stream and process zone from interaction with oxygen. The conducted experiments with the developed nozzle showed that burning of the diamond particles prior to their arrival at the molten pool was drastically reduced.

- It was found that the diamond particles which interacted with the penetrated iron from the substrate, showed a drastically higher degree of decomposition as opposed to those that were not in the vicinity of iron. In the presence of iron, diamond particles are surrounded by two layers. The primary layer is an iron rich layer and second is a titanium rich layer surrounding the iron rich layer. This indicates that in the presence of iron and titanium, iron has a greater affinity to react with diamond.

- The DSC experiments revealed that mechanism of reaction between titanium and diamond is completely different from that of iron and diamond. In respect of titanium-diamond, it was found that the reaction starts with transformation of α-Ti $\rightarrow$ β-Ti at 880-900°C. It was also found that a layer of TiC is formed around diamond particles by diffusing titanium into the surface of diamond particles which results in nucleation of TiC on the diamond surface. As this layer grows, the diffusion of titanium into the surface of diamond becomes more difficult, thus the growth of the TiC layer

slows down until stops completely at a certain thickness. This TiC layer acts as a passive protection for diamond particles. The diamond particle does not experience any decomposition while surrounded by a TiC layer with a thickness of less than 2 micron. On the other hand, it was revealed that no melting of titanium particles occurs whereas some solid sintering of Ti particles happens. It was also revealed that when the TiC layer reaches its maximum thickness, the interfacial bonding between the TiC layer and the diamond particles becomes very weak and brittle in a way that it can be detached from the diamond particle.

- It was found that the reaction between iron and diamond starts before transformation of ferrite to austenite begins (below 900°C). Carbon atoms start detaching from their network in diamond, and diffuse into iron particles. This causes the iron-carbon solution to melt at temperatures around 1150°C. The melting causes higher levels of diamond decomposition and higher solution of carbon in iron. Although the solubility of carbon in iron is limited, detaching of carbon atoms from diamond continues past the solubility limit, resulting in super saturation of iron matrix and presence of large graphite inclusions in the iron matrix. On the other hand, iron diffuses into the decomposed diamond particles accelerating the decomposition. This results in a significant carbon atoms detachment from the diamond particles. As a result, high fraction of the remaining carbon atoms decompose to graphite or react with the iron. In fact, not only does the iron react with the diamond, but it also acts as a catalyzer for diamond graphitization.

- Results of the DSC study are in complete agreement with the experiments showing that contact with iron has a highly detrimental effect on diamond particles and it should be prevented.

- The DSC experiments using mixtures of copper-diamond and tin-diamond showed that no wetting or chemical reaction occurred between any of these metals and the diamond particles although complete melting of copper and tin occurred in the two mixtures. The results of this study showed that the existence of titanium in the matrix is necessary.

- Experimental results and DSC analysis revealed that the presence of iron at the vicinity of diamond particles significantly degrades the deposition. Therefore, it is critical to prevent dilution from the substrate. Optimum process parameters which can minimize the dilution were determined by experimental analysis. Using these parameters, diamond degradation in the deposition was drastically reduced.

- While a minimum dilution level was acquired using the determined optimum parameters, it is important to note that dilution cannot reach a zero level, since a good substrate-deposition bonding requires a thin layer of the substrate to be melted. On the other hand, the process conditions changes during a long deposit due to accumulation of heat in the substrate which results in excessive energy at leading edge of the melt pool which in turn increases the dilution. To address this issue, an intermediate layer with the composition of Cu-20Sn weight percent with thickness of 0.5 mm was deposited on a mild steel substrate. This intermediate layer improved the deposition in several ways. Firstly, it caused that the presence of iron in the deposition became negligible. Secondly, the melting point of the substrate (which is the intermediate layer) drastically decreases from around 1500°C of mild steel to around 900°C for the copper-tin alloy. This reduces the required effective input energy for strong deposit-substrate bonding by 30-40 percent. This in turn decreases the maximum temperature of the molten pool and increases the cooling rate. These

two factors reduced the amount of the occurred graphitization to the point where graphitization level was near non-existent. The decrease in the maximum temperature of the melt pool and increase in cooling rate resulted in a decrease in the thickness of interfacial TiC layer to a range of 150-350 nm, which is considered as an optimum range. Moreover, the higher cooling rate resulted in a more uniform diamond particles distribution across the clad cross section.

- The substrates with and without the intermediate layer were pre-heated to 700°C prior to performing the deposition. The pre-heating decreased the required effective input energy by approximately 16.7 to 17.5 percent for the substrate without intermediate layer and 15 percent for the substrate with intermediate layer. The pre-heating had no effect on presence of iron in the deposition on the substrates with the intermediate layer, since without pre-heating, the presence of iron in the deposit was already negligible, however it reduced the dilution in the deposition on the substrates when no intermediate layer was present.

- Effects of process parameters on dilution, clad substrate bonding, and aspect ratio were studied. Using experimental analysis, an equation was developed to calculate the aspect ratio from the process parameters. Furthermore, for minimizing dilution, obtaining strong clad-substrate bonding, and obtaining acceptable aspect ratio a set of inequalities (constraints) to be satisfied by process parameters was determined. From these constraints the process window was obtained.

In summary, through theoretical and experimental studies, this research developed a practical and reliable metal matrix diamond composite fabrication technology using laser deposition technique. The new fabrication technology can be used in developing high performance tools and highly wear resistance surfaces.

7.2 Recommendations for Future Work

Based upon the described materials in this study the followings are recommended for a possible future work:

- In case of large scale depositions, the accumulated heat in the substrate increases the melt pool temperature and decreases the cooling rate. This is similar to pre-heating the substrate while not decreasing the effective input energy to the process which definitely results in the degradation of deposit as it was explained in this thesis. Therefore, measuring the melt pool temperature and cooling rate in real time and change the process parameters accordingly to maintain a constant melt pool temperature and cooling rate is inevitable. This procedure has been developed in ALFα lab by using a thermal camera and it has been verified for the deposition of stainless steel on mild steel substrate [94]. It is highly recommended that this closed loop feedback control system to be applied for the deposition of metal matrix diamond composite.

- Use of a powder feeder that is capable of heating the matrix separately and then mix it with diamond particles prior to sending the mixture to the nozzle is recommended. Similar to pre-heating the substrate, pre-heating the matrix decreases the required effective input energy into the process zone.

- Material characterization of the matrix and study of the influence of process parameters on the developed phases inside the matrix. As mentioned in Chapter 2, the matrix strength and the strength of clad-substrate bonding is of great importance. Mechanical and wear properties of the deposit are highly influenced by developed phases in the deposit. Therefore, the developed phases in the clad and the clad-

substrate bonding region should be identified and their effect on the properties of the deposit should be investigated. The effect of process parameters on the alterations of the developed phases can be studied and optimum parameters for obtaining the most advantageous combination of phases and suppression of intermetallic phases can be identified. Mechanical properties of the matrix such as ductility, toughness, and hardness can also be studied. Furthermore, wear properties of the matrix and the deposit as a whole should be studied.

APPENDICES

Appendix A

Process parameters of second and third sets of blown powder laser cladding experiments

Table A.1: Process parameters of second and third sets of blown powder laser cladding experiments

Clad Number	Power (W)	Scan speed (mm/s)	Powder feed rate (g/min)	Beam diameter (mm)	Carrier gas flow rate (dL/min)
43	200	3.33	0.125	1.5	3
44	200	6.66	0.125	1.5	3
45	200	10	0.125	1.5	3
46	200	13.33	0.125	1.5	3
47	200	16.66	0.125	1.5	3
48	200	20	0.125	1.5	3
49	200	23.33	0.125	1.5	3
50	300	3.33	0.125	1.5	3
51	300	6.66	0.125	1.5	3
52	300	10	0.125	1.5	3
53	300	13.33	0.125	1.5	3
54	300	16.66	0.125	1.5	3
55	300	20	0.125	1.5	3
56	300	23.33	0.125	1.5	3
57	400	3.33	0.125	1.5	3
58	400	6.66	0.125	1.5	3
59	400	10	0.125	1.5	3
60	400	13.33	0.125	1.5	3
61	400	16.66	0.125	1.5	3

62	400	20	0.125	1.5	3
63	400	23.33	0.125	1.5	3
64	600	3.33	0.125	1.5	3
65	600	6.66	0.125	1.5	3
66	600	10	0.125	1.5	3
67	600	13.33	0.125	1.5	3
68	600	16.66	0.125	1.5	3
69	600	20	0.125	1.5	3
70	600	23.33	0.125	1.5	3
71	700	3.33	0.125	1.5	3
72	700	6.66	0.125	1.5	3
73	700	10	0.125	1.5	3
74	700	13.33	0.125	1.5	3
75	700	16.66	0.125	1.5	3
76	700	20	0.125	1.5	3
77	700	23.33	0.125	1.5	3
78	800	3.33	0.125	1.5	3
79	800	6.66	0.125	1.5	3
80	800	10	0.125	1.5	3
81	800	13.33	0.125	1.5	3
82	800	16.66	0.125	1.5	3
83	800	20	0.125	1.5	3
84	800	23.33	0.125	1.5	3
85	200	3.33	0.044	1.5	3

86	200	6.66	0.044	1.5	3
87	200	10	0.044	1.5	3
88	200	13.33	0.044	1.5	3
89	200	16.66	0.044	1.5	3
90	200	20	0.044	1.5	3
91	200	23.33	0.044	1.5	3
92	300	3.33	0.044	1.5	3
93	300	6.66	0.044	1.5	3
94	300	10	0.044	1.5	3
95	300	13.33	0.044	1.5	3
96	300	16.66	0.044	1.5	3
97	300	20	0.044	1.5	3
98	300	23.33	0.044	1.5	3
99	400	3.33	0.044	1.5	3
100	400	6.66	0.044	1.5	3
101	400	10	0.044	1.5	3
102	400	13.33	0.044	1.5	3
103	400	16.66	0.044	1.5	3
104	400	20	0.044	1.5	3
105	400	23.33	0.044	1.5	3
106	600	3.33	0.044	1.5	3
107	600	6.66	0.044	1.5	3
108	600	10	0.044	1.5	3
109	600	13.33	0.044	1.5	3

110	600	16.66	0.044	1.5	3
111	600	20	0.044	1.5	3
112	600	23.33	0.044	1.5	3
113	700	3.33	0.044	1.5	3
114	700	6.66	0.044	1.5	3
115	700	10	0.044	1.5	3
116	700	13.33	0.044	1.5	3
117	700	16.66	0.044	1.5	3
118	700	20	0.044	1.5	3
119	700	23.33	0.044	1.5	3
120	800	3.33	0.044	1.5	3
121	800	6.66	0.044	1.5	3
122	800	10	0.044	1.5	3
123	800	13.33	0.044	1.5	3
124	800	16.66	0.044	1.5	3
125	800	20	0.044	1.5	3
126	800	23.33	0.044	1.5	3

Appendix B

Binary Phase Diagrams of Matrix and Substrate Constituents

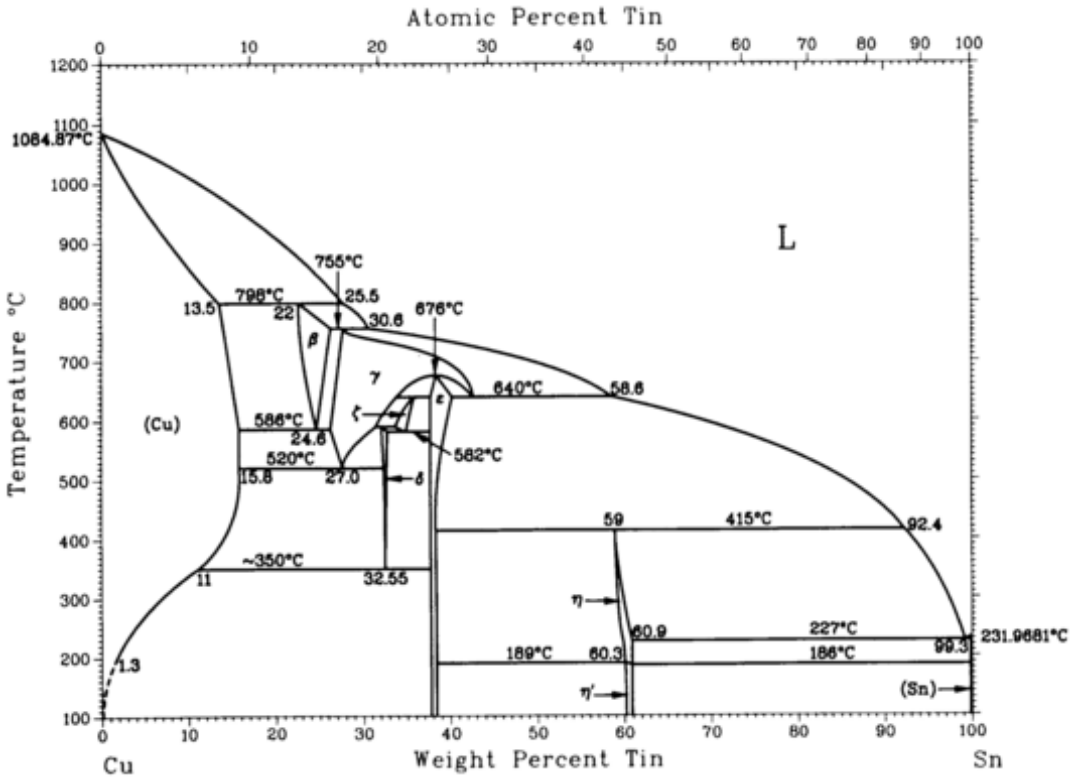

Figure B.1: Copper Tin phase diagram [9]

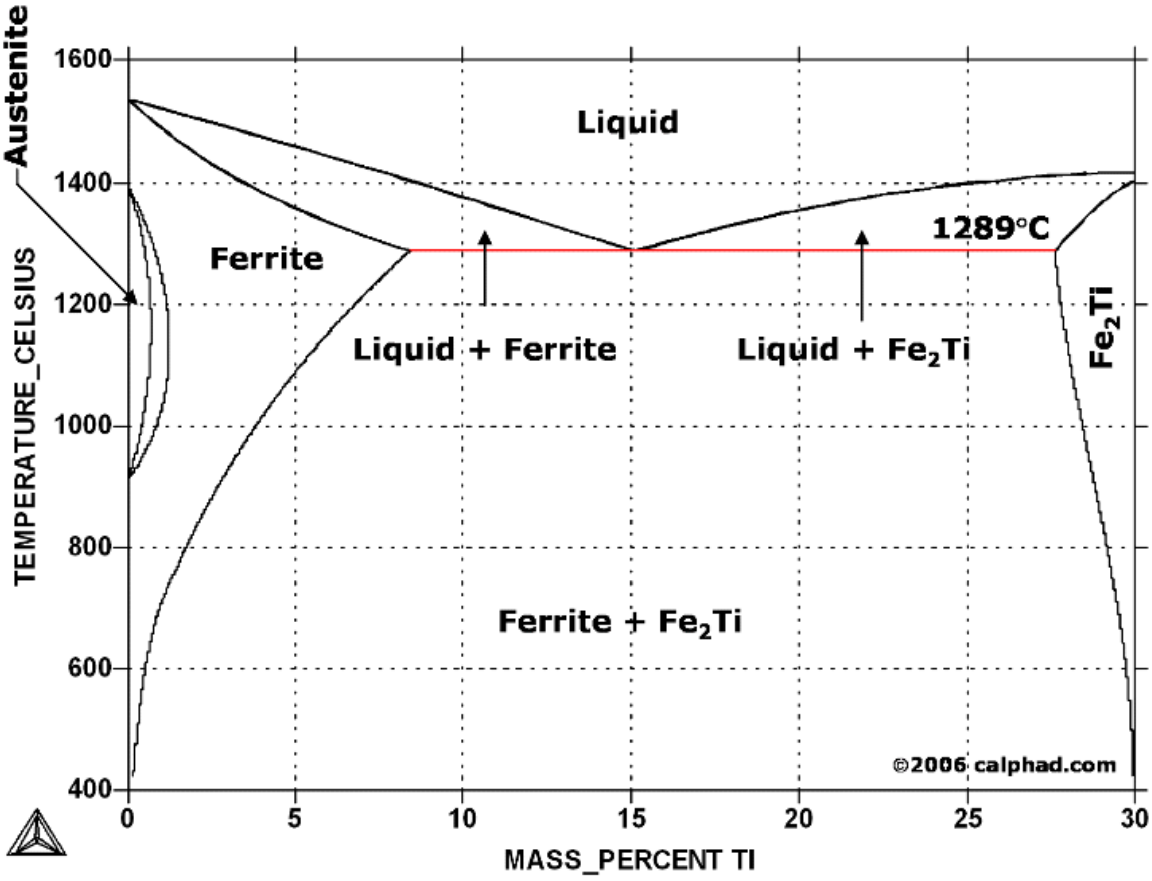

Figure B.2: Iron Titanium phase diagram [10]

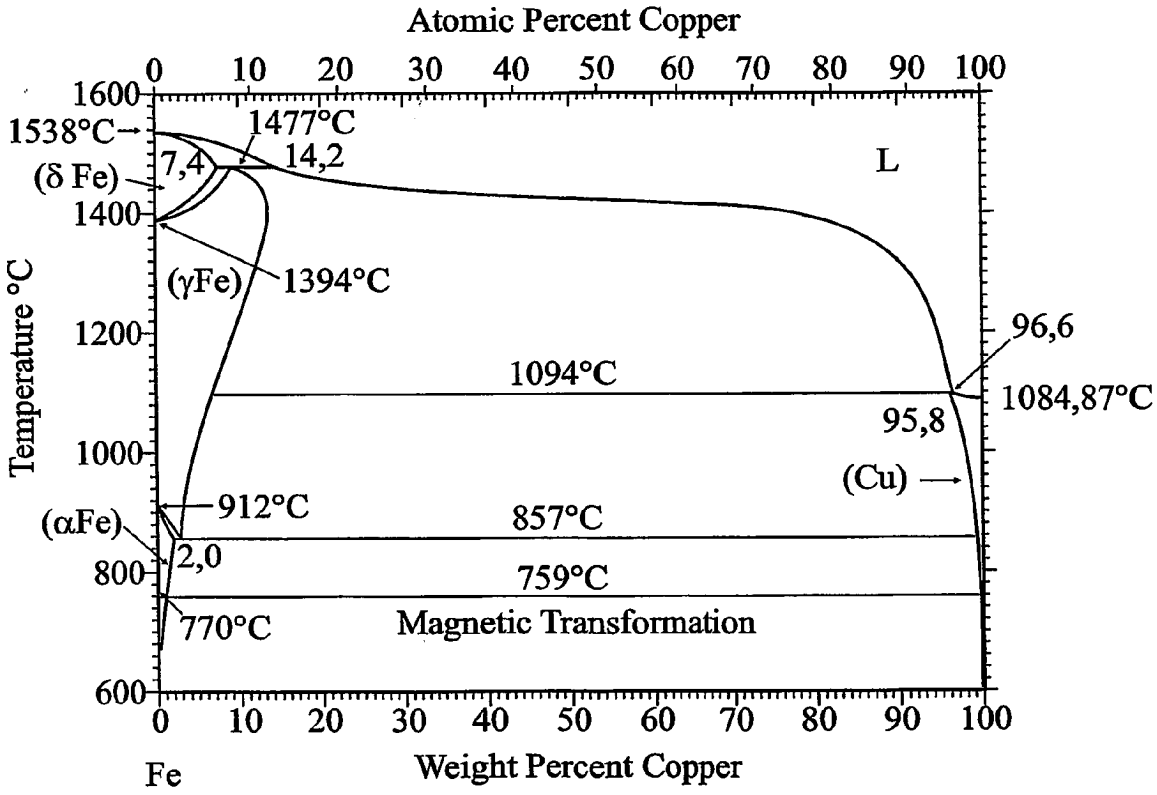

Figure B.3: Copper Iron phase diagram [9]

References

[1] G. Davies and T. Evans. Graphitization of diamond at zero pressure and at a high pressure. *Proceedings of the Royal Society of London. Series A, Mathematical and Physical Sciences*, 328(1574):413–427, 1972. xv, xvii, 16, 17, 21, 22

[2] V.D. Andreev. Spontaneous graphitization and thermal disintegration of diamond at T>2000K. *Physics of the Solid State*, 41(4):627–632, 1999. xv, xvii, 18, 19, 20, 21, 22

[3] J. Ion. *Laser Processing of Engineering Materials*. 2005. xv, 153, 154

[4] L.F.a Mei, G.Y.a Chen, B.b Zhang, G.G.a Chen, and K.a Huang. Measurement of YAG laser absorptance by artificial diamond and cubic boron nitride. *Optics and Laser Technology*, 41(6):770–777, 2009. xv, 153, 154, 155

[5] Genyu Chen, Lifang Mei, Bi Zhang, Chunrong Yu, and Kangjian Shun. Experiment and numerical simulation study on laser truing and dressing of bronze-bonded diamond wheel. *Optics and Lasers in Engineering*, 48(3):295 – 304, 2010. xv, 153, 154

[6] H.O. Pierson. *Handbook of carbon, graphite, diamond, and fullerenes: properties, processing, and applications*. William Andrew Publishing, 1993. xvii, 5, 6, 7, 13, 22, 23, 98, 108, 160

[7] EP Bundy. The P, T phase and reaction diagram for elemental carbon. *Geophys. Res*, 85:6930–6936, 1980. xvii, 10, 11

[8] J. Konstanty. *Powder metallurgy diamond tools*. Elsevier Science Ltd, 2005. xvii, 7, 8, 23, 24, 25, 26, 27, 28, 29, 30, 34, 36, 90, 91, 102, 120, 158, 175, 176

[9] [online]. ASM Handbooks Online. URL: http://products.asminternational.org/hbk/index.jsp, 2015. [Online; accessed 10-June-2015]. xix, xxiii, 45, 96, 202, 204

[10] [online]. Iron titanium phase diagram. URL: http://www.calphad.com/iron-titanium.html, 2015. [Online; accessed 10-June-2015]. xix, xxiii, 100, 203

[11] J. Lin. Temperature analysis of the powder streams in coaxial laser cladding. *Optics and Laser Technology*, 31(8):565–570, 1999. xxii, 149, 150

[12] K.E. Spear. Diamond-ceramic coating of the future. *Journal of the American Ceramic Society*, 72(2):171 – 91, 1989. 6, 7, 8, 9, 74

[13] Donald W. Olsen. Diamond, industrial 2003. Technical report, US Geological Survey (USGS), 2003. 7

[14] C. Owers. Industrial diamond: applications, economics and a view to the future. *Industrial Diamond Review*, 60(586):176–7, 2000. 8

[15] J. Konstanty. Production parameters and materials selection of powder metallurgy diamond tools. *Powder Metallurgy*, 49(4):299 – 306, 2006. 8

[16] Donald W. Olsen. Diamond, industrial 2008. Technical report, US Geological Survey (USGS), 2010. 8, 9

[17] Donald W. Olsen. Diamond, industrial 2009. Technical report, US Geological Survey (USGS), 2010. 9

[18] Donald W. Olsen. Diamond, industrial 2015. Technical report, US Geological Survey (USGS), 2015. 9

[19] DA Porter and KE Easterling. *Phase transformation in metals and alloys, 2nd edn;*. New York, Chapman and Hall, 1992. 10, 11, 13, 14, 15, 16

[20] VR Howes. The graphitization of diamond. *Proceedings of the Physical Society*, 80:648–662, 1962. 16, 17

[21] H.P. Bovenkerk, E.P. Bundy, H.T. Hall, H.M. Strong, and R.H. Wentorf, Jr. Preparation of diamond. *Nature (London)*, 184(4693):1094 – 1098, 1959. 16

[22] FP Bundy, HP Bovenkerk, HM Strong, and RH Wentorf Jr. Diamond-graphite equilibrium line from growth and graphitization of diamond. *The Journal of Chemical Physics*, 35:383, 1961. 16

[23] Glyn I. Harris. Long life resin bond wheels. *Industrial Diamond Review*, 49(532):123 – 125, 1989. 26

[24] A. TRENKER and H. SEIDEMANN. High-vacuum brazing of diamond tools. *Industrial diamond review*, 62(592):49–51, 2002. 30

[25] A. Lang and HW Bergmann. Herstellung diamanthaltiger, enkonturnaher metallmatrix-verbundwerkstoffe durch laserstrahlbeschichten. *Materialwissenschaft und Werkstofftechnik*, 27(5):215–226, 1996. 30, 35

[26] Anon. Sintering and brazing all in one. *Metal Powder Report*, 53(10):30 – 32, 1998. 31, 35, 36, 37

[27] Ehsan Toyserkani, Amir Khajepour, and Stephen Corbin. *Laser Cladding*. Boca Raton, Fl. : CRC Press, 2005. 31, 33, 39, 40, 41, 43, 50, 51, 54, 151, 180, 181

[28] L. Sexton. Laser cladding: repairing and manufacturing metal parts and tools. volume 4876, pages 462 – 9, USA, 2003. 33

[29] P.M. Scott, M. Nicholas, and B. Dewar. The wetting and bonding of diamonds by copper-base binary alloys. *Journal of Materials Science*, 10(11):1833 – 40, 1975. 34, 91

[30] B. Dewar, M. Nicholas, and P.M. Scott. The solid phase bonding of copper, nickel and some of their alloys to diamonds. *Journal of Materials Science*, 11(6):1083 – 90, 1976. 34

[31] Wen-Chung Li, Cheng Liang, and Shun-Tian Lin. Epitaxial interface of nanocrystalline tic formed between cu-10sn-15ti alloy and diamond. *Diamond and Related Materials*, 11(7):1366 – 73, 2002. 37, 91, 93

[32] C. Chan, J. Mazumder, and M.M. Chen. A two-dimensional transient model for convection in laser melted pool. *Metallurgical Transactions A (Physical Metallurgy and Materials Science)*, 15A(12):2175 – 84, 1984. 39, 40, 173

[33] A.F.A.a Hoadley and M.b Rappaz. A thermal model of laser cladding by powder injection. *Metallurgical Transactions B*, 23(5):631–642, 1992. 39

[34] M. Picasso, C.F. Marsden, J.-D. Wagniere, A. Frenk, and M. Rappaz. A simple but realistic model for laser cladding. *Metallurgical Transactions B (Process Metallurgy)*, 25(2):281 – 291, 1994. 42, 43, 149

[35] AFH Kaplan and G. Groboth. Process analysis of laser beam cladding. *Journal of manufacturing science and engineering*, 123(11):609–614, 2001. 42, 44

[36] E. Toyserkani, A. Khajepour, and S. Corbin. Three-dimensional finite element modeling of laser cladding by powder injection: effects of powder feedrate and travel speed on the process. *Journal of Laser Applications*, 15(3):153 – 60, 2003. 45

[37] E. Toyserkani, A. Khajepour, and S. Corbin. 3-D finite element modeling of laser cladding by powder injection: effects of laser pulse shaping on the process. *Optics and Lasers in Engineering*, 41(6):849 – 67, 2004. 45

[38] GUO LI-FENG. *Modelling of Laser Cladding of Magnesium Alloys with Pre-Placed Powders*. PhD thesis, The Hong Kong Polytechnic University, 2005. 46, 49, 50, 51, 53, 54

[39] W.M. Steen. *Laser material processing*. Springer Verlag, 2003. 49, 52, 59

[40] Warren M. Rohsenow, James P. Hartnett, and Young I. Cho. *Handbook of Heat Transfer (3rd Edition)*. McGraw-Hill, 1998. 52, 53

[41] YS Touloukian, RW Powell, CY Ho, and PG Klemens. *Thermophysical Properties of Matter-The TPRC Data Series. Volume 1. Thermal Conductivity-Metallic Elements and Alloys*. Storming Media, 1970. 54

[42] M.N. Rahaman. *Ceramic processing and sintering*. M. Dekker, 2003. 64

[43] D.S. Knight and W.B. White. Characterization of diamond films by Raman spectroscopy. *Journal of Materials Research*, 4(2):385 – 93, 1989. 74, 75, 76, 78, 80, 82, 84

[44] E. Smith and G. Dent. *Modern Raman spectroscopy: a practical approach*. Wiley, 2005. 74

[45] D.J. Gardiner, P.R. Graves, and H.J. Bowley. *Practical Raman Spectroscopy*. Springer Verlag, 1989. 74

[46] A. Cuesta, P. Dhamelincourt, J. Laureyns, A. Martinez-Alonso, and J.M.D. Tascon. Raman microprobe studies on carbon materials. *Carbon*, 32(8):1523 – 1532, 1994. 75

[47] F. Tuinstra and J.L. Koenig. Raman spectrum of graphite. *The Journal of Chemical Physics*, 53:1126, 1970. 75

[48] R.J. Nemanich and S.A. Solin. First- and second-order Raman scattering from finite-size crystals of graphite. *Physical Review B (Condensed Matter)*, 20(2):392 – 401, 1979. 75, 76

[49] P. Lespade, R. Al-Jishi, and M.S. Dresselhaus. Model for Raman scattering from incompletely graphitized carbons. *Carbon*, 20(5):427 – 31, 1982. 75, 76

[50] L.G. Cancado, K. Takai, T. Enoki, M. Endo, Y.A. Kim, H. Mizusaki, A. Jorio, L.N. Coelho, R. Magalhaes-Paniago, and M.A. Pimenta. General equation for the determination of the crystallite size La of nanographite by Raman spectroscopy. *Applied Physics Letters*, 88(16):163106 – 1, 2006. 75, 76

[51] L.G. Cancado, K. Takai, T. Enoki, M. Endo, Y.A. Kim, H. Mizusaki, N.L. Speziali, A. Jorio, and M.A. Pimenta. Measuring the degree of stacking order in graphite by Raman spectroscopy. *Carbon*, 46(2):272 – 5, 2008. 75, 76, 77

[52] R.J. Nemanich, G. Lucovsky, and S.A. Solin. Infrared active optical vibrations of graphite. *Solid State Communications*, 23(2):117 – 20, 1977. 76

[53] Pierre Lespade, Andre Marchand, Michel Couzi, and Francis Cruege. Characteristics of carbon materials by Raman microspectrometry. *Carbon*, 22(4-5):375 – 385, 1984. 76

[54] H. Wilhelm, M. Lelaurain, E. McRae, and B. Humbert. Raman spectroscopic studies on well-defined carbonaceous materials of strong two-dimensional character. *Journal of Applied Physics*, 84(12):6552 – 6558, 1998. 76

[55] P.A. de Chalus. Metal powders for optimum grain retention. *Industrial Diamond Review*, 54(563):170 – 172, 1994. 90

[56] JR Chalkley and DM Thomas. The tribological aspects of metal-bonded diamond grinding wheels. *POWDER MET*, 12(24):582–597, 1969. 91

[57] J. Konstanty. Developing a better understanding of the bonding and wear mechanisms involved in using diamond impregnated tools. In *International Workshop on Diamond Tool Production as held at the EURO PM 99*, pages 97–106, 1999. 91

[58] F.P. Bowden and D. Tabor. *The friction and lubrication of solids*. Oxford University Press, USA, 2001. 91

[59] Andrzej Romanski, Jan Lachowski, and Janusz Konstanty. Diamond retention capacity: Evaluation of stress field generated in a matrix by a diamond crystal. *Industrial Diamond Review*, 66(3):43 – 45, 2006. 91

[60] S.W. Webb. Crystal retention improves ROI and performance of diamond tools. *Finer Points(USA),*, 12(1):8, 2000. 91

[61] A. Saidi, A. Chrysanthou, J.V. Wood, and J.L.F. Kellie. Characteristics of the combustion synthesis of TiC and Fe-TiC composites. *Journal of Materials Science*, 29(19):4993 – 8, 1994. 93

[62] J.F. Shackelford and W. Alexander. *CRC materials science and engineering handbook*. CRC, 2001. 97

[63] W. Steen and J. Mazumder. *Laser Material processing*. Springer-Verlag London Limited, 2010. 108, 151, 152, 154, 158, 159, 178, 179

[64] Günther Höhne, Wolfgang F Hemminger, and H-J Flammersheim. *Differential scanning calorimetry*. Springer, 2003. 121, 128, 129

[65] G.P. Krielaart, C.M. Brakman, and S. Van Der Zwaag. Analysis of phase transformation in Fe-C alloys using differential scanning calorimetry. *Journal of Materials Science*, 31(6):1501 – 1508, 1996. 123

[66] W. Bendick and W. Pepperhoff. On the α/γ phase stability of iron. *Acta Metallurgica*, 30(3):679 – 84, 1982. 123

[67] R.L. Orr and J. Chipman. Thermodynamic functions of iron. *Transactions of the Metallurgical Society of AIME*, 239(5):630 – 633, 1967. 123

[68] Wiiliam J Boettinger, UR Kattner, KW Moon, and JH Perepezko. *DTA and heat-flux DSC measurements of alloy melting and freezing*. Citeseer, 2006. 128, 129

[69] J. Lin. Laser attenuation of the focused powder streams in coaxial laser cladding. *Journal of Laser Applications*, 12(1):28 – 33, 2000. 149

[70] W.-B. Li, H. Engstrom, J. Powell, Z. Tan, and C. Magnusson. Redistribution of the beam power in laser cladding by powder injection. *Lasers in Engineering*, 5(3):175 – 183, 1996. 149

[71] Yunchang Fu, A. Loredo, B. Martin, and A.B. Vannes. A theoretical model for laser and powder particles interaction during laser cladding. *Journal of Materials Processing Technology*, 128(1-3):106 – 112, 2002. 150

[72] J. Liu, L. Li, Y. Zhang, and X. Xie. Attenuation of laser power of a focused Gaussian beam during interaction between a laser and powder in coaxial laser cladding. *Journal of Physics D: Applied Physics*, 38(10):1546–1550, 2005. 150

[73] U. de Oliveira, V. Ocelík, and J.Th.M. De Hosson. Analysis of coaxial laser cladding processing conditions. *Surface and Coatings Technology*, 197(2-3):127–136, July 2005. 150

[74] J. Lin and B.-C. Hwang. Coaxial laser cladding on an inclined substrate. *Optics and Laser Technology*, 31(8):571–578, 1999. 150

[75] Andrew J. Pinkerton and Lin Li. Modelling powder concentration distribution from a coaxial deposition nozzle for laser-based rapid tooling. *Journal of Manufacturing Science and Engineering*, 126(1):33, 2004. 150, 151

[76] Andrew J Pinkerton. An analytical model of beam attenuation and powder heating during coaxial laser direct metal deposition. *Journal of Physics D: Applied Physics*, 40(23):7323–7334, 2007. 150, 151, 152

[77] O. O. Diniz Neto and R. Vilar. Physical-computational model to describe the interaction between a laser beam and a powder jet in laser surface processing. *Journal of Laser Applications*, 14(1):46, 2002. 150

[78] O. O. Diniz Neto, a. M. Alcalde, and R. Vilar. Interaction of a focused laser beam and a coaxial powder jet in laser surface processing. *Journal of Laser Applications*, 19(2):84, 2007. 150

[79] A.J. Pinkerton and L. Li. A verified model of the behaviour of the axial powder stream concentration from a coaxial laser cladding nozzle. 2002. 151

[80] J. Lin. Numerical simulation of the focused powder streams in coaxial laser cladding. *Journal of Materials Processing Technology*, 105(1):17–23, 2000. 151

[81] R.R. Unocic and J.N. DuPont. Process efficiency measurements in the laser engineered net shaping process. *Metallurgical and Materials Transactions B (Process Metallurgy and Materials Processing Science)*, 35B(1):143 – 52, 2004. 151

[82] Jichang Liu and Lijun Li. Effects of powder concentration distribution on fabrication of thin-wall parts in coaxial laser cladding. *Optics and Laser Technology*, 37(4):287 – 92, 2005. 152

[83] J. Lin and W.M. Steen. Design characteristics and development of a nozzle for coaxial laser cladding. *Journal of Laser Applications*, 10(2):55–63, 1998. 152

[84] T.R. Tucker, A.H. Clauer, I.G. Wright, and J.T. Stropki. Laser-processed composite metal cladding for slurry erosion resistance. *Thin Solid Films*, 118(1):73–84, 1984. 152

[85] J.-M.a Jouvard, D.F.a Grevey, F.a Lemoine, and A.B.b Vannes. Continuous wave Nd:YAG laser cladding modeling: A physical study of track creation during low power processing. *Journal of Laser Applications*, 9(1):43–50, 1997. 152

[86] W.W. Duley. Laser material interactions of relevance to metal surface treatment. Number 115, pages 3–16, 1986. 154

[87] Craig F Bohren and Donald R Huffman. *Absorption and scattering of light by small particles*. John Wiley & Sons, 1983. 158

[88] W M. Steen, V M. Weerasinghe, and P Monson. Some aspects of the formation of laser clad tracks, 1986. 169, 178, 179, 180

[89] H. Gedda, J. Powell, G. WahlstroIm, W.B. Li, H. EngstroIm, and C. Magnusson. Energy redistribution during CO_2 laser cladding. *Journal of Laser Applications*, 14(2):78, 2002. 169

[90] G.M. Oreper, T.W. Eagar, and J. Szekely. Convection in arc weld pools. *Welding Journal*, 62(11):307 – 312, 1983. 173

[91] J. Mazumder. Overview of melt dynamics in laser processing. *Optical Engineering*, 30(8):1208 – 19, 1991. 173

[92] P.L. Hurricks. Some metallurgical factors controlling the adhesive and abrasive wear resistance of steels. a review. *Wear*, 26(3):285 – 304, 1973. 176

[93] E. Kannatey-Asibu. *Principles of Laser Materials Processing*. 2008. 180

[94] Mohammad H Farshidianfar, Amir Khajepour, and Adrian Gerlich. Real-time control of microstructure in laser additive manufacturing. *The International Journal of Advanced Manufacturing Technology*, pages 1–14, 2015. 193

Index